# Stimulated Brillouin scattering in chalcogenide microfiber sensors and random fiber lasers

Haiyang Wang

A thesis submitted in partial fulfillment of the
requirements for the Degree of
**Doctor of Philosophy**
in
**Physics**

Ottawa-Carleton Institute of Physics
Department of Physics
Faculty of Science
University of Ottawa

**Abstract**

Stimulated Brillouin scattering (SBS), the interaction between two optical waves and an acoustic wave, has been extensively studied in optical fiber sensors and random fiber lasers over the previous three decades. Brillouin fiber sensors are essential for structural health monitoring. Brillouin fiber sensors provide high resolution, distributed detection, and absolute strain and temperature measurements over a wide dynamic range. Brillouin sensing has mostly been studied in conventional single-mode fibers (SMF). The low nonlinearity and large Young's modulus of SMFs have limits in many applications. Chalcogenide fibers with high nonlinearity and low Young's modulus are of particular interest for Brillouin scattering investigations and sensing applications. Coherent laser sources with small frequency drift and low intensity noise are essential for optical communication, sensing, and metrology. SBS with high gain and narrow linewidth in optical fibers contributes to single-mode Brillouin random fiber lasers (BRFL) working with a low threshold. Previous studies of BRFLs with weak scattering distributed feedback have failed to address frequency drift and intensity noise. Random fiber grating (RFG) distributed feedback with strong scattering can manipulate mode dynamics of BRFLs. In this thesis, we demonstrate that chalcogenide microfibers can improve Brillouin sensing, and that RFG distributed feedback can stabilize Brillouin random fiber lasing. Furthermore, we present the detection of acoustic waves using chalcogenide microfiber sensors.

In the first part of this thesis, we explore SBS characterizations and Brillouin sensing in chalcogenide microfibers. Chapter 4 describes the fabrication and simulation of polymethyl methacrylate (PMMA) coated chalcogenide ($As_2Se_3$) microfibers. Chalcogenide-PMMA ($As_2Se_3$-PMMA) microfibers are mechanically robust enough for regular handling, allowing for Brillouin strain and temperature sensing. We present a SBS model to calculate the Brillouin gain spectrum of chalcogenide microfibers. Chalcogenide microfibers with ultrahigh nonlinearity give rise to Brillouin sensing under low pump power. Chapter 5 investigates wide-range strain sensing in single-core chalcogenide microfibers based on Brillouin frequency shift and bandwidth. SBS sensing is characterized using the Brillouin optical time domain analysis (BOTDA) technique. Chalcogenide-PMMA microfibers with lower Young's modulus than SMFs lead to a larger strain measurement range. Chapter 6 explores SBS characterizations and Brillouin sensing in high-birefringence chalcogenide microfibers with dual-core and elliptical-core shapes. Different responses in two polarization axes of the high-birefringence microfibers are used to distinguish two parameter variations. Different pairs of pump-probe modes in elliptical-core fibers allow for both intermode SBS and intramode SBS to be experimentally measured.

In the second part of this thesis, we show that the frequency drift of SBS random fiber

lasers can be reduced by a random fiber grating array (RFGA), a random fiber grating ring (RFGR), and acoustic wave coupling. RFGs have strong scattering due to high refractive index modulations by an external femtosecond pulse laser. Chapter 7 demonstrates that the strong scattering RFGA-based BRFL has a long-lived lasing mode of 12 s and slight frequency drift of 51 kHz/s at high pump power. This is enabled by light localization in the RFGA resulting from wave interference and multiple scattering. Photon trapping in the same path over thousands of round trips offers coherent lasing without mode hopping. Chapter 8 presents the frequency-stabilized BRFL based on the RFGR distributed feedback. The RFGR consisting of a RFG and a high split ratio coupler exhibits narrow linewidth due to the circulating propagation of light within the ring. Taking the advantages of self-adjusting random states with slight frequency differences to small thermal and acoustic variations and self-injection locking through the high-Q RFGR, the BRFL has mode hopping free operation over 14.9 s with a small frequency drift of ∼340 kHz. Chapter 9 investigates the dynamics of the dual-wavelength orthogonal polarized BRFL based on polarization-maintaining (PM) fibers. Acoustic wave coupling is introduced in the all-PM BRFL when the pump light is aligned at 45 degrees from the slow axis of the PM fiber due to the changed polarization and overlapped gain spectrum in the birefringence fiber-based laser. Due to the higher peak in the overlapping gain region, the frequency drift in the BRFL with acoustic wave coupling is reduced by around 1 MHz compared to the BRFL without acoustic wave coupling. The multi-peaks of Pearson's correlation coefficient and replica symmetry breaking confirm acoustic wave coupling in the BRFL.

Appendix A investigates acoustic wave sensing in dual-core chalcogenide microfibers. The acoustic wave is driven by the mechanical stress from a piezoelectric transducer, which leads to pressure on the dual-core microfiber. The phase change of the propagating light in the dual-core microfiber is detected by intensity variations. The chalcogenide fiber with low Young's modulus has large strain sensitivity, leading to a high-frequency ultrasound measurement. The ultrasound sensing range is increased in the microfiber with a small core diameter and close core separation because of the steep spectral slope of the interference spectrum. The fused dual-core microfiber achieves a broadband ultrasound range of 20 kHz to 80 MHz with an average signal-to-noise ratio of 31 dB.

**Statement of Originality**

This work contains no material accepted for awarding any other degree or diploma in any university or tertiary institution and contains no material previously published or written by another person, except where due reference has been made in the text.
I give consent to this copy of my thesis, when deposited in the University Library, being available for loan and photocopying.

Signed : . . . . . .
Date : . . . . . .

Supervisor : Prof. Xiaoyi Bao

**Acknowledgements**

First and foremost, I would like to express my deepest appreciation to my supervisor, Prof. Xiaoyi Bao, who opened a new door and steered me through my Ph.D. study. She is a great person with a profound knowledge of physics and critical thinking. I was inspired after each discussion since she always gave me valuable advice that deepened my understanding of the physics behind the problem. This thesis would not have been possible without her great sense of intuition. I would also like to thank Prof. Liang Chen for his valuable advice in our weekly group seminars and informative discussions during the past four years.

I would like to thank Dr. Song Gao for helping me fabricate the chalcogenide-PMMA microfiber. His passion and seriousness about scientific research guided me, and I have learned so much from him. I also thank Dr. Chams Baker for helping me with device fabrication. He also inspired me with some exciting ideas regarding the applications of the chalcogenide-PMMA microfiber. I would also like to express my great gratitude to Dr. Ping Lu, who assisted in fabricating random fiber gratings and offered me some valuable suggestions for writing this thesis. I would like to thank Dr. Zichao Zhou for the helpful discussions and assistance with the random fiber grating simulation. I want to thank Dr. Bhavaye Saxena for helping me understand the simulation of the Brillouin scattering enabling the consolidation of the calculated results presented in this thesis. Many thanks to Mr. Chen Chen for thoughtful discussions on the random grating ring. I would also like to thank Mr. Liam Kelly, who helped me calibrate the ultrasound transducer. I also want to thank Mr. Ole Krarup for his discussions and suggestions on nonlinear fiber optics. It is a great pleasure to work with them during my Ph.D.

I would like to thank Mr. Yuan Wang and Dr. Liang Zhang for their tremendous assistance and guidance with my experiments. I would also like to thank other group members, Mr. Gerard Tatel, Dr. Pedro Tovar, Mrs. Wenwen Ma, Dr. Zhuo Wang, Dr. Jianxia Liu, Dr. Huibo Fan, and Dr. Benoit Vanus, for discussions in group seminars.

I'm also thankful to Dr. Le Qiao, Mr. Kaiyi Zhang, Mr. Bin Cheng, Ms. Bingxin Xu, and Mr. Chuanjing Li for hosting parties and happy traveling moments.

I thank the China Scholarship Council (CSC) and the University of Ottawa for funding this project. My Ph.D. study would not have been possible without their generous support.

Last but not least, my most enormous gratitude goes to my parents for all their thoughtfulness and encouragement.

Finally, I am incredibly grateful to my wife, Tingting Cao, for her emotional support and understanding during my Ph.D. study.

# List of Abbreviations

| | |
|---|---|
| AFG | Arbitrary Function Generator |
| AOM | Acousto-Optical Modulator |
| ASE | Amplified Spontaneous Emission |
| BDG | Brillouin Dynamic Grating |
| BFS | Brillouin Frequency Shift |
| BOCDA | Brillouin Optical Correlation Domain Analysis |
| BOTDA | Brillouin Optical Time-Domain Analysis |
| BOTDR | Brillouin Optical Time-Domain Reflectometry |
| BRFL | Brillouin Random Fiber Laser |
| CW | Continuous Wave |
| DCM | Dual-Core Microfiber |
| DPP-BOTDA | Differential Pulse-Width Pair Brillouin Optical Time-Domain Analysis |
| DSH | Delayed Self-Heterodyne |
| ECL | External Cavity Laser |
| ECORE | Elliptical Core |
| EDFA | Erbium-Doped-Fiber-Amplifier |
| EOM | Electro-Optic Modulator |
| ER | Extinction Ratio |
| ES | Electrostriction Stress |
| ESA | Electrical Spectrum Analyzer |
| FBG | Fiber Bragg Grating |
| FC | Fiber Coupler |
| FEM | Finite Element Method |
| FG | Function Generator |
| FP | Fabry–Pérot |

| | |
|---|---|
| FPI | Fabry–Pérot Interferometer |
| FSBS | Forward Stimulated Brillouin Scattering |
| FSR | Free Spectral Range |
| FUT | Fiber Under Test |
| FWHM | Full Width at Half Maximum |
| FWM | Four-Wave Mixing |
| FRM | Faraday Rotator Mirror |
| GAWBS | Guided Acoustic Wave Brilluiouin Scattering |
| LP | Linear Polarizer |
| MSF | Microstructure Fiber |
| MZI | Mach-Zehnder Interferometer |
| NIST | National Institute of Standards and Technology |
| OFDR | Optical Frequency-Domain Analysis |
| OTDR | Optical Time-Domain Analysis |
| OSA | Optical Spectrum Analyzer |
| OSC | Oscilloscope |
| PBS | Polarization Beam Splitter |
| PC | Polarization Controller |
| PD | Photodetector |
| PER | Polarization Extinction Ratio |
| PGIF | Inverse-Parabolic Graded-Index Fiber |
| PM | Polarization-Maintaining |
| PMMA | Polymethyl Methacrylate |
| POF | Polymer Optical Fiber |
| POFBG | Polymer Optical Fiber Bragg Grating |
| PPP-BOTDA | Pulse Prepump Brilliouin Optical Time Domain Analysis |
| PSD | Power Spectral Density |
| PZT | Piezoelectric Transducer |
| RF | Radio Frequency |
| RFG | Random Fiber Grating |
| RFGA | Random Fiber Grating Array |
| RFGR | Random Fiber Grating Ring |
| RFL | Random Fiber Laser |
| RIN | Relative Intensity Noise |
| RL | Random Laser |
| RS | Rayleigh Scattering |

| | |
|---|---|
| RSB | Replica Symmetry Breaking |
| SBS | Stimulated Brillouin Scattering |
| SMA | SubMiniature Version A |
| SMF | Single Mode Fiber |
| SMSR | Side-Mode Suppression Ratio |
| SNR | Signal-to-Noise Ratio |
| SRS | Stimulated Raman Scattering |
| STD | Standard Deviation |
| TPG | Transient Population Grating |
| UV | Ultraviolet |
| WDM | Wavelength Division Multiplexer |
| XOR | Exclusive Or |

# Table of Contents

# 1 Introduction

## 1.1 Overview

Since Léon Brillouin first proposed the theoretical prediction of Brillouin scattering in 1922 [1], Brillouin scattering has been considered to be fundamental in optical physics and applications. Stimulated Brillouin scattering (SBS), involving the interaction between intense lasing beams and an acoustic wave, was first experimentally demonstrated in quartz and sapphire crystals in 1964 [2]. SBS is an inelastic scattering process that enables the incident wavelength to be shifted by a certain amount. The optical fiber produced by Charles Kao in 1966 provided a new platform to investigate SBS [3]. SBS in optical fibers was experimentally measured several years later by Ippen and Stolen [4]. Due to the transverse geometry of the fiber, the directions of the scattered light are both forward and backward. The backward Brillouin scattering can generate a high-intensity Stokes wave in the direction opposite to the incident light, while the forward Brillouin scattering is extremely weak [5].

Over the past few decades, there has been a significant increase in the investigation of Brillouin fiber sensing. Brillouin fiber sensors have many advantages, such as high accuracy due to the frequency revolved interrogation, high spatial resolution, and distributed sensing ability. SBS in single-mode fibers (SMF) has proved its eligibility for monitoring oil and gas pipelines, and civil engineering health, such as bridges, tunnels, and dams [6, 7]. SBS is a nonlinear process governed by the nonlinear parameter ($\gamma$). The nonlinear parameter is given by $\gamma = k_0 n_2 / A_{eff}$, where $n_2$ is the nonlinear refractive index, $A_{eff}$ is the effective mode field and $k_0 = 2\pi/\lambda$ is the wave-number with $\lambda$ being the wavelength. The value of $\gamma$ in the silica-based SMF is too small to be used in applications requiring short lengths [5]. The weak Brillouin scattered signal in short SMFs leads to limits in sensing. To solve this

problem, highly nonlinear chalcogenide fibers consisting of one or more chalcogen elements such as sulfur (S), selenium (Se), and tellurium (Te) have been developed [8]. The most popular chalcogenide $As_2Se_3$ fiber has a nonlinear refractive index 600 times larger than the silica-based SMF at 1.55 μm [9]. The high nonlinearity of the $As_2Se_3$ fiber gives rise to SBS generation in a short length under low pump power, allowing for practical sensing applications.

The SBS process produces high Brillouin gain in the opposite direction of the incident light resulting in the amplification of the optical wave with the resonant Brillouin frequency. Brillouin gain can be used to fabricate lasers by placing the gain fiber inside well-defined resonant cavities (conventional fiber lasers), or disordered cavities (random fiber lasers). Compared to stimulated Raman scattering (SRS) in SMFs, SBS has a higher gain coefficient and narrower gain bandwidth [5]. Therefore, SBS-based RFLs can achieve a single lasing mode and a low threshold. The first Brillouin fiber laser was studied based on a Fabry-Pérot (FP) resonator geometry in 1976 [10]. Since then, Brillouin cavity lasers with narrow linewidth in advanced configurations and their applications in sensing have been developed [11, 12]. In contrast to conventional lasers with well-defined cavities, random lasers (RL) are achieved by multiple light scattering in disordered gain media. The RL with non-resonant feedback was achieved by replacing one mirror of the FP cavity with a scattering surface [13]. The random nature of RLs creates a new class of optical lasing. The combination of Brillouin scattering and random lasing in optical fibers, so-called Brillouin random fiber lasers (BRFL), is particularly interesting because the simple and cost-effective lasing system exhibits high efficiency, suppressed self-pulsations, good frequency stabilization, and low intensity noise.

In this thesis, we investigate SBS in chalcogenide microfiber sensing and polarization-maintaining (PM) random fiber lasing. The first objective of this thesis is to investigate SBS and its sensing characterizations in chalcogenide microfibers. The second objective of this thesis is to study the dynamics of Brillouin random fiber lasers in PM fibers based on different distributed feedback and light propagation mechanisms to reduce frequency drift and intensity noise.

## 1.2 Motivation and Thesis contribution

### 1.2.1 Motivation

SBS has been widely used in optical fiber sensors and fiber lasers. SBS sensors are primarily concerned with widely-used communication fibers, such as SMFs. However, silica-

based SMFs have limits in many SBS sensing applications due to their low nonlinearity, large Young's modulus, and low sensitivity to environmental variations. High nonlinear chalcogenide fibers allow for short-length SBS sensors at low pump power. Chalcogenide microfibers with low Young's modulus and high design flexibility offer a method to measure large strain and multiple parameters. The motivation of SBS sensing in this thesis is to develop wide-strain and multi-parameter Brillouin sensing in chalcogenide microfibers.

Brillouin fiber lasers have attracted attention due to the narrow gain bandwidth and high gain coefficient of SBS. In Brillouin fiber lasers with resonant cavities, the round-trip accumulated phase after reflectors must equal some integer multiple of $2\pi$. The frequencies of cavity modes satisfy $c/(2nl)$, where $c$ is the light velocity in a vacuum, $n$ is the fiber's refractive index, and $l$ is the cavity length. Therefore, the lasing emission exhibits discrete modes at specific resonant frequencies. Additional devices with the narrow filter effect should be added to a resonant cavity to suppress multiple modes. Resonant cavities based on Bragg fiber gratings or ring structure make all reflections at the same peak of longitudinal modes. Any disturbance from temperature or vibration induces mode hopping and large frequency drift. BRFLs based on non-resonance feedback can suppress self-pulsations thanks to many random modes with different phases, wavelengths, and amplitude. BRFLs based on kilometers-long Rayleigh scattering (RS) distributed fibers generate many random modes with large frequency separations leading to strong intensity fluctuations and high relative intensity noise (RIN). RS-based BRFLs also exhibit large frequency drift due to hopping between different modes. We need to manipulate random modes in the BRFLs with short random feedback. The motivation of SBS random fiber lasing in this thesis is to reduce frequency drift and RIN using random fiber grating (RFG) distributed feedback.

### 1.2.2 Thesis contribution

This thesis introduces SBS in chalcogenide microfiber sensing and PM random fiber lasing. Major contributions of this thesis include :

(1) We present a wide-range strain sensor based on a single-core chalcogenide microfiber using Brillouin optical time-domain analysis (BOTDA). The chalcogenide microfiber with a core diameter of 2.5 µm enables a strain measurement as high as 15000 µε. The chalcogenide fiber exhibits a linear change in Brillouin frequency shift (BFS) and a nonlinear change in Brillouin linewidth with increasing strain. In contrast to polymer optical fiber sensors, chalcogenide microfiber sensors do not have the strain memory effect due to the larger Young's modulus. Chalcogenide microfiber sensors can monitor civil infrastructures such as railways and bridges with steel structures that need to withstand a larger strain than the breaking strain of silica fibers (1%).

(2) We explore a dual-core chalcogenide microfiber for simultaneous strain and temperature Brillouin sensing. Brillouin gain spectra are measured experimentally in the dual-core microfiber with a core diameter of 2 µm, which agree with the calculated results. The temperature coefficients are -3.83 MHz/°C and -3.33 MHz/°C, and the strain coefficients are -0.061 MHz/µε and -0.035 MHz/µε in two axes. The dual-core microfiber can be used for simultaneous temperature and strain sensing because of the decorrelated temperature and strain coefficients in two polarization axes. The maximum temperature and strain measurement errors are estimated to be 1 °C and 33 µε, respectively. We also investigate SBS in high-birefringence elliptical-core chalcogenide microfibers. The birefringence is tailorable by tapering the elliptical-core chalcogenide fiber to different core diameters. Both experimental and numerical results demonstrate that a high birefringence of $\sim 10^{-3}$ to $\sim 10^{-2}$ and a large BFS difference of ∼6 MHz to ∼30 MHz are achieved as the core diameter of the minor axis of the microfiber is decreased from 1.50 µm to 0.87 µm. The high nonlinear chalcogenide microfibers enable Brillouin sensing at a low pump power of 9 dBm.

(3) We demonstrate that the frequency drift of the SBS random fiber laser is reduced using strong scattering random fiber grating array (RFGA) distributed feedback. Wave interference and multi-scattering of light between RFG pairs in the RFGA lead to photon localization. The RFGA exhibits high finesse peaks at high pump power due to wave interference in multiple FP cavities formed between RFG pairs. Multiple modes are suppressed by the high finesse peaks. The change of mode number confirms the power-dependent bandwidth change of the reflection spectrum as a function of pump power. Single-mode lasing is achieved when the pump power is higher than 20 mW. The spectrum evolution of the beat frequency between the pump laser and the BRFL is continuously measured to show the stabilization of the BRFL. A long-lived lasing mode of 12 s with a small frequency drift of 620 kHz and a low correlation coefficient change of 4.5% is achieved at the pump power of 117 mW due to photon localization in the RFGA, in which the photon follows the same path length. The weak RS-based BRFL shows a larger frequency drift (6 MHz) with faster mode hopping (0.3 s) compared to the RFGA-based BRFL, confirming the contribution of photon localization of strong scattering feedback in frequency stabilization. Weak intensity fluctuations with Gaussian distribution and maintained replica symmetry at high pump power indicate the long-lived single-mode lasing operation in the RFGA-based BRFL. Our research provides a novel approach to passively stabilizing the frequency of BRFLs without the need for active phase locking laser mechanisms, resulting in a straightforward and reasonably priced system.

(4) We investigate the frequency-stabilized BRFL based on the random fiber grating ring (RFGR) resonator. The reflection spectrum of the RFGR shows narrow linewidth peaks due to the recirculating light propagating in the ring, which is confirmed by ex-

perimental and calculated results. The high-Q RFGR works as a narrow filter to select one mode within the Brillouin gain bandwidth. Many random modes with small frequency differences in the RFGR compensate for small external variations. The Brillouin random lasing receives optical feedback from the high-Q RFGR leading to self-injection locking. Therefore, the BRFL has a small lasing frequency drift of ∼340 kHz without mode hopping over 14.9 s. Compared to the low-Q RFG-based BRFL, the side-mode suppression ratio (SMSR) is increased by 20 dB in the high-Q RFGR-based BRFL. Due to the suppression of multiple modes and the reduction of gain competition, The BRFL exhibits low frequency noise and low intensity noise at high frequencies. The high-Q RFGR distributed feedback provides an all-optical locking mechanism for stabilizing the frequency of optical lasing.

(5) We present acoustic wave coupling in the dual-wavelength orthogonal polarized BRFL based on the PM fiber. The dual-wavelength BRFL is generated by pumping the light at 45 degrees from the slow axis of the PM fiber. Acoustic wave coupling occurs because the BFS difference of 5 MHz between two principal axes (corresponding to the birefringence difference of $10^{-4}$) is smaller than the Brillouin gain bandwidth of 20 MHz, resulting in the overlapping of two acoustic modes within the gain bandwidth. The frequency drift is reduced by around 1 MHz through acoustic wave coupling because of the high gain peak in the overlapping region. The multiple peaks of Pearson's correlation coefficient spectra and replica symmetry breaking are measured due to the acoustic wave coupling induced mode coupling. The exploration of spectra correlation, intensity fluctuation, and frequency drift in the random laser with acoustic wave coupling has an influential effect on the future design of random fiber lasers for practical applications in coherent light sources and optical sensing.

(6) We study broadband ultrasound sensing in dual-core chalcogenide microfibers. The chalcogenide microfiber has a high strain sensitivity due to its low Young's modulus. The wavelength-dependent refractive index difference between two modes in one polarization axis increases with decreased core diameter, allowing for the increased spectral slope of the interference spectrum. The detected signal is proportional to the spectral slope of the interference spectrum. As a result, the dual-core microfiber with a high spectral slope has a large ultrasound sensing range. The ultrasound sensing from 20 kHz to 80 MHz is measured using the dual-core chalcogenide microfiber with a core diameter of 0.5 μm.

## 1.3 Thesis outline

This thesis is structured as following :

Chapter 1 introduces an overview of Brillouin scattering, thesis motivation, thesis

contribution, and thesis outline. Chapter 2 reviews the background of Brillouin fiber sensors and random fiber lasers based on different mechanisms. Chapter 3 presents the fundamentals of Brillouin scattering and Brillouin scattering sensing measurement. The theory of Brillouin random fiber lasers is presented. Light propagation in strong scattering artificial random fiber grating feedback and weak scattering Rayleigh scattering feedback are discussed. The applications of Brillouin random fiber lasers and the characterizations of BRFL are discussed and summarized in detail.

Chapter 4 presents the theoretical calculation of SBS and the fabrication of chalcogenide microfibers. The SBS model is built based on the elastodynamic equation. The Brillouin gain spectrum of the chalcogenide microfiber is calculated. The fabrication of chalcogenide-PMMA microfibers is presented.

Chapter 5 investigates wide-range strain measurement based on SBS in single-core chalcogenide microfibers. The strain sensor is characterized by measuring the Brillouin gain spectrum, such as Brillouin frequency shift and Brillouin linewidth. Chapter 6 explores SBS in high-birefringence elliptical-core and dual-core chalcogenide microfibers, and the application of the dual-core microfiber for simultaneous strain and temperature Brillouin sensing.

Chapter 7 investigates a stabilized BRFL with photon localization enabled by RFGA distributed feedback. Photon localization in the strong scattering RFGA leads to a long-lived lasing mode with small frequency drift. The weak Rayleigh scattering distributed feedback-based BRFL with fast mode hopping within a large frequency range is also discussed.

Chapter 8 studies a BRFL with reduced frequency fluctuation based on a RFGR resonator. The narrow linewidth of the RFGR is confirmed experimentally and numerically. The mode evolution, frequency noise, and intensity noise of the BRFL are discussed when the Brillouin random lasing frequency is and is not in resonance with the peak frequency of the RFGR.

Chapter 9 presents acoustic wave coupling in a dual-wavelength orthogonal-polarized Brillouin random fiber based on a PM fiber. The intensity statistics, intensity noise, frequency drift, Parisi overlap parameter, and Pearson's correlation coefficient are measured for the random lasers with and without acoustic wave coupling.

Chapter 10 summarizes the main results of this thesis and proposes possible perspectives for future research with chalcogenide microfiber sensing and noise-reduced Brillouin random fiber lasing. Appendix A presents broadband acoustic wave sensing based on dual-core chalcogenide microfibers.

# 2 Background

This chapter introduces the background and fundamental concepts of Brillouin scattering. Section 2.1 gives a brief overview of acoustic waves, including the generation of acoustic waves driven by optical waves and the generation of acoustic waves driven by electric fields. In section 2.2, Brillouin fiber sensors based on different mechanisms and Brillouin sensing in chalcogenide fibers are reviewed. In section 2.3, random fiber lasers based on various gain and feedback mechanisms and temporal and spectral dynamics are discussed.

## 2.1 Acoustic waves

Acoustic waves are mechanical waves generated by the displacement of atoms or particles over time in materials. Due to the 3D response of acoustic wave propagation in media, acoustic wave propagation is expressed by tensor quantities. Acoustic waves can be generated and enhanced by optical waves in an optical medium (non-piezoelectric material) through electrostrictive stress or by electric fields in a piezoelectric material via mechanical stress. The acoustic wave generated in an optical medium by light pumping through electrostriction enables stimulated Brillouin scattering (SBS). The acoustic wave generated by a piezoelectric transducer induces mechanical stress, which affects the physical quantities of optical fibers and modulates the optical phase of propagating light.

### 2.1.1 Acoustic waves in non-piezoelectric materials

#### Modes of acoustic waves

Acoustic waves propagating in non-piezoelectric materials mainly consist of longitudinal and transverse acoustic waves. For the longitudinal acoustic wave, the motion of particles in a medium is parallel to the direction of wave propagation, as shown in Fig. 2.1(a). For the shear acoustic wave, the motion of particles in a medium is perpendicular to the direction of wave propagation, as shown in Fig. 2.1(b). The expansion and contraction in the z-direction caused by the motion of particles of the longitudinal wave lead to density fluctuations, while there is no density change for the shear wave. Another type of acoustic wave, called the surface acoustic wave, is caused by the vibrations of many particles at the surface of a medium.

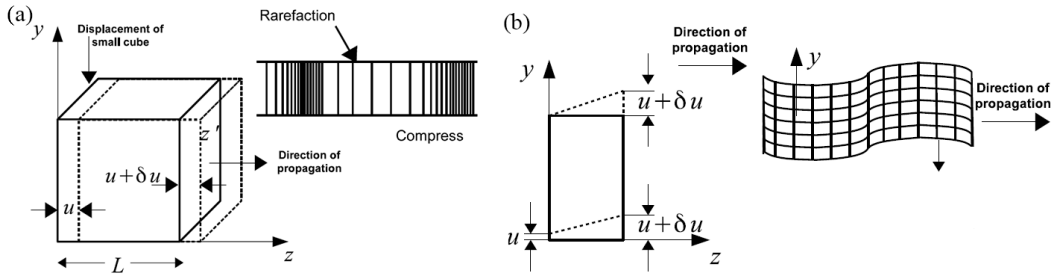


FIGURE 2.1 – (a) Longitudinal and (b) shear acoustic waves propagation [14]

#### Displacement, stress and strain

When an external force is applied to a solid, it produces stress on its surface. Stress results in strain, which causes atoms or particles in the solid to move away from their equilibrium positions. Displacement is the distance of a particle from its original position. In order to generalize the physical quantities of acoustic waves to include all possible components in solids, it is necessary to use tensor quantities. Displacement is typically represented by the vector $\mathbf{u}$, which has components in the $x$, $y$, and $z$ directions ($u_x$, $u_y$, and $u_z$), and each of components can be a function of three Cartesian components $x$, $y$, and $z$ of the vector $\mathbf{r}$. Therefore, strain will be a tensor $\mathbf{S}$ with nine components. Strain components are defined as [15]

$$S_{ii} = \frac{\partial u_i}{\partial i} \tag{2.1}$$

$$S_{ij} = \frac{1}{2}\left(\frac{\partial u_i}{\partial j} + \frac{\partial u_j}{\partial i}\right) \tag{2.2}$$

where $i, j = x, y, z$. $S_{ij}$ represents the symmetric component, and therefore $S_{ij} = S_{ji}$. Contracted notation has been introduced to reduce the number of indices from two to one : (11) $\leftrightarrow$ (1), (22) $\leftrightarrow$ (2), (33) $\leftrightarrow$ (3), (23) = (32) $\leftrightarrow$ (4), (13) = (31) $\leftrightarrow$ (5), (12) = (21) $\leftrightarrow$ (6). The strain tensor is expressed as

$$\mathbf{S} = \begin{bmatrix} S_{xx} & S_{xy} & S_{xz} \\ S_{yx} & S_{yy} & S_{yz} \\ S_{zx} & S_{zy} & S_{zz} \end{bmatrix} = \begin{bmatrix} S_1 & \frac{1}{2}S_6 & \frac{1}{2}S_5 \\ \frac{1}{2}S_6 & S_2 & \frac{1}{2}S_4 \\ \frac{1}{2}S_5 & \frac{1}{2}S_4 & S_3 \end{bmatrix} \tag{2.3}$$

A stress tensor is required to represent the state of stress in a solid. Each element of the stress tensor $T_{ij}$ represents the $i_{th}$ component of force per area acting on the infinitesimal $j_{th}$ surface

$$T_{ij} = \frac{F_i}{A_j}, \tag{2.4}$$

where $F_i$ is the applied force and $A_j$ is the plane of action. $T_{ii}$ and $T_{ij}$ represent longitudinal stress and shear stress, respectively. Shear stress components $T_{ij} = T_{ji}$ because internal stress does not raise any net rotation of the solid. The stress tensor is given by

$$\mathbf{T} = \begin{bmatrix} T_{xx} & T_{xy} & T_{xz} \\ T_{yx} & T_{yy} & T_{yz} \\ T_{zx} & T_{zy} & T_{zz} \end{bmatrix} = \begin{bmatrix} T_1 & T_6 & T_5 \\ T_6 & T_2 & T_4 \\ T_5 & T_4 & T_3 \end{bmatrix} \tag{2.5}$$

Strain is linearly proportional to stress for a small deformation, known as Hooke's law. The relationship between stress and strain can be generalized to non-piezoelectric solids using tensors :

$$T_{ij} = \sum_{k,l=1}^{3} c_{ijkl} S_{kl} \tag{2.6}$$

where the elastic constant $c_{ijkl}$ characterizes the elastic behavior of a solid in a small deformation. The four indices of the $c_{ijkl}$ result in $3^4 = 81$ elements in the elastic tensor. Since both strain tensor $S_{kl}$ and stress tensor $T_{ij}$ are symmetric, at most six of the nine elements can be unique. Using contracted notation, Eq. (2.6) is rewritten as

$$T_I = \sum_{J=1}^{6} c_{IJ} S_J \tag{2.7}$$

where the elastic tensor is given by

$$c_{IJ} = \begin{bmatrix} c_{11} & c_{12} & c_{13} & c_{14} & c_{15} & c_{16} \\ c_{21} & c_{22} & c_{23} & c_{24} & c_{25} & c_{26} \\ c_{31} & c_{32} & c_{33} & c_{34} & c_{35} & c_{36} \\ c_{41} & c_{42} & c_{43} & c_{44} & c_{45} & c_{46} \\ c_{51} & c_{52} & c_{53} & c_{54} & c_{55} & c_{56} \\ c_{61} & c_{62} & c_{63} & c_{64} & c_{65} & c_{66} \end{bmatrix} \tag{2.8}$$

In an elastic and isotropic material, such as an optical fiber, it looks the same in the $x$, $-x$, $y$, $-y$ , $z$, and $-z$ directions, which indicates $c_{11} = c_{22} = c_{33}$ and $c_{44} = c_{55} = c_{66}$, and all other diagonal terms are zero because of mirror symmetry. Thus, the stress-strain relation in optical fibers reduces to only 3 components as follows :

$$\begin{bmatrix} T_1 \\ T_2 \\ T_3 \\ T_4 \\ T_5 \\ T_6 \end{bmatrix} = \begin{bmatrix} c_{11} & c_{12} & c_{12} & 0 & 0 & 0 \\ c_{12} & c_{11} & c_{12} & 0 & 0 & 0 \\ c_{12} & c_{12} & c_{11} & 0 & 0 & 0 \\ 0 & 0 & 0 & c_{44} & 0 & 0 \\ 0 & 0 & 0 & 0 & c_{44} & 0 \\ 0 & 0 & 0 & 0 & 0 & c_{44} \end{bmatrix} \begin{bmatrix} S_1 \\ S_2 \\ S_3 \\ S_4 \\ S_5 \\ S_6 \end{bmatrix} \tag{2.9}$$

**Wave propagation equation**

Considering a material subjected to an external force, the force acting on each surface $ds$ is given by $\mathbf{T} \cdot \mathbf{n}$, where $\mathbf{n}$ is the unit vector of surface normal. Then the integral surface force acting on particles is $\int_s \mathbf{T} \cdot \mathbf{n}\ ds$. In addition, the force on the body is the summation of internal force $\mathbf{f}$ acting on each infinitesimal volume $dV$, which is expressed as $\int_V \mathbf{f}\ dV$. According to Newton's law of motion, the relationship between forces in equilibrium is given by [16]

$$\int_s \mathbf{T} \cdot \mathbf{n}\ ds + \int_V \mathbf{f}\ dV = \int_V \rho \frac{\partial^2 \mathbf{u}}{\partial t^2}\ dV \tag{2.10}$$

where $\rho$ is the mass density of the material. If the particle volume is sufficiently small, Eq. (2.10) is rewritten as

$$\nabla \cdot \mathbf{T} = \rho \frac{\partial^2 \mathbf{u}}{\partial t^2} - \mathbf{f} \tag{2.11}$$

where

$$\nabla \cdot \mathbf{T} = \lim_{dV \to 0} \frac{\int_s \mathbf{T} \cdot \mathbf{n}\ ds}{dV} \tag{2.12}$$

which is equivalent to

$$\frac{\partial T_{ij}}{\partial u_j} + f_i = \rho \frac{\partial^2 u_i}{\partial t^2} \tag{2.13}$$

Equation (2.13) is known as the wave propagation equation in an elastic material.

### 2.1.2 Electrostriction driven by optical waves

Electrostriction, also known as the electrostrictive force, describes the generation of acoustic waves in the presence of optical waves in an optical medium. Electrostriction changes the medium's density resulting in a third-order nonlinear optical response that gives rise to SBS. Electrostriction grows by the fourth power of the material's refractive index, producing strong nonlinear effects in chalcogenide fibers [17]. SBS refers to the interaction of optical waves and the acoustic wave. The Brillouin scattered light is shifted to a higher frequency known as the anti-Stokes wave and a lower frequency known as the Stokes wave by the electrostriction-induced refractive index grating. In quantum mechanics, the scattering process for the Stokes wave and the anti-Stokes wave can be seen as phonon generation and phonon annihilation, respectively. For Stokes wave scattering, a pump photon (with the frequency of $\omega_p$ and the wave number of $k_p$) is converted to a low-frequency Stokes photon (with the frequency of $\omega_s$ and the wave number of $k_s$) through the scattering from an acoustic wave and creating a phonon (with the frequency of $\Omega$ and wave number of q). For anti-Stokes wave scattering, a pump photon is converted to a high-frequency anti-Stokes photon (with the frequency of $\omega_{as}$ and wave number of $k_{as}$) through the scattering from an acoustic wave and absorbing a phonon. Stokes wave scattering and anti-Stokes wave scattering must satisfy the conservation of energy and momentum, as shown in Fig. 2.2. SBS has enabled distributed optical sensing [18–20], Brillouin lasing [21–23], the generation of slow and fast light [24, 25], microwave photonic filters [26, 27], Brillouin gyroscopes [28], and the generation of frequency combs [29].

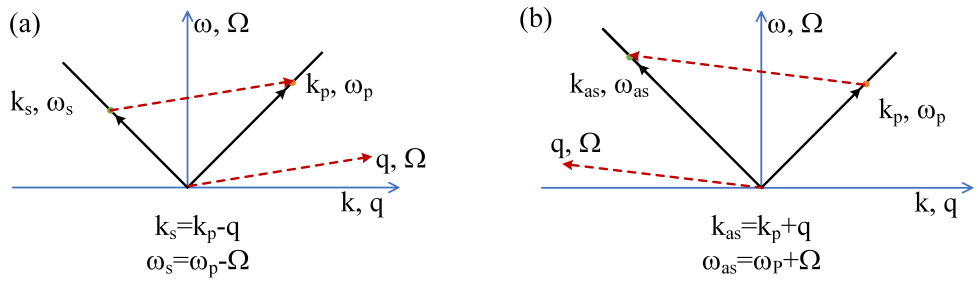


FIGURE 2.2 – Phase matching conditions and scattering directions of backward (a) Stokes Brillouin scattering ; (b) anti-Stokes Brillouin scattering.

### 2.1.3 Acoustic waves in piezoelectric materials

#### Mechanical stress driven by electric fields

Piezoelectric materials lack a center of inversion symmetry, where the positive charge does not coincide with the negative charge in the center. When an electric field is applied to a piezoelectric material, two nearby atoms that are not identical will not travel the same distance leading to the material's mechanical deformation. The effect is reversible in the piezoelectric material. The mechanical stress applied to the material is converted into an electrical signal because dipole moments form a charge distribution in the medium. The relationships between strain, stress, and electric field are given by piezoelectric constitutive relations [30]

$$T_I = c_{IJ}^E S_J - e_{Ij} E_j \tag{2.14}$$

$$D_i = \epsilon_{ij}^S E_j + e_{IJ} S_J \tag{2.15}$$

where $e_{Ij}$ is the piezoelectric stress constant, $E_j$ is the electric field, $D_i$ is the electrical displacement, and $\epsilon_{ij}$ is the permittivity constant. The most popular ultrasonic transducers that can translate an electrical signal into mechanical stress are piezoelectric transducers.

#### Detection of acoustic waves

Acoustic waves that impinge on an elastic medium, such as an optical fiber, can be measured because they induce strain on the medium, which causes the density change of the material. The density change of the material modulates the phase of the propagating light in the medium. which can be detected by optical fiber sensors. Acoustic wave measurements are crucial for non-destructive structural monitoring and biomedical imaging. Optical fiber-based acoustic sensors have many advantages over traditional piezoelectric acoustic sensors, such as high sensitivity, nonconductivity, and resistance to electromagnetic interference.

For a sinusoidal acoustic wave emitted from a piezoelectric transducer, the stress along an optical fiber due to acoustic pressure is given by [31]

$$T^{\text{stress}}(t) = T_0^{\text{stress}} \cos\left(\frac{2\pi}{\lambda_s} z - \omega_s t\right) \tag{2.16}$$

where $T_0^{\text{stress}}$ is the acoustic wave stress amplitude, and $\lambda_s$ and $\omega_s$ are the wavelength and frequency of the acoustic wave, respectively. In elastic and isotropic materials, the stress-strain relation from Eq. (2.9) is rewritten as [32]

$$\begin{bmatrix} S_1 \\ S_2 \\ S_3 \\ S_4 \\ S_5 \\ S_6 \end{bmatrix} = \frac{1}{E} \begin{bmatrix} 1 & -v & -v & 0 & 0 & 0 \\ -v & 1 & -v & 0 & 0 & 0 \\ -v & -v & 1 & 0 & 0 & 0 \\ 0 & 0 & 0 & G & 0 & 0 \\ 0 & 0 & 0 & 0 & G & 0 \\ 0 & 0 & 0 & 0 & 0 & G \end{bmatrix} \begin{bmatrix} T_1 \\ T_2 \\ T_3 \\ T_4 \\ T_5 \\ T_6 \end{bmatrix} \tag{2.17}$$

where $E$ and $v$ are Young's modulus and Poisson's ratio, respectively, and $G = 2(1 + v)$. The strain in the direction of fiber axis is expressed as

$$S(t) = T_0^{\text{stress}} \frac{(1 - 2v)}{E} \cos\left(\frac{2\pi}{\lambda_s} z - \omega_s t\right) \tag{2.18}$$

The phase of light propagating in the fiber is expressed as $\phi = L\beta$, where $L$ is the fiber length and $\beta$ is the propagation constant. The phase is changed due to the variation of fiber length and refractive index. The stress-induced phase modulation is given by

$$\Delta\phi = \beta\Delta L + L\Delta\beta \tag{2.19}$$

where $\Delta\beta$ is the propagation constant change and $\Delta L$ is the fiber length change.

The propagation constant change depends on the refractive index change $\Delta n$ through the elasto-optic effect. The refractive index change is given by [33]

$$\Delta\left(\frac{1}{n^2}\right)_i = \sum_{j=1}^{6} p_{ij} S_j \tag{2.20}$$

where $p_{ij}$ is the strain-optic tensor. Because the acoustic wave propagates longitudinally along the fiber axis, shear strain elements $S_4$,$S_5$ and $S_6$ are zero. Therefore, the change in the refractive index is expressed as

$$\Delta n = -\frac{1}{2} T_0^{\text{stress}} \frac{(1 - 2v)}{E} \cos\left(\frac{2\pi}{\lambda_s} L - \omega_s t\right) (2p_{12} + p_{11})(n^3) \tag{2.21}$$

where $p_{11}$ and $p_{12}$ are elasto-optic coefficients and $n$ is the refractive index of the fiber.

The mechanical strain induces a deformation along the $z$ axis of the fiber. A point $z$ is translated into a new position $z'$ under the acoustic wave, which is given by [34]

$$z' = z + \int_0^z S(\xi) d\xi \tag{2.22}$$

Then, $\Delta L$ caused by the mechanical effect is expressed as

$$\Delta L = T_0^{\text{stress}} \frac{(1-2\upsilon)}{E} \frac{\lambda_s}{2\pi} \left[ \sin\left( \frac{2\pi}{\lambda_s} L - \omega_s t \right) + \sin\left(\omega_s t\right) \right] \tag{2.23}$$

Acoustic sensors based on fiber Bragg gratings (FBG), Fabry-Pérot interferometers (FPI), and Mach-Zehnder interferometers (MZI) have been demonstrated [35–37]. Mechanical stress-induced phase modulation causes a wavelength shift in the spectrum, which induces periodical intensity change at the same frequency as the acoustic wave. Due to the large Young's modulus and low strain sensitivity, high-frequency ultrasound sensing is limited in silica fiber-based sensors.

## 2.2 Brillouin fiber sensors

Optical fiber sensing is crucial in various applications, including structural health monitoring, chemical and biological sensing, and medical diagnosing. Fiber sensors can be categorized into Rayleigh scattering sensing, Brillouin scattering sensing, and Raman scattering sensing based on scattering mechanisms. The diagram of Rayleigh, Brillouin, and Raman backscattering in optical fibers is shown in Fig. 2.3. Rayleigh scattering induced by the inhomogeneity of the fiber core is an elastic scattering, which means the frequency of scattered light is the same as the incident light. Brillouin and Raman are inelastic scatterings leading to the shifted frequency of the scattered light. Brillouin scattering shifts the frequency of the incident light by a few GHz in the opposite direction in optical fibers. Raman scattering resulting from the interaction of light and molecular vibrations enables the frequency shift of tens of THz in optical fibers [5]. On both sides of the Rayleigh scattering peak, there are two peaks associated with the Stokes wave and the anti-Stokes wave for Raman and Brillouin scatterings.

### 2.2.1 Classes of Brillouin fiber sensing

SBS-based optical fiber sensors have gained significant attention in recent decades. The frequency shift of Brillouin scattered light is proportional to the local velocity of the acoustic wave and material's refractive index, which is linearly dependent on temperature or strain [38]. Any thermal or acoustic disturbance along the optical fiber will cause the change in BFS, which can be demodulated using Brillouin gain spectra. There are four types of Brillouin fiber sensing based on different mechanisms :

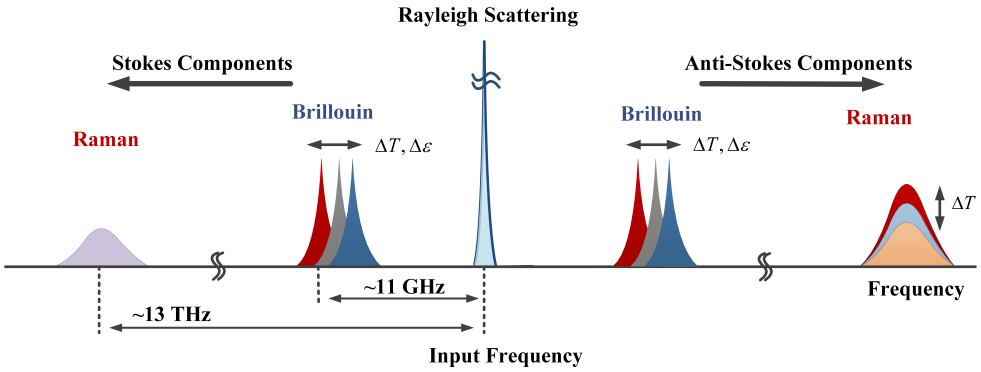


FIGURE 2.3 – Scattering phenomena used in optical fiber sensing.

## Distributed SBS fiber sensing

Distributed sensors have been demonstrated in single-mode fibers (SMF) based on different Brillouin scattering technologies. Spatial resolution is a crucial factor that determines the small-size events associated with temperature or strain variation. Distributed temperature sensing with 100 m spatial resolution in the 1.2 km silica fiber based on Brillouin optical time-domain analysis (BOTDA) was first demonstrated in 1990 [39]. The spatial resolution and measurement range of BOTDA-based sensors have significantly increased over the past few decades [40, 41]. The spatial resolution of the BOTDA technique is limited to 1 m because the acoustic wave lifetime is around 10 ns. Several techniques associated with BOTDA have been proposed and demonstrated to overcome the spatial resolution limit, including differential pulse-width pair Brillouin optical time-domain analysis (DPP-BOTDA) [42] and pulse prepump Brillouin optical time domain analysis (PPP-BOTDA) [43]. High spatial resolution on the order of centimeters was achieved by measuring the differential Brillouin gain signal rather than the Brillouin gain spectrum. Compared to BOTDA techniques, spatial resolution is improved significantly based on the correlation technique known as Brillouin optical correlation domain analysis (BOCDA). The first BOCDA with 40 cm spatial resolution based on the frequency-modulated pump and probe waves was proposed and demonstrated in 2000 [44]. Later, 3 mm spatial resolution was experimentally demonstrated in a more advanced optical fiber system using the same technique [45]. Recently, 200 µm spatial resolution was demonstrated on a silicon–chalcogenide photonic waveguide using BOCDA [46]. The high-resolution technique provides a method for characterizing photonic-integrated devices.

### Brillouin dynamic grating sensing in high-birefringence fibers

In a high-birefringence fiber, optical waves in the slow and fast axes experience different BFS owing to their refractive index difference. A Brillouin dynamic grating (BDG) is produced by two counter-propagating pump waves with a frequency difference of Brillouin frequency shift (BFS). When two counter-propagating waves in the slow (fast) axis are pumped into the birefringence fiber, a probe wave in the fast (slow) axis of the high birefringence fiber can be scattered by the BDG. The maximum efficiency of the four-wave mixing (FWM) process is obtained when the phase-matching condition is satisfied [47]

$$\nu_B = \frac{2n_s\nu V_a}{c} = \frac{2n_f(\nu + \Delta\nu)V_a}{c} \tag{2.24}$$

where $n_s$ and $n_f$ are the refractive indices in the slow and fast axes, respectively, and $V_a$ is the acoustic wave velocity. The frequency offset ($\Delta\nu$) between pump and probe waves is expressed as

$$\Delta\nu = \frac{\Delta n}{n}\nu \tag{2.25}$$

where $\Delta n = n_s - n_f$ is the fiber birefringence. The frequency difference between the pump wave and the probe wave is proportional to the fiber birefringence. The distributed birefringence of the fiber can be directly estimated using the local value of the frequency offset. Distributed birefringence measurement with 40 cm resolution in a 3 km polarization-maintaining (PM) fiber was demonstrated [48]. The BDG technique can be utilized for fiber sensing because the local birefringence linearly changes with external variations. Distributed temperature measurement with 1.2 cm spatial resolution was investigated in a PM fiber by using a long pump pulse in one polarization axis to excite the BDG and a short probe pulse in the orthogonal polarization axis to read out sensing information [49]. Distributed transverse load and salinity sensors were demonstrated based on BDG [50, 51].

### Forward Brillouin scattering fiber sensing

Forward stimulated Brillouin scattering (FSBS), also known as guided acoustic wave Brillouin scattering (GAWBS), is another Brillouin scattering process involving the interaction of optical waves and transverse acoustic waves. The frequency shift of FSBS is on the order of megahertz, depending on the fiber geometry. Transverse acoustic modes responsible for forward light scattering in optical fibers are classified into the polarized radial mode ($R_{0,m}$) and depolarized torsional-radial mode ($TR_{2,m}$). The radial mode produces the phase modulation of light via strain-induced refractive index change, whereas the torsional-radial mode produces the phase modulation of light via both strain-induced

refractive index change and strain-induced birefringence change. The cut-off frequency of $R_{0,m}$ modes is given by [52]

$$f_{0,m} = [V_d/(2\pi a)]\,\xi_m \tag{2.26}$$

with

$$\left(1-\alpha^2\right) J_0(\xi) = \alpha^2 J_2(\xi) \tag{2.27}$$

where $V_d$ is the longitudinal acoustic velocity, $a$ is the radius of the fiber cladding, $\xi_m$ is the $m$ order solution of Eq. (2.27), $\alpha = V_s/V_d$ with $V_s$ being the shear acoustic velocity, and $J_0$ and $J_2$ are the zero- and second-order Bessel functions. The cut-off frequencies for $TR_{2,m}$ modes are expressed as

$$f_m = V_s\xi_m/(2\pi a) \tag{2.28}$$

with

$$\begin{vmatrix} \left(3-\frac{\xi_m^2}{2}\right) J_2(\alpha\xi_m) & \left(6-\frac{\xi_m^2}{2}\right) J_2(\xi_m) - 3\xi_m J_3(\xi_m) \\ J_2(\alpha\xi_m) - \alpha\xi_m J_3(\alpha\xi_m) & \left(2-\frac{\xi_m^2}{2}\right) J_2(\xi_m) + \xi_m J_3(\xi_m) \end{vmatrix} = 0 \tag{2.29}$$

where $J_3$ is the third-order Bessel function.

Acoustic impedance sensing has been proposed using FSBS because the acoustic impedance difference between the fiber material and the external medium determines the acoustic reflectivity at the fiber's boundary. As a result, the acoustic impedance of external medium can be detected optically by measuring the decay rate and linewidth of transverse acoustic modes [53].

### Surface and hybrid Brillouin sensing in microfibers

Different from Brillouin scattering in conventional optical fibers, where the light guided into the core is only sensitive to shear and longitudinal acoustic waves, sub-wavelength diameter microfibers exhibit rich dynamics of photon–phonon interactions. Light propagating in sub-wavelength microfibers can generate surface acoustic waves due to strong coupling with the boundary [54]. In microfibers, both the photo-elastic effect and the moving-boundary effect dominate the interaction of optical and acoustic fields. Acoustic strain induces the material refractive index change due to the photo-elastic effect. The strength of photo-elastic effect is given by $\eta_{\mathrm{pe}} = -n^3 p_{11}\pi d u_{\mathrm{s}}/4$, where $d$ is the fiber diameter and $u_{\mathrm{s}}$ is the surface acoustic wave displacement [55]. The strength of moving boundary effect is proportional to the refractive index difference and radius of the fiber as expressed by $\eta_{\mathrm{mb}} = (n_{\mathrm{glass}} - n_{\mathrm{air}})\,\pi d u_{\mathrm{s}}$. Therefore, the optical field experiences the vibrating boundary effect in small diameter waveguides with larger surface-to-volume ratio and higher index difference [56]. The relation between the Brillouin gain coefficient and the optical and acoustic mode fields is given by [57]

$$G_B(\Omega) = Q_m \frac{2\omega_p L(\Omega)}{\bar{m}_{\text{eff}}\Omega_m^2} \left| \int f_{\text{mb}} dl + \int f_{\text{pe}} dA \right|^2 \tag{2.30}$$

where $Q_m$ is the acoustic energy quality factor, $\bar{m}_{\text{eff}} = \int \rho \left|\mathbf{u}_m\right|^2 / \max \left|\mathbf{u}_m\right|^2 dA$ is the effective linear mass density of the acoustic mode with displacement profile $\mathbf{u}_m$ and the mass density $\rho$, and $f_{\text{mb}}$ and $f_{\text{pe}}$ are the line and area overlap integrals representing the moving boundary and photo-elastic effects, respectively. The moving boundary overlap integrand, photo-elastic overlap integrand, and the associated deviation and simplification can be found in [57]. The Brillouin gain coefficient can be calculated by adding the coupling coefficient of two effects. The calculated Brillouin gain map for silica microfibers with a diameter ranging from 0.5 µm to 2.3 µm is plotted in Fig. 2.4(a). The black curve depicts acoustic frequencies under the phase-matching condition for the pure longitudinal acoustic wave. The microfiber with a small diameter generates both surface and hybrid acoustic waves. The strength of the surface acoustic wave increases with decreasing diameter as expected. The mode profiles of the surface and hybrid acoustic waves are shown in Fig. 2.4(b). The energy of the surface acoustic mode is mainly on the surface of the microfiber, while the hybrid acoustic wave exhibits mechanical ripples in the microfiber because of the interference between transverse and longitudinal acoustic waves in the microfiber.

The surface Brillouin scattering is sensitive to environmental variations because the waves travel along the surface of microfibers. A Brillouin refractive index sensor in a silica microfiber has been demonstrated [58]. Experimental results show that BFS linearly depends on the external refractive index. Multiple Brillouin peaks corresponding to different acoustic waves were observed, which agrees with the calculated results. The Brillouin peaks of hybrid acoustic waves have different frequency responses, allowing simultaneous temperature and gas pressure sensing [59]. Temperature and strain sensing based on surface Brillouin scattering in silica microfibers were numerically demonstrated [60].

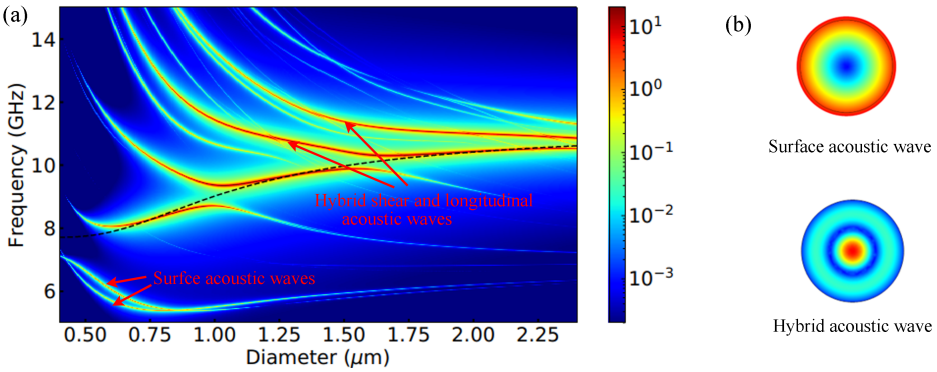


FIGURE 2.4 – (a) Calculated Brillouin gain as a function of diameter in the single-mode microfiber. (b) Surface acoustic mode and hybrid acoustic mode.

### 2.2.2 Chalcogenide fiber Brillouin sensing

Chalcogenide fibers with a high nonlinear coefficient and low Young's modulus have been good candidates for investigating Brillouin scattering and its applications in sensing and lasing [61, 62]. $As_2Se_3$ has garnered interest among chalcogenide compositions because of its high nonlinearity at 1550 nm. SBS in single-mode $As_2Se_3$ fibers has been demonstrated, showing a ∼134 times larger Brillouin gain coefficient than that of silica-based SMFs [63]. High Brillouin gain of $As_2Se_3$ fibers gives rise to Brillouin amplification and Brillouin lasers [64]. The nonlinearity was increased by 60 times by tapering the $As_2Se_3$ microfiber to a diameter of 1.2 μm owing to the small effective mode area [65]. The unprotected chalcogenide microfiber can not be utilized in sensing applications because it is extremely fragile and cannot be removed from its tapering apparatus without rupturing. The $As_2Se_3$ microfiber with a core diameter of 0.8 μm was fabricated by coating a polymethyl methacrylate (PMMA) cladding on an $As_2Se_3$ fiber, achieving an ultrahigh nonlinearity of 133 $W^{-1}m^{-1}$ [66]. The schematic of the $As_2Se_3$-PMMA microfiber is shown in Fig. 2.5(a). The thick PMMA cladding gives sufficient mechanical robustness for normal handling. SBS was investigated in the PMMA coated $As_2Se_3$ microfiber [67]. Tailorable Brillouin gain spectra at different core diameters are plotted in Fig. 2.5(b). The $As_2Se_3$ microfiber with PMMA cladding offers a new approach for Brillouin sensing applications that have never been done in fragile chalcogenide microfibers. Transverse load sensing was proposed and demonstrated theoretically and experimentally in the $As_2Se_3$-PMMA microfiber [68]. The high sensitivity of 0.08±0.02 MHz/N was achieved in the load range of 0 to 4 kg. The temperature, strain, and salinity sensing based on wavelength shift in dual-core $As_2Se_3$-PMMA microfibers was demonstrated [69, 70]. Similarly, many Brillouin sensing applications with a high resolution of MHz can be achieved in $As_2Se_3$-PMMA microfibers.

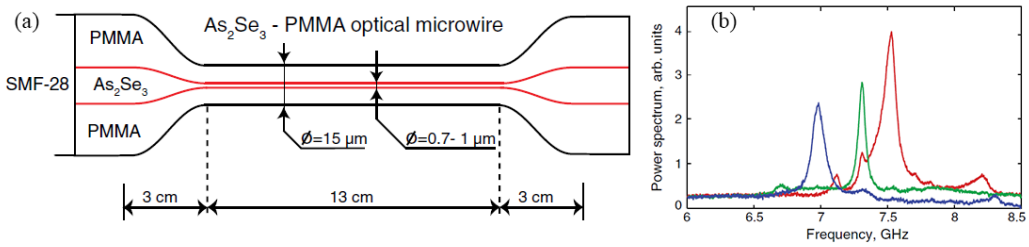


FIGURE 2.5 – (a) Schematic of the $As_2Se_3$-PMMA microfiber. (b) Brillouin spectra measured in three chalcogenide microfibers [67].

## 2.3 Random fiber lasers

Random lasers (RL) in disordered media have attracted much attention in recent years. The schematic of the conventional cavity laser and the RL is shown in Fig. 2.6. Conventional lasers consist of a gain medium and a fixed cavity that provide coherent feedback to the gain medium. RLs with a disordered cavity take advantage of the multiple scattering of photons. Compared to conventional lasers, RLs have more complicated scattering paths. The random nature of light propagation in RLs gives rise to unique properties and many potential applications in imaging, sensing, and secure communication [71–74]. RLs with various disordered structures, such as powders, dyes, planar waveguides, and porous glass, have been demonstrated [75–78]. Random fiber lasers (RFL) with transverse confinement imposed by the fiber geometry have a low threshold and stable lasing. The RFL was first demonstrated in a hollow core photonic crystal fiber [79]. The 250 nm rutile particles in a Rhodamine 6G solution were selectively inserted into the hollow core as the scattering gain medium. Due to the quasi-one-dimensional geometry, the lasing efficiency is two orders of magnitude higher than high-dimensional RLs. Later, RFLs based on distributed feedback in SMFs were proposed and demonstrated [80–82]. In distributed RFLs, randomly scattered light from the distributed feedback medium traveling in the gain medium gives rise to complex light paths, producing many modes with exotic wavelengths, phases, and amplitude. There are three main types of random distributed feedback fibers : RS fibers, random FBG arrays, and random fiber gratings (RFG). RFLs can be divided into three main categories based on gain mechanisms, such as SBS, stimulated Raman scattering (SRS), and erbium-doped fiber (EDF).

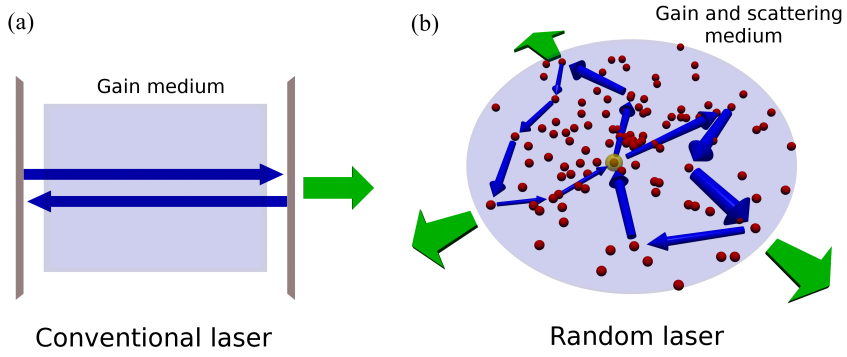


FIGURE 2.6 – Schematic of (a) the cavity laser ; (b) the random laser [83].

### 2.3.1 Different random distributed feedback fibers

#### RFL based on RS distributed feedback

Rayleigh scattering (RS) in optical fibers is induced by the thermodynamically frozen inhomogeneity with a scale that is smaller than the incident wavelength. Photons are elastically scattered by RS along the fiber. The RFL with RS distributed feedback has attracted attention since it was first experimentally reported in a 83 km long SMF-based random open cavity [80]. Figure 2.7 shows the schematic of the RS-based RFL. Backscattered RS in the distributed feedback fiber is relatively weak (backscattering coefficient of $4.5\times10^{-5}$ $km^{-1}$ [80]) because the majority of the scattered photons leak out of the fiber core, as shown in the inset of Fig. 2.7. As a result, a long fiber is necessary to achieve high-efficiency RFLs based on coherent RS distributed feedback because the accumulation of RS provides enough feedback strength. Rayleigh scattered photons are continuously amplified by Raman gain in the fiber. Random lasing occurs when the gain in the random cavity is larger than the loss. Low pump power is required in the RFL due to the accumulated Raman gain and RS feedback strength in the tens of kilometers long random cavity. However, the ultra-long random cavity supports many random modes in the random system. More random modes are excited at higher pump power. High-density modes compete for the same gain resulting in strong intensity and frequency fluctuations. In addition, the long fiber is sensitive to external variations. Any disturbance will change the propagation of light in the random cavity leading to fast mode hopping and high intensity noise. RFLs based on RS feedback with different structures have been demonstrated [84,85]. The length of distributed feedback fiber is limited to hundreds of meters due to the intrinsic weak RS. RFLs with short feedback are necessary to reduce frequency and intensity fluctuations.

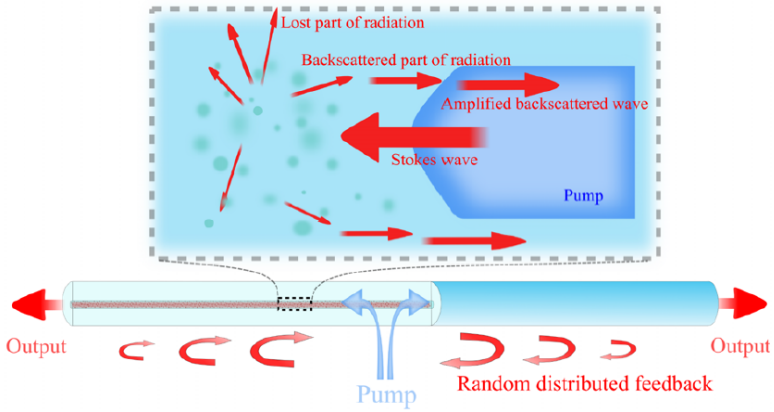


FIGURE 2.7 – The schematic of the RFL with a distributed RS fiber [86].

### RFL based on random FBG distributed feedback

Fiber gratings have higher refractive index fluctuations and stronger scattering than RS optical fibers. Random distances between adjacent FBGs add the random nature of a FBG array. The RFL based on the random FBG array in an Er/Ge co-doped SMF was first demonstrated in 2009 [87]. The schematic diagram of the random FBG array-based RFL is shown in Fig. 2.8(a). A pump laser with 980 nm is utilized to generate the random lasing at 1535 nm in the Er/Ge gain medium. The random FBG array was fabricated in the fiber core by exposing it to ultraviolet (UV) light. The random FBG array consists of tens of FBGs with random spaces ranging from 4.2 mm to 5.8 mm between neighboring FBGs. Such a low degree of randomness generated by tens of random FBGs allows a few low-Q random peaks within the narrow FBG bandwidth as plotted in Fig. 2.8(b). The number of peaks increases with increasing gratings due to light interference in more gratings, which leads to more modes with random phase, amplitude, and wavelength in the RFL. The large gain bandwidth (tens of nanometers) in the Er/Ge gain medium allows multiple modes to be amplified to overcome the loss in the random cavity. Mode coupling in the gain bandwidth induces large intensity and frequency fluctuations. Wave interference in the random FBG array gives rise to light localization, in which the localization length is smaller than the length of the random medium. Light localization in the random FBG array is confirmed by the wavelength-dependent intensity map calculated using the transfer matrix method.

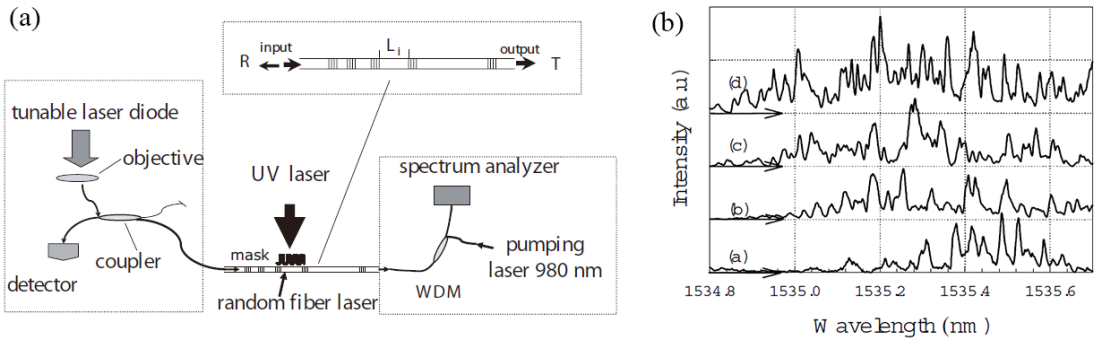


FIGURE 2.8 – (a) Schematic of the random FBGs based RFL. (b) Reflection spectra of FBG arrays with seven, fourteen, twenty, and thirty one gratings from bottom to top [87].

To increase the degree of randomness in fiber grating-based RFLs, a continuous fiber grating based on randomly distributed phase errors was fabricated [88]. The new technique increases the number of gratings to around 1000 without increasing the grating length. The grating-based RFL exhibits a low threshold of 3 mW due to the strong scattering of the grating. The single-mode operation is possible by changing the grating length and pump power. The random grating with low-Q peaks can be utilized as the random distributed

feedback of the short-cavity RFL with broad gain bandwidth and low density of modes in the short random cavity. RFLs with a cavity length of kilometers and a narrow gain bandwidth, such as SBS-based RFLs, have high-density modes with small frequency separations. After scattering from the low-Q random grating distributed feedback, many modes will be amplified in the gain medium. The RFL will be similar to the cavity laser showing multimode lasing at a fixed separation of kHz. High-Q random distributed feedback is required to demonstrate the single-frequency RFLs with narrow gain and long cavity length.

### RFL based on RFG distributed feedback

Fiber gratings with random periods, so-called RFGs, were fabricated by the plane-by-plane inscription method. The fiber's refractive index is modulated spot by spot with random periods by the exposure of a femtosecond-infrared pulse laser. The fabrication setup and the detailed fabrication procedure of the RFG are provided in [89]. The scattering points of the RFG are significantly increased over a short length. There are around $10^5$ index modulation spots in a 5 cm long RFG. The random fiber grating array (RFGA) consisting of tens of RFGs with a similar distance between two gratings was fabricated to increase the scattering points and scattering strength further. Figure 2.9(a) shows the schematic of the RFGA. The modulation periods in each RFG are randomly varied between 0.5180 µm and 0.5464 µm corresponding to a broad backscattering wavelength range from 1500 nm to 1580 nm. The modulation spots in each 5 mm-long RFG are around $10^4$. The RFGA with tens of RFGs has a total modulation spot of greater than $10^5$, which is more than two orders of magnitude larger than the random FBG. Many modification spots give rise to a large ensemble of random states with small differences in the cavity length (so-called random modes). Figure 2.9(b) shows the reflection spectrum of the single RFG and the RFGA. The reflection spectrum of the RFGA shows narrower linewidth peaks with 10 dB

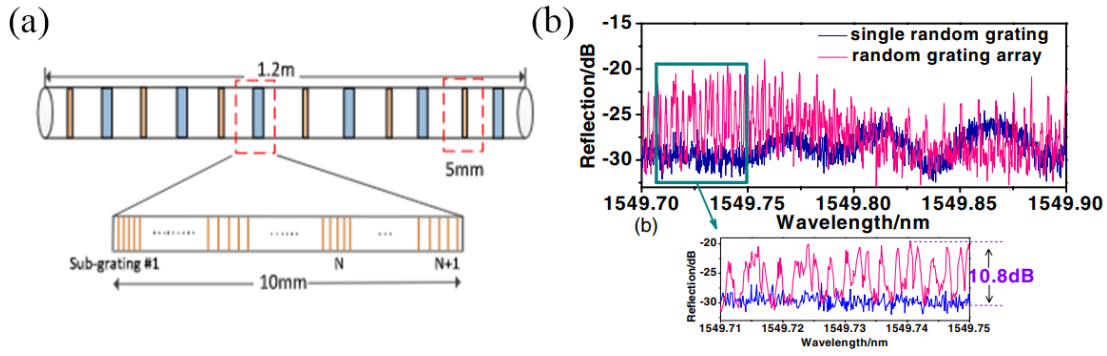


FIGURE 2.9 – (a) Schematic of RFGA. (b) The reflection spectrum of the RFGA and the single RFG [90].

higher reflection than the single RFG because of wave interference in more Fabry-Pérot (FP) cavities formed between RFG pairs in the RFGA. The high-Q RFGA distributed feedback with the narrow filter effect can select modes in the Brillouin gain bandwidth. In addition, wave interference and multi-scattering in the strong scattering RFGA give rise to light localization, which will be discussed in the next chapter.

The RFG-based RFL has been demonstrated as plotted in Fig. 2.10(a). Two pump lights with equal power from the same laser source are launched into two ends of the 12 km gain SMF to generate the Brillouin Stokes wave. Due to the stronger scattering of the RFG than RS in the SMF, the random feedback induced by the RFG pair dominates the scattering of the Stokes wave. Without the RFG pair, RS within the effective amplification length near both ends of the fiber provides random feedback of the Stokes wave. The RFG consisting of many FP interferometers acts as the narrow filter for filtering out some modes. Figure 2.10(b) shows the relative intensity noise (RIN) of the RFLs with and without the RFG pair. Compared to the RS feedback-based RFL, the RFL with the RFG pair suppresses RIN due to reduced longitudinal modes. In addition, the RFG has a weaker dependence on thermal and acoustic variations than the RS fiber, leading to low intensity noise in the frequency range below 1 kHz [91].

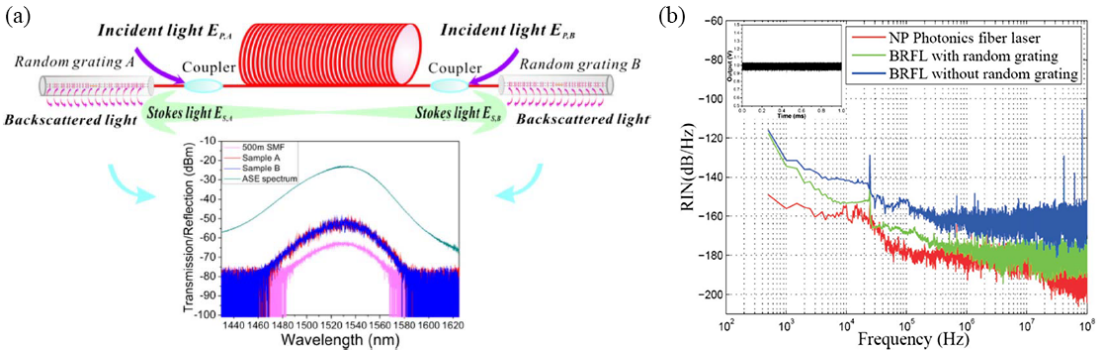


FIGURE 2.10 – (a) Configuration of RFL with random grating-based FP resonator, (b) RIN of the RFLs with random grating and without random grating [92].

### 2.3.2 Different gain mechanisms

#### RFL based on EDF gain

The EDF is made by incorporating rare-earth element erbium ions $Er^{3+}$ in the fiber core. $Er^{3+}$ ions can absorb light at one wavelength and emit it at other wavelengths because the ions have a variety of excited states. Figure 2.11 shows the energy level diagram of $Er^{3+}$ ions. Lasing wavelengths commonly used as the pump light of the EDF are 980 nm and

1480 nm. When the pump laser at 980 nm is injected into the EDF, $Er^{3+}$ ions will be excited from the ground state to the higher state level, where $Er^{3+}$ ions only stay for around 1 μs and make a non-radiative decay to the metastable state. The long lifetime of 10 ms in the state is enough to accumulate the ions for the buildup of population inversion, which leads to optical amplification by the emission of photons at a wide wavelength range from 1520 nm to 1570 nm to the low energy level. The scheme of 1480 nm pump light is known as in-band pumping. The pump preferentially raises ions to the high sublevels of the metastable state, and fall to the lower sublevels where they are available for stimualted emission [93]. Since the process of absorption and emission access to different levels within metastable state, population inversion can be achieved.

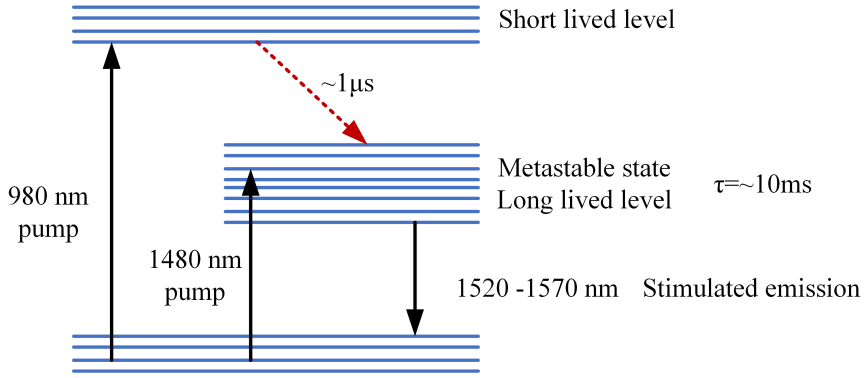


FIGURE 2.11 – Energy level scheme of ground and first two excited states of $Er^{3+}$ ions.

The RFL based on the randomly distributed FBG array in the EDF was first proposed in 2007 [94]. The experiment was then thoroughly illustrated in random FBG arrays with different lengths [87]. The laser system pumped at 980 nm shows a typical laser threshold behavior at the wavelength of 1535.5 nm. Single-mode lasing was achieved by changing the number of the random FBG array and the pump power. Later, half-open cavity EDF-RFLs based on RS distributed feedback were demonstrated [82, 95]. The schematic diagram of the RS-based EDF-RFL is plotted in Fig. 2.12. The EDF is pumped by a 980/1480 nm laser through a wavelength division multiplexer (WDM). The narrow bandwidth FBG with a central wavelength at the high gain position of the EDF is utilized to reflect the selected wavelength from the amplified emission of the EDF. The reflected light is sent to the RS random distributed feedback fiber. The EDF-RFL with RS distributed feedback shows a single peak around 1550 nm with a signal-to-noise ratio (SNR) of 40 dB and a 3 dB linewidth of 0.23 nm [96]. A low threshold power of 10 mW is achieved thanks to the FBG-based half-opened cavity and the efficient EDF gain fiber. The frequency noise of the EDF-RFL with RS distributed feedback was demonstrated and theoretically analyzed [97]. The thermal frequency noise is suppressed due to the Lorentzian envelope attributed by

Rayleigh scattering in the long fiber cavity. A compact EDF-RFL was demonstrated by replacing the kilometers-long RS feedback fiber with the short $CO_2$-laser-processed random grating feedback [98]. The RFL presents a lower RIN due to the reduced mode density and low acoustic and thermal sensitivities. In contrast to the single-wavelength RFLs we discussed above, the EDF gain with a typical bandwidth of tens of nanometers is a good candidate for wide-range tunable RFLs and multi-wavelength RFLs [99, 100].

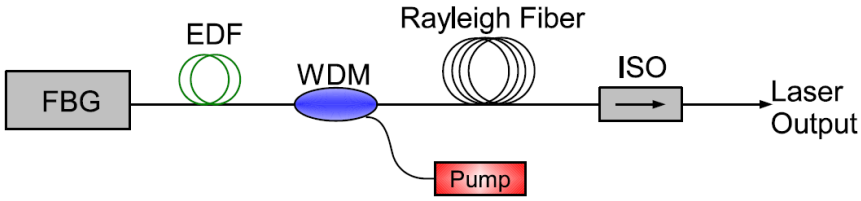


FIGURE 2.12 – Schematic of the RFL based on EDF a with half-opened cavity [101].

### RFL based on SRS gain

SRS is a nonlinear interaction between the pump and the vibrational modes of molecules in a medium. During the scattering process, as the molecule makes a transition to an excited vibrational state, the scattered Stokes photon with energy $\hbar\omega_s$ is red-shifted with respect to the pump photon with energy $\hbar\omega_p$. When the pump light with high power is injected into the medium, the energy of the pump wavelength is transferred to the frequency-downshifted Stokes wave via the scattering process, which can be used for light amplification and lasing. The SRS gain of SMFs has a frequency range of 40 THz with a peak frequency of 13 THz [5]. The RFL based on SRS gain was first proposed in 2010 [80]. The setup of the RFL is similar to Fig 2.7. Two equal-power pump lasers with a wavelength of 1455 nm are pumped into the center of a SMF in opposite directions. Lasing is generated when the amplified backscattered light in the Raman gain bandwidth is larger than the loss of the distributed cavity. After the lasing threshold of 1.6 W, the output power linearly increases with pump power, as shown in Fig. 2.13(a). Compared to the observable mode structure in the Raman cavity fiber laser with two FBGs at the ends of the gain fiber [102], no mode structure was observed in the random Raman RFL at the pump power well above the threshold (2.4 mW), leading to flat amplitudes without large intensity fluctuations over 2.5 ms. The lasing output spectra at the powers above the threshold are plotted in Fig 2.13(b), showing two narrow peaks (less than 1.5 nm) with stable lasing frequencies at high gain positions of the Random gain bandwidth. Thanks to the broad Raman gain bandwidth on the order of THz, the lasing wavelength can be tuned over a large wavelength

range. The tunable wavelength range of 35 nm with nearly the same SNR (∼50 dB) for all wavelengths was demonstrated experimentally [81]. SRS-based RFLs have been designed to improve the characterizations including multi-wavelength operation [103], high-power emission [104], and narrow bandwidth [105], offering an approach to achieving distributed amplification [106] and optical fiber sensing [107].

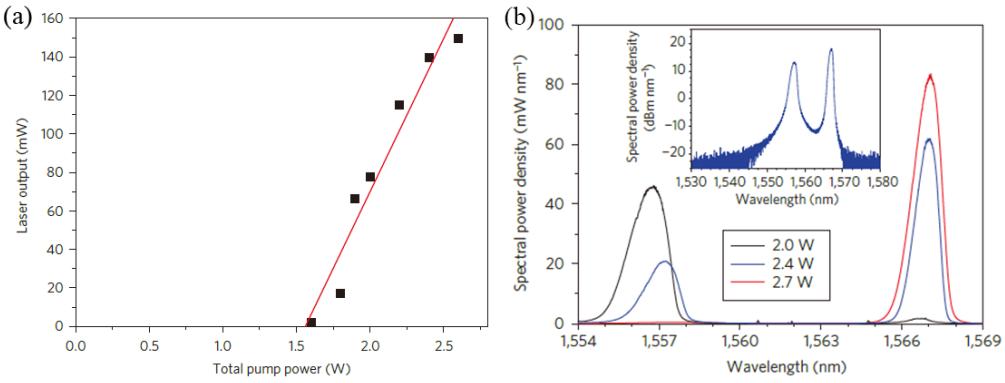


FIGURE 2.13 – (a) Raman RFL power as a function of input pump power, (b) Laser spectra at different input pump powers [80].

### RFL based on SBS gain

Compared to SRS, SBS has a much narrower linewidth (tens of MHz) and a higher gain coefficient in optical fibers, which causes a lower threshold and lower noise in SBS-based RFLs. The BRFL with a configuration of cooperative SBS and distributed RS in a high-loss SMF was first demonstrated [108]. The Stokes wave generated in the 300 m SMF is backscattered by the RS in the same fiber, which acts as the seed of Brillouin amplification. The BRFL with Brillouin gain and random distributed feedback in the high loss fiber leads to a high threshold and strong intensity fluctuations. The BRFL with a half-open cavity has been proposed and demonstrated [109]. The working principle of the BRFL is shown in Fig. 2.14(a). The backscattered Stokes wave is generated when the pump light is injected into the SBS gain fiber. The Stokes light from the SBS gain fiber is then sent into the distributed feedback fiber. The Rayleigh-scattered Stokes wave is then routed back to the SBS gain fiber to produce a random cavity. The Brillouin gain and distributed feedback fibers are a 25 km SMF and a 5.4 km nonuniform SMF, respectively. The high Brillouin gain and strong distributed scattering in the long fibers lead to a low threshold, as shown in Fig. 2.14(b). The BRFL with RS distributed feedback exhibits a frequency drift of 10 MHz because of the narrow gain bandwidth. Lasing modes are randomly generated at the high gain position of the Brillouin bandwidth leading to a Gaussian distribution frequency drift over a long time. Due to complex paths in the weak RS fiber-based RFL,

it is challenging to reduce frequency drift further. In addition, the BRFL shows a few narrow linewidth spikes at high pump power, which leads to mode coupling and significant intensity fluctuations [109].

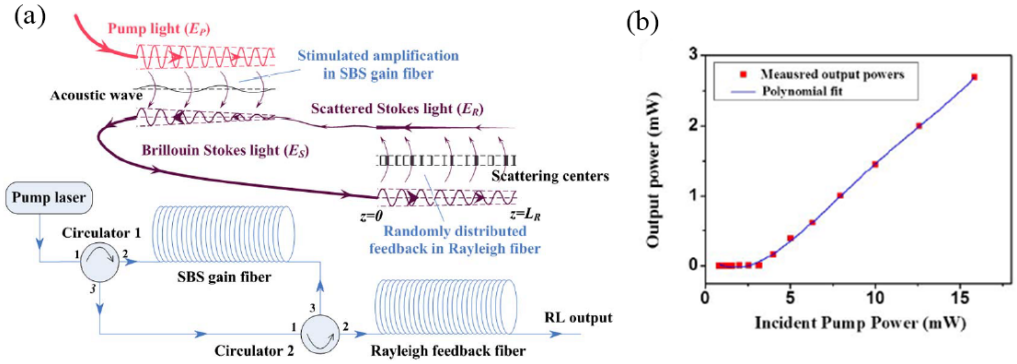


FIGURE 2.14 – (a) Schematic of the BRFL. (b) Laser power versus pump power [109].

Different narrow linewidth filters, such as FPI and double-coupler fiber ring [110, 111], are inserted into the open cavity of BRFLs to suppress the number of modes. The reduced gain competition gives rise to stabilized frequency and low intensity fluctuations. Temperature and acoustic variations change the polarization state of lasing light in the SMF random cavity. Therefore, BRFLs based on SMFs still suffer from high intensity and frequency noises due to polarization-sensitive Brillouin gain. BRFLs with all PM fibers have been demonstrated to eliminate the effect of external disturbances on laser characterizations [112, 113]. PM fiber-based BRFLs have some advantages over SMF-based BRFLs : 1) the preserved polarization state of linear polarized light in the PM fiber suppresses frequency and intensity fluctuations under external perturbations, 2) the PM gain fiber has a smaller effective mode field diameter of 6.48 µm than that of the SMF (10.4 µm), which provides a higher Brillouin gain coefficient and low lasing threshold, 3) two-dimensional stresses from Boron-doped-silica rods introduce different BFSs in the slow and fast axes, providing a unique way to generate the dual-wavelength orthogonal polarized BRFL. All-PM BRFLs provide an approach to studying the role of the acoustic wave in the noise contribution [114]. FWM is introduced in the all-PM BRFL to measure noise properties with time. The working principle of acoustic wave detection in the BRFL is shown in Fig. 2.15. The BRFL is generated by pumping the incident light in the slow axis of the PM fiber. A probe wave in the fast axis of the PM fiber is utilized to detect the acoustic wave in the BRFL. When the frequency of the probe wave satisfies the phase matching condition, it is possible to measure the dynamics of the generated acoustic wave in the BRFL. The distributed detection of the acoustic wave in the all-PM BRFL was also demonstrated [115]. Both static and dynamic acoustic measurements were achieved based on

BOTDA and optical time domain reflectometry (OTDR) techniques, revealing the phase noise of the BRFL.

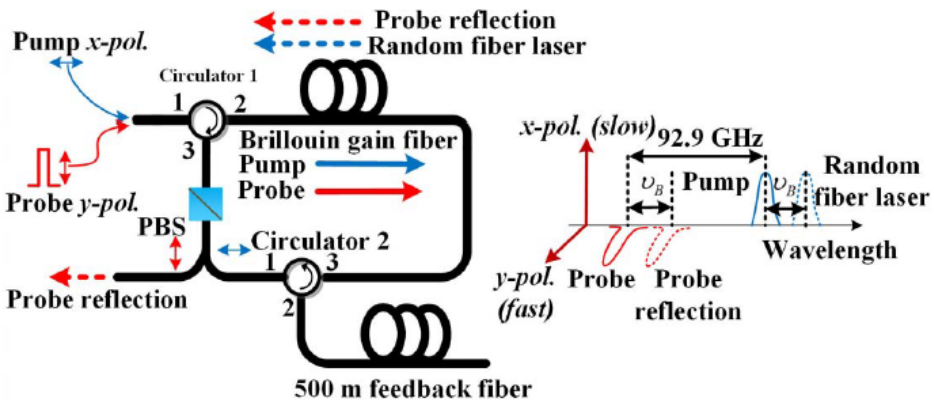


FIGURE 2.15 – Operation principle of acoustic wave detection in BRFL [114].

### 2.3.3 Temporal and spectral properties

RFLs with complex paths have presented rich spectral and temporal properties, providing a new platform for underlying laser physics exploration. Lasing emission in both time and frequency domains is an essential gateway to understanding the buildup process and lasing characterizations of RFLs. The temporal and spectral properties are power-dependent because of different mode distributions in the random system at different pump powers. Spectral dynamics, intensity statistics and replica symmetry breaking (RSB) in RFLs are reviewed :

#### Spectral dynamics

Observation of spectral dynamics provides a method to reveal the complex nature of lasing spectra in RFLs. There are different ways to measure the real-time spectro-temporal evolution of RFLs with various gain mechanisms. In the RFL based on SRS [116], the real-time spectro-temporal evolution was proposed and demonstrated by scanning a FPI with a sampling rate of 180 Hz and a resolution of 2 pm. The spectral evolution exhibits many narrow spikes with varying powers and wavelengths, as shown in Fig. 2.16(a). Spectral correlation between different spectra was demonstrated for the first time by calculating the Pearson correlation, as shown in Fig. 2.16(b), revealing the existence of mutual dependence between lasing modes. The spectral evolution of the EDF-based RFL with random distributed FBGs was performed using a Finisar 1500 s spectrum analyzer with an acquisition

rate of 10 Hz and a spectral resolution of 1.2 pm. The spectral evolution shows narrow lines at several specific wavelengths varying over time [117]. Each line corresponds to a localized mode enabled by light localization in the strong scattering random FBG-based RFL. The large EDF gain bandwidth of tens of nanometers allows hopping among many modes over time. The above methods with a spectral resolution of picometers are inadequate to measure the narrow linewidth SBS-based RFLs. The heterodyne method was proposed for the spectral evolution measurement of SBS-based RFLs. The high resolution of less than 1 kHz allows for measuring the mode dynamics of the narrow-linewidth SBS gain-based RFL [118]. The BRFL with RS distributed feedback shows fast mode hopping because of complex lasing paths in the weak RS feedback.

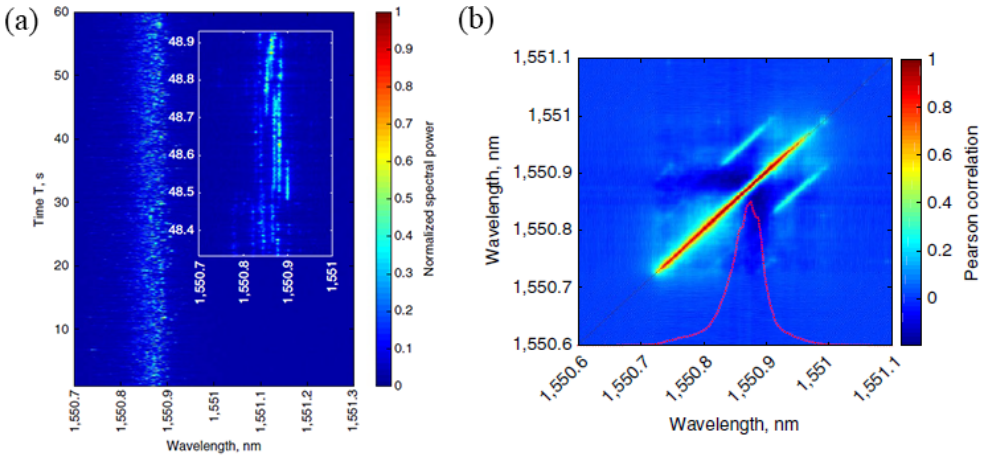


FIGURE 2.16 – (a) Real-time spectro-temporal evolution. (b) Spectral correlations [116].

### Intensity statistics

Stable distribution, also called $\alpha$-stable Lévy distribution, was proposed by Lévy in 1925 during the investigation of the behavior of sums of independent random variables [119]. Intensity statistics in RLs were characterized by $\alpha$-stable Lévy distribution, showing different possible fluctuations [120–122]. Lévy index $\alpha \in (0, 2]$ governs the intensity fluctuation. The probability distribution exhibits the Lévy behavior in the range of $0 < \alpha < 2$ and the Gaussian behavior at the boundary value $\alpha = 2$. The Lévy distribution with heavy tail indicates the high probability of extreme events and strong intensity fluctuations, while the Gaussian distribution suggests weak intensity fluctuations. In the one-dimensional erbium-doped RFL [123], different statistical regimes of intensity fluctuations were measured with increasing pump power. An initial Gaussian regime at the pump power below the threshold is followed by a Lévy regime at the pump power near the threshold, and the Gaussian regime is recovered again at the pump power well above the threshold. The probability density

functions of three distributions are shown in Fig. 2.17. Different intensity distributions are attributed to complex mode structures in the RFL, which strongly depend on pump power. The intensity statistics in the SRS-based RFL were also investigated, showing similar statistical behaviors to the EDF-based RFL [124].

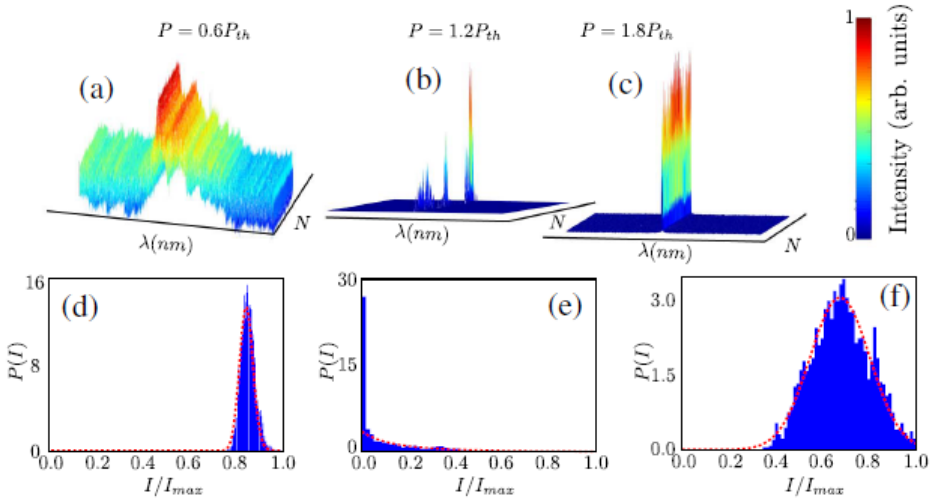


FIGURE 2.17 – Intensity spectra for each input power (a) below, (b) around, and (c) above the threshold. (d)–(f) PDFs of maximum intensities [123].

### Replica symmetry breaking

RLs have many random states produced by the complex random cavity. Multiple random modes will be excited over the loss to compete for the limited gain at high pump power. Strong coupling between random modes leads to the glassy behavior of RLs, while no gain competition and the independent oscillation of modes make RLs in the paramagnetic regime. RSB was first proposed and demonstrated in RLs to reveal the glassy behavior and the nature of randomness. RSB is characterized by the Parisi overlap parameter ($q$), which represents the correlation of intensity fluctuations of spectral emission between traces [125]. The position of the maximum probability of $q$ distribution $q_{\max}$ is introduced to characterize the glassy behavior. The distributions of $q$ and the values of $q_{\max}$ at different pump energies were measured as shown in Fig. 2.18. The values of $q_{\max}$ are centered around zero at pump energies below the threshold because random modes from spontaneous emission are independent and do not interact in the paramagnetic regime. The values of $q_{\max}$ are around one when increasing pump energies above the threshold. Many random modes are excited above the noise level in the gain bandwidth by stimulated emission. Mode coupling in the gain bandwidth induces the glassy phase behavior and RSB. The transition from

the photonic uncorrelated paramagnetic to the photonic spin-glass phase with increasing pump power was demonstrated in the erbium-doped RFL by calculating the Parisi overlap parameter, suggesting RSB and the glassy behavior [126]. Multiple modes attributed to mode coupling and the glassy behavior in the RFL were confirmed by speckle contrast measurements. RSB was also measured in the RFG-based BRFL under the pump power above the threshold [127]. The RFG with enhanced scattering centers induces strong coupling between many random modes.

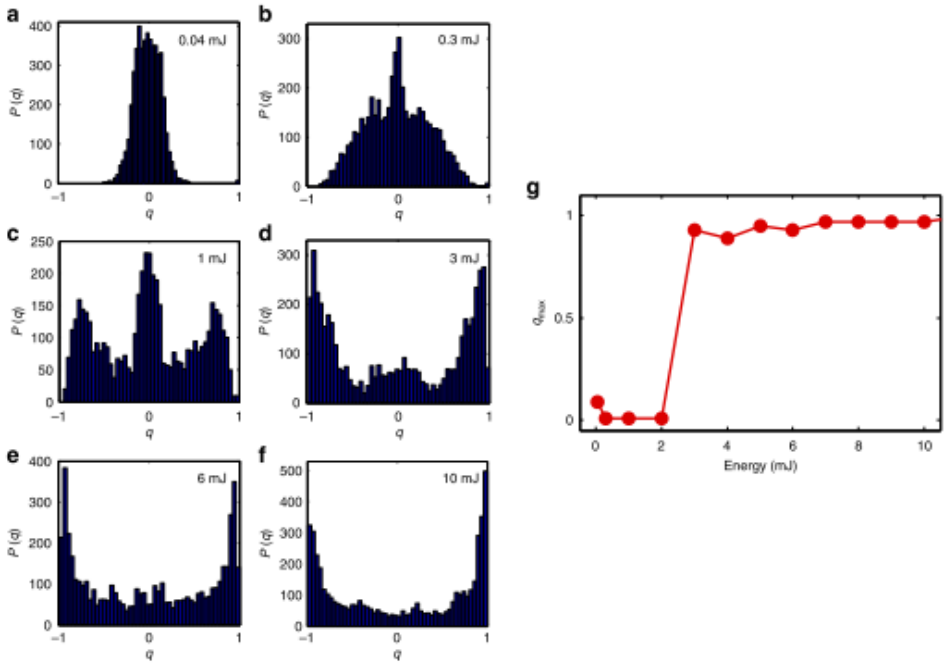


FIGURE 2.18 – (a-f) Distribution of the overlap $q$ at different pump energy, and (g) $q_{\max}$ versus pumping. [125].

# 3 Theory of SBS in fiber sensing and random fiber lasing

This chapter presents the theory of stimulated Brillouin scattering (SBS) and its applications in fiber sensing and random fiber lasing. Section 3.1 introduces the fundamental physics of Brillouin scattering, including spontaneous Brillouin scattering and SBS. Section 3.2 studies the SBS sensing principle in optical fibers and SBS measurement based on different techniques. Section 3.3 presents the theory of different distributed feedback fibers, characterizations of Brillouin random fiber lasers (BRFL), and a summary of BRFL applications.

## 3.1 Brillouin scattering in fibers

### 3.1.1 Spontaneous Brillouin scattering

Brillouin scattering occurs in optical fibers as a result of fluctuations in the dielectric constant caused by changes in the macroscopic thermodynamic quantities such as density ($\rho$), entropy ($s$), pressure ($p$), and temperature ($T$). By assuming that $\rho$ and $T$ are independent thermodynamic variables in the variation of the dielectric constant ($\Delta\epsilon$), we obtain :

$$\Delta\epsilon = \left(\frac{\partial\epsilon}{\partial\rho}\right)_T \Delta\rho + \left(\frac{\partial\epsilon}{\partial T}\right)_\rho \Delta T \tag{3.1}$$

Temperature variation-induced $\Delta\epsilon$ can be ignored in comparison to density fluctuation-induced $\Delta\epsilon$ because it only accounts for about 2% of the total $\Delta\epsilon$ [128]. We can relate

density to pressure and entropy using thermodynamics :

$$\Delta\rho = \left(\frac{\partial\rho}{\partial p}\right)_s \Delta p + \left(\frac{\partial\rho}{\partial s}\right)_p \Delta s \tag{3.2}$$

The first term describes pressure fluctuations known as acoustic waves, which gives rise to Brillouin scattering. The second term stems from entropy fluctuations corresponding to Rayleigh scattering. We will discuss the first term that causes Brillouin scattering. By substituting the first term in Eq. (3.2) into Eq. (3.1), we obtain :

$$\Delta\epsilon = \left(\frac{\partial\epsilon}{\partial\rho}\right)_T \left(\frac{\partial\rho}{\partial p}\right)_s \Delta p = \frac{\gamma_e}{\rho_0}\left(\frac{\partial\rho}{\partial p}\right)_s \Delta p \tag{3.3}$$

where $\gamma_e = \rho_0 \left(\frac{\partial\epsilon}{\partial\rho}\right)_T$ is the electrostrictive constant with $\rho_0$ being the mean density of the fiber material. The equation of motion for an acoustic wave is given by [129]

$$\frac{\partial^2\Delta\tilde{p}}{\partial t^2} - \Gamma'\nabla^2\frac{\partial\Delta\tilde{p}}{\partial t} - V_a^2\nabla^2\Delta\tilde{p} = 0 \tag{3.4}$$

where tilder denotes a quantity that varies rapidly in time, $V_a$ is the acoustic velocity in the fiber material and $\Gamma'$ is the damping parameter that is given by

$$\Gamma' = \frac{1}{\rho}\left[4/3\eta_s + \eta_b + \kappa/C_p(\gamma - 1)\right] \tag{3.5}$$

where, $\eta_s$ and $\eta_b$ are the shear and the bulk viscosity coefficients, respectively, $\kappa$ is the thermal conductivity, $C_p$ is the compressibility and $\gamma$ is the adiabatic index. One solution of Eq. (3.4) can be written as

$$\Delta\widetilde{p} = \Delta p e^{i(qz-\Omega t)} + c.c. \tag{3.6}$$

By substituting the expression for $\Delta\widetilde{p}$ given by Eq. (3.6) into Eq. (3.4), the wave equation is transformed into :

$$-\Omega^2 - i\Gamma' q^2\Omega + V_a q^2 = 0 \tag{3.7}$$

We rewrite this equation in a more general form :

$$q^2 = \frac{\Omega^2}{V_a^2 - i\Gamma'\Omega} \approx \left(\frac{\Omega}{V_a}\right)^2\left(1 + i\frac{\Omega\Gamma'}{V_a^2}\right) \tag{3.8}$$

The acoustic wave has a complex propagation constant $q$ that describes the attenuation. The phonon lifetime is related to the acoustic attenuation, which is given by $\tau_p = 1/q^2\Gamma'$.

We calculate the scattered light by acoustic waves using the following wave equation [129] :

$$\frac{\partial^2 \widetilde{E}}{\partial z^2} - \frac{n^2}{c^2}\frac{\partial^2 \widetilde{E}}{\partial t^2} = \frac{1}{\epsilon_0 c^2}\frac{\partial^2 \widetilde{P}}{\partial t^2} \tag{3.9}$$

where the polarization $\widetilde{P}$ is given by

$$\widetilde{P} = \epsilon_0 \Delta\epsilon \widetilde{E_0} = \epsilon_0 \left(\frac{\partial \epsilon}{\partial \rho}\right)\left(\frac{\partial \rho}{\partial p}\right)\Delta p \widetilde{E_0} \tag{3.10}$$

We assume that the incident optical field with a angular frequency $\omega$ and wavenumber $k$ in the medium is expressed as

$$\widetilde{E}_0(z,t) = E_0 e^{i(kz-\omega t)} + c.c. \tag{3.11}$$

By substituting the expressions of Eqs. (3.6), (3.10) and (3.11) into Eq. (3.9), we obtain :

$$\begin{aligned}\frac{\partial^2 \widetilde{E}}{\partial z^2} - \frac{n^2}{c^2}\frac{\partial^2 \widetilde{E}}{\partial t^2} = -\frac{\gamma_e}{\rho_0 c^2}(\frac{\partial \rho}{\partial p})_s[(\omega-\Omega)^2 E_0 \Delta p^* e^{i((k-q)z-(\omega-\Omega)t)} + \\ (\omega+\Omega)^2 E_0 \Delta p e^{i((q+k)z-(\omega-\Omega))t} + c.c.]\end{aligned} \tag{3.12}$$

Two frequency components, including the Stokes wave with a frequency of $\omega - \Omega$ and the anti-Stokes wave with a frequency of $\omega + \Omega$, are obtained during the interaction of the incident electromagnetic wave and the acoustic wave. For the Stokes wave, it must satisfy energy and momentum conservation :

$$\omega_p = \omega_s + \Omega \tag{3.13}$$

$$k_p = k_s + q \tag{3.14}$$

where $\omega_{p,s}$ and $k_{p,s}$ are the frequencies and wave vectors of the pump and Stokes waves, respectively, and $\Omega$ and $q$ are the frequencies and wave vectors of the acoustic wave. The dispersion relationship between the wave vector and angular frequency of the optical wave is given by

$$|k_{\mathrm{p,s}}| = \frac{2\pi n}{\lambda_{\mathrm{p,s}}} \tag{3.15}$$

where $\lambda_{\mathrm{p}}$ and $\lambda_{\mathrm{s}}$ are the wavelength of pump and Stokes waves, respectively. The dispersion

relationship for the acoustic wave is expressed as

$$|q| = \frac{2\pi}{\lambda} = \frac{\Omega}{V_a} \tag{3.16}$$

Eq. (3.16) can be rewritten as :

$$\Omega = |q|V_a \approx 2V_a|k_p|\sin(\theta/2) \tag{3.17}$$

where $\theta$ is the angle between pump and Stokes waves. Figure 3.1 shows the phase matching conditions of the Stokes wave in backward and forward Brillouin scattering. In single-mode fibers (SMF), the relevant Brillouin scattering directions are the backward scattering with $\theta = 180°$ and forward scattering with $\theta = 0$.

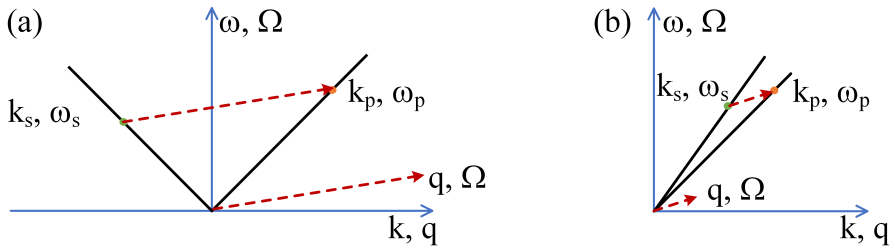


FIGURE 3.1 – Phase-matching diagrams for the Stokes wave in (a) backward Brillouin scattering and (b) forward Brillouin scattering.

### 3.1.2 Stimulated Brillouin scattering

Spontaneous Brillouin scattering stems from the thermal fluctuation of density in the presence of incident light with low power ; while SBS is caused by the high pump power above the threshold or launching another light at the Stokes frequency from the opposite end of the material in addition to the pump light. The counter-propagating Stokes wave and pump wave with a frequency difference of the Brillouin resonance lead to electrostriction. Molecules will restructure themselves under the electrostrictive force, changing the density of the material. The variation of dielectric constant is related to the density change, which is given by $\Delta\epsilon = (\partial\epsilon/\partial\rho)\,\Delta\rho$. Hence, the field energy density change of a material is expressed as [129]

$$\Delta u = \frac{1}{2}\epsilon_0 E^2 \Delta\epsilon = \frac{1}{2}\epsilon_0 E^2 \left(\frac{\partial\epsilon}{\partial\rho}\right)\Delta\rho \tag{3.18}$$

The work required to compress the material must be equivalent to the change in energy density according to the first law of thermodynamics. Consequently, the work done per

unit volume is given by

$$\Delta w = -p_{st}\frac{\Delta\rho}{\rho} = \Delta u \tag{3.19}$$

Hence, the electrostrictive pressure ($p_{st}$) is written as

$$p_{st} = -\frac{1}{2}\epsilon_0\rho\left(\frac{\partial\epsilon}{\partial\rho}\right)E^2 = -\frac{1}{2}\epsilon_0\gamma_e E^2 \tag{3.20}$$

Using the density change $\Delta\rho = -(\partial\rho/\partial p)\Delta p$, we find that the change of the material density is :

$$\Delta\rho = \frac{1}{2}\varepsilon_0\rho C\gamma_e E^2 \tag{3.21}$$

where $C = (\partial\rho/\partial p)/\rho$ is the compressibility.

The SBS process by electrostriction is illustrated in Fig. 3.2. If the pump wave and the signal wave are counter-propagating in the fiber, whose frequency difference is equal to the Brillouin resonant frequency in the medium, a beat signal with variable intensity will be created. The generated acoustic wave with the Brillouin resonant frequency will change the material density through electrostriction. The changed density will result in a refractive index grating moving through the material at the speed of sound due to the electro-optic effect. Finally, the interference can be strengthened by the energy transfer between the pump and signal waves caused by the diffraction of the grating.

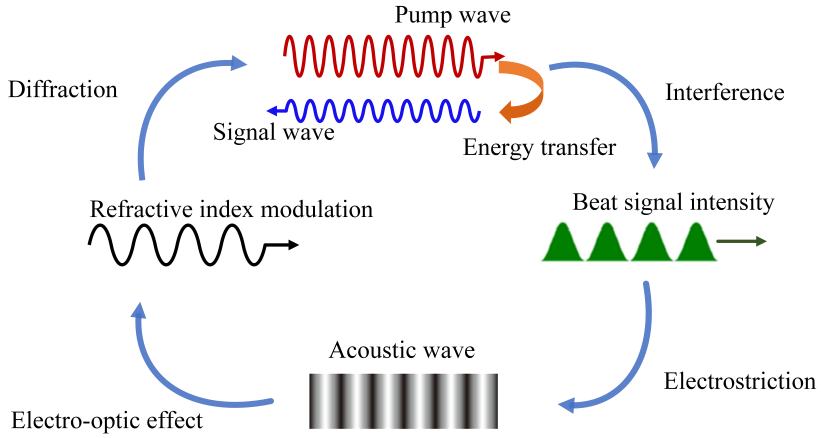


FIGURE 3.2 – Illustration of the SBS process.

To derive equations that govern the evolution of the acoustic wave during the SBS process, we first consider the electric waves ($\tilde{E}_p$ and $\tilde{E}_s$) and the acoustic wave (represented by the material density fluctuation $\tilde{\rho}$) involved into the process :

$$\tilde{E}_p(z,t) = A_p(z,t)e^{i(k_p z-\omega_p t)} + c.c. \tag{3.22}$$

$$\tilde{E}_s(z,t) = A_s(z,t)e^{i(k_s z-\omega_s t)} + c.c. \tag{3.23}$$

$$\tilde{\rho}(z,t) = \rho_0 + \rho(z,t)e^{i(qz-\Omega t)} + c.c. \tag{3.24}$$

For the present of the external electrostrictive force during the SBS process, the equation of motion of the acoustic wave in Eq. (3.4) is rewritten as

$$\frac{\partial^2\tilde{\rho}}{\partial t^2} - \Gamma'\nabla^2\frac{\partial\tilde{\rho}}{\partial t} - {V_a}^2\nabla^2\tilde{\rho} = \nabla\cdot\mathbf{f} \tag{3.25}$$

with

$$\nabla\cdot\mathbf{f} = \nabla\cdot(\nabla p_{st}) = \epsilon_0\gamma_e q^2\left[A_p A_s^* e^{i(qz-\Omega t)} + \text{ c.c. }\right] \tag{3.26}$$

Substituting Eqs. (3.24) and (3.26) into Eq. (3.25), and applying slowly varying amplitude approximation, the steady-state solution of acoustic amplitude is given by

$$\rho(z,t) = \epsilon_0\gamma_e q^2\frac{A_p A_s^*}{\Omega_B^2 - \Omega^2 - i\Omega\Gamma_B} \tag{3.27}$$

where $\Omega_B \equiv \omega_p - \omega_s$ is the Brillouin frequency shift of the medium and $\Gamma_B = q^2\Gamma'$ is the Brillouin linewidth, which is the inverse of the photon lifetime. The nonlinear polarization under the electric fields is given by

$$\tilde{P}_p = \epsilon_0\gamma_e\rho_0^{-1}\rho A_s e^{i(k_p z-\omega_p t)} + c.c. \tag{3.28}$$

$$\tilde{P}_s = \epsilon_0\gamma_e\rho_0^{-1}\rho A_p e^{i(k_s z-\omega_s t)} + c.c. \tag{3.29}$$

Substituting Eqs. (3.22), (3.23) and (3.28), (3.29) into (3.9), we obtain the steady-state solution :

$$\frac{dI_p}{dz} = -gI_p I_s \tag{3.30}$$

$$\frac{dI_s}{dz} = -gI_p I_s \tag{3.31}$$

where the intensity is expressed as $I_i = 2n\epsilon_0 c A_i A_i^*$ with $i = p, s$ and the SBS gain factor $g$ is given by

$$g = g_0\frac{(\Gamma_B/2)^2}{(\Omega_B-\Omega)^2 + (\Gamma_B/2)^2} \tag{3.32}$$

with

$$g_0 = \frac{\gamma_e^2\omega^2}{nV_a c^3\rho_0\Gamma_B} \tag{3.33}$$

Hence, the Brillouin gain has a Lorentzian spectral shape with the gain bandwidth of $\Delta v_B = \Gamma_B/(2\pi)$. In optical fibers, the phonon lifetime $T_B = 1/\Gamma_B$ is typically less than

10 ns.

## 3.2 Brillouin fiber sensing measurement

### 3.2.1 Principle of Brillouin fiber sensing

Using Eq. (3.17) at $\theta = 180°$ for counter-propagating optical waves in SBS, we obtain Brillouin frequency shift (BFS) ($v_B$) :

$$v_B = \frac{2n_{eff}V_a}{\lambda} \tag{3.34}$$

where $\lambda$ is the pump wavelength and $n_{eff}$ is the effective refractive index. The acoustic velocity $V_a$ is related to the physical quantities of the fiber material :

$$V_a = \sqrt{\frac{1-\sigma}{(1-2\sigma)(1+\sigma)}\frac{E}{\rho}} \tag{3.35}$$

where $\sigma$ is the Poisson's ratio, $E$ is the Young's modulus and $\rho$ is the density of fiber. Within a small range, BFS is linearly dependent on strain and temperature :

$$v_B(T,\varepsilon) = v_{B0} + C_T\,(T - T_0) + C_\varepsilon\,(\varepsilon - \varepsilon_0) \tag{3.36}$$

where $C_T$ is the temperature coefficient, $C_\varepsilon$ is the strain coefficient and $v_{B0}$ is the Brillouin frequency shift at the reference temperature $T_0$ and strain $\varepsilon_0$. Any thermal or acoustic disturbance will affect the effective refractive index and acoustic velocity, which can be demodulated by the change of BFS. Temperature and strain coefficients are dependent on the fiber material and geometry.

### 3.2.2 Heterodyne detection

Brillouin scattering measurement based on the heterodyne detection technique is shown in Fig. 3.3. The light from a pump laser is injected into one end of the fiber under test (FUT) through a circulator to generate the Stokes wave. The beat signal is created by combining the pump laser (local oscillator) with the Stokes wave via a coupler. The beat optical signal is converted to an electric signal by a photodetector (PD), and the Brillouin gain spectrum is measured by an electrical spectrum analyzer (ESA). This method is commonly used for Brillouin scattering measurement owing to its simple configuration. However, it can not be utilized for distributed Brillouin sensing along the fiber.

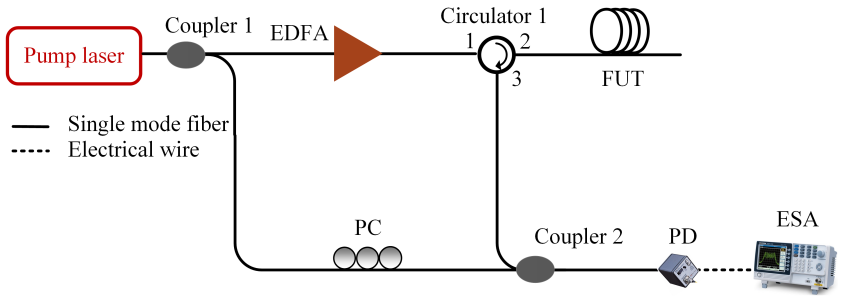


FIGURE 3.3 – Heterodyne detection setup. EDFA : Erbium doped fiber amplifier ; FUT : fiber under test ; PC : polarization controller ; PD : photodetector ; ESA : electrical spectrum analyzer.

For distributed Brillouin sensing, the pulsed light after an electro-optic modulator (EOM) is launched into the FUT as plotted in Fig. 3.4. This setup is known as Brillouin optical time-domain reflectometry (BOTDR). Since Brillouin scattering occurs at any position along the fiber, Stokes signals from different positions reach the coupler at different instances of time. The position of each Stokes signal can be calculated using the speed of light in the FUT. By measuring the distributed BFS, it is possible to determine the variation at a particular location. The record time $t$ and interaction location $z$ are given by

$$z = (c/n)\,\frac{t}{2} \tag{3.37}$$

where $c$ is the speed of light in vacuum and $n$ is the refractive index of the fiber. The spatial resolution is determined by the pulse duration $\Delta t$, which is expressed as

$$\Delta z = (c/n)\,\frac{\Delta t}{2} \tag{3.38}$$

The spatial resolution of BOTDR is limited to 1 m for SMFs due to the 10 ns lifetime of the acoustic wave. A pulse duration of less than 10 ns will induce a broadened Brillouin gain spectrum and less accurate measurement.

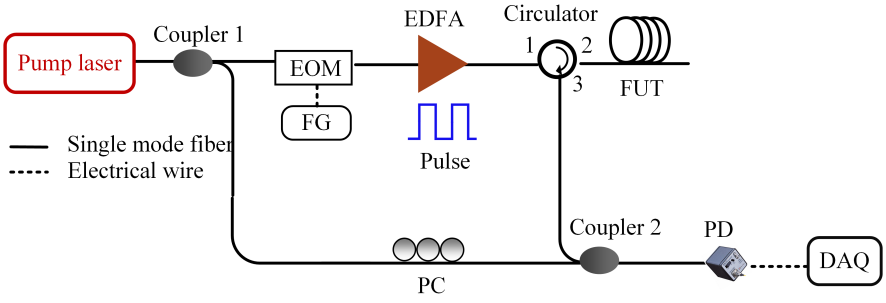


FIGURE 3.4 – BOTDR setup. EOM : electro-optic modulator ; FG : function generator.

### 3.2.3 Brillouin optical time-domain analysis

Another technique for distributed Brillouin scattering measurement is Brillouin optical time-domain analysis (BOTDA). A short pump pulse and a continuous wave (CW) probe are injected into two ends of the FUT, as illustrated in Fig. 3.5(a). When the CW probe wave is downshifted by the Brillouin resonant frequency of the FUT, the pump and probe waves interact, resulting in the SBS process. The CW probe wave in the Brillouin resonant frequency is amplified due to energy transfer from the pump pulse. The Brillouin gain spectrum at any position along the fiber can be obtained by sweeping the frequency of the CW wave. In contrast, if the probe wave has an up-shifted Brillouin resonant frequency compared to the pump wave, which is the anti-Stokes frequency, the probe wave gives energy to the pump pulse, and the detected CW signal experiences a Brillouin loss.

The experimental setup of BOTDA is shown in Fig. 3.5(b). The CW light from a pump laser is split into two branches by a coupler. In the lower branch, the short pump pulse is generated after an EOM driven by a function generator (FG). In the upper branch, the probe wave with two sidebands is generated, and the lower frequency sideband is selected as the Stokes wave after a narrow bandwidth filter. The amplitude of the probe wave at different frequencies can be obtained by sweeping the frequency using a radio-frequency (RF) source around the estimated BFS. The continuously changing amplitude of the probe wave is measured using a PD and an oscilloscope (OSC). The local Brillouin gain spectrum at each fiber section can be reconstructed according to amplitude variations at different frequencies.

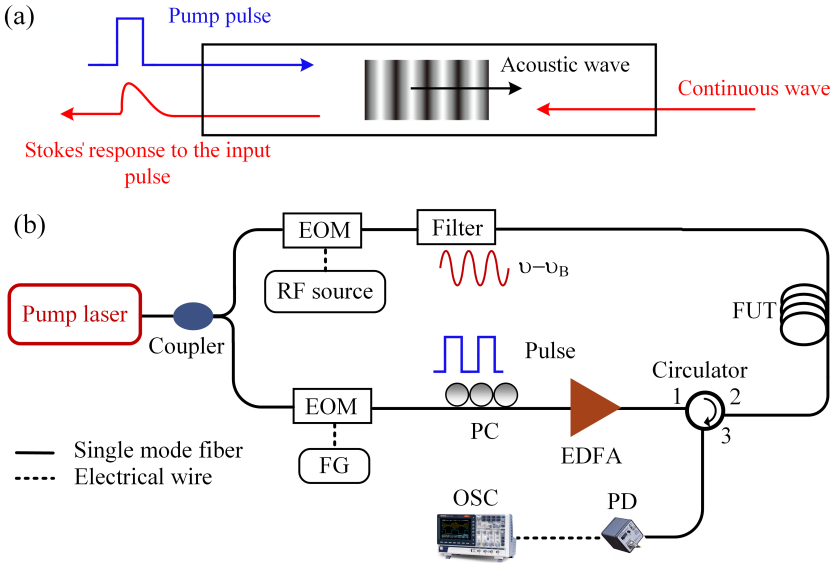


FIGURE 3.5 – (a) BOTDA mechanism (b) BOTDA setup. RF : radio-frequency.

### 3.2.4 Brillouin optical correlation domain analysis

In pulse-based Brillouin scattering measurement methods, the detected spectrum is given by the convolution of the acoustic resonance spectrum and the pulse spectrum. With decreasing pulse width below the phonon lifetime, the detected gain spectrum broadens, which limits measurement accuracy. The spatial resolution can be improved by the position-resolved Brillouin response, which can be obtained through the correlation between counter-propagating pump and probe waves. Figure 3.6 shows the position selecting measurement by Brillouin optical correlation domain analysis (BOCDA). The pump and probe waves are counter-propagating in the fiber. SBS occurs when the frequency difference between the pump and probe waves satisfies the Brillouin resonant frequency of the FUT. When modulation frequency ($f_m$) is applied to those two waves, SBS only occurs at the correlation peak point, where two waves are highly coherent because the frequency difference is constant in one specific position. At other positions, the frequency of the pump wave changes continuously relative to the probe wave, resulting in a suppression of Brillouin interaction. When the laser frequency $f_m$ is changed, distributed measurement becomes possible because the correlation peak point is shifted. For BOCDA, the spatial resolution is determined by the width of the correlation peak :

$$\Delta z = \frac{c}{n} \cdot \frac{\Delta \upsilon_{\mathrm{B}}}{2\pi f_{\mathrm{m}} \cdot \Delta f} \tag{3.39}$$

where $\Delta f$ is the modulation amplitude and $\Delta \upsilon_{\mathrm{B}}$ is the Brillouin gain bandwidth. The measurement range ($d_{\mathrm{m}}$) is limited by the interval of correlation peaks, and is given by

$$d_{\mathrm{m}} = \frac{c}{n} \cdot \frac{1}{2f_{\mathrm{m}}} \tag{3.40}$$

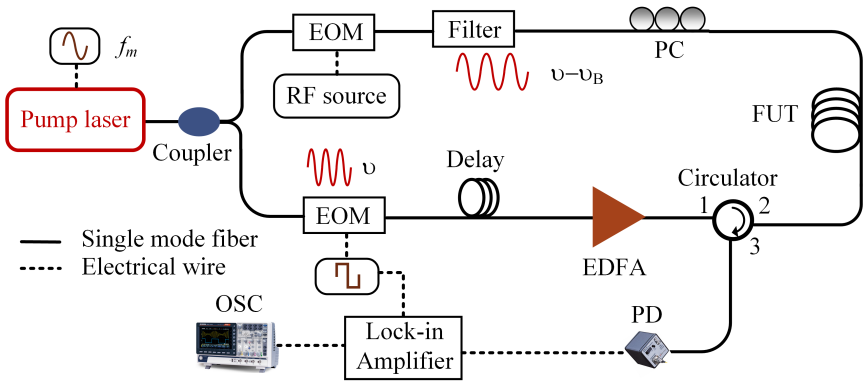


FIGURE 3.6 – BOCDA setup.

## 3.3 Brillouin random fiber lasers

### 3.3.1 Light localization in strong scattering random media

The concept of localization for electrons in disordered solids was first proposed by Anderson [130]. Coherent scattering of electrons from the disorder can bring transport to a complete halt due to quantum mechanical wave interference. Light localization is an effect that stems from coherent multiple scattering and wave interference in extremely strong scattering optical random media [131]. Light localization in various dimensions of random lasers (RL) has been widely demonstrated over the last two decades. Light localization in three-dimensional RLs is difficult to observe because it requires very large refractive index contrasts that are not available in low-loss optical materials, while light localization in one- and two-dimensional RLs is possible due to the controlled localization length by the index contrast, the size of the particles, and the amount of disorder [132, 133]. Random modes exhibit higher Q values in one-dimensional strong scattering RLs because they are more localized and have fewer propagation paths. Lasing modes in the one-dimensional RL are long-term stable around their localization positions. In order to observe Anderson localization of light, the localization length should be smaller than the system length. The localization length $\xi$ in one-dimensional media is given by [76]

$$\xi \sim -\frac{L}{2\ln\langle T(L)\rangle} \tag{3.41}$$

where $L$ is the system length and $\langle T(L)\rangle$ is the average transmission. It has been shown that light localization is possible in one-dimensional RLs with strong scattering media [87, 134].

### 3.3.2 Random distributed feedback mechanisms

There are two types of random distributed feedback in BRFLs ; one with localization in the scattering enhanced random fiber grating (RFG) and the other without localization in the weak Rayleigh scattering (RS) fiber. Due to the inhomogeneity of the fiber core, optical fibers have variations in density and refractive index, leading to Rayleigh backscattered light with random amplitude and phase. The backscattered RS depends on the scattering coefficient and fiber length. The backscattering coefficient in SMFs is $4.5\times10^{-5}$ km$^{-1}$ [80]. The calculated reflectivity is approximately $-47$ dB for a 200 m SMF. The BRFL based on weak RS feedback exhibits low-Q resonances and a high threshold. The RFG with random refractive index modulation periods can be utilized as the distributed feedback of BRFLs. The randomly changed periods along the short RFG allow the generation of many random

modes with a small frequency difference. Refractive index fluctuations of each scatter in RFGs are around $10^{-4}$ to $10^{-5}$, which are three orders of magnitude higher than intrinsic refractive index fluctuations in RS fibers [91]. A high-efficiency BRFL can be achieved using the RFG distributed feedback. The random fiber grating array (RFGA) consisting of tens of single RFGs with similar separation between neighboring RFGs can be seen as a stack of Fabry-Pérot (FP) cavities, which leads to the multiple interference of light. The BRFL based on the RFGA can exhibit high-Q resonances and a low threshold.

The reflection spectra of a 200 m RS fiber, a 5 cm single RFG, and a 8 m RFGA are measured as shown in Fig. 3.7. The RFG and RFGA exhibit reflection over a broad wavelength range owing to the index modulation planes with the random spatial interval from 0.5180 µm to 0.5464 µm. RFGA shows a strong reflection of -8 dB, as plotted in Fig. 3.7(a). Many RFGs with high refractive index modulation spots enables strong backscattering of the RFGA. The random separations between inscription spots reduce interference and increase diffraction, leading to many high-Q random modes, which are critical in random fiber lasers (RFL). The combination of interference and diffraction leads to discrete FPI elements that hold photons. Therefore, the reflection spectra of the RFGA shows a complex interference pattern with a random fluctuation of ∼10 dB. The RFGA exhibits much narrow peaks, as shown in the inset of Fig. 3.7(a), due to multiple wave interference between more FP cavities formed by many strong scattering RFG pairs with similar distance in the RFGA. The RFGA with sharp interference peaks is a type of FP narrow linewidth filter, which can suppress modes in BRFLs. The RFGA distributed feedback with tens of RFGs provides a large number of random modes with small frequency difference. The reflection spectrum of the single RFG shows a reflection of -30 dB, which is more than 20 dB lower than that of the RFGA. Therefore, photons confine in the random medium for a shorter time. The broad reflection bandwidth of the RFG allows multiple modes operation in a random cavity, which leads to increased gain competition. Fast mode

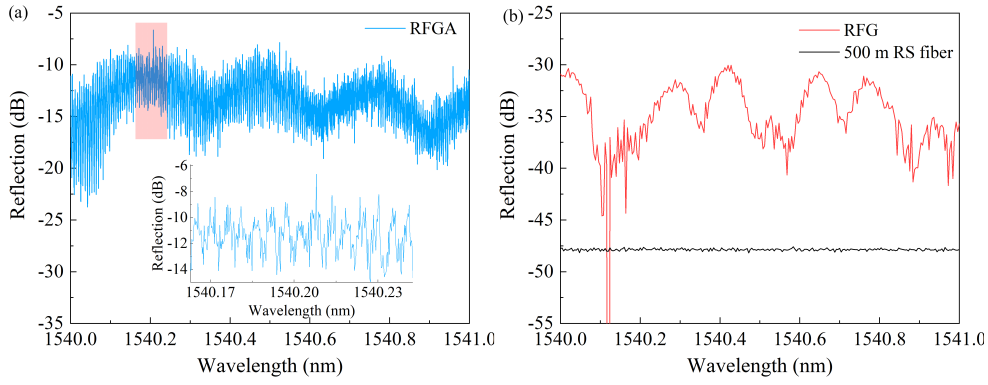


FIGURE 3.7 – The reflection spectra of the 8 m RFGA, 5 cm RFG, and 200 m RS fiber.

hopping over a certain time and many modes propagation in the gain region are expected because of the large bandwidth of the RFG feedback. The 200 m RS fiber has a much smaller refection of -47 dB due to the weak backscattering coefficient of the PM fiber. The weak interference fluctuation of the RS fiber is attributed to the averaging smoothing by numerous ultra-weak Rayleigh scatters with random phase.

Figure 3.8 shows the working principle of weak scattering in the RS fiber and strong scattering in the RFGA. The schematic of a single RFG with thousands of sub-gratings is plotted in the inset of Fig. 3.8(b). Light localization in strong scattering random media has been demonstrated, in which multi-scattering waves in forward and backward directions follow the same path leading to constructive wave interference [135]. Similarly, photons can be confined inside the disordered strong scattering RFGA because wave interference in the multi-scattering random medium gives rise to photon localization. The RFGA-based BRFL is in the regime of Anderson localization, and photons follow the same path in the BRFL, which prolongs the lasing lifetime. For the weak RS distributed feedback without light localization, photons propagate by means of a random-walk process for each round trip. The random modes with random phases compete for the available gain until the modes with the highest gain over the loss survive for lasing.

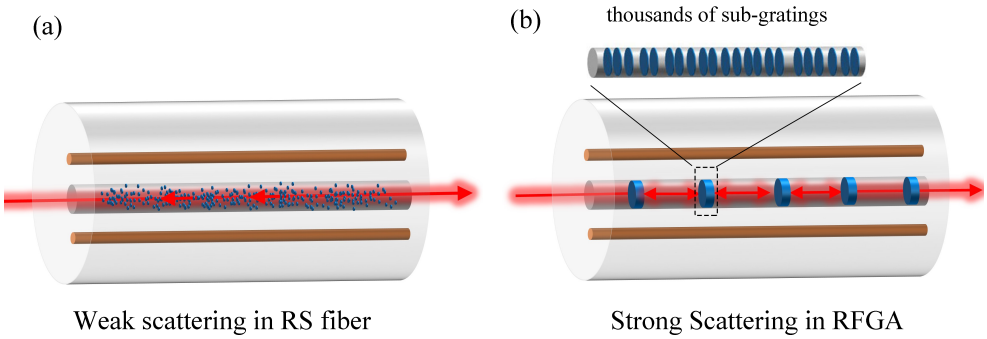


FIGURE 3.8 – The schematic of (a) weak scattering in PM RS fiber ; (b) strong scattering in PM RFGA.

### Weak Rayleigh scattering from the inhomogeneity of media

RS is an elastic scattering given by much smaller molecules than the wavelength of incident light, which can be described by the model of induced dipole radiation. The incident electromagnetic wave causes the sinusoidal change of charge distribution over time inside the molecule generating a vector potential. The electromagnetic radiation induced by the vector potential drives a dipole oscillation. As a result, the molecule re-emits multiple radiation components with the same frequency as the incident light. When the molecule is

much smaller than the wavelength of incident light, the oscillating dipole fields are given by [136]

$$\mathbf{E} = \frac{1}{4\pi\epsilon_0}\left\{k^2(\mathbf{n}\times\mathbf{p})\times\mathbf{n}\frac{e^{ikr}}{r} + [3\mathbf{n}(\mathbf{n}\cdot\mathbf{p}) - \mathbf{p}]\left(\frac{1}{r^3} - \frac{ik}{r^2}\right)e^{ikr}\right\} \tag{3.42}$$

$$\mathbf{H} = \frac{ck^2}{4\pi}(\mathbf{n}\times\mathbf{p})\frac{e^{ikr}}{r}\left(1 - \frac{1}{ikr}\right) \tag{3.43}$$

where $\mathbf{p}$ is the dipole momentum, $k$ is the scattered wave number and $r$ the distance from the dipole to the observed point. Considering the radiation zone ($kr \gg 1$), Eq. (3.42) and Eq. (3.43) can be rewritten as

$$\mathbf{H} = \frac{ck^2}{4\pi}(\mathbf{n}\times\mathbf{p})\frac{e^{ikr}}{r} \tag{3.44}$$

$$\mathbf{E} = Z_0\mathbf{H}\times\mathbf{n} \tag{3.45}$$

where $Z_0 = \sqrt{\epsilon_0\mu_0}$ is the impedance of free space. The time-averaged power radiation per unit solid angle by the dipole momentum is given by

$$\frac{dP}{d\Omega} = \frac{1}{2}\,\mathrm{Re}\left[r^2\mathbf{n}\cdot\mathbf{E}\times\mathbf{H}^*\right] \tag{3.46}$$

Substituting Eq. (3.45) and Eq. (3.44) into Eq. (3.46), we obtain :

$$\frac{dP}{d\Omega} = \frac{c^2Z_0}{32\pi}k^4\left|(\mathbf{n}\times\mathbf{p})\times\mathbf{n}\right|^2 = \frac{c^2Z_0}{32\pi}k^4\left|\mathbf{p}\right|^2\sin(\theta)^2 \tag{3.47}$$

If the components of $\mathbf{p}$ have the same phase, Eq. (3.47) can be rewritten as

$$\frac{dP}{d\Omega} = \frac{c^2Z_0}{32\pi}k^4\left|\mathbf{p}\right|^2\sin(\theta)^2 \tag{3.48}$$

where $\theta$ is angle between $\mathbf{n}$ and $\mathbf{p}$. The total power radiated by the field, which is independent of the relative phases of the components of $\mathbf{p}$, is expressed as

$$P = \frac{c^2Z_0k^4}{12\pi}\left|\mathbf{p}\right|^2 \tag{3.49}$$

Equation (3.49) reveals that the scattering power is proportional to wave number $k^4$ (or in wavelength $(1/\lambda)^4$). This dependence on frequency is known as Rayleigh's law and the dipole scattering is known as RS. In BRFLs, the Brillouin signal can be scattered randomly by RS from the random scattering centers and amplified in the gain fiber, generating the Brillouin lasing with random nature. Light follows different paths over time in the RS distributed feedback fiber without photon localization owing to the single scattering of ultra-weak RS. In the RS-based RFL, lasing modes hop randomly on each round trip,

resulting in a short lasing lifetime and large lasing frequency drift [118]. Long fiber lengths are required for the RS distributed feedback-based high-efficiency BRFLs owing to the weak scattering strength and accumulation nature of RS. The long RS fiber induces a large density of modes with small frequency separations in the gain bandwidth, which increases the gain competition. In addition, the long fiber is sensitive to external variations such as thermal and acoustic fluctuations, leading to large lasing frequency drift and strong intensity fluctuations.

**Strong multi-scattering in enhanced random grating media**

RFGs with random periods and high refractive index modulation spots display random nature and strong scattering. Fiber Bragg gratings (FBG) with the same modulation period introduce negligible phase change of photons in grating spots, whereas RFGs with random periods cause different phases in grating spots. High index modulation spots with random periods produce many Fresnel reflection boundaries to hold photons. They can be represented as many matrices with different phase and amplitude values. In contrast to single scattering in the weak RS fiber, multiple scattering occurs in the strong scattering RFG. Wave interference in the multiple scattering RFG leads to light localization. Since photons can be trapped in the RFG with light localization, the photon lifetime of the RFG-based BRFL is expected to increase. Light propagation in random gratings with multiple scattering centers can be understood based on the work of Berry and Klein [137]. The transmission amplitude of RFG can be calculated from the stack recursion equation. The transmission amplitude for the first two random grating scattering centers ($T_{12}$) is the coherent sum of all the multiplied reflected and transmitted waves

$$T_{12} = T_1T_2 + T_1R_2R_{1\_}T_2 + T_1R_2R_{1\_}R_2R_{1\_}T_2 + \cdots = \frac{T_1T_2}{1 - R_{1\_}R_2} \tag{3.50}$$

where $T_{\mathrm{i}}$ and $R_{\mathrm{i}}$ represent the transmission and reflection amplitudes of forward waves for $i_{th}$ random grating centers, respectively, and $T_{\mathrm{i}\_}$ and $R_{\mathrm{i}\_}$ of backward waves for $i_{th}$ random grating centers. The quantities in Eq. (3.50) have random phase owing to the random grating periods of the RFG. The average of any function of the transmitted intensity over the random phase is given by [137]

$$\left\langle f\left(|T_{12}|^2\right)\right\rangle = \frac{1}{2\pi}\int_0^{2\pi} \mathrm{d}\phi f\left(\frac{|T_1|^2\,|T_2|^2}{(1 - |R_{1\_}R_2|\exp\{\mathrm{i}\phi\})^2}\right) \tag{3.51}$$

The average logarithmic transmitted intensity over random phase is expressed as

$$\left\langle \log\left(|T_{12}|^2\right)\right\rangle = \log\left(|T_1|^2\right) + \log\left(|T_2|^2\right) - \frac{1}{2\pi}\int_0^{2\pi} \mathrm{d}\phi \log\left(1+|R|^2 - 2|R|\exp\{\mathrm{i}\phi\}\right) \tag{3.52}$$

where $R = R_{1\_}R_2$. Because of $|R_{1\_}R_2| < 1$, the integral in Eq. (3.52) is given by

$$\begin{aligned}\int_0^{2\pi} \mathrm{d}\phi \log\left(1+|R|^2 - 2|R|\exp\{\mathrm{i}\phi\}\right) &= 2\pi\left(\log\left(\frac{1+|R|^2+\sqrt{(1+|R|^2)^2-(2|R|)^2}}{2}\right)\right)\\ &= 0\end{aligned} \tag{3.53}$$

Therefore, Eq. (3.52) is rewritten as

$$\left\langle \log\left(|T_{12}|^2\right)\right\rangle = \log\left(|T_1|^2\right) + \log\left(|T_2|^2\right) \tag{3.54}$$

Assuming $\tau_k$=$|T_k|^2$ is the intensity transmissivity of the $k_{th}$ scattering center, the effective transmission of the whole random grating is given by

$$\tau_{Neff} = \exp\left\{\sum_{k=1}^{N} \log\tau_k\right\} = \exp[-N\log(1/\tau_k)] \approx \tau_k^N \tag{3.55}$$

The above equation illustrates the exponential decay of transmissivity with increasing scattering centers, which follows light localization in the strong scattering fiber random grating array [138]. Photons take a long time to leave the medium because the transmission is exponentially small in the localization regime [139]. The extremely strong scattering disordered RFGA with light localization offers opportunities for realizing highly coherent emission with small frequency drift in Brillouin random lasing systems.

### 3.3.3 Characterization of Brillouin random fiber lasers

#### Lasing mode evolution measurement

Spectral dynamics reveals the complex nature of random lasers. The high-resolution heterodyne-based method can measure the complex mode behavior of narrow linewidth BRFLs. The output of the BRFL is combined with a local oscillator through a coupler, as shown in Fig. 3.9. The beat signal with a frequency difference between two lasers can be continuously detected by a high-speed PD and recorded on an ESA. There is a trade-off between the time interval of traces and the detected frequency range. The interval can be shortened to milliseconds by setting the frequency range to tens of MHz. The frequency

drift of modes and the coherent properties of the BRFL can be characterized by measuring the mode evolution over a long time. The beat signal can also be continuously measured by an OSC to observe the mode behavior within milliseconds.

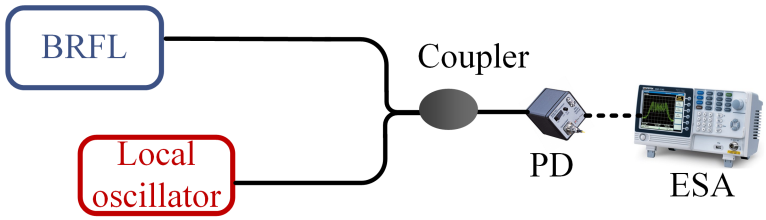


FIGURE 3.9 – Experimental setup of the lasing mode measurement of BRFL.

**Relative intensity noise measurement**

Relative intensity noise (RIN), which describes optical power fluctuations, is a crucial parameter in lasers. The temporal trace of the output intensity of an ideal laser is flat without intensity fluctuation. However, all lasers are subject to spontaneous emission, which results in variations in output intensity due to the random wavelength, polarization, and phase of photons. Another limit is shot noise caused by the conversion of photons into electrons when measuring optical power using a photodetector. Due to electrons having discrete energy levels, the energy of electrons obtained from photon absorption in the photodetector is a discrete process. Shot noise is produced by the randomness of discrete photons and electrons. Thermal noise is generated in the photodetector, even in the absence of an input signal, because thermal agitation of electrons induces small current variations. In RFLs, intensity noise is dominated by two factors : 1) mode competition. In RFLs with strong scattering feedback and high gain, some photons can return to their initial locations more often than others, which allows many modes to co-exist in the gain bandwidth. High noise peaks at high frequencies over hundreds of kHz (corresponding to kilometers-long cavity length) are generated owing to mode coupling in the gain bandwidth, 2) external variations. The amplitude and phase of light scattered by the distributed feedback medium and amplified in the gain medium are susceptible to temperature change and vibration, which results in high intensity noise at low frequencies around tens of kHz. RIN is expressed as

$$\mathrm{RIN} = \frac{\langle \Delta P \rangle}{P} \tag{3.56}$$

where $P$ is the average optical power, $\Delta P$ is the optical power fluctuation, and $\langle\rangle$ denotes the time average. The spectral density of intensity noise can be calculated through the

Fourier transform of the autocorrelation function of the power fluctuation :

$$\mathrm{RIN}(f) = \frac{1}{P^2}\int_{-\infty}^{+\infty}\langle \Delta P(t)\Delta P(t+\tau)\rangle e^{i2\pi f\tau}d\tau \tag{3.57}$$

The temporal intensity trace of the BRFL is measured using a PD and an OSC, as shown in Fig. 3.10. RIN is calculated manually by the Fourier transform of the temporal trace.

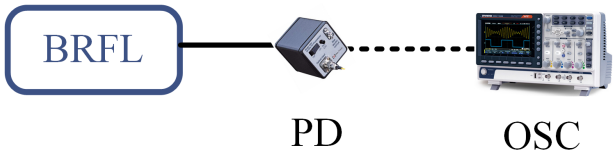


FIGURE 3.10 – Experimental setup of laser RIN measurement.

**Frequency noise measurement**

Frequency noise is used to describe the level of fluctuations of the instantaneous lasing frequency. The electric field of the incident laser is given by

$$E(t) = E_0 e^{i[\omega_0 t+\phi(t)]} \tag{3.58}$$

where $E_0$ is the magnitude of the electric field, $\omega_0$ is the angular frequency of the laser, and $\phi(t)$ is the time-dependent phase noise of the laser. The instantaneous frequency is obtained by calculating the deviation of the phase in Eq. (3.58) :

$$v(t) = \frac{1}{2\pi}\frac{d\left[\omega_0 t+\phi(t)\right]}{dt} = v_0 + \frac{1}{2\pi}\frac{d\phi(t)}{dt} = v_0 + \frac{1}{2\pi}\dot{\phi}(t) \tag{3.59}$$

where $v_0 = \omega_0/2\pi$ is the optical frequency of the laser and $\dot{\phi}(t)/2\pi$ is the time-dependent frequency fluctuation. Considering a time delay interferometer system, the detected output returns a signal with a noisy phase $\phi(t+\tau)-\phi(t)$, where $\tau$ is the interferometer delay. We are interested in the frequency noise of $\Delta v(t) \equiv (\dot{\phi}(t+\tau)-\dot{\phi}(t))/(2\pi)$. The time-shifting property of the Fourier transform is given by

$$S_v(f) = S_w\left(2 - e^{2\pi i f\tau} - e^{-2\pi i f\tau}\right) = 4\sin^2(\pi f\tau)S_w \tag{3.60}$$

with

$$S_w = \frac{1}{4\pi^2}\int_{-\infty}^{\infty}\langle\dot{\phi}(t+\tau)\dot{\phi}(t)\rangle e^{-2\pi i f\tau}d\tau \tag{3.61}$$

where $S_w$ is the frequency noise spectral density. The relationship between the phase noise and frequency noise is given by [140]

$$S_\phi(f) = \frac{1}{f^2} S_{v(\tau)}(f) = 4\frac{\sin^2(\pi f\tau)}{f^2} S_w \tag{3.62}$$

We convert the phase noise to frequency noise by dividing out the response function, $4\pi^2\tau^2 \operatorname{sinc}^2(\pi f\tau)$, where $\operatorname{sinc}(z) \equiv \sin z/z$.

The frequency noise spectrum is measured using an imbalanced symmetric 3×3 coupler fiber interferometer based on the demodulation of the phase difference reflected by Faraday rotator mirrors (FRMs) [141]. The experimental setup is shown in Fig. 3.11. The BRFL output is injected into a 3×3 coupler after the circulator. Two of the three output parts are reflected by two FRMs with a delay time of $\tau$, and one of them is reflection-free by tightly bending. The FRM reflects light with 90° rotation of the polarization state to remove the polarization fading of the interferometer. Interference fringes are measured by detecting the signal from the left ports of the coupler. Following the derivation in [142], the differential phase fluctuation $\Delta\phi(t) = \phi(t+\tau) - \phi(t)$ of the laser under test accumulated in the delay time $\tau$ can be obtained by measuring the three intensity outputs $I_1(t)$, $I_2(t)$ and $I_3(t)$ as following

$$\Delta\phi = \arctan\left(\frac{X_2'(t)}{X_1'(t)}\right) - \overline{\arctan\left(\frac{X_2'(t)}{X_1'(t)}\right)} \tag{3.63}$$

where $X_1'(t)$ and $X_2'$ are given by

$$\begin{pmatrix} X_1'(t) \\ X_2'(t) \\ X_3'(t) \end{pmatrix} = \begin{pmatrix} \eta_1 & \varsigma_1 & \xi_1 \\ \eta_2 & \varsigma_2 & \xi_2 \\ \eta_3 & \varsigma_3 & \xi_3 \end{pmatrix}^{-1} \begin{pmatrix} I_1(t) \\ I_2(t) \\ I_3(t) \end{pmatrix} \tag{3.64}$$

where $\eta_n = 2r_n c_{n1} c_{n2} \cos(\theta'_{n2} + \theta_{21} - \theta'_{n1} - \theta_{11})$, $\varsigma_n = 2r_n c_{n1} c_{n2} \sin(\theta'_{n2} + \theta_{21} - \theta'_{n1} - \theta_{11})$, $\xi_n = r_n\left[(c_{n1})^2 + (c_{n2})^2\right]$ and $c_{nm} = p_{mm} b'_{nm} b_{m1}$ with $n = 1, 2, 3$ is the output port number of the interferometer, and $m = 1, 2$ is the interference arm port number. $p_{mm}$ is the transmission loss of the interference arm, $b_{mn}$ and $\theta_{mn}$ are the splitting ratio and phase delay from the port $n$ to port $m$ of the coupler, $b'_{mn}$ and $\theta'_{mn}$ are the splitting ratio and phase delay from the port $m$ to port $n$ of the coupler, and $r_n$ is the responsivity of PDs. The parameters $\eta_n, \varsigma_n, \xi_n$ are constant for the setup once the devices and structure are determined. The power spectral density of differential phase fluctuation $\Delta\phi(t)$ and differential frequency fluctuation $\Delta v(t)$ can be calculated by the power spectral density estimation method [143].

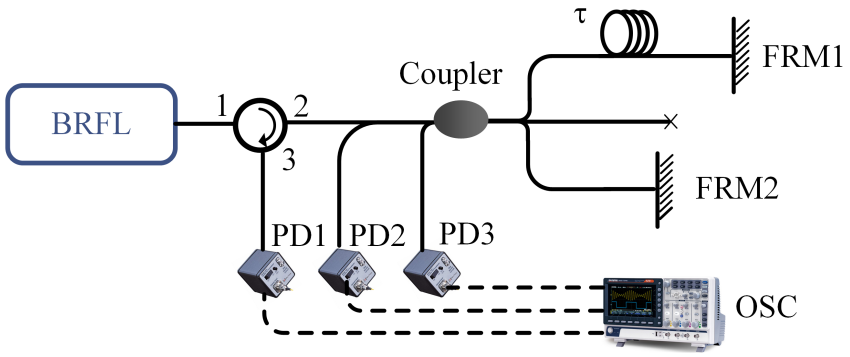


FIGURE 3.11 – Experimental setup for the laser phase and frequency noise measurement.

**Linewidth measurement**

The delayed self-heterodyne (DSH) technique is a high-precision method to characterize the laser linewidth [144]. The DSH method is based on the unbalanced Mach-Zehnder interferometers (MZI) with a larger delay time between two paths than the coherent time of the laser to ensure uncorrelation between two traces. A schematic of the experimental setup is shown in Fig. 3.12. The lasing output is split into two paths by the 50/50 fiber coupler. The optical frequency of one path is shifted with respect to the other path using an acousto-optical modulator (AOM) with a driving frequency of 200 MHz, and the other path is delayed by a time interval of $\tau$ using a 200 km fiber. An optical attenuator and a PC are inserted into the MZI to obtain the optimum contrast of the beat signal. The beat signal of two paths is detected by a PD and recorded on an ESA.

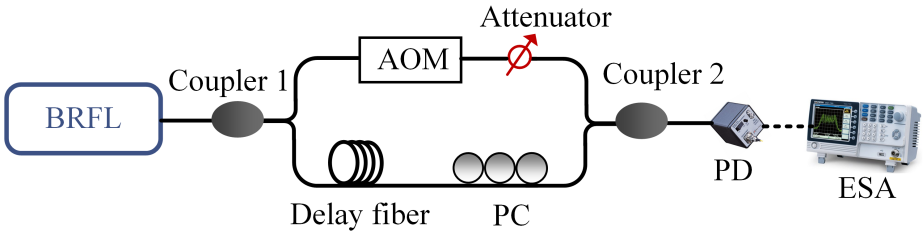


FIGURE 3.12 – Experimental setup of laser linewidth measurement.

The total electric field received on the PD is given by

$$E_d(t) = E_1 e^{i}((\omega_0 + \Omega)t + \phi(t)) + E_2 e^{i}(\omega_0(t + \tau_0) + \phi(t + \tau_0)) \tag{3.65}$$

where $E_0$ is the electric field of laser, $\omega_0$ is the laser frequency, $\tau_0$ is the time delay of one arm with respect to the other arm, and $\Omega$ is the offset frequency between two arms.

Assuming stationary fields, the autocorrelation of the photocurrent depends only on the intensity correlation function of the detected total field [145, 146]

$$R_l(\tau) = e\eta G_T^{(2)}(0)\delta(t) + \eta^2 G_T^{(2)}(\tau) \tag{3.66}$$

with

$$G_T^{(2)}(\tau) = \langle E_d(t)E_d^*(t)E_d(t+\tau)E_d^*(t+\tau)\rangle \tag{3.67}$$

where $G_T^{(2)}$ is the optical intensity correlation function, $e$ is the electronic charge, $q$ is the detector sensitivity and $\delta(t)$ is the Dirac delta function. The intensity autocorrelation function is written as

$$G_T^2(\tau) = \left(E_1^2 + E_2^2\right)^2 + 2E_1^2E_2^2\cos\left(2\pi f_M\tau\right)\begin{cases} e^{-2\pi\Delta v\tau}, |\tau| < \tau_0 \\ e^{-2\pi\Delta v\tau_0}, |\tau| > \tau_0 \end{cases} \tag{3.68}$$

where $\Delta v$ is the intrinsic linewidth of laser under test. The power spectral density of the delay self-heterodyne signal is derived by the Fourier transformation of Eq. (3.68) :

$$S_I(\omega) = \eta^2\left(E_1^2 + E_2^2\right)^2\delta\left(\frac{\omega}{2\gamma}\right) + E_1^2E_2^2e^{-2\gamma\tau_0}\left\{\begin{array}{l}\delta\left(\frac{\omega-\Omega}{2\gamma}\right) + \frac{1/\pi}{1+\left(\frac{\omega-\Omega}{2\gamma}\right)^2}[e^{2\gamma\tau_0} - \\ \frac{\sin\left(\frac{\omega-\Omega}{2\gamma}\right)4\gamma^2\tau_0}{\omega-\Omega} - \cos\left(\frac{\omega-\Omega}{2\gamma}\right)2\gamma\tau_0]\end{array}\right\} \tag{3.69}$$

where $2\gamma = 2\pi\Delta v$. When the fiber delay line in longer than the coherent length of laser under test ($\tau_0 \gg 2\pi/\gamma$), the power spectral density can be written in Lorentzian function

$$\begin{aligned} S_I(\omega) &= \eta^2\left(\left(E_1^2 + E_2^2\right)^2\delta\left(\frac{\omega}{2\gamma}\right) + E_1^2E_2^2\frac{1/\pi}{1+\left(\frac{\omega-\Omega}{2\gamma}\right)^2}\right) \\ &= \eta^2\left(\left(E_1^2 + E_2^2\right)^2\delta\left(\frac{\omega}{2\gamma}\right) + E_1^2E_2^2\frac{(4\gamma/2)^2/\pi}{(4\gamma/2)^2 + (\omega-\Omega)^2}\right) \end{aligned} \tag{3.70}$$

The above equation indicates that the beat spectrum has a true Lorentzian linewidth of $2\Delta v$, which is twice the linewidth of the laser under test.

### 3.3.4 Brillouin random fiber laser applications

BRFLs with narrow lasing linewidth and complex random nature have attracted attention in random number generation and high-resolution laser linewidth measurement. Due to stochastic intensity fluctuations with unpredictable amplitude in the BRFL, random number generation with a bit rate of 5 Mbps was demonstrated [147]. The schematic diagram of random bit sequence generation in the BRFL is shown in Fig. 3.13. The intensity

statistics show the Gaussian distribution as plotted in Fig. 3.13(c), which means that the time series of power fluctuations are independent of both recent history and the current one. Simple post-processing with exclusive or (XOR) was used after collecting the output intensity data to remove the residual bias in the BRFL, which improves the randomness of the obtained data and increases the probability of passing the National Institute of Standards and Technology (NIST) statistical test. The bit rate is limited to a few MHz owing to the narrow Brillouin gain bandwidth of SMFs. Random bit generation with a bit rate of 71 MHz was demonstrated by employing a nonuniform tapered fiber with a broadband Brillouin gain bandwidth of 350 MHz as Brillouin gain and distributed feedback of the BRFL [148]. The truly random number generator is achieved in real-time without requiring post-processing procedures thanks to benefits from various Brillouin frequencies and strong inhomogeneity of the nonuniform fiber. The physical random number generator has the potential to be used in practical real-time security communication systems because of its high speed without post-processing steps.

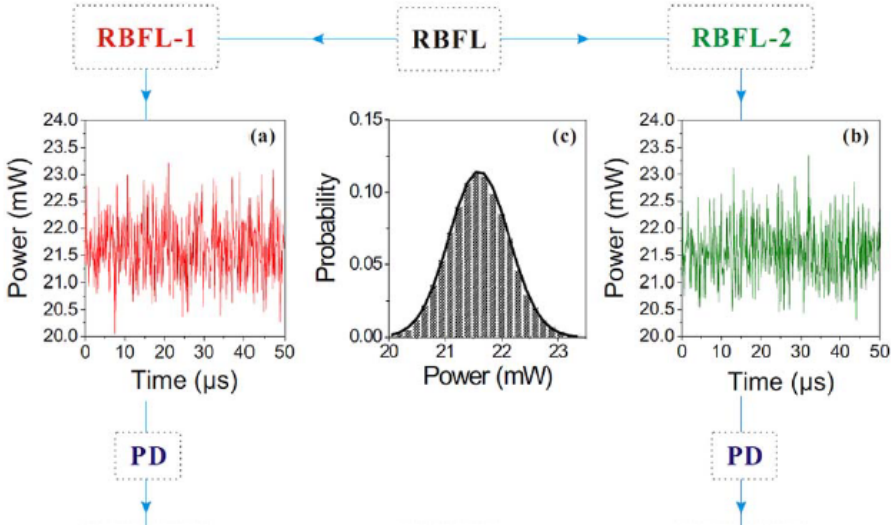


FIGURE 3.13 – Schematic diagram of the random bit sequence generation using the RBFL [147].

BRFLs with narrow linewidths can be used to characterize lasing linewidth without the hundreds of kilometers-long delay fiber in the DSH method. The experiment setup for lasing linewidth measurement based on the BRFL is plotted in Fig. 3.14 [149]. The laser under test is split into two paths via the 50/50 coupler. One path is the output of the laser under test, and the other is injected into the gain fiber for the generation of the BRFL with a linewidth of ∼1 kHz as the local oscillator. The BRFL is combined with the laser under test through another 50/50 coupler to generate a beat signal. The laser under test with

a linewidth larger than the BRFL linewidth can be detected. The measured linewidths of the NP photonics laser and the ECL laser are 2.79 kHz and 15.40 kHz, respectively, which agree with the values obtained by the traditional DSH approach.

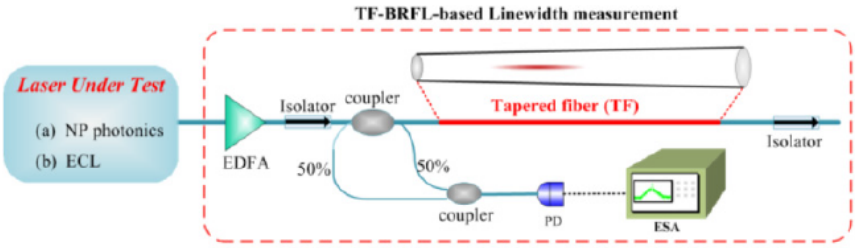


FIGURE 3.14 – Tapered fiber-BRFL based laser linewidth measurement setup for (a) the NP fiber laser ; (b) the external cavity laser (ECL) [149].

# 4 Simulation and fabrication of chalcogenide-PMMA microfibers

In this chapter, we present a theoretical model of stimulated Brillouin scattering (SBS) and the fabrication of chalcogenide microfibers. The SBS model is built by solving the elastodynamic equation. Brillouin gain spectra and acoustic wave profiles are calculated by solving the kinetic energy of the phonon wavepacket at different phase match conditions. The theoretical model will be used in the two following chapters as a theoretical reference. The fabrication processes of $As_2Se_3$-PMMA microfibers are introduced, and the corresponding setups and fibers in all steps are given.

## 4.1 Numerical SBS model

### 4.1.1 Elastodynamic equation

Electrostriction in the SBS process is described by the elastodynamic equation [150]

$$\rho\frac{\partial^2 u_i}{\partial t^2} - \left[c_{ijkl}u_{k,l} + \eta_{ijkl}\frac{\partial u_{k,l}}{\partial t}\right]_{,j} = -[T_{ij}^{\mathrm{es}}]_{,j} \tag{4.1}$$

where $u_i$ is the displacement field, $\rho$ is the material density, $c_{ijkl}$ and $\eta_{ijkl}$ are the elastic tensor and elastic viscosity, respectively, and $T_{ij}^{\mathrm{es}} = -\epsilon_0\chi_{klij}E_kE_l^*$ is the electrostriction stress tensor in the presence of electrical fields of the optical pump wave $E_k$ and the Stokes wave $E_l$ with $\chi_{klij} = \epsilon_{im}\epsilon_{jn}p_{klmn}$ the susceptibility tensor, $\epsilon_{ij} = n^2\delta_{ij}$ the relative dielectric tensor, and $p_{klmn}$ the photoelastic tensor. Indices placed after a comma indicate partial derivatives are taken, e.g., $A_{ij,j} = \sum_j \partial A_{ij}/\partial x_j$. Elastic losses are incorporated into the

elastodynamic equation by considering a complex elastic tensor $c_{ij} + i\omega\eta_{ij}$. We assume $\eta_{ij} = c_{ij}/Q_f$, where $Q_f$ is the product of quality factor $Q$ and frequency $f$.

SBS is the third-order parametric process involving two optical fields and one acoustic field. For Brillouin scattering, a pump optical field with central frequency $\omega_1$ and wavenumber $k_1$ can produce a downshifted Stokes optical field characterized by a central frequency $\omega_2$ and wavenumber $k_2$ when scattering by an acoustic wave with a frequency $\omega$ and wavenumber $k$. Conserved energy and momentum should be required under the phase matching condition. The frequency and wave vector of the acoustic wave are given by $\omega = \omega_1 - \omega_2$ and $k = k_1 - k_2$. The total optical field is the superposition of two magnetoelectric waves with the frequency of $\omega_1$ and $\omega_2$ :

$$E(r, z; t) = E^1(r)e^{i(\omega_1 t - k_1 z)} + E^2(r)e^{i(\omega_2 t - k_2 z)} \tag{4.2}$$

The counter-propagating pump and Stokes waves in optical fibers give rise to SBS with $k \approx 2k_1$. The co-propagating optical waves in fibers lead to forward stimulated Brillouin scattering (FSBS) with $k_1 \approx k_2$ and $k \approx 0$. The following ansatz is assumed for the acoustic wave because there is only one source term at the frequency $\omega = \omega_1 - \omega_2$ and wave vector $k = k_1 - k_2$ :

$$u_i(r, z; t) = \bar{u}_i(r)e^{i(\omega t - kz)} \tag{4.3}$$

where the displacement field $\bar{u}_i(r)$ is the transverse profile of the acoustic wave. A finite element model (FEM) is used for the calculation because the displacement field is supposed to be a continuous field defined on an arbitrary configuration of different materials with precise boundary conditions.

The FEM can be derived from the elastodynamic equation. By substituting Eqs. (4.2) and (4.3) into Eq. (4.1), we obtain :

$$-\rho\omega^2\bar{u}_i e^{-ikz} - \left[(c_{ijkl} + i\omega\eta_{ijkl})\left(\bar{u}_k e^{-ikz}\right)_{,l}\right]_{,j} = -[T^{es}_{ij}e^{-ikz}]_{,j} \tag{4.4}$$

The elastic equation is written in a variational form by left-multiplying the virtual displacement $(\bar{v}_i e^{-ikz})^*$ and integrating over the cross-section of the fiber :

$$-\omega^2 \int_\sigma \mathrm{d}\sigma\rho\bar{v}_i^*\bar{u}_i - \int_\sigma \mathrm{d}\sigma\bar{v}_i^* e^{ikz}\left[T_{ij}e^{-ikz}\right]_{,j} = -\int_\sigma \mathrm{d}\sigma\bar{v}_i^* e^{ikz}[T^{es}_{ij}e^{-ikz}]_{,j} \tag{4.5}$$

with

$$T_{ij}e^{-ikz} = (c_{ijkl} + i\omega\eta_{ijkl})\left(\bar{u}_k e^{-ikz}\right)_{,l} \tag{4.6}$$

Green's theorem is applied to transform integrals involving a divergence operator to

integrals involving the gradient of the test function :

$$\int_\sigma \mathrm{d}\sigma a_i \left[b_{ij}\right]_{,j} = \int_\sigma \mathrm{d}\sigma \left[a_i b_{ij}\right]_{,j} - \int_\sigma \mathrm{d}\sigma \left[a_i\right]_{,j} b_{ij} = \oint_{\delta\sigma} \mathrm{d}\delta\sigma a_i b_{ij} n_j - \int_\sigma \mathrm{d}\sigma \left[a_i\right]_{,j} b_{ij} \tag{4.7}$$

Thus, Eq. (4.5) is rewritten as

$$\begin{aligned} -\omega^2 \int_\sigma \mathrm{d}\sigma \rho \bar{v}_i^* \bar{u}_i + \int_\sigma \mathrm{d}\sigma \left[\bar{v}_i^* e^{ikz}\right]_{,j} \left(T_{ij} e^{-ikz}\right) + \int_\sigma \mathrm{d}\sigma \left[\bar{v}_i^* e^{ikz}\right]_{,j} \left(T_{ij}^{es} e^{-ikz}\right) \\ = \oint_{\delta\sigma} \mathrm{d}\delta\sigma \bar{v}_i^* e^{ikz} (T_{ij} e^{-ikz}) n_j + \oint_{\delta\sigma} \mathrm{d}\delta\sigma \bar{v}_i^* e^{ikz} T_{ij}^{es} e^{-ikz} n_j \end{aligned} \tag{4.8}$$

The natural boundary condition $T_{ij} - T_{ij}^{es} = 0$ is applied along the closed loop $\delta\sigma$, which means that the total stress disappears on the boundary of the fiber. Hence, Eq. (4.8) is transformed into :

$$\begin{aligned} -\omega^2 \int_\sigma \mathrm{d}\sigma \rho \bar{v}_i^* \bar{u}_i + \int_\sigma \mathrm{d}\sigma \left[\bar{v}_i^* e^{ikz}\right]_{,j} \left(T_{ij} e^{-ikz}\right) + \int_\sigma \mathrm{d}\sigma \left[\bar{v}_i^* e^{ikz}\right]_{,j} T_{ij}^{es} e^{-ikz} \\ = \oint_{\delta\sigma} \mathrm{d}\delta\sigma \bar{v}_i^* e^{ikz} \left(T_{ij} - T_{ij}^{es}\right) e^{-ikz} n_j = 0 \end{aligned} \tag{4.9}$$

Under this condition, the boundary integral vanishes. The weak formulation of the elastodynamic equation can be coded using a finite element method language. By exploiting the dependence on $k$, we obtain :

$$\begin{aligned} -\omega^2 \int_\sigma \mathrm{d}\sigma \rho \bar{v}_i^* \bar{u}_i + \int_\sigma \mathrm{d}\sigma \bar{v}_{i,j}^* \left(c_{ijkl} + i\omega\eta_{ijkl}\right) \bar{u}_{k,l} \\ + ik \int_\sigma \mathrm{d}\sigma \left[\bar{v}_i^* \left(c_{i3kl} + i\omega\eta_{i3kl}\right) \bar{u}_{k,l} - \bar{v}_{i,j}^* \left(c_{ijk3} + i\omega\eta_{ijk3}\right) \bar{u}_k\right] \\ + k^2 \int_\sigma \mathrm{d}\sigma \bar{v}_i^* \left(c_{i3k3} + i\omega\eta_{i3k3}\right) \bar{u}_k = \int_\sigma \mathrm{d}\sigma \bar{v}_{i,j}^* T_{ij}^{es} + ik \int_\sigma \mathrm{d}\sigma \bar{v}_i^* T_{i3}^{es} \end{aligned} \tag{4.10}$$

For practical computations, the Galerkin nodal finite element method is then employed to convert the integral into a linear equation. The converted linear equation is given by [150]

$$\left(C - \omega^2 M\right) U = \left(X_0 + ikX_1\right) T_{es} \tag{4.11}$$

with the stiffness matrix $C = C_0 + ikC_1 + k^2 C_2$, the mass matrix $M$, and $X = X_0 + ikX_1$. $U$ and $T^{es}$ are the vectors of the nodal values of $\bar{u}_i$ and $T_{ij}^{es}$, respectively.

The kinetic energy of the phonon wavepacket is determined by the calculated displacement field. The kinetic energy of the acoustic wave is given by [150]

$$E_{ke} = \frac{1}{4} \int_\sigma \mathrm{d}r \rho \omega^2 u_i(r)^* u_i(r) \tag{4.12}$$

The elastic or potential energy is expressed by

$$E_p = \frac{1}{4}\int_{\sigma} \mathrm{d}r u_{i,j}(r)^* c_{ijkl} u_{k,l}(r) \tag{4.13}$$

The elastic energy would be equal to the kinetic energy if the solution was in a normal mode. The internal energy is the sum of the kinetic and elastic energies :

$$E = E_{ke} + E_p \approx 2E_{ke} \tag{4.14}$$

Acoustic mode distributions at certain frequencies can be obtained by calculating the kinetic energy, and Brillouin gain spectra can be calculated by scanning the detuning frequency $\omega$. SBS and FSBS are calculated by setting $k$=2$k_1$ and $k = 0$, respectively.

### 4.1.2 Mode profile and Brillouin gain spectrum

The parameters used for calculating the Brillouin spectrum of $As_2Se_3$-PMMA microfibers are shown in Table 4.1. The optical mode of the single-core $As_2Se_3$-PMMA microfiber with a core diameter of 2 µm is calculated using the tangential vector finite element model [151]. The acoustic field of SBS is then calculated using the optical field by setting $k$=2$k_1$. Figure 4.1(a) shows the fundamental optical mode of the single-core microfiber at the wavelength of 1550 nm. The acoustic mode profiles and the Brillouin gain spectrum are calculated using the kinetic energy. The acoustic mode L01 at 7.65 GHz is shown in Fig. 4.1(b). The acoustic mode L02 induced by the acoustic impedance mismatch between the $As_2Se_3$ core and PMMA cladding is shown in Fig. 4.1(c). The rippling behavior in the acoustic modes suggests interference between transverse and longitudinal acoustic modes. Unlike the Brillouin peak of the longitudinal acoustic wave in SMF, boundary conditions in the microfiber with a much smaller diameter induce strong coupling between shear and longitudinal acoustic waves, resulting in richer dynamics of light interaction. The hybrid and surface acoustic modes were experimental and theoretically demonstrated in microfi-

TABLE 4.1 – $As_2Se_3$ and PMMA parameters for SBS calculation.

| | $n$ | $\rho$[1] | $p_{11}$ | $p_{12}$ | $p_{44}$ | $c_{11}$[2] | $c_{12}$[2] | $c_{44}$[2] | $Q_f$[3] |
|---|---|---|---|---|---|---|---|---|---|
| $As_2Se_3$ | 2.674 | 4640 | 0.314 | 0.266 | 0.024 | 23.5 | 9.5 | 6.99 | 7000 |
| PMMA | 1.481 | 1187 | 0.3 | 0.297 | 0.0015 | 6.63 | 4.34 | 1.145 | 20 |

[1] $\rho$ : Kg/m$^3$
[2] $c_{11}$,$c_{12}$ and $c_{44}$ : GPa
[3] $Q_f$ : GHz

bers [54]. Surface Brillouin scattering is the interaction between optical waves and a surface acoustic wave via electrostriction. Figure 4.1(d) shows the calculated field of the surface acoustic wave in the $As_2Se_3$-PMMA microfiber. The energy is mainly localized below the surface of the microfiber. The calculated Brillouin gain spectrum is plotted in Fig. 4.1(e). Brillouin peaks appear when the detuning frequency satisfies the phase-matching condition. The secondary peak with a small amplitude indicates the low acousto-optic coupling coefficient between the high-order acoustic mode and fundamental optical mode. High pump power is required when measuring the surface acoustic mode due to the low gain of the surface acoustic wave as plotted in the inset of Fig. 4.1(e).

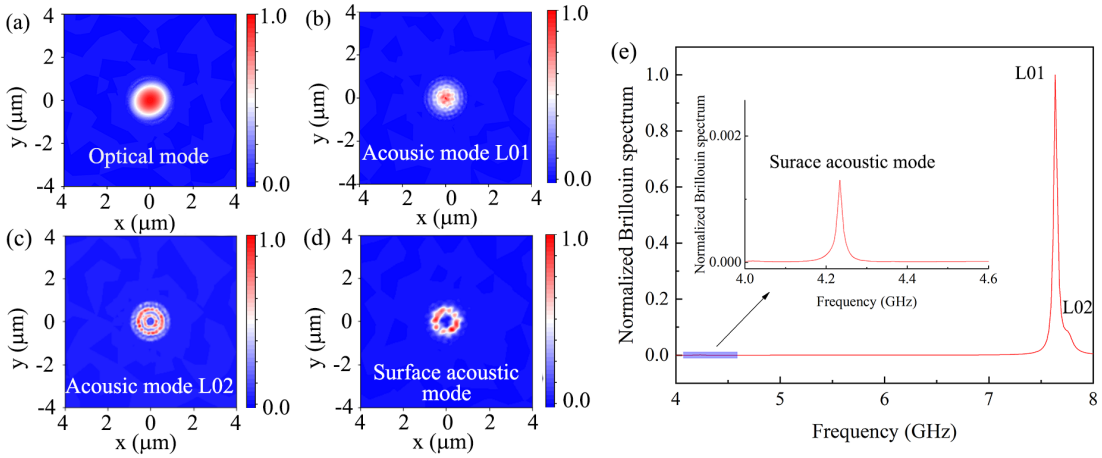


FIGURE 4.1 – (a) Optical mode. (b) Acoustic mode L01. (c) Acoustic mode L02. (d) Surface acoustic mode. (e) Calculated backscattering Brillouin gain spectrum for a single-core $As_2Se_3$-PMMA taper with a core diameter of 2 µm. Inset : the gain spectrum of surface acoustic wave.

## 4.2 Fabrication of chalcogenide-PMMA microfibers

### 4.2.1 Preparation of the chalcogenide fiber and PMMA tube

The $As_2Se_3$-PMMA fiber is fabricated by coating PMMA on the $As_2Se_3$ fiber. The $As_2Se_3$ fiber with a core diameter of 100 µm, a cladding diameter of 170 µm and a numerical aperture of 0.18 is provided by Coractive High-Tech company. The $As_2Se_3$ fiber is immersed in acetone for several hours to remove its coating material (acrylate). The PMMA tube with an inner diameter of 3.6 mm and an outer diameter of 9.7 mm is placed in an oven at 80 °C for two weeks to remove moisture due to PMMA's hydrophilic nature. If the moisture is not removed, bubbles arise in the PMMA when it is softened at 220 °C ; this leads to inconsistencies which break the $As_2Se_3$ fiber core during the tapering process.

The moisture-removed PMMA tube is annealed in the oven at 150 °C for one hour to eliminate internal stresses. The elongated PMMA microtube with an inner diameter of around 400 µm is fabricated by tapering the PMMA tube. Photos of the initial PMMA tube, elongated PMMA microtube, and $As_2Se_3$ fiber are shown in Fig. 4.2.

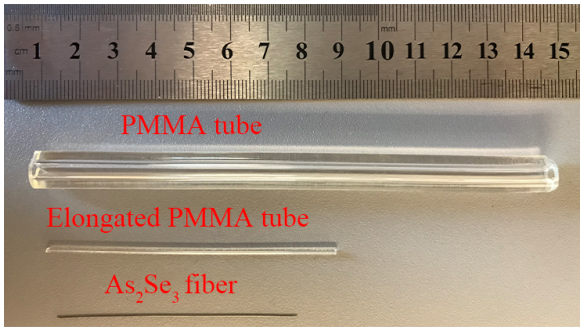


FIGURE 4.2 – Photos of the PMMA tube, PMMA microtube and $As_2Se_3$ fiber.

### 4.2.2 Fabrication of the chalcogenide-PMMA preform

The $As_2Se_3$-PMMA preform is fabricated by the rod-in-tube drawing technique. The $As_2Se_3$ fiber without coating is inserted into the elongated PMMA microtube. The item is then inserted into the PMMA tube to form an assembly with a core-cladding structure. The assembly is mounted on two spinning mandrel stages with a rotating rate of 3 rotations/min, as shown in Fig. 4.4. The assembly is heat-softened for 12 hours by a resistive heater that moves back and forward to obtain the $As_2Se_3$-PMMA preform. The temperature of the heater is 220 °C. The moving velocity of the heater is 12 µm/s, which is controlled by stage 3. Due to the collapse of the PMMA tube on the core at the temperature, we obtain the single-core $As_2Se_3$-PMMA preform with the $As_2Se_3$ core and the PMMA cladding. Two $As_2Se_3$ fibers are inserted into the PMMA microtube to fabricate the dual-core $As_2Se_3$-PMMA preform. The PMMA microtube allows two cores to be connected, suggesting high contrast of the transmission spectrum when light travels between two $As_2Se_3$ cores. The assembly with two $As_2Se_3$ fibers is heated for four days to fabricate an elliptical-core $As_2Se_3$-PMMA preform. The long heating period ensures that two $As_2Se_3$ fibers are fused to obtain an elliptical core shape.

The preform is drawn to fibers using the setup as shown in Fig.4.4(a). There are three stages, a thermocouple probe and a heater in the setup. Drawing velocities of two stages (stage 2 and stage 3) are given by

$$D_m^2(V_d + V_f) = D_p^2 V_f \tag{4.15}$$

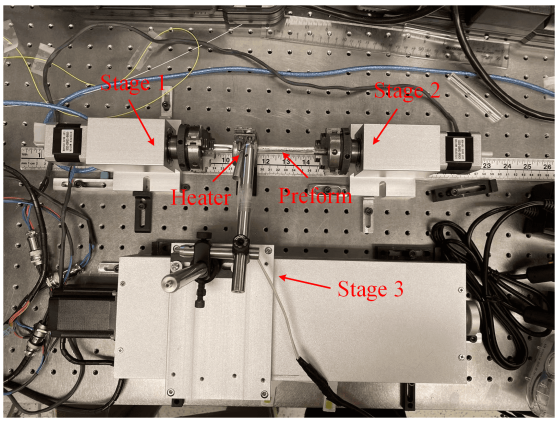


FIGURE 4.3 – Preform fabrication setup.

where $D_m$ and $D_p$ are the diameters of $As_2Se_3$-PMMA fiber and $As_2Se_3$-PMMA preform, respectively, and $V_d$ and $V_f$ are the velocities of stage 2 and stage 3, respectively. The preform is fixed on stages 1 and 2 and heated at 220 °C when drawing it to a small diameter. $As_2Se_3$-PMMA fibers are fabricated by drawing the preform to 1/4 of the original diameter. In our case, the drawing velocity $V_d$ is 187.5 µm/s and the feed velocity $V_f$ is 12.5 µm/s. The fiber is drawn again to reduce by half the diameter, which enables the maximum coupling efficiency between the $As_2Se_3$ fiber and the SMF. Figure 4.4 shows images of the $As_2Se_3$-PMMA preform and $As_2Se_3$-PMMA fibers with different diameters.

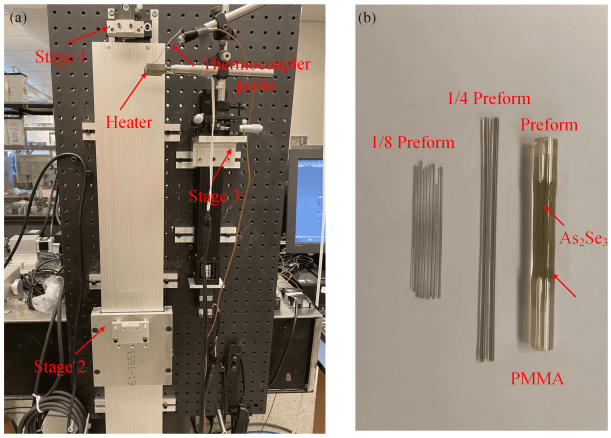


FIGURE 4.4 – (a) Drawing setup. (b) Photos of $As_2Se_3$-PMMA preforms.

### 4.2.3 Polishing the chalcogenide-PMMA fiber

Fiber polishing determines fiber loss and transmission properties. Figure 4.5 shows the polishing setup consisting of a fiber hold, polishing papers, and two cameras. There are two polishing methods : flat polishing and angle polishing. Due to the large Fresnel reflection

at the end of the hybrid fiber using flat polishing, the backscattered Stokes signal from the hybrid fiber is weaker than the pump signal, which limits Brillouin scattering sensing. To suppress Fresnel reflection, the ends of the hybrid fiber are angle polished. The hybrid fiber is fixed on the fiber holder, whose angle can be adjusted. The polishing paper is placed on a rotating stage to polish the ends of the hybrid fiber. The polishing papers with the particle size of 30 µm, 9 µm, 5 µm, 3 µm, 1 µm, and 0.3 µm are utilized to get a clean fiber end. An optical microscope image of a polished single-core $As_2Se_3$-PMMA fiber end facet is shown in the inset of Fig 4.5.

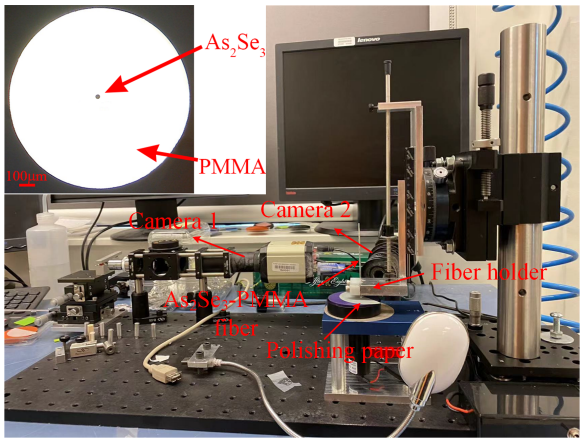


FIGURE 4.5 – Polishing setup. Inset : an optical microscope image of a polished single-core $As_2Se_3$-PMMA fiber end facet

### 4.2.4 Coupling the chalcogenide fiber and SMF

The $As_2Se_3$-PMMA fiber is coupled with SMFs using UV glue.The coupling setup consists of two stages, a camera, a microscope, and a UV lamp, as shown in Fig. 4.6. The end-polished $As_2Se_3$-PMMA fiber is fixed on stage 1 and aligned to the camera by moving stage 2. One polished end of SMF is fixed on stage 1, and the other is connected to a broadband light source. Transmission loss can be minimized by aligning the SMF and the $As_2Se_3$-PMMA fiber using stage 1, which is monitored by a power meter connected with the camera. The butt-coupling interfaces are permanently fixed using UV-cured epoxy. The insertion loss of the coupled $As_2Se_3$-PMMA fiber is around 2 dB due to the Fresnel reflection from hybrid fiber-SMF interfaces.

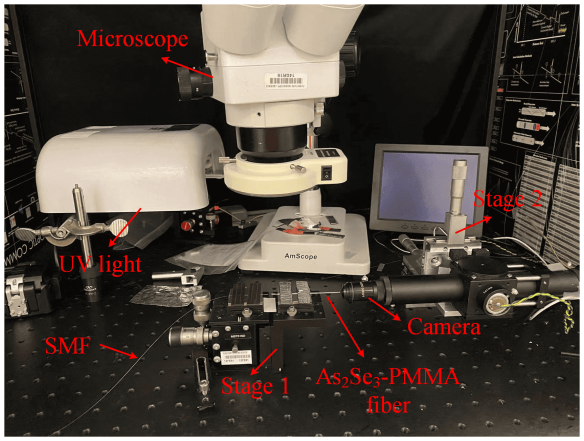


FIGURE 4.6 – Coupling setup

### 4.2.5 Tapering the chalcogenide-PMMA fiber

Figure 4.7 presents the fiber tapering setup. It consists of three linear bearings, three motorized translation stages, and a resistive heater. Each end of the fiber is clamped onto a mount to keep it in place during the tapering process. The mounts are made to be parallel and level before the tapering process. The temperature of the heater is 220 °C at the beginning of the tapering process. The temperature is automatically reduced with decreasing core diameter. Stage 1 and stage 2 are utilized to stretch the fiber at a given velocity, and stage 3 moves back and forward to sweep the heater along the fiber. For a given taper profile, a Matlab program generates files containing the information of sweeping velocity and pulling velocity. A Labview program reads the information to control the movement of the stages. The tapered fiber with a core diameter of micrometers is repeatable because the motorized translation stages are precisely controlled by the Labview and Matlab programs. The profile of the tapered $As_2Se_3$-PMMA fiber with a waist region of

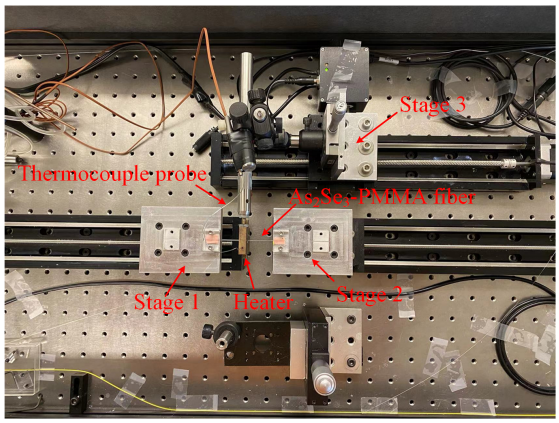


FIGURE 4.7 – Tapering setup

$L_w = 10\,\text{cm}$ and a core diameter of $D_{As_2Se_3}$ =1.5 µm is plotted in Fig. 4.8(a). The position from 2.2 cm to 12.2 cm and from 12.2 cm to 15.6 cm corresponds to the waist section and transition section as shown in Fig. 4.8(b). The microfiber has a thick cladding diameter of $D_{PMMA}$ =88.5 µm, which increases mechanical robustness and reduces the chances of breaking during operation.

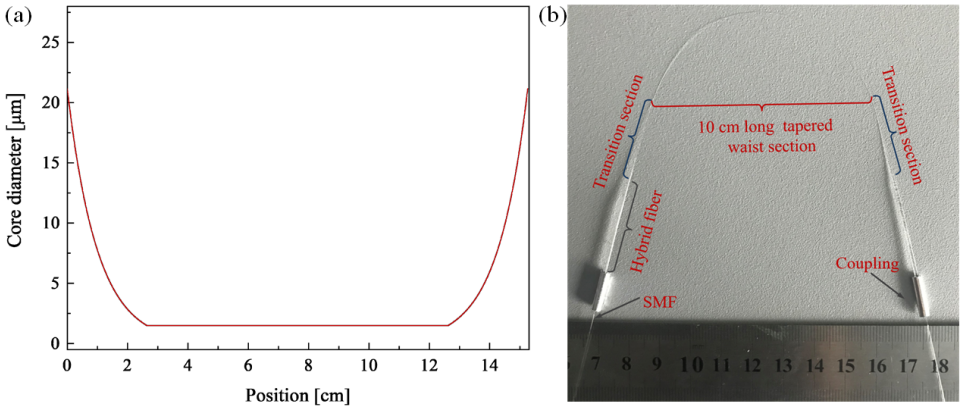


FIGURE 4.8 – (a) Tapered fiber profile. (b) An image of a tapered fiber.

# 5 Wide-range strain sensing based on Brillouin frequency shift and linewidth in a chalcogenide hybrid microfiber


**Haiyang Wang**, Song Gao, Chams Baker, Yuan Wang,
Liang Chen and Xiaoyi Bao,
Optics Express. 28(15), 22933-22945 (2020) ;
https ://doi.org/10.1364/OE.397683

## Author contributions

H.W. performed the experiment and simulation ; H.W., X.B. and L.C. contributed to analyzing experimental results ; H.W. and X.B. wrote the paper ; H.W., S.G. and C.B. fabricated chalcogenide microfibers ; H.W. and Y.W. built experimental setup ; All authors discussed experimental results and provided feedback on the paper ; X.B. supervised the overall project.

## Summary

We have seen in the previous chapter the fabrication of chalcogenide microfibers coated with PMMA. The thick PMMA cladding on the chalcogenide core provides mechanical strength for sensing applications. Brillouin strain sensing based on the single-mode fiber (SMF) has been demonstrated [152]. To increase the sensing range for applications in railways and bridges that need to withstand larger strain than the strain limit of 1% in SMFs, polymer optical fiber (POF) Brillouin sensing with a wide strain range (linear Brillouin frequency shift change within 3%) was experimentally demonstrated owing to its small Young's modulus [153]. However, POFs with large Brillouin bandwidth (around 150 MHz without strain) and the memory effect lead to a significant strain inaccuracy [154, 155]. In this chapter, we propose and demonstrate wide-range strain Brillouin sensing based on the single-core chalcogenide-PMMA microfiber. The chalcogenide microfiber has Young's modulus (17.8 GHz) lower than that of SMFs (72 GHz) while larger than that of POFs (3.5 GPa), leading to the wide-range sensing of 15000 $\mu\varepsilon$ without the memory effect. Brillouin frequency shift (BFS) and Brillouin linewidth are utilized to characterize strain measurement. Low pump power is required in the tens of centimeters-long chalcogenide-PMMA microfiber because of its ultra-high nonlinearity. The chalcogenide-PMMA microfiber with a narrower gain bandwidth (60 MHz without strain) and no relaxation behavior compared to POFs provides more accurate strain measurement. In POFs, broad Brillouin bandwidth was investigated with increasing strain, but no explanation for the change was provided. Similar broad bandwidth is measured in the strain sensor based on the chalcogenide-PMMA microfiber. Deformation occurs in certain positions of the microfiber at large strain, leading to the non-uniformity of the microfiber. The coexistence of numerous frequency components along the non-uniformity microfiber causes a broad Brillouin bandwidth, which is confirmed by measuring the distributed Brillouin gain spectra along the microfiber using the Brillouin optical time-domain analysis (BOTDA) technique.

Research Article | Vol. 28, No. 15 / 20 July 2020 / Optics Express 22933
Optics EXPRESS

# Wide-range strain sensor based on Brillouin frequency and linewidth in an $As_2Se_3$-PMMA hybrid microfiber

HAIYANG WANG, SONG GAO, CHAMS BAKER, YUAN WANG, LIANG CHEN, AND XIAOYI BAO

*University of Ottawa, Department of Physics, Ottawa, Ontario K1G 6N5, Canada*

**Abstract:** We propose a wide-range strain sensor based on Brillouin frequency and linewidth in a 50 cm-long $As_2Se_3$-polymethyl methacrylate ($As_2Se_3$-PMMA) hybrid microfiber with a core diameter of 2.5 $\mu$m. The distributed information over the hybrid microfiber is measured by a Brillouin optical time-domain analysis (BOTDA) system. The wide dynamic range strain from 0 to 15000 $\mu\varepsilon$ is enabled by measuring the Brillouin frequency and linewidth due to the low Young's modulus of $As_2Se_3$ core and the high mechanical strength of PMMA cladding. The deformation of the $As_2Se_3$-PMMA hybrid microfiber is observed when the strain is greater than 1500 $\mu\varepsilon$ by measuring the distributed Brillouin frequency and Brillouin linewidth over the 50 cm-long hybrid microfiber. The measured errors based on the Brillouin frequency in the range of 0-1500 $\mu\varepsilon$ and 1500-15000 $\mu\varepsilon$ are 42 $\mu\varepsilon$ and 105 $\mu\varepsilon$, respectively. The measured error based on the Brillouin linewidth is 65 $\mu\varepsilon$ at 0-1500 $\mu\varepsilon$ and the maximum error is 353 $\mu\varepsilon$ when the tensile strain is 15000 $\mu\varepsilon$. No strain memory effect is observed compared with the polymer optical fiber due to Young's modulus in $As_2Se_3$ is larger than that in polymer. Numerical simulations are developed to accurately predict the strain dependence of Brillouin frequency in the $As_2Se_3$-PMMA hybrid microfiber.



## 1. Introduction

Optical fiber strain measurement plays an important role in structural health monitoring [1–3] and human motion detection [4]. Optical fiber sensors for measuring wide-range strain have been extensively demonstrated in the last few decades. A strain sensor with a wide-range of 20000 $\mu\varepsilon$ and an uncertainty of 33 $\mu\varepsilon$ has been proposed in a polymer optical fiber (POF) based on the multi-mode interference [5]. The POF sensor was measured based on an optical spectrum analyzer (OSA) which has limited resolution leading to low strain resolution of 1.73 pm/$\mu\varepsilon$ corresponding to 0.22 GHz/$\mu\varepsilon$. The wide-range strain was also measured based on Brillouin scattering in POF to improve the measurement resolution [6–8]. The POF has broad Brillouin spectrum linewidth as it is a multi-mode fiber, which requires high pump power; in addition, the POF strain sensor has a memory effect at wide dynamic range due to the low Young's modulus, which affects its strain accuracy [9]. Recently, chalcogenide-PMMA hybrid optical fiber fabricated by using chalcogenide ($As_2Se_3$) as the core and PMMA as the cladding is attracting lots of attention. Coating PMMA on $As_2Se_3$ provides sufficient mechanical robustness and flexibility, which allows the fabrication of tapers with $As_2Se_3$ core diameters at the sub-wavelength scale. The fabrication of $As_2Se_3$-PMMA taper was proposed due to its ultrahigh nonlinearity $\gamma$=133 $(Wm)^{-1}$ [10]. The tapered $As_2Se_3$-PMMA hybrid fiber has been reported for measuring ultrasound [11], transverse load [12], stimulated Brillouin scattering (SBS) [13], and supercontinuum [14]. Here, we are exploring the possibility of using $As_2Se_3$-PMMA hybrid microfiber based on BOTDA for wide-range strain sensing. As Young's modulus for $As_2Se_3$ is 17.8 GPa [15], while the POF is 3.5 GPa [16], we do not observe the strain memory effect over the 15000 $\mu\varepsilon$ range. This

#397683 https://doi.org/10.1364/OE.397683
Journal © 2020 Received 13 May 2020; revised 22 Jun 2020; accepted 6 Jul 2020; published 17 Jul 2020

Optics EXPRESS

means the strain measurement is repeatable, even though the uncertainty is higher. Taking the advantages of the high refractive index of $As_2Se_3$ for strong SBS amplification and low peak power requirement due to small core size fabrication for the single-mode operation has not been explored yet. The ultrahigh nonlinearity of $As_2Se_3$ also enables low peak power of pump pulse for SBS generation. The PMMA with mechanical flexibility protects the $As_2Se_3$ core and allows the wide-range strain sensing. To the best of our knowledge, the Brillouin frequency shift (BFS) and Brillouin linewidth dependence on strain over wide-range strain sensing in the $As_2Se_3$-PMMA hybrid microfiber has not been demonstrated yet. Due to the ultrahigh nonlinear coefficient and the small core size of the $As_2Se_3$-PMMA hybrid microfiber compared with POFs, the low power requirement in pump pulse for SBS generation makes it a promising candidate for wide-range strain sensing, which can be applied for monitoring civil infrastructures such as railway and bridge with steel structures that require large strain beyond that of $SiO_2$ limited to less than 1%.

In this paper, we demonstrate a wide-range strain sensor based on Brillouin frequency and linewidth in an $As_2Se_3$-PMMA hybrid microfiber of 50 cm long with a core diameter of 2.5 $\mu$m. BOTDA setup is employed for tensile strain sensing as it provides the location information. The fabrication process, Brillouin strain sensing principle, and the numerical simulations of the hybrid microfiber are introduced. Experimental results show that SBS is excited using only 8 dBm peak power of the pump pulse, and a wide-range strain up to 15000 $\mu\varepsilon$ is measured based on BFS and Brillouin linewidth. When the strain is larger than 1500 $\mu\varepsilon$, the hybrid microfiber is deformed which is detected by measuring the distributed BFS and Brillouin linewidth. The strain errors based on BFS measurement in the range of 0-1500 $\mu\varepsilon$ and 1500-15000 $\mu\varepsilon$ are 42 $\mu\varepsilon$ and 105 $\mu\varepsilon$, respectively. For strain dependence of Brillouin linewidth, the error is 65 $\mu\varepsilon$ at 0-1500 $\mu\varepsilon$ and the maximum error is 353 $\mu\varepsilon$ when the tensile strain is 15000 $\mu\varepsilon$.

## 2. Fabrication and sensing principle

### 2.1. Fabrication of $As_2Se_3$-PMMA fiber

The $As_2Se_3$-PMMA fiber is fabricated by the rod-in-tube drawing technique [17]. The fabrication requires the following steps. A 7 cm-long $As_2Se_3$ fiber is inserted into an elongated PMMA microtube before inserting it into a 13 cm-long PMMA tube which is placed in the oven before fabricating to eliminate moisture. The assembly is then heat-softened by a resistive heater at a constant temperature of 220 °C to obtain an $As_2Se_3$-PMMA preform. Finally, the preform is drawn to a fiber with the $As_2Se_3$ core diameter of 21.25 $\mu$m and the PMMA cladding diameter of 1.2 mm. The photos of the initial PMMA tube, the elongated PMMA microtube, and the $As_2Se_3$ fiber are shown in Fig. 1(a). Figure 1(b) shows an optical microscope image of a polished $As_2Se_3$-PMMA fiber end facet without tapering.

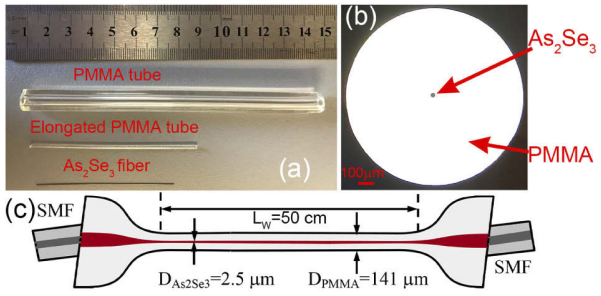


**Fig. 1.** (a) Photos of the PMMA tube, the elongated PMMA microtube and the $As_2Se_3$ fiber. (b) Cross-section of an end polished $As_2Se_3$-PMMA fiber without tapering. (c) Schematic of 50 cm-long angle-coupled $As_2Se_3$-PMMA hybrid microfiber with a core diameter of 2.5 $\mu$m.

Optics EXPRESS

### 2.2. Coupling and tapering of the $As_2Se_3$-PMMA fiber

The hybrid fiber is then angle coupled with single-mode fibers (SMF) before the tapering process. To suppress the undesired Fresnel reflection of the hybrid fiber/SMF interfaces and maximize the transmission coefficient, the end faces of the hybrid fiber and SMFs are polished at the angle of 5 degrees for the $As_2Se_3$-PMMA fiber and 10 degrees for SMFs. The butt-coupling interfaces are permanently fixed using UV-cured epoxy. The $As_2Se_3$-PMMA fiber is further tapered to a 50 cm-long microfiber with a core diameter of 2.5 $\mu$m using the heat-brush method [18]. The total loss of the tapered fiber is ~ 4 dB, including a ~ 2 dB insertion loss at hybrid fiber/SMF interfaces and a ~ 2 dB propagation loss over 50 cm length. Figure 1(c) shows the schematic of the coupled $As_2Se_3$-PMMA hybrid microfiber, including a tapered waist-length of $L_w = 50$ cm, a core diameter of $D_{As_2Se_3} = 2.5$ $\mu$m and a cladding diameter of $D_{PMMA} = 141$ $\mu$m.

### 2.3. Principle of Brillouin strain sensing

The relationship between the BFS ($\nu_B$) experienced by scattered light in the SBS process and longitudinal acoustic velocity ($V_L$) in the $As_2Se_3$-PMMA hybrid microfiber is given by [19]

$$\nu_B = \frac{2n_{eff}V_L}{\lambda_p} = \frac{2n_{eff}}{\lambda_p}\sqrt{\frac{1-\sigma}{(1-2\sigma)(1+\sigma)}\frac{E}{\rho}} \tag{1}$$

where $\lambda_p$ is the pump wavelength, $n_{eff}$ is the effective refractive index, $\sigma$ is the Poisson's ratio, $E$ is Young's modulus and $\rho$ is the density of the $As_2Se_3$ as the SBS occurs in the core of the hybrid fiber. The hybrid microfiber can be used for strain sensing based on BFS as the $n_{eff}$ and $V_L$ are dependent on the strain variation. The linear dependence between strain variation ($\Delta\varepsilon$) and the change of BFS ($\Delta\nu_B$) is expressed as

$$\Delta\nu_B(\varepsilon) = \nu_B\left(\frac{1}{n_{eff}}\frac{\partial n_{eff}}{\partial\varepsilon} + \frac{1}{V_L}\frac{\partial V_L}{\partial\varepsilon}\right)\Delta\varepsilon \tag{2}$$

where $\partial n_{eff}/\partial\varepsilon$ is the photo-elastic coefficient and $\partial V_L/\partial\varepsilon$ is the acousto-elastic coefficient.

## 3. Numerical simulations

An analytical model, refined by numerical simulation, is developed to predict strain dependence of BFS using the finite-element method (FEM). Here, fundamental optical mode and acoustic modes are calculated at the operating wavelength $\lambda_p = 1550$ nm by solving optical propagation and mechanical equations. These are written as [20]

$$\nabla^2 E + \left(\frac{2\pi}{\lambda}\right)(n^2 - {n_{eff}}^2)E = 0 \tag{3}$$

$$\nabla^2 u_j + \left(\frac{\Omega_j^2}{V_{L,j}^2} - {\beta_{a,j}}^2\right)u_j = 0 \tag{4}$$

where $E$ and $u_j$ are the spatial distribution of optical field and acoustic field, respectively, $n_{eff}$ is the effective refractive index of the optical mode, $V_{L,j}$ and $\beta_{a,j}$ are the longitudinal velocity and propagation constant of the $j$th acoustic mode, and $\Omega_j$ is the Brillouin frequency shift of the $j$th acoustic mode. The phase-matching condition leads to the relation $\beta_{a,j} \approx 2\beta_{opt}$, where $\beta_{opt}$ is the propagation constant of the optical mode. The parameters for calculating the optical and acoustic modes are shown in Table 1. The profiles of fundamental optical mode and two acoustic modes (L01 and L02) in the hybrid microfiber with the core diameter of 2.5 $\mu$m are plotted in Fig. 2(a). The large acoustic impedance difference between the $As_2Se_3$ core and the PMMA cladding confines the acoustic fields in the core ($1.044\times10^7$ kg/m$^2$/s for $As_2Se_3$ and $1.86\times10^6$ kg/m$^2$/s

Optics EXPRESS

for PMMA [21]). We also observe that the distribution of acoustic mode L02 tends to spread to the interface between the $As_2Se_3$ core and PMMA cladding. Since the longitudinal acoustic velocity of PMMA is greater than that of the core, the acoustic mode L02 has larger acoustic velocity than that of the acoustic mode L01, as shown in Fig. 2(b). Then the overlap between the fundamental mode and the $j$th acoustic mode is calculated using the acousto-optic coupling efficiency given by [22,23]

$$I_j = \frac{(\int(|E|)^2 u_j * dxdy)^2}{\int(|E|)^4 dxdy \int(|u_j|)^2 dxdy} \tag{5}$$

The calculated acousto-optic coupling efficiencies of four acoustic modes are $I_1$ =0.423, $I_2$ =0.076, $I_3$ =0.024 and $I_4$ =0.0005. Finally, the superposition of the Brillouin gain spectrum of each acoustic mode is calculated using Lorentzian function [22,23]

$$S(\nu) = g_B \sum_j I_j \frac{(\Gamma/2)^2}{(\Gamma/2)^2 + (\nu - \nu_B^j)^2} \tag{6}$$

where the Brillouin gain is given by $g_B = 4\pi n_{eff}^8 p_{12}^2/(c\lambda_p^3 \rho V_L \Gamma)$ with $p_{12}$ being the photo-elastic tensor, $\Gamma$ is the Brillouin linewidth and is set to 60 MHz for the $As_2Se_3$-PMMA fiber [12]. Figure 2(c) shows the simulation of the Brillouin spectrum of the hybrid microfiber. The result shows two peaks at 7.726 GHz and 7.854 GHz for acoustic modes L01 and L02, respectively. The calculated gain peaks induced by other acoustic modes are not considered as their contributions to the Brillouin gain spectrum are negligible due to small acousto-optic efficiencies. The intensity of the peak at 7.726 GHz is higher than that of 7.854 GHz as the acoustic-optic coupling efficiency is larger which results in a higher gain from the acoustic mode L01. The field patterns of two acoustic modes are shown in Fig. 2(e)–2(f).

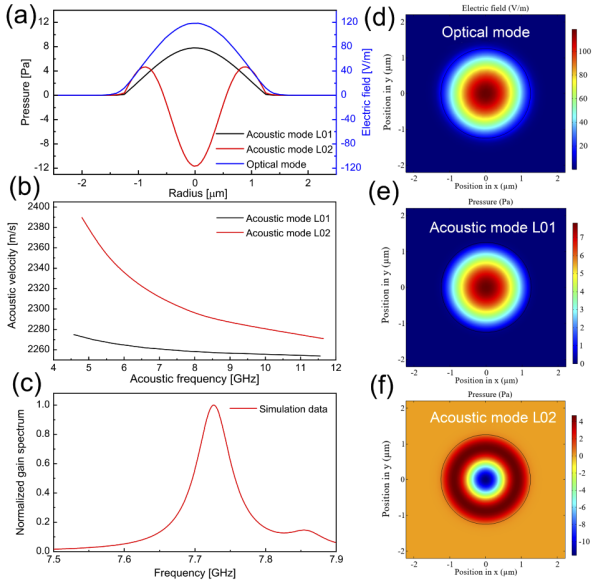


**Fig. 2.** (a) Profiles of optical mode (blue) and acoustic modes L01 (black) and L02 (red). (b) The acoustic velocity of acoustic modes L01 (black) and L02 (red). (c) Simulated Brillouin spectrum of the hybrid fiber. (d) The electric field of the fundamental mode. (e,f) Acoustic mode L01 at 7.726 GHz and acoustic mode L02 at 7.854 GHz.

Optics EXPRESS

**Table 1. $As_2Se_3$ and PMMA parameters used for Brilloin gain spectrum calculation.**

| | $n$ [12] | $\rho$ (Kg/m$^3$) [24] | $V_L$ (m/s) [15,25] | $E$ (GPa) | $\sigma$ [12] | $p_{12}$ [24] |
|---|---|---|---|---|---|---|
| $As_2Se_3$ | 2.674 | 4640 | 2261 | 17.8 | 0.202 | 0.266 |
| PMMA | 1.481 | 1187 | 2690 | 3.5 | 0.327 | 0.297 |

According to Eq. (2), the change of effective refractive index $n_{eff}$ and longitudinal acoustic velocity $V_L$ is considered when calculating the strain dependence of BFS. For the isotropic material, such as fibers, subjected to the tensile strain $\varepsilon$, the longitudinal acoustic velocity $V_L^{\varepsilon}$ is given by [26]

$$V_L^{\varepsilon} = V_L^0(1 + KE\varepsilon) \tag{7}$$

where $V_L^0$ is the longitudinal acoustic velocity without strain and longitudinal acousto-elastic coefficient $K$ is given by

$$K = \frac{1}{2(\lambda + 2\mu)(3\lambda + 2\mu)}\left(\frac{\lambda + \mu}{\mu}(4\lambda + 10\mu + 4m) + \lambda + 2l\right) \tag{8}$$

where $m$ and $l$ are the Murnaghan's third order elastic constant ($m = -4.2 \times 10^{10}$ Pa and $l = -5.0 \times 10^{10}$ Pa for chalcogenide glass [27]), and the Lame's elastic constant $\lambda$ and $\mu$ are calculated by

$$\mu = \frac{E\sigma}{(1 + \sigma)(1 - 2\sigma)} \tag{9}$$

$$\lambda = \frac{E\sigma}{2(1 + \sigma)} \tag{10}$$

The strain dependence of refractive index is obtained using [28]

$$n_{\varepsilon} = n_0 - CE\varepsilon \tag{11}$$

where $n_0$ is the refractive index without strain, and $C$ is the photo-elastic coefficient (for $As_2Se_3$, $C$=-30×10$^{-12}$ Pa$^{-1}$ [29]). The product of acoustic-elastic coefficient and Young's modulus is $KE = -3.5 \times 10^{-6}/\mu\varepsilon$ and the product of photo-elastic coefficient and Young's modulus is $CE = -5.3 \times 10^{-7}/\mu\varepsilon$. The shift of BFS under different strain values is then calculated using the new effective refractive index and longitudinal acoustic velocity. The calculated BFS decreases with increasing strain as the negative change of longitudinal acoustic velocity is larger than the positive change of effective refractive index. The calculated strain coefficient is -0.0255 MHz/$\mu\varepsilon$. The calculated strain dependence of BFS will be discussed in the next section to compare with experimental results.

## 4. Experimental results

### 4.1. Experiment setup and Brillouin spectra

To obtain location information and improve the accuracy of strain measurement, experiments are conducted by employing a BOTDA system. The strain sensor based on BFS and Brillouin linewidth can be measured at an accuracy of ~ MHz/$\mu\varepsilon$ instead of the OSA accuracy of ~ GHz/$\mu\varepsilon$ [30]. The spectrum of each location of the $As_2Se_3$-PMMA hybrid microfiber is measured using the distributed system, which allows us to measure the strain at which the microfiber is deformed. Figure 3 illustrates the BOTDA setup. The light source is a tunable optical fiber laser, and the operating wavelength is set to 1550 nm. The continuous wave (CW) light is divided by a 50:50 coupler into two paths. The upper path transfers light into a 20 ns pump pulse with a high extinction ratio (ER) using two electro-optic modulators (EOM) driven by a dual-channel

Optics EXPRESS

function generator (FG). The signal to noise ratio of the BOTDA sensor system can be increased by using the high ER pump pulse. An Erbium-doped-fiber-amplifier (EDFA) is used to amplify the pulse to 8 dBm peak power. The amplified spontaneous emission (ASE) is then filtered out by a tunable filter. The pump pulse is injected into one end of the 50 cm-long microfiber through an optical circulator. In the lower path, the EOM generates two sidebands with a frequency shift from 7.5 to 7.9 GHz, corresponding to the BFS of the $As_2Se_3$-PMMA microfiber. The power of two sidebands is amplified by an EDFA, and then selected by a 2 GHz narrow bandwidth filter as the probe wave, whose frequency can be swept by a radio frequency (RF) generator. The probe wave is injected into the FUT opposite to the propagation direction of the pump. The two polarization controllers (PC) are used to change the polarization states of both of pump pulse and probe wave to make sure that they are co-polarized along with the microfiber. The FUT is fixed by two clamps to linear translation stages to induce the axial strain. The resulting backscattered signal is detected using a photodetector (PD), and the Brillouin spectra are recorded using an oscilloscope (OSC) with a 5 GS/s sampling rate.

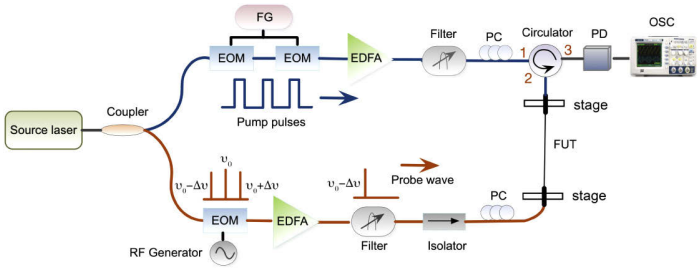


**Fig. 3.** Experimental setup for strain measurement based on BOTDA in an $As_2Se_3$-PMMA hybrid mcirofiber. The abbreviations here denote: EOM, Electro-Optic Modulator; FG, Function Generator; EDFA, Erbium-Doped-Fiber-Amplifier; PC, Polarization Controller; RF, Radio Frequency. FUT, Fiber Under Test; PD, Photo Detector; OSC, Oscilloscope.

The backscattering trace is recorded in the time domain and is converted to frequency and length information using the sweeping range of RF generator and the sampling rate of OSC. All experimental results are measured at the room temperature of 22 °C and the room humidity of 38%. Figure 4(a) shows the Brillouin spectrum in the 25 cm position of the $As_2Se_3$-PMMA microfiber with a core diameter of 2.5 $\mu$m without strain. The Brillouin spectrum is excited using only 8 dBm peak power of the pump pulse due to the ultrahigh nonlinearity and the small core size of the $As_2Se_3$-PMMA hybrid microfiber. The main peak of BFS is 7.728 GHz which is slightly different from that of the numerical simulation result of 7.726 GHz as the fabrication process gives the 10% error of the core diameter [13]. Figure 4(a) also shows a secondary peak at 7.848 GHz arising from the acoustic mode L02. Figure 4(b) shows the time-varying gain profile of the 7.728 GHz probe wave when the pump pulse with 20 ns linewidth passes through the 50 cm-long hybrid microfiber. The gain exists in the position from 0.5 to 1.5 m because of the 20 ns pump pulse corresponding to 1 m length. Although the pulse length is longer than that of the hybrid microfiber, the BFS and Brillouin linewidth difference in each position over the 50 cm-long hybrid microfiber can be clearly identified due to the non-uniformity of the microfiber. The distributed BFS and Brillouin linewidth are obtained from the Brillouin spectra by sweeping the frequency of the probe wave, as plotted in Fig. 4(c). The Stokes trace of the main peak is clearly shown in the distributed Brillouin spectrum, while the Stokes trace of the secondary peak is too weak to be seen as its small Brillouin gain.

Optics EXPRESS

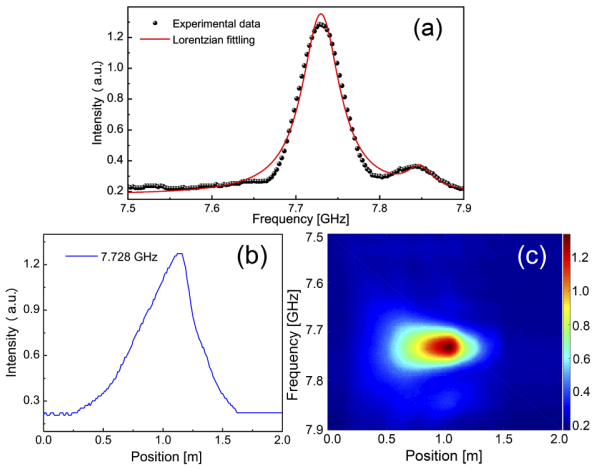


**Fig. 4.** (a) Experimental normalized Brillouin spectrum in the 25 cm position of the microfiber with a core diameter of 2.5 $\mu$m (black circles) and Lorentzian fitting (red solid trace). (b) Stokes trace at 7.728 GHz. (c) Distributed Brillouin spectrum when sweeping the probe frequency from 7.5 to 7.9 GHz.

### *4.2. Strain dependence of Brillouin frequency and linewidth*

The 50 cm-long $As_2Se_3$-PMMA microfiber is fixed by the two clamps to the linear translation stages with a resolution of 1 $\mu$m. The tensile strain is then induced by using the linear translation stages at steps of 100 $\mu$m, which corresponds to the tensile strain of 2000 $\mu\varepsilon$ for the fiber length of 50 cm. The experimental and simulated normalized Brillouin spectra at the 25 cm position of the $As_2Se_3$-PMMA microfiber with a core diameter of 2.5 $\mu$m for an increasing strain from 0 to 15000 $\mu\varepsilon$ are plotted in Fig. 5. We can observe that the experimental BFS (circles) decreases with increasing strain. It is related to the fact that increasing tensile strain reduces the longitudinal acoustic velocity as we expected in simulation. Remarkably close agreement on the strain dependence of BFS is obtained between the experimental and simulated results. Since the maximum difference of BFS between simulation and experiment in the range of 0-1500 $\mu\varepsilon$ is 2.5 MHz, the error is 95 $\mu\varepsilon$ in the comparison between numerical and the experimental results. The maximum difference of BFS is 10.4 MHz in the range of 1500-15000 $\mu\varepsilon$, which means the maximum error is 388 $\mu\varepsilon$. The plots in Fig. 5 also show that Brillouin gain shape is dramatically changed, and the Brillouin linewidth is broadened with increasing strain, unlike the SMF which has the constant linewidth with strain [31]. The linewidth of the spectra is constant in simulation as we did not consider the change of linewidth caused by the deformation of the microfiber.

The measured distributed BFS of the $As_2Se_3$-PMMA hybrid microfiber for increasing tensile strain is plotted in Fig. 6(a). The BFS in each position of the microfiber can be measured for the 20 ns pump pulse due to the non-uniform waist region of the microfiber. The horizontal dash lines represent the average values of the BFS over the 50 cm-long microfiber. The BFS in different positions of the hybrid microfiber without strain has tiny fluctuation, and the standard deviation is only 0.3 MHz due to the small non-uniformity of the $As_2Se_3$ core. The difference in BFS over the 50 cm-long microfiber can be clearly seen at 3000 $\mu\varepsilon$ as the great difference in core diameter in some positions resulting from the deformation of the microfiber at large strain. The microfiber is deformed at large strain due to low Young's modulus of the $As_2Se_3$ and PMMA materials and the non-uniformity of the microfiber. The difference is noticeable at 9000 $\mu\varepsilon$ in which the standard deviation reaches 5.3 MHz. The standard deviations as a function of strain in the $As_2Se_3$-PMMA hybrid microfiber with core diameters of 2.5 $\mu$m and 2.3 $\mu$m are plotted in

Optics EXPRESS

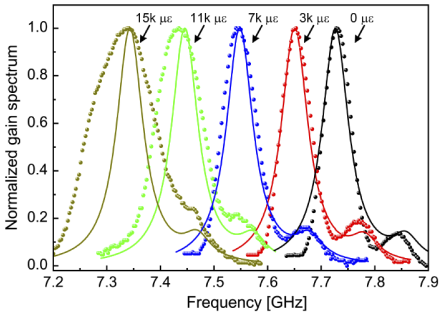


**Fig. 5.** Experimental normalized Brillouin spectra (circles) and simulated Brillouin spectra (solid traces) of the hybrid microfiber with a core diameter of 2.5 $\mu$m for 0 $\mu\varepsilon$ (black), 3000 $\mu\varepsilon$ (red), 7000 $\mu\varepsilon$ (blue), 11000 $\mu\varepsilon$ (green) and 15000 $\mu\varepsilon$ (yellow).

Fig. 6(b). The microfiber with a core diameter of 2.3 $\mu$m has a greater standard deviation than that of 2.5 $\mu$m even without strain as the large end-face reflection between the $As_2Se_3$-PMMA fiber and SMFs, which induces the gain fluctuation when measuring the Brillouin spectra. In Fig. 6(a), we observe that the BFS has a small difference at the center of the hybrid microfiber. Thus the Brillouin spectra at the 25 cm position of the hybrid microfiber with increasing axial strain are used for analyzing the BFS. Figure 6(c) and Figure 6(d) show the tensile strain dependence of the BFS in the $As_2Se_3$-PMMA microfiber with different core diameters in two strain ranges. Both of core diameters show that the BFS decreases linearly with the strain increases in the two ranges. The linear relation between strain and BFS can be related to the deformation only occurs at certain position of the microfiber and may not be reflected at central frequency. Strain coefficients of BFS in two ranges are shown in Table 2. The slopes in two ranges have a small difference of 0.0004 MHz/$\mu\varepsilon$ for the fiber with a core diameter of 2.5 $\mu$m, which may be induced by the gain fluctuation at large strain and fitting errors.

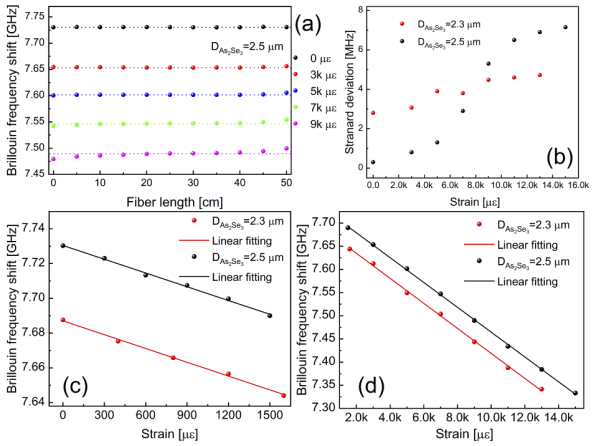


**Fig. 6.** (a) Distributed BFS over the 50 cm-long microfiber with a core diameter of 2.5 $\mu$m in different strain values (circles), and the average BFS (horizontal dash lines). (b) Standard deviation for the increasing strain in the microfiber with the core diameter of 2.3 $\mu$m and 2.5 $\mu$m. (c) BFS versus the strain increase from 0 to 1500 $\mu\varepsilon$ in 25 cm position of the fiber with core diameters of 2.3 $\mu$m and 2.5 $\mu$m. (d) BFS versus the strain increase from 1500 to 15000 $\mu\varepsilon$ in 25 cm position of the fiber.

Optics EXPRESS

**Table 2. Strain coefficients and errors of Brillouin frequency and linewidth of the $As_2Se_3$-PMMA microfiber with core diameters of 2.5 $\mu$m and 2.3 $\mu$m, respectively. C: Coefficient, BF: Brillouin frequency, BW: Brillouin linewidth.**

| Core diameters | 2.5 $\mu$m | | 2.3 $\mu$m | |
|---|---|---|---|---|
| Parameters | C (MHz/$\mu\varepsilon$) | Error ($\mu\varepsilon$) | C (MHz/$\mu\varepsilon$) | Error ($\mu\varepsilon$) |
| BF (0-1.5k $\mu\varepsilon$) | -0.0264 | 42 | -0.0265 | 47 |
| BF (1.5k-15k $\mu\varepsilon$) | -0.0268 | 105 | -0.027 | 210 |
| BL (0-1.5k $\mu\varepsilon$) | 0.0023 | 65 | 0.0029 | 113 |
| BL (1.5k-15k $\mu\varepsilon$) | $8.6E{-}7\Delta\varepsilon$-0.0014 | 353 | $1.08E{-}6\Delta\varepsilon$-0.0017 | 515 |

Figure 7(a) shows the distributed Brillouin linewidth over the 50 cm-long $As_2Se_3$-PMMA hybrid microfiber at different tensile strain values. The Brillouin linewidth decreases in the same trend along the tapered fiber over the strain of 0-1500 $\mu\varepsilon$. There are two contributing factors for this decrease: 1) the PMMA cladding is non-uniform along the fiber during fabrication and tapering processes. The PMMA plays the role of an acoustic damper due to its large elastic loss and low density [13]. Thus, the large diameter of the PMMA induces small Brillouin linewidth; 2) the intensity of the pump pulse affects the Brillouin linewidth. The large Brillouin linewidth can be obtained for the low intensity of the pump pulse. When the pump pulse is launched into the fiber, the intensity of the pulse is gradually increased, which means the decrease of the Brillouin linewidth along the fiber. We observe that the linewidth broadens in a different trend at 3000 $\mu\varepsilon$ and it is obvious when the strain is 15000 $\mu\varepsilon$. This can be related to the combined effect of the decreased power with increasing strain and the deformation of the microfiber in large strain. For the $As_2Se_3$-PMMA microfiber, there are internal stress between $As_2Se_3$ core and PMMA cladding as PMMA has a large thermal coefficient comparing with the $As_2Se_3$. When the microfiber is elongated with small strain, it is not deformed. In the case, the power decreases linearly with strain due to PMMA cladding induced the stress on the $As_2Se_3$ core, which is similar to that in panda fiber where stress rods are pressed into the core leading to increased attenuation with strain [32]. The linear decreased power in the fiber under small strain from 0 to 1500 $\mu\varepsilon$ results in a linear increase of linewidth, as shown in Fig 7(b). The dependence between strain and linewidth in the range of 1500-15000 $\mu\varepsilon$ for two core diameters of the $As_2Se_3$-PMMA hybrid microfiber are shown in Fig. 7(c). The nonlinear relationship means that the hybrid microfiber is deformed in large strain. The non-uniform localized strain induced by the deformation of the hybrid microfiber enlarges the localized strain range resulting in the nonlinear broadened Brillouin linewidth. Strain coefficients and errors of Brillouin linewidth of the $As_2Se_3$-PMMA hybrid microfiber with core diameters of 2.3 $\mu$m and 2.5 $\mu$m are shown in Table 2.

### *4.3. Relaxation and hysteresis measurement*

The BFS as a function of time is measured at 7000 $\mu\varepsilon$ and 15000 $\mu\varepsilon$ in the $As_2Se_3$-PMMA microfiber with a core diameter of 2.5 $\mu$m, as shown in Fig. 8(a). We can see that the BFS at 7000 $\mu\varepsilon$ is constant with time, while the BFS at 15000 $\mu\varepsilon$ has a fluctuation with time induced by the Brillouin gain fluctuation at large strain. In two cases, no relaxation behavior is observed, which is different with the large strain sensor based on the POF as Young's modulus in $As_2Se_3$ is larger than that in polymer. Figure 8(b) shows the BFS for both increasing and decreasing strain in the microfiber with a core diameter of 2.5 $\mu$m. The strain is increased to 15000 $\mu\varepsilon$ and then decreased to 0 $\mu\varepsilon$ in a step of 1000 $\mu\varepsilon$. It can be seen that the BFS shows the same value for both increasing and decreasing strain at $< 9000$ $\mu\varepsilon$; above this value, there is a slight difference in the strain cycle. The difference is due to the fluctuation of the BFS at large strain, as illustrated in Fig 8(a). The maximum difference is 4 MHz corresponding to the maximum error of 149 $\mu\varepsilon$, which is $< 1\%$ of the strain we measured. The error in the increasing and

Optics EXPRESS

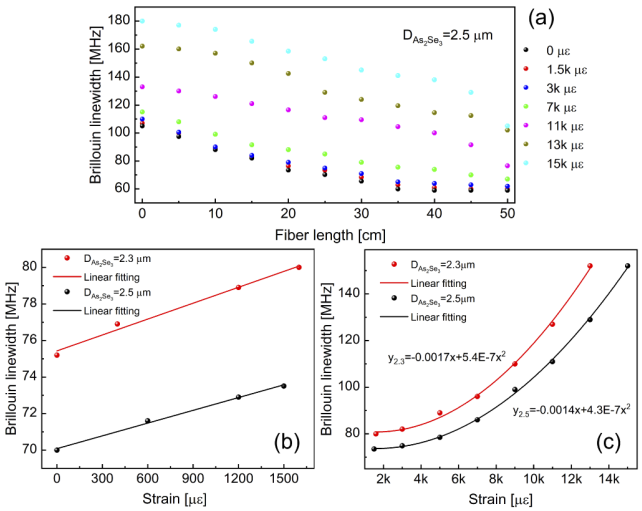


**Fig. 7.** (a) Distributed Brillouin linewidth over the 50 cm-long microfiber the $As_2Se_3$-PMMA fiber with a core diameter of 2.5 $\mu$m for an increasing strain. (b) Linewidth versus the strain increase from 0 to 1500 $\mu\varepsilon$ in 25 cm position of the hybrid fiber with core diameters of 2.3 $\mu$m and 2.5 $\mu$m. (c) Linewidth versus the strain increase from 1500 to 15000 $\mu\varepsilon$ in 25 cm position of the hybrid fiber.

decreasing cycle is close to the error induced by the linear fitting of BFS at large strain range. Thus, the $As_2Se_3$-PMMA microfiber shows hysteresis free behavior and good repeatability for the wide-range strain measurement.

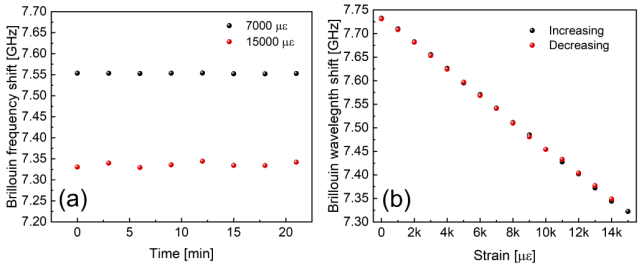


**Fig. 8.** (a) BFS as a function of time at 7000 $\mu\varepsilon$ and 15000 $\mu\varepsilon$ in 25 cm position of the hybrid fiber with the core diameter of 2.5 $\mu$m. (b) BFS versus the increasing and decreasing strain in 25 cm position of the hybrid fiber with the core diameter of 2.5 $\mu$m.

### *4.4. Temperature dependence of Brillouin frequency and linewidth*

The dependence of Brillouin frequency and Brillouin linewidth on temperature variation is also investigated. Figure 9(a) shows the linear change of BFS with increasing temperature from 25 °C to 55 °C. The temperature sensitivity is -1.25 MHz/°C, which is similar to the temperature measurement in the tapered dual-core $As_2Se_3$-PMMA fiber [33]. Figure 9(b) shows the Brillouin linewidth as a function of temperature. We can see that the Brilloin linewidth remains constant over the temperature range of 25 - 55 °C as the $As_2Se_3$-PMMA microfiber is not deformed, which is different from the Brillouin linewidth change at large strain. Due to the different thermal expansion coefficient between the $As_2Se_3$ core and PMMA cladding, the strain is induced on the

Optics EXPRESS

core by the cladding along the fiber. The fluctuation with a standard deviation of 0.4 MHz may be due to the thermally induced strain on the $As_2Se_3$ core.

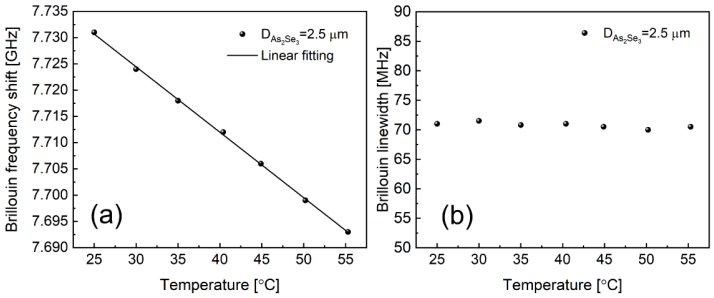


**Fig. 9.** (a) BFS and (b) Brillouin linewidth as a function of temperature in 25 cm position of the hybrid fiber with the core diameter of 2.5 $\mu$m.

## 5. Conclusion

In conclusion, we have calculated and experimentally demonstrated a strain sensor based on Brillouin frequency shift and linewidth in a 50 cm-long $As_2Se_3$-PMMA microfiber with a core diameter of 2.5 $\mu m$ for wide-range strain measurement. Experimental results have demonstrated the linear strain dependence of the Brillouin frequency shift and nonlinear dependence of the linewidth in a wide-range strain up to 15000 $\mu\varepsilon$. The deformation of the hybrid microfiber is measured when the strain larger than 1500 $\mu\varepsilon$ by measuring the distributed Brillouin frequency shift and linewidth over the 50 cm-long hybrid microfiber. The calculated errors of strain dependence of BFS in range of 0-1500 $\mu\varepsilon$ and 1500-15000 $\mu\varepsilon$ are 42 $\mu\varepsilon$ and 105 $\mu\varepsilon$, respectively. The errors of strain based on linewidth are 65 $\mu\varepsilon$ from 0 to 1500 $\mu\varepsilon$ and 353 $\mu\varepsilon$ when the axial strain is 15000 $\mu\varepsilon$. In general, the $As_2Se_3$-PMMA hybrid microfiber provides huge potential for wide-range strain sensing.

## Funding

China Scholarship Council; Natural Sciences and Engineering Research Council of Canada (06071-RGPIN-2015); Canada Research Chairs (75-67138).

## Acknowledgment

The authors are thankful to Coractive Inc. for providing the $As_2Se_3$ fiber that is utilized in the fabrication of our single-core $As_2Se_3$-PMMA hybrid microfibers.

## Disclosures

The authors declare no conflicts of interest.

## References

1. M. Mokhtar, K. Owens, J. Kwasny, S. Taylor, P. Basheer, D. Cleland, Y. Bai, M. Sonebi, G. Davis, A. Gupta, I. Hogg, B. Bell, W. Doherty, S. McKeague, D. Moore, K. Greeves, T. Sun, and K. T. V. Grattan, "Fiber-optic strain sensor system with temperature compensation for arch bridge condition monitoring," IEEE Sens. J. **12**(5), 1470–1476 (2012).
2. P. Moyo, J. Brownjohn, R. Suresh, and S. Tjin, "Development of fiber bragg grating sensors for monitoring civil infrastructure," Eng. Structures **27**(12), 1828–1834 (2005).
3. H. Tam, T. Lee, S. Ho, T. Haber, T. Graver, and A. Mendez, "Utilization of fiber optic bragg grating sensing systems for health monitoring in railway applications," Struct. Heal. Monit. Quantification, Validation, Implementation **1** (2007).

Optics EXPRESS


4. J. Guo, M. Niu, and C. Yang, "Highly flexible and stretchable optical strain sensing for human motion detection," Optica **4**(10), 1285–1288 (2017).
5. J. Huang, X. Lan, H. Wang, L. Yuan, T. Wei, Z. Gao, and H. Xiao, "Polymer optical fiber for large strain measurement based on multimode interference," Opt. Lett. **37**(20), 4308–4310 (2012).
6. N. Hayashi, Y. Mizuno, and K. Nakamura, "Brillouin gain spectrum dependence on large strain in perfluorinated graded-index polymer optical fiber," Opt. Express **20**(19), 21101–21106 (2012).
7. Y. Mizuno, N. Matsutani, N. Hayashi, H. Lee, M. Tahara, H. Hosoda, and K. Nakamura, "Brillouin characterization of slimmed polymer optical fibers for strain sensing with extremely wide dynamic range," Opt. Express **26**(21), 28030–28037 (2018).
8. A. Leal-Junior, A. Frizera, H. Lee, Y. Mizuno, K. Nakamura, T. Paixão, C. Leitão, M. F. Domingues, N. Alberto, P. Antunes, P. André, C. Marques, and M. J. Pontes, "Strain, temperature, moisture, and transverse force sensing using fused polymer optical fibers," Opt. Express **26**(10), 12939–12947 (2018).
9. K. Nakamura, I. R. Husdi, and S. Ueha, "A distributed strain sensor with the memory effect based on the pof otdr," in *17th International Conference on Optical Fibre Sensors*, vol. 5855 (International Society for Optics and Photonics, 2005), pp. 807–810.
10. C. Baker and M. Rochette, "Highly nonlinear hybrid asse-pmma microtapers," Opt. Express **18**(12), 12391–12398 (2010).
11. S. Gao, C. Baker, W. Cai, L. Chen, and X. Bao, "10 khz-34 mhz ultrasound detection based on a dual-core hybrid taper," APL Photonics **4**(11), 110805 (2019).
12. B. Saxena, C. Baker, X. Bao, and L. Chen, "High birefringent brillouin frequency shifts in a single-mode as 2 se 3-pmma microtaper induced by a transverse load," Opt. Lett. **44**(19), 4789–4792 (2019).
13. J.-C. Beugnot, R. Ahmad, M. Rochette, V. Laude, H. Maillotte, and T. Sylvestre, "Reduction and control of stimulated brillouin scattering in polymer-coated chalcogenide optical microwires," Opt. Lett. **39**(3), 482–485 (2014).
14. D. D. Hudson, S. Antipov, L. Li, I. Alamgir, T. Hu, M. El Amraoui, Y. Messaddeq, M. Rochette, S. D. Jackson, and A. Fuerbach, "Toward all-fiber supercontinuum spanning the mid-infrared," Optica **4**(10), 1163–1166 (2017).
15. N. Soga, M. Kunugi, and R. Ota, "Elastic properties of se and as2se3 glasses under pressure and temperature," J. Phys. Chem. Solids **34**(12), 2143–2148 (1973).
16. C. Ishiyama and Y. Higo, "Effects of humidity on young's modulus in poly (methyl methacrylate)," J. Polym. Sci., Part B: Polym. Phys. **40**(5), 460–465 (2002).
17. C. Baker, S. Gao, L. Chen, and X. Bao, "Self-inscribed antisymmetric long-period grating in a dual-core as2se3-pmma fiber," Opt. Express **25**(11), 12409–12414 (2017).
18. C. Baker and M. Rochette, "A generalized heat-brush approach for precise control of the waist profile in fiber tapers," Opt. Mater. Express **1**(6), 1065–1076 (2011).
19. C. Zhang, W. Li, X. Bao, L. Chen, and M. Du, "Tensile strain dependence of the brillouin gain spectrum in carbon/polyimide coated fibers," Opt. Lett. **32**(17), 2565–2567 (2007).
20. L. Tartara, C. Codemard, J.-N. Maran, R. Cherif, and M. Zghal, "Full modal analysis of the brillouin gain spectrum of an optical fiber," Opt. Commun. **282**(12), 2431–2436 (2009).
21. B. Saxena, C. Baker, X. Bao, and L. Chen, "Simultaneous generation of guided-acoustic-wave brillouin scattering and stimulated-brillouin-scattering in hybrid as 2 se 3-pmma microtapers," Opt. Express **27**(10), 13734–13743 (2019).
22. S. Dasgupta, F. Poletti, S. Liu, P. Petropoulos, D. J. Richardson, L. Grüner-Nielsen, and S. Herstrøm, "Modeling brillouin gain spectrum of solid and microstructured optical fibers using a finite element method," J. Lightwave Technol. **29**(1), 22–30 (2011).
23. C. Sabatier, S. Girard, L. Mescia, A. Ladaci, T. Robin, B. Cadier, A. Boukenter, Y. Ouerdane, and E. Marin, "Combined experimental and simulation study of the fiber composition effects on its brillouin scattering signature," J. Lightwave Technol. **37**(18), 4619–4624 (2019).
24. J.-C. Beugnot, R. Ahmad, M. Rochette, V. Laude, H. Maillotte, and T. Sylvestre, "Tunable stimulated brillouin scattering in hybrid polymer-chalcogenide tapered fibers," in *Nonlinear Optics and Its Applications VIII; and Quantum Optics III*, vol. 9136 (International Society for Optics and Photonics, 2014), p. 91360O.
25. A. N. Norris, "An inequality for longitudinal and transverse wave attenuation coefficients," J. Acoust. Soc. Am. **141**(1), 475–479 (2017).
26. S. Chaki and G. Bourse, "Guided ultrasonic waves for non-destructive monitoring of the stress levels in prestressed steel strands," Ultrasonics **49**(2), 162–171 (2009).
27. M. Brassington, A. Miller, and G. Saunders, "Higher order elasticity of amorphous as2s3," Philos. Mag. B **43**(6), 1049–1063 (1981).
28. W. Zou, Z. He, A. D. Yablon, and K. Hotate, "Dependence of brillouin frequency shift in optical fibers on draw-induced residual elastic and inelastic strains," IEEE Photonics Technol. Lett. **19**(18), 1389–1391 (2007).
29. P. Anderson and A. Varshneya, "Stress-optic coefficient of ge as se chalcogenide glasses," J. Non-Cryst. Solids **168**(1-2), 125–131 (1994).
30. S. Gao, C. Baker, L. Chen, and X. Bao, "Approach for temperature-insensitive strain measurement using a dual-core as 2 se 3-pmma taper," Opt. Lett. **43**(7), 1523–1526 (2018).
31. M. Nikles, L. Thevenaz, and P. A. Robert, "Brillouin gain spectrum characterization in single-mode optical fibers," J. Lightwave Technol. **15**(10), 1842–1851 (1997).

Optics EXPRESS

32. Q. Yu, X. Bao, and L. Chen, "Strain dependence of brillouin frequency, intensity, and bandwidth in polarization-maintaining fibers," Opt. Lett. **29**(14), 1605–1607 (2004).
33. H. Wang, S. Gao, C. Baker, Y. Wang, L. Chen, and X. Bao, "Stimulated brillouin scattering in a tapered dual-core as 2 se 3-pmma fiber for simultaneous temperature and strain sensing," Opt. Lett. **45**(12), 3301–3304 (2020).

# 6 Experimental investigation of SBS in high-birefringence chalcogenide-PMMA microfibers

Reproduce from :
**Haiyang Wang**, Song Gao, Chams Baker, Yuan Wang,
Liang Chen and Xiaoyi Bao,
Optics Letter. 45(12), 3301-3304 (2020) ;
https ://doi.org/10.1364/OL.391734 ;

## Author contributions

X.B. preformed the initial idea of the experiment ; H.W. designed and conceived the experiment ; H.W. and X.B. and L.C. analyzed experimental data ; H.W. and X.B. wrote the paper ; H.W., S.G., and C.B. fabricated chalcogenide microfibers ; H.W. and Y.W. developed experimental setup ; All authors discussed experimental and calculated results and provided feedback on the paper. X.B. supervised all aspects of this project.

Reproduce from :
**Haiyang Wang**, Chams Baker, Liang Chen and Xiaoyi Bao,
Optics Letter. 46(5), 945-948. (2021) ;
https ://doi.org/10.1364/OL.418137

## Author contributions

H.W. and C.B. performed experimental observations and characterizations ; H.W., X.B., C.B. and L.C. performed analysis ; H.W., C.B. and X.B. wrote the paper ; C.B. and H.W. fabricated chalcogenide microfibers ; H.W. designed experimental setup and performed numerical simulation ; X.B. supervised the overall project ;

We thank Dr. Bhavaye Saxena for providing the initial code of Brillouin scattering simulation.

## 6.1 SBS in a dual-core chalcogenide-PMMA microfiber for simultaneous temperature and strain sensing

### Summary

The previous chapter demonstrated the single-core chalcogenide-PMMA microfiber for wide-range strain Brillouin sensing. The single-core microfiber with one dominated acoustic mode can only be utilized for single parameter sensing. The chalcogenide-PMMA microfiber is sensitive to temperature variation. Temperature change affects the accuracy of strain measurement owing to the strain–temperature cross-sensitivity effect on Brillouin frequency shift (BFS). Discrimination of strain and temperature Brillouin sensing requires different responses of two acoustic modes, which can stem from two polarization axes of birefringence fibers. High-birefringence dual-core microfibers can be produced thanks to the design flexibility of chalcogenide-PMMA fibers. Due to an order of magnitude difference in thermal-expansion coefficients between the chalcogenide cores and the PMMA cladding [156], temperature and strain sensitivities are decorrelated by thermally induced strain on the cores. The asymmetric core geometry of the dual-core microfiber indicates different BFS responses to temperature or strain in two polarization axes. The following section presents stimulated Brillouin scattering (SBS) in the dual-core chalcogenide microfiber and its application in simultaneous temperature and strain Brillouin sensing. SBS characterizations in dual-core microfibers can be analyzed using the Brillouin model presented in Chapter 4 as a reference.

# Stimulated Brillouin scattering in a tapered dual-core $As_2Se_3$-PMMA fiber for simultaneous temperature and strain sensing

HAIYANG WANG[1], SONG GAO[1], CHAMS BAKER[1], YUAN WANG[1], LIANG CHEN[1], AND XIAOYI BAO[1]

[1]University of Ottawa, Department of Physics, Ottawa, Ontario K1G 6N5, Canada

Compiled September 9, 2022

**Chalcogenide fibers are currently being widely used in nonlinear optical signal processing as they exhibit ultrahigh nonlinearity. Here, we propose a sensor based on stimulated Brillouin scattering (SBS) for simultaneous temperature and strain measurement in a dual-core tapered $As_2Se_3$-Polymethyl methacrylate ($As_2Se_3$-PMMA) fiber using a Brillouin optical time-domain analysis (BOTDA) system. Different Brillouin frequency responses under temperature and strain variations and the separation of Brillouin frequency shifts (BFS) in two principal polarization axes are demonstrated experimentally over a 50 cm-long tapered dual-core hybrid microfiber. The temperature coefficients are -3.8272 MHz/°C and -3.3302 MHz/°C, and the strain coefficients are -0.06143 MHz/$\mu\epsilon$ and -0.03463 MHz/$\mu\epsilon$. Due to the different temperature and strain dependences of Brillouin frequency peaks in two polarizations, temperature and strain resolutions of 1 °C and 33 $\mu\epsilon$ are realized respectively. Numerical simulations are also reported to account for the BFS difference in two polarization axes.** 

http://dx.doi.org/10.1364/ao.XX.XXXXXX

## 1. INTRODUCTION

$As_2Se_3$ glass has nonlinearity hundreds of times larger than that of silica [1]. Hybrid fibers achieved by coating PMMA on the $As_2Se_3$ wire to provide sufficient mechanical robustness and flexibility allow the fabrication of taper with diameters at the sub-wavelength scale [2, 3]. Hybrid $As_2Se_3$-PMMA microtapers were fabricated and ultrahigh nonlinearity up to $\gamma$=133 $(Wm)^{-1}$ was measured in [4]. Beugnot *et al*. investigated SBS in PMMA-coated $As_2Se_3$ optical microfibers and reported both the reduction and control of the Brillouin shift [5]. The $As_2Se_3$-PMMA hybrid fiber is also a good candidate for load measurement due to the lower value of Young's modulus. Transverse load sensor based on SBS in a single-core $As_2Se_3$-PMMA microtaper was reported by Saxena *et al*. [6]. However, the sensing performance of the single-core hybrid fiber sensor can be affected by cross environmental variations such as temperature and strain. Some solutions based on SBS have been proposed for multi-parameter sensing to improve sensing accuracy. A multi-parameter sensor based on the unique sharp index profile of an inverse-parabolic graded-index fiber (IPGIF) was achieved due to multiple spaced Brillouin peaks which provide the availability of abundant choices of different sensitivities to environmental variables [7]. Another multi-parameter fiber sensor was reported by using SBS in a microstructure fiber (MSF) due to the dependence of the Brillouin spectrum of the high birefringence on optical polarizations [8]. Dual-core hybrid microtapers for two parameters sensing by measuring wavelength shifts for a particular minimum in both axes have been demonstrated in [9, 10]. Those measurements are based on the optical spectrum analyzer (OSA), which has limited resolution leading to a lower temperature and strain resolution ($\sim$60 GHz/°C and $\sim$1 GHz/$\mu\epsilon$). On the other hand, Brillouin frequency can be measured by the accuracy of 1 MHz, which has a resolution of hundreds of times better than the OSA accuracy of 0.02 nm corresponding to 2.5 GHz. Here, we are exploring the possibility of SBS for both temperature and strain in tapered dual-core $As_2Se_3$-PMMA fiber based on BOTDA. To the best of our knowledge, the dual-core hybrid fiber has never been reported in sensing based on SBS. Due to the ultrahigh nonlinear coefficient of dual-core $As_2Se_3$-PMMA microtaper compared with IPGIF and MSF, the low power requirement in pump and Stokes waves for SBS generation makes it a promising candidate for dual-parameter Brillouin sensing.

In this letter, we demonstrate the dependence of Brillouin frequency responses on two principal polarization axes to realize simultaneous temperature and strain measurement in a 50 cm-long tapered dual-core $As_2Se_3$-PMMA hybrid fiber with a core diameter of 2 $\mu m$ based on a BOTDA system. The experimental results show that the temperature coefficients are -3.8272 $\pm$ 0.08586 MHz/°C and -3.3302 $\pm$ 0.05673 MHz/°C, and the strain coefficients are -0.06143 $\pm$ 0.00042 MHz/$\mu\epsilon$ and -0.03463 $\pm$ 0.00145 MHz/$\mu\epsilon$. The maximum errors for temperature and strain measurements are calculated to be 1 °C and 33 $\mu\epsilon$, respectively. Numerical simulations, including the mode profiles, kinetic energy densities and the separation of BFS in two polarizations, are also demonstrated.

## 2. FABRICATION

The dual-core hybrid taper is fabricated from an assembly, including two $As_2Se_3$ fibers and a PMMA tube, which is heat-softened by a heater. The PMMA tube is collapsed caused by the surface tension on the $As_2Se_3$ fibers to obtain an $As_2Se_3$-PMMA perform, which is drawn to a hybrid fiber. The cross-section of a polished dual-core $As_2Se_3$-PMMA fiber is shown in Fig. 1(a). The ends of SMFs are angle polished and butt-coupled to one core of the dual-core hybrid fiber with different polished angles. The butt-coupling interfaces are permanently fixed using UV-cured epoxy. Angle coupling can suppress Fresnel reflection at the interfaces between SMFs and the hybrid fiber, and maximize the transmission coefficient. The hybrid fiber is then tapered using heat-brush method [11]. Figure 1(b) shows a dual-core $As_2Se_3$-PMMA taper, including a waist length of $L = 50$ cm, a core diameter of $D_{As_2Se_3} = 2\,\mu$m and a cladding diameter of $D_{PMMA} = 113\,\mu$m. When the light launches into one of the two cores, they continuously couple between the cores; as a result, both of the symmetric (even mode) and antisymmetric (odd mode) supermodes are excited in the fiber, and they have different propagation constants.

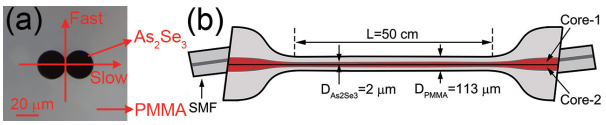


**Fig. 1.** (a) Cross-section of a polished dual-core $As_2Se_3$-PMMA hybrid fiber; (b) Configuration of angle-coupled tapered dual-core $As_2Se_3$-PMMA hybrid fiber and SMFs.

## 3. SIMULATION

Finite-element method (FEM) simulations of a dual-core $As_2Se_3$-PMMA microtaper with a core diameter of $2\,\mu m$ are demonstrated. Figure 2(a)-(d) show four supermode profiles of the dual-core fiber, including even mode and odd mode for each of two polarization axes. The odd mode and even mode in slow axis exhibit effective refractive index $n_s^o = 2.6150$ and $n_s^e = 2.6197$, respectively, and the two modes in fast axis exhibit effective refractive index $n_f^o = 2.6141$ and $n_f^e = 2.6198$, respectively. The frequency shift in the SBS process is given by

$$v_{B,j} = \frac{2n_j^i V_a}{\lambda_p} \tag{1}$$

where $v_{B,j}$ is the BFS, $i$ is the odd or even mode, $j$ is the fast axis or slow axis, $V_a$ is the acoustic phase velocity (for $As_2Se_3$, $V_a = 2250$ ms$^{-1}$ [12]) and $\lambda_p$ is the pump wavelength. The SBS spectrum originates from the interaction of even mode and odd mode with acoustic field through electrostriction as two modes in the same polarization propagate in the fiber. The separation of BFS in two polarization axes $\Delta v_B \approx 2.2$ MHz.

SBS spectra based on elastodynamics equation that governs the interaction of optical fields with acoustic field are calculated, as defined by

$$\rho \frac{\partial u_i^2}{\partial t^2} - [c_{ijkl} u_{k,l} + \eta_{ijkl} \frac{\partial u_{k,l}}{\partial t}]_{,j} = -T_{ij,j}^{es} \tag{2}$$

where $\rho$ is the material density, $u_i$ is the displacement field, $c_{ijkl}$ and $\eta_{ijkl}$ are the rank-4 elastic and viscosity tensors respectively, $T_{ij}^{es} = -\epsilon_0 \chi_{klij} E_k E_l^*$ is the electrostriction stress (ES) tensor in the presence of electrical fields of the optical pump and Stokes wave $E_k$ and $E_l$, with $\chi_{klij} = \epsilon_{im}\epsilon_{jn} p_{klmn}$ and $p_{klmn}$ is the rank-4 photoelastic tensor. Here, elastic losses are incorporated into the elastodynamic equation by considering a complex elastic tensor $c_{ij} + i\omega\eta_{ij}$. Assuming $\eta_{ij} = c_{ij}/Q_f$, where $Q_f$ is the product of quality factor Q and frequency f. This $Q_f$ product is assumed to be a constant for a given material. For SBS, both energy and momentum must be conserved. The frequency and wave vector of acoustic wave are given by $\omega = \omega_1 - \omega_2$ and $k = k_1 - k_2$, where $\omega_1$ and $k_1$ are the central frequency and wave vector of the pump and $\omega_2$ and $k_2$ are the central frequency and wave vector of the Stokes. If the pump and Stokes wave are counter-propagating in the fiber, a situation of SBS, $k \approx 2k_1$. As there is only one source term at frequency $\omega$ and wave vector $k$, the following ansatz is assumed for the acoustic wave.

$$u_i(r, z; t) = u_i(r) e^{i(kz - \omega t)} \tag{3}$$

where the displacement field $u_i(r)$ is the transverse profile of the acoustic wave. The elasticdynamtic equation can be simplified using Green's theorem and Galerkin FEM procedure in [13]. The field is calculated by setting $k = 2k_1$. The Brillouin spectra for the dual-core $As_2Se_3$-PMMA microtaper are obtained by calculating kinetic energy of the acoustic wave as a function of detuning frequency between the two optical fields, as defined by

$$E = \frac{1}{4} \iint_\sigma \rho\omega^2 u_i(r)^* u_i(r) \mathrm{d}r \tag{4}$$

The kinetic energy distributions for selected frequencies of the dual-core $As_2Se_3$-PMMA fiber, shown in Fig. 2(e)-(h), are confined within two $As_2Se_3$ cores because the acoustic impedance mismatch between $As_2Se_3$ cores and PMMA cladding (for PMMA, $V_a = 2690$ ms$^{-1}$ [14]). The light interaction is complex for the hybrid taper with a core diameter of $2\,\mu m$ because a strong coupling of shear and longitudinal displacements is induced in such a fiber at sub-wavelength scale [15]. The me-

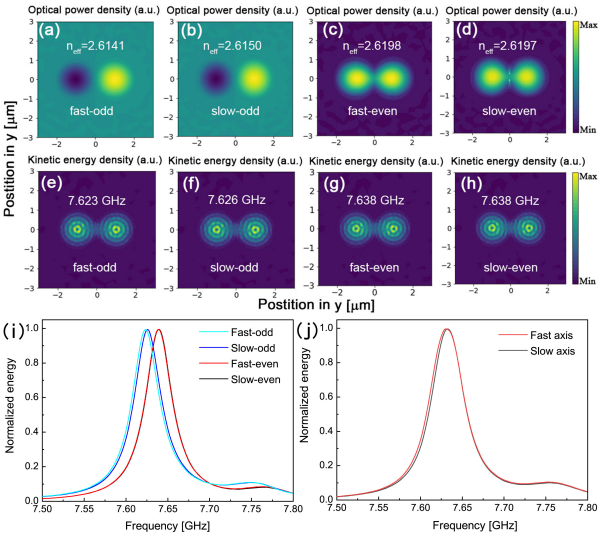


**Fig. 2.** Numerical simulations of the daul-core micortaper: (a)-(d) Four optical supermodes; (e)-(h) Kinetic energy density for selected frequencies in the presence of different modes; (i) SBS spectra of four modes; (j) SBS spectra in two polarization axes.

chanical ripples in the cores are due to the interference between the transverse and longitudinal acoustic waves that are both generated in this microtaper. The kinetic energy distributions are the same due to the elastodynamic model mainly relies on the nonlinear electrostrictive force $T_{ij} = \chi_{klij} E_k E_l^*$. Figure 2(i) shows the simulation SBS spectra of the four supermodes as a function of detuning frequency. Due to both of even and odd modes propagate in the fiber, the resulting spectra are the combination of the two modes in each of the fast and slow axes. The overlap spectra in two polarization axes are plotted in Fig. 2(j). We can see the Brillouin frequency separation in two polarization axes $\Delta v_B = 2$ MHz. Figure 2(j) also shows secondary peaks around 7.75 GHz as a result of acoustic impedance mismatch between $As_2Se_3$ cores and PMMA cladding.

## 4. EXPERIMENTAL RESULTS

Before testing SBS, the interference spectra are measured to ensure that the coupling between cores in the dual-core fiber. The transmission spectra of the microtaper in two polarization axes are plotted in Fig. 3. The minimum is observed when the effective refractive index difference of even mode and odd mode satisfies the condition $\phi_d(\lambda) = 2\pi\Delta n_{eff} L_w/\lambda = (2m+1)\pi$, where $\Delta n_{eff}$ is the effective refractive index difference between the even mode and odd mode, $L_w$ is the taper length and m is an integer. Due to the difference in propagation constants between odd and even modes in two polarization axes, two spectra exhibit different periodic oscillations.

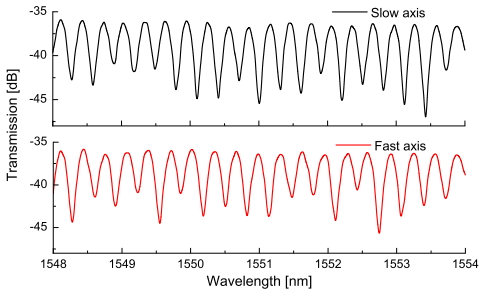


**Fig. 3.** Interference spectra of fast and slow polarization axes in a 50 cm-long dual-core taper with a core diameter of 2 $\mu m$.

Since OSA can only measure continuous wave response of dual-core tapered fiber for its temperature and strain responses without location information, a BOTDA system is used for temperature and strain sensing. Here, we are exploring BOTDA for two purposes: 1) Pulse signal gives location information; 2) The Brillouin frequency can be measured at an accuracy of 1 MHz instead of the OSA accuracy of ~GHz. BOTDA setup is illustrated in Fig. 4. Incoming light from a laser operating at 1550 nm is split into two paths by a fiber coupler (FC). The upper branch transfers light into high extinction ratio pump pulse with 20 ns bandwidth using two electro-optic modulators (EOM) driven by a dual-channel function generator (FG). The pulse is then amplified by an Erbium-doped-fiber-amplifier (EDFA) and then amplified spontaneous emission (ASE) is filtered out by a tunable filter. The tapered dual-core $As_2Se_3$-PMMA fiber allows only 8 dBm peak power for SBS generation due to its small core diameter and ultrahigh nonlinear coefficient. The EOM in the lower branch generates two sidebands and the higher frequency sideband is then filtered out by a narrow filter, and only the lower frequency sideband remains as the Stokes wave whose frequency can be swept by a radio frequency (RF) generator. The two polarization controllers (PC) are used to change the polarization states of pump pulse and Stokes wave to make sure that they are copolarized along the microtaper in two principal polarization axes.

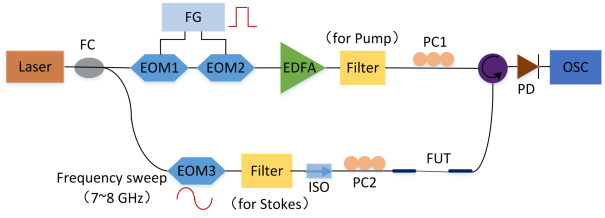


**Fig. 4.** BOTDA Setup for tapered dual-core $As_2Se_3$-PMMA fiber; FC: Fiber Coupler; EOM: Electro-Optic Modulator; FG: Function Generator; EDFA: Erbium-Doped-Fiber-Amplifier; PC: Polarization Controller; ISO: Isolator; FUT: Fiber under test; PD: Photo-diode; OSC: Oscilloscope.

Figure 5(a) shows Brillouin gain spectra in two polarization axes of the dual-core tapered $As_2Se_3$-PMMA fiber. As can be seen, the Brillouin frequency separation between two polarization axes is $\Delta v_B = 3$ MHz, in good agreement with the simulation result; in addition, the spectral width of the Brillouin gain is ~75 MHz (FWHM) in dual-core microtaper which is broader than that of single-core microtaper with the same core diameter(~60 MHz) [16]. This can be understood by noting that the resulting spectrum is the overlap of different SBS spectra originating from the electrostriction through individual even mode and odd mode in each polarization axis. The secondary peaks shown in simulations are not measured in two polarization axes as the low peak power of the pump pulse and most of the power from the pump is transferred to the main Brillouin peak. Measured and simulated shifts of the two Brillouin frequency peaks in two polarization axes of the dual-core $As_2Se_3$-PMMA microtaper are shown in Table 1. The BFS between simulations and experimental results are slightly different as 10% error for the core diameter and the distance between cores when fabricating the dual-core fiber. Figure 5(b) and Figure 5(c) show the distributed Brillouin spectra in fast axis and slow axis, respectively, obtained by controlling the state of polarizations of pump pulse and Stokes wave. We can identify the Brillouin frequency shifts at any position of the fiber over the taper length from the two distributed spectra. The intensity is the largest at the center range because the 50 cm-long dual-core fiber is fully cov-

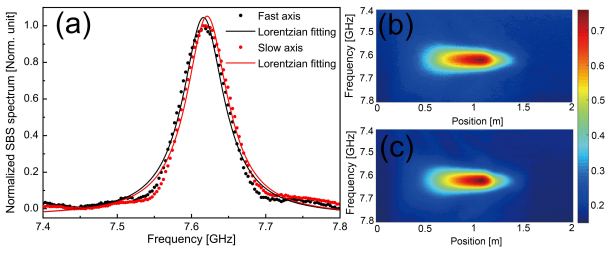


**Fig. 5.** (a) Experimental Brillouin spectrum of the dual-core $As_2Se_3$-PMMA fiber; (b) BOTDA trace for the Stokes wave in fast axis; (c) BOTDA trace for the Stokes wave in slow axis.

ered by the pump pulse with 20 ns bandwidth. The dual-core $As_2Se_3$-PMMA taper can measure temperature variation due to the large thermally induced strain on the $As_2Se_3$ cores by the PMMA cladding. The taper can be applied for strain sensing due to the lower value of Young's modulus. Two polarization axes have different Brillouin frequency responses to temperature and strain because of the asymmetric geometrical structure of the dual-core hybrid fiber. We can thus use the dual-core fiber to measure temperature and strain simultaneously.

**Table 1. Measured and simulated Brillouin frequency peaks, and temperature and strain coefficients in two axes of the dual-core $As_2Se_3$-PMMA taper.**

| | Fast axis | Slow axis |
|---|---|---|
| Measured Brillouin peak (GHz) | 7.616 | 7.619 |
| Simulated Brillouin peak (GHz) | 7.631 | 7.633 |
| Temperature coefficient (MHz/°C) | -3.8272 | -3.3302 |
| Strain coefficient (MHz/$\mu\epsilon$) | -0.06143 | -0.03463 |

The dual-core $As_2Se_3$-PMMA microtaper is placed in the oven to measure the temperature sensing performance and the strain is induced by fixing the fiber in the linear translation stages which can be adjusted at steps of 15 $\mu m$ corresponding to the strain of 300 $\mu\epsilon$ for the fiber length of 50 cm. The dependence of BFS on temperature and strain variations in two polarizations are plotted in Fig. 6. Figure 6(a) shows the temperature coefficients in fast and slow axes are -3.8272 MHz/°C and -3.3302 MHz/°C, respectively. The BFS of the dual-core taper under temperature variation are due to the large thermally induced strain on cores by cladding resulting from the large diameter difference in core and cladding (1/56), and the different thermal expansion coefficients between $As_2Se_3$ core and PMMA cladding ($\alpha_{As_2Se_3}$=0.2×10$^{-4}$/°C [17] and $\alpha_{PMMA}$=2.02×10$^{-4}$/°C [18]). The Brillouin frequency decreases as the temperature increases due to the negative strain optic coefficient of chalcogenide glass [19]. Figure 6(b) shows the similar BFS under strain variations and the strain coefficients in fast and slow axes are -0.06143 MHz/$\mu\epsilon$ and -0.03463 MHz/$\mu\epsilon$, respectively. The strain measurement verifies that the BFS under temperature variation is dominated by thermally induced strain. The temperature and strain coefficients in fast and slow axes are shown in Table 1. The errors of the temperature in two polarization axes are ± 0.08586 MHz/°C and ± 0.05673 MHz/°C and the errors of the strain are ± 0.00042 MHz/$\mu\epsilon$ and ± 0.00145 MHz/$\mu\epsilon$.

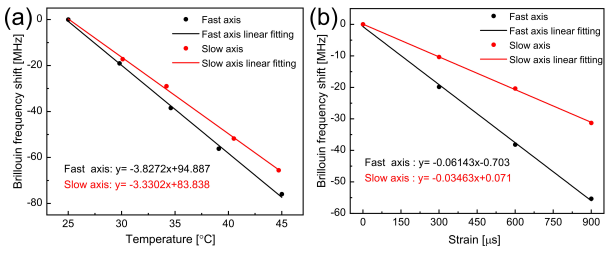


**Fig. 6.** Measured BFS as a function of (a) temperature and (b) strain in fast and slow axes of the dual-core hybrid $As_2Se_3$-PMMA microtaper.

The BFS in fast axis and slow axis can be expressed as $\Delta\nu_{B,i} = C_i^T\Delta T + C_i^\epsilon\Delta\epsilon$, where $i$=$f$ or $s$. A character matrix $M_{T,\epsilon}$ is defined to express these relations

$$\begin{bmatrix} \Delta\nu_{B,f} \\ \Delta\nu_{B,s} \end{bmatrix} = M_{T,\epsilon}\begin{bmatrix} \Delta T \\ \Delta\epsilon \end{bmatrix} = \begin{bmatrix} C_f^T & C_f^\epsilon \\ C_s^T & C_s^\epsilon \end{bmatrix}\begin{bmatrix} \Delta T \\ \Delta\epsilon \end{bmatrix} \quad (5)$$

where $\Delta\nu_{B,f}$ and $\Delta\nu_{B,s}$ represent the frequency shift of Brillouin gain spectra in fast and slow axes, $\Delta T$ and $\Delta\epsilon$ are temperature and strain variations, $C_f^T$ and $C_s^T$ are temperature sensitivity coefficients, and $C_f^\epsilon$ and $C_s^\epsilon$ are strain sensitivity coefficients. The character matrix $M_{T,\epsilon}$ can be used for simultaneous temperature and strain sensing because of the decorrelated temperature and strain coefficients in the two polarization axes. The maximum errors for temperature and strain are then estimated to be 1 °C and 33 $\mu\epsilon$, respectively.

In conclusion, We have calculated and experimentally demonstrated a Brillouin sensor for simultaneous temperature and strain measurement in a tapered dual-core $As_2Se_3$-PMMA fiber based on BOTDA. Due to the asymmetric geometrical structure of the dual-core hybrid fiber, different Brillouin frequency responses are measured in two principal polarization axes, which can be applied to realize simultaneous temperature and strain sensing. This dual-core $As_2Se_3$-PMMA hybrid microtaper opens another way based on stimulated Brillouin scattering for simultaneous temperature and strain measurement.

**Funding.** Canada Research Chairs (75-67138); Natural Sciences and Engineering Research Council of Canada (NSERC) (06071-RGPIN-2015); China Scholarship Council (CSC).

**Acknowledgement.** The authors are thankful to Coractive Inc. for providing the $As_2Se_3$ multimode fiber

**Disclosures.** The authors declare no conflicts of interest.

## REFERENCES

1. G. Lenz, J. Zimmermann, T. Katsufuji, M. Lines, H. Hwang, S. Spälter, R. Slusher, S.-W. Cheong, J. Sanghera, and I. Aggarwal, Opt. Lett. **25**, 254 (2000).
2. C. Baker, S. Gao, L. Chen, and X. Bao, Opt. express **25**, 12409 (2017).
3. R. Ahmad, M. Rochette, and C. Baker, Opt. letters **36**, 2886 (2011).
4. C. Baker and M. Rochette, Opt. express **18**, 12391 (2010).
5. J.-C. Beugnot, R. Ahmad, M. Rochette, V. Laude, H. Maillotte, and T. Sylvestre, Opt. letters **39**, 482 (2014).
6. B. Saxena, C. Baker, X. Bao, and L. Chen, Opt. Lett. **44**, 4789 (2019).
7. Y. Xu, M. Ren, Y. Lu, P. Lu, X. Bao, L. Wang, Y. Messaddeq, and S. LaRochelle, Opt. letters **41**, 1138 (2016).
8. A. Minardo, R. Bernini, W. Urbanczyk, J. Wojcik, N. Gorbatov, M. Tur, and L. Zeni, Opt. letters **33**, 2329 (2008).
9. S. Gao, C. Baker, L. Chen, and X. Bao, IEEE Photonics Technol. Lett. **30**, 79 (2017).
10. S. Gao, C. Baker, L. Chen, and X. Bao, IEEE Photonics Technol. Lett. **30**, 1155 (2018).
11. C. Baker and M. Rochette, Opt. Mater. Express **1**, 1065 (2011).
12. K. S. Abedin, Opt. express **14**, 4037 (2006).
13. J.-C. Beugnot and V. Laude, Phys. Rev. B **86**, 224304 (2012).
14. B. Hartmann and J. Jarzynski, J. applied physics **43**, 4304 (1972).
15. J.-C. Beugnot, S. Lebrun, G. Pauliat, H. Maillotte, V. Laude, and T. Sylvestre, Nat. communications **5**, 1 (2014).
16. B. Saxena, C. Baker, X. Bao, and L. Chen, Opt. express **27**, 13734 (2019).
17. J. Sanghera and I. Aggarwal, J. Non-Crystalline Solids **256**, 6 (1999).
18. X. Li, Z. Cao, Q. Shen, and Y. Yang, Mater. Lett. **60**, 1238 (2006).
19. P. Anderson and A. Varshneya, J. non-crystalline solids **168**, 125 (1994).

## 6.2 SBS in elliptical-core chalcogenide-PMMA microfibers

### Summary

The previous section demonstrated SBS in dual-core chalcogenide-PMMA microfibers. It is challenging to observe the relationship between birefringence and BFS owing to the high-order modes of the dual-core microfiber. High-birefringence elliptical-core chalcogenide-PMMA microfibers can be designed to study the effect of birefringence on Brillouin gain spectra and BFS difference. The birefringence can be tailored by tapering the elliptical-core microfiber to different diameters. The following section presents SBS characterizations in high-birefringence elliptical-core chalcogenide microfibers. The birefringence and polarization-extinction ratio of the elliptical-core microfibers with different core diameters are measured. We compare the calculated BFS difference to the measured BFS difference for the elliptical-core microfibers. Brillouin gain spectra can be shaped and controlled in elliptical-core chalcogenide microfibers, as demonstrated in the following section. Both experimental and numerical results show that high birefringence induces large BFS difference between two polarization axes for the intramode SBS of LP01-LP01. Furthermore, the intermode SBS of LP01-LP11 is demonstrated in the elliptical-core microfiber with a large core diameter.

# Stimulated Brillouin scattering in high-birefringence elliptical-core $As_2Se_3$-PMMA microfibers

HAIYANG WANG[1], CHAMS BAKER[1], LIANG CHEN[1], AND XIAOYI BAO[1]

[1]University of Ottawa, Department of Physics, Ottawa, Ontario K1N 6N5, Canada

Compiled September 9, 2022

**In this paper, we design and fabricate elliptical-core (ECORE) chalcogenide-polymethyl methacrylate ($As_2Se_3$-PMMA) microfibers to explore birefringence impact on stimulated Brillouin scattering. Numerical simulations based on the finite-element method and elastodynamic equation are utilized to calculate the phase and group birefringence and Brillouin gain spectra of the fundamental mode in three ECORE $As_2Se_3$-PMMA microfibers at different core diameters. Experimentally measured and numerically calculated results show that as the core diameter of the minor axis of an ECORE microfiber with a ratio of 1.108 is reduced from 1.50 μm to 0.87 μm, a high group birefringence of $\sim 10^{-3}$ to $\sim 10^{-2}$ and a large Brillouin frequency shift difference of ∼6 MHz to ∼30 MHz are achieved, while the Brillouin gain spectra are broadened significantly from ∼70 MHz to ∼140 MHz. The high-birefringence ECORE $As_2Se_3$-PMMA microfiber is important for Brillouin sensing due to the tailorable high birefringence and ultrahigh nonlinearity.** 

http://dx.doi.org/10.1364/ao.XX.XXXXXX

## 1. INTRODUCTION

Polarization-maintaining fibers (PMF) have attracted attention in optical fiber sensors and fiber lasers due to the strong birefringence and the ability to preserve the polarization state of propagating light. The high birefringence of PMFs is achieved by making the core shape elliptical or by adding stress rods on both sides of a circular core as is the case in PANDA fibers [1] and bow-tie fibers [2]. Stimulated Brillouin scattering (SBS) has been investigated in elliptical-core (ECORE) PMFs [3] and stress-induced PMFs [4–6] made from silica glass. Sensing based on Brillouin dynamic grating (BDG) has been proposed and demonstrated in silica-based PMFs [7, 8]. Due to the small nonlinearity of silica glass, a high pump power > 20 dBm is required for SBS generation. To investigate SBS at a low pump power, PMFs with high nonlinearity materials are required. Recently, an ultrahigh nonlinearity of $\gamma$=133 $(Wm)^{-1}$ has been demonstrated in an $As_2Se_3$-PMMA microfiber with a core diameter of 0.8 μm [9], which is $\sim 10^4$ times larger than that of silica-based fibers. SBS generation in 50 cm long $As_2Se_3$-PMMA microfibers has been achieved at a low pump power of 8 dBm [10, 11]. To the best of our knowledge, Brillouin scattering in ECORE chalcogenide microfiber has never been reported. Here, we design and fabricate a high-birefringence ECORE $As_2Se_3$-PMMA fiber with sub-wavelength diameters to characterize the Brillouin gain spectra. The ECORE microfiber with a high birefringence is good for dual-parameter sensing based on fast and slow axes detection using the Brillouin spectrum, as it has less spectral shape distortion due to the large BFS separation between fundamental mode and high order modes. For low-birefringence silica-based ECORE fiber, its small BFS separation leads to distorted Brillouin spectrum. In addition, the ECORE microfiber with tailorable Brillouin gain spectra and ultrahigh nonlinearity is helpful in improving Brillouin sensing resolution at a low pump power.

In this letter, we experimentally characterize and numerically investigate birefringence impact on SBS in tapered ECORE $As_2Se_3$-PMMA microfibers using Brillouin optical time-domain analysis (BOTDA) and the finite-element method (FEM). Three ECORE $As_2Se_3$-PMMA microfibers with a ratio of 1.108 at different minor-axis core diameters of 1.50 μm, 1.05 μm and 0.87 μm are designed and fabricated, and the group birefringence and Brillouin gain spectra for the fundamental mode of $LP_{01}$ are experimentally measured and numerically calculated. Both experimental and numerical results show that the group birefringence, BFS difference, and Brillouin linewidth increase as the core diameter decreases. A high group birefringence of $\sim 10^{-2}$ and a large BFS difference of ∼30 MHz are calculated and measured for the ECORE $As_2Se_3$-PMMA microfibers at the minor-axis core diameter of 0.87 μm.

The fabrication of the ECORE $As_2Se_3$-PMMA fiber is similar to that of dual-core $As_2Se_3$-PMMA fiber reported in Ref. [12]. To fabricate an ECORE $As_2Se_3$-PMMA preform, an assembly with two $As_2Se_3$ fibers and a PMMA tube is placed on a spinning mandrel and heated at 220 °C for four days. The long heating time ensures that two $As_2Se_3$ fibers are fused together to obtain a single fiber with an elliptical shape. Figure 1(a) shows the cross-section image of the polished end of an ECORE $As_2Se_3$-PMMA fiber. The major and minor axes of the fabricated ECORE fiber without tapering are $a = 29.13$ μm and $b = 26.30$ μm, respectively, and the ratio is $a/b = 1.108$. The ECORE fiber is angle-coupled with single-mode fibers (SMF) to minimize Fresnel reflections from the interfaces between the SMFs and the ECORE fiber. The ECORE fibers are then tapered to three different diameters using

the heat-brush method [13]. There are two tapering processes to make the ECORE fiber at sub-wavelength scale with a 50 cm waist length; 1) an ECORE $As_2Se_3$-PMMA fiber with a core diameter of $b$ =26.30 μm is tapered to $b$ =8 μm, as shown in Fig. 1(b); 2) the tapered fiber is drawn again to sub-wavelength scale, such as $b$ =1.50 μm, as shown in Fig. 1(c). ECORE microfiber A has a core diameter of $a$ =1.66 μm and $b$ =1.50 μm, a cladding diameter of $D_c$ =73.3 μm, and a waist length of $L_w$=50 cm. The parameter values for ECORE microfiber B are $a$ =1.16 μm, $b$ =1.05 μm, $D_c$ =55.6 μm, and $L_w$=50 cm, and for ECORE microfiber C are $a$ =0.96 μm, $b$ =0.87 μm, $D_c$ =41.8 μm, and $L_w$=50 cm. The total transmission loss of microfibers A, B, and C are ∼5.5 dB, ∼7 dB, and ∼9 dB, respectively. These microfibers are stable in air due to the large diameter of PMMA cladding, which allows SBS measurement at different temperatures and strains.

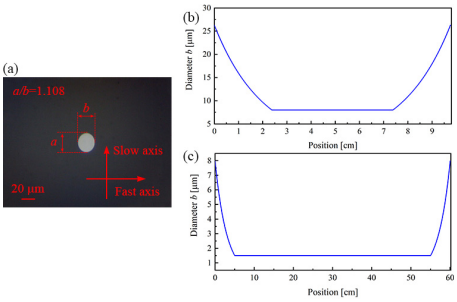


**Fig. 1.** (a) Cross-section image of the end of an elliptical-core $As_2Se_3$-PMMA fiber: $a$ =29.13 μm and $b$ =26.30 μm. (b) First tapering process. (c) Second tapering process.

The effective refractive index, phase and group birefringence, BFS and BFS difference of the $LP_{01}$ mode of ECORE microfibers with different minor-axis core diameters are calculated based on the FEM. The phase birefringence ($B_{phase}$) is defined by $B_{phase}$=$n_{slow} - n_{fast}$, where $n_{slow}$ and $n_{fast}$ are the effective refractive indices in slow and fast axes, respectively. The $B_{phase}$ is calculated as a function of $b$ at a ratio of $a/b$ = 1.108, as shown in Fig. 2(a). The value of $B_{phase}$ is significantly increased from $2\times10^{-3}$ to $2.5\times10^{-2}$ when $b$ is decreased from 1.8 μm to 0.6 μm. The elliptical-core microfiber at sub-wavelength scale has a large birefringence due to the light propagates in both core and cladding, which induces a rapid change of effective refractive index with small core diameter difference. Effective refractive index ($n_{eff}$) includes the contribution of the waveguide and material. When the boundary condition is changed, even though a/b is constant, $n_{fast}/n_{slow}$ is not constant, as it dependents on the eigenvalue of the modes for the core and cladding boundary instead of the ratio of elliptical core size. As a result, the birefringence will change accordingly, so does the Brillouin frequency separation between two polarization axes. The calculated $B_{phase}$ for ECORE microfibers A, B, and C are $2.5\times10^{-3}$, $6.7\times10^{-3}$, and $1.17\times10^{-2}$, respectively. The group birefringence ($B_{group}$) is defined by $B_{group}$=$n_{g,slow} - n_{g,fast} = B_{phase} - \lambda(\mathrm{d}B_{phase}/\mathrm{d}\lambda)$, where $n_{g,slow}$ and $n_{g,fast}$ are the group indices in slow and fast axes, respectively. The calculated $B_{group}$ for ECORE microfibers A, B, and C are $-4.4\times10^{-3}$, $-1.01\times10^{-2}$, and $-1.59\times10^{-2}$, respectively. The relationship between the BFS ($v_B$) and $n_{eff}$ is given by

$$v_B = \frac{2n_{eff}V_a}{\lambda_p} \quad \textbf{(1)}$$

where $V_a$ is the acoustic velocity ($V_a$ = 2261 $m/s$ for $As_2Se_3$ [10]) and $\lambda_p$ is the wavelength of the pump laser. The BFS difference ($\Delta v_B$) is then calculated from $B_{phase}$ using $\Delta v_B = 2B_{phase}V_a/\lambda_p$.

A numerical model of the interaction between optical fields and acoustic waves in Brillouin scattering is developed based on elastodynamic equation. The elastodynamic equation is

$$\rho\frac{\partial {u_i}^2}{\partial t^2} - [c_{ijkl}u_{k,l} + \eta_{ijkl}\frac{\partial u_{k,l}}{\partial t}]_{,j} = [\epsilon_0\chi_{klij}E_kE_l^*]_{,j} \quad \textbf{(2)}$$

where $\rho$ is the material density, $u_i$ is the displacement field, $c_{ijkl}$ and $\eta_{ijkl}$ are the rank-4 elastic and viscosity tensors, the right-hand side term is the electrostriction stress tensor with $E_k$ and $E_l$ being electrical fields of pump and probe waves, and $\chi_{klij} = \epsilon_{im}\epsilon_{jn}p_{klmn}$ with $p_{klmn}$ being the rank-4 photoelastic tensor. In the SBS process, the displacement field of an acoustic wave is calculated by setting the wave vector of the acoustic wave to $k = k_1 - k_2 \approx 2k_1$, where $k_1$ and $k_2$ are the wave vectors of pump and probe waves. Kinetic energy given by $E = \frac{1}{4}\int\int_\sigma \rho\omega^2 u_i(r)^* u_i(r)\mathrm{d}r$ is utilized to obtain SBS gain as a function of optical frequency. The simplification of the elastodynamic equation is presented in Ref. [14]. The parameter values of $As_2Se_3$ and PMMA used for the calculation are obtained from Ref. [15]. Figure 2(b) shows the numerically calculated BFS in fast and slow axes (circles) and BFS difference (squares) as a function of $b$ obtained by solving Eq. 2. Figure 2(b) also shows the analytically calculated BFS in fast and slow axes (solid lines), and BFS difference (dashed line) obtained using Eq. 1. With increased $b$, the BFS increases due to the increased effective refractive index, while the BFS difference decreases as large core diameter gives rise to low phase birefringence.

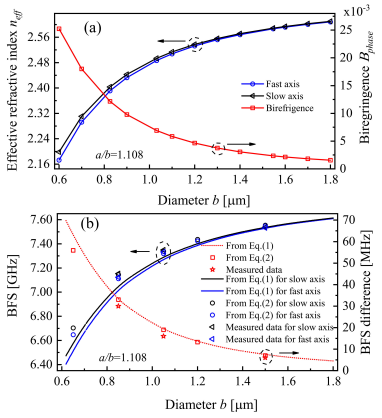


**Fig. 2.** (a) Calculated effective refractive index of fast and slow axes, and phase birefringence in ECORE microfiber as a function of core diameter $b$. (b) Calculated and measured FBS and BFS difference as a function of core diameter $b$.

Figure 3(a) presents a schematic setup for the measurement of group birefringence. Linearly polarized light after a polarization beam splitter (PBS) is aligned at 45° from the slow axis using a polarization controller (PC1) to excite equal power in two polarization axes. An interference spectrum is generated when the light passes the ECORE microfiber due to the wavelength-dependent phase difference in two polarization axes. The measured interference spectra are plotted in Fig. 3(c-e). The wavelength difference ($\Delta\lambda$) between two adjacent interference troughs for ECORE microfibers A, B and C are 1.05 nm, 0.5 nm and

0.27 nm, respectively. Group birefringence is calculated from $\Delta\lambda$ using $B_{group} = \lambda^2/(\Delta\lambda L_w)$. The measured group birefringence for ECORE microfibers A, B and C are $4.5\times10^{-3}$, $9.5\times10^{-3}$, and $1.77\times10^{-2}$, respectively. The measured and calculated group birefringence are summarized in Table 1. As the measured group birefringence using the interference spectrum is an absolute value, the measured and calculated group birefringence have opposite sign. The slight difference between the measured and calculated group birefringence is due to the error of the core diameter and the waist length induced by the tapering process. The polarization extinction ratio (PER) of the ECORE microfiber is investigated before measuring its Brillouin gain spectra. The PER is given by PER=10log$(P_{max}/P_{min})$, where $P_{max}$ is the maximum optical power in one polarization axis and $P_{min}$ is the minimum optical power in the other polarization axis. Figure 3(a,b) show a schematic of the experimental setup for measuring the PER of the ECORE microfibers. Linearly polarized light after the PBS is aligned with the slow axis or the fast axis of an ECORE microfiber using PC1. PC2 is utilized to align the polarization of the ECORE microfiber output with that of the free space polarizer which is set to 0 ° or 90 °. In this case, the minimum contrast of the interference spectrum and the maximum power in the slow axis or the fast axis are measured. The minimum output power in the slow axis or the fast axis is then measured by adjusting the polarizer to 90 ° or 0 °. The PERs in the fast and slow axes are 16.1 dB and 16.6 dB for ECORE microfiber A, 16.9 dB and 16.5 dB for ECORE microfiber B, 15.0 dB and 15.3 dB for ECORE microfiber C, respectively. In all cases, the PER is greater than 15 dB, which is large enough to maintain the polarization state of the propagating light in the ECORE microfibers.

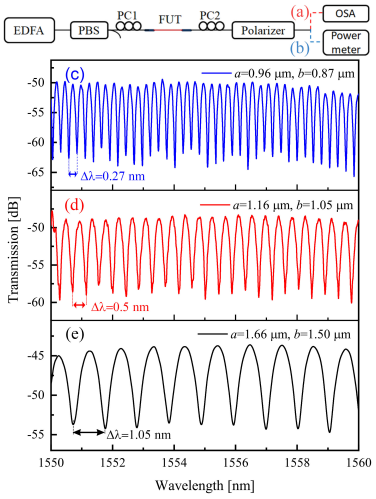


**Fig. 3.** (a,b) Experimental setup for measuring group birefringence and PER; EDFA: Erbium-doped-fiber-amplifier; PC: polarization controller; FUT: fiber under test; PBS: polarization beam splitter; OSA: optical spectrum analyzer. (c-e) The interference spectra of microfibers for different core diameters.

Figure 4 presents a schematic of the BOTDA setup for measuring the Brillouin spectra of the ECORE microfibers. The red path is utilized for the generation and amplification of high extinction ratio pump pulses with 20 ns duration and 9 dBm peak power. The blue path is utilized for the generation of the probe wave whose frequency is swept by controlling the radio frequency generator. The pump pulses and probe wave are injected into the opposite ends of the microfiber, and the SBS amplification is observed and measured using an oscilloscope (OSC).

**Table 1. Measured and calculated BFS difference and group birefringence of three elliptical-core microfibers for $b$ of 0.87 μm, 1.05 μm and 1.50 μm at a ratio of 1.108.**

| Core diameter $b$ (μm) | 0.87 | 1.05 | 1.50 |
|---|---|---|---|
| Measured birefringence $B_{group}(10^{-3})$ | 17.7 | 9.5 | 4.5 |
| Calculated birefringence $B_{group}$ $(10^{-3})$ | -15.9 | -10.1 | -4.4 |
| Measured BFS difference (MHz) | 6 | 16 | 30 |
| Calculated BFS difference (MHz) | 7 | 19 | 33 |

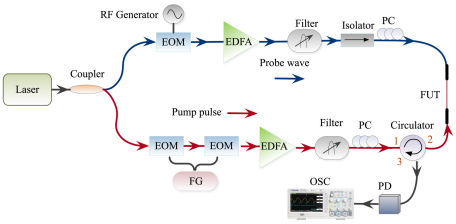


**Fig. 4.** BOTDA setup for measuring the SBS of the microfibers. EOM: electro-optic modulator; FG: function generator; RF: radio frequency; PD: photodetector; OSC: oscilloscope.

The experimentally measured Brillouin gain spectra of the $LP_{01}$ mode and their Lorentzian fittings in two polarization axes of the tapered ECORE $As_2Se_3$-PMMA microfibers at different core diameters are shown in Fig. 5 using circles and solid lines, respectively. The numerically calculated Brillouin gain spectra of the $LP_{01}$ mode of the ECORE microfibers based on the elastodynamic equation are added into Fig. 5 using dashed lines. The red and black colors represent the data in the fast and slow axes, respectively. The measured BFSs of ECORE microfiber A with $b$ =1.50 μm are 7.532 GHz and 7.538 GHz in the fast and slow axes, respectively, and the BFS difference is 6 MHz, as shown in the solid lines of Fig. 5(a). The measured BFS difference for ECORE microfibers B and C with $b$ =1.05 μm and $b$ =0.87 μm are 16 MHz and 30 MHz, respectively. The BFS difference increases with decreased core diameter due to the increased phase birefringence. The Brillouin gain spectra of the $LP_{11}$ mode of ECORE fiber demonstrated in Ref. [3] were not observed in this experiment as the small SBS efficiency between $LP_{11}$ modes and the low input pump power of 9 dBm, which is not enough to excite the SBS of $LP_{11}$ mode. The numerically calculated BFS difference is 7 MHz, 19 MHz, and 33 MHz for the ECORE $As_2Se_3$-PMMA microfibers at $b$ of 1.50 μm, 1.05 μm, and 0.87 μm, respectively. The measured BFS (triangles) and BFS difference (stars) of the ECORE microfibers are added into Fig. 2(b) for comparison. Figure 2(b) shows that the numerically calculated BFS (circles) and BFS difference (squares) obtained by solving Eq. 2 are in better agreement with the experimentally measured BFS and BFS difference than the analytically calculated BFS (solid lines) and BFS difference (dashed line) obtained using Eq. 1. The analytically calculated BFS using Eq. 1 has a larger error as the change of the acoustic velocity for the ECORE microfibers at different core diameters is not accounted for. The experimen-

tally measured and numerically calculated BFS difference for the ECORE $As_2Se_3$-PMMA microfibers at $b$ of 0.87 μm, 1.05 μm and 1.50 μm are presented in Table 1. Due to the tailorable higher birefringence on the order of $\sim 10^{-2}$ to $\sim 10^{-3}$ in the ECORE $As_2Se_3$-PMMA microfiber, the $LP_{11}$ mode has a larger BFS separation with the $LP_{01}$ mode, thus the ECORE microfiber has a better Brillouin spectrum fitting for BFS measurement, which has a better potential for optical sensing applications, such as dual-parameter sensing based on fast and slow axes measurement, compared with the sensing in silica-based ECORE fibers with a birefringence of $\sim 10^{-4}$.

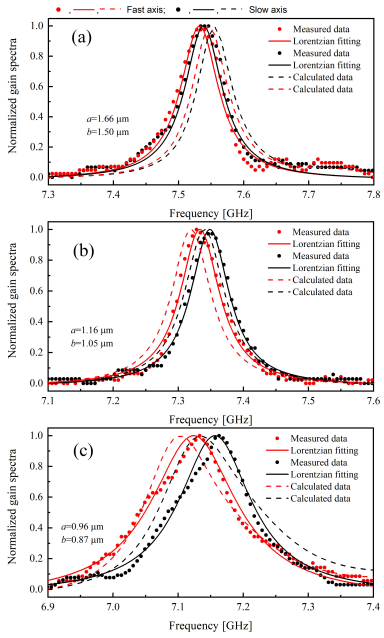


**Fig. 5.** Measured and calculated Brillouin gain spectra of the fast and slow axes of the ECORE microfibers at the core diameter of (a) $b$ =1.50 μm; (b) $b$ =1.05 μm; (c) $b$ =0.87 μm.

Figure 5 shows that the Brillouin gain spectra of the ECORE microfibers are broadened with decreased core diameter. The Brillouin linewidth of the fast and slow axes as a function of $b$ are experimentally measured and numerically calculated, and obtained values are plotted in Fig. 6. The phonon lifetime is accounted for by incorporating a complex elastic tensor, $c_{ij} + i\omega\eta_{ij}$, into the elastodynamic equation, where $\eta_{ij} = c_{ij}/Q_f$ with $Q_f$ being the product of quality factor ($Q$) and frequency ($f$). The value of $Q_f$ is 2000 and 70 for $As_2Se_3$ and PMMA, respectively [15]. The broadening of the Brillouin linewidth is calculated for an ECORE microfiber with a small core diameter. The measured Brillouin linewidth is broadened from ~70 MHz to ~140 MHz as $b$ decreases from 1.50 μm to 0.87 μm. The measured and calculated Brillouin linewidths sharply increase when $b$ is reduced to 0.87 μm. A similar trend was reported for circular-core $As_2Se_3$-PMMA microfibers, as plotted in Fig. 6 using solid line [16]. The Brillouin spectra of small-core $As_2Se_3$-PMMA microfibers are significantly broadened due to the large elastic loss and low density of PMMA cladding. As the inverse relation between Brillouin linewidth and Brillouin frequency shift measurement accuracy, the high sensing accuracy can be obtained in the microfiber with a large core diameter corresponding to small linewidth. The sensing resolution can be further improved using Brillouin dynamic grating for distributed measurement in the high-birefringent ECORE microfiber.

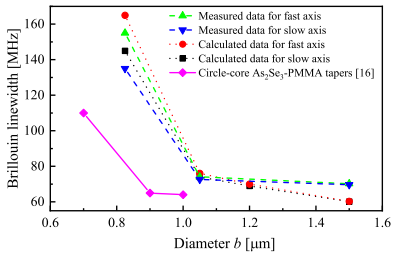


**Fig. 6.** Measured and calculated Brillouin linewidth of fast and slow axes of the ECORE microfibers as a function of $b$.

In conclusion, we have designed and fabricated three elliptical-core $As_2Se_3$-PMMA microfibers and investigated the birefringence and Brillouin gain spectra of fundamental mode. Both experimentally measured and numerically calculated results show that as the core diameter decreases, the birefringence and BFS difference in two polarization axes increase, while the Brillouin spectra are broadened. A large group birefringence on the order of $1.77\times10^{-2}$ and a large Brillouin frequency shift difference of 30 MHz are measured in the elliptical-core microfiber with $a$=0.96 μm and $b$=0.87 μm, which agrees with the calculated results. The elliptical-core $As_2Se_3$-PMMA microfiber is a good candidate for Brillouin sensing due to the high birefringence, tailorable Brillouin gain spectra and low operational power.

**Funding.** Canada Research Chairs (75-67138); Natural Sciences and Engineering Research Council of Canada (NSERC) (DG-2020-06302); China Scholarship Council (CSC).

**Acknowledgement.** We thank Coractive Inc. for providing the $As_2Se_3$ fiber.

**Disclosures.** The authors declare no conflicts of interest.

## REFERENCES

1. Y. Sasaki, T. Hosaka, M. Horiguchi, and J. Noda, J. lightwave technology **4**, 1097 (1986).
2. N. Shibata, Y. Sasaki, K. Okamoto, and T. Hosaka, J. Light. Technol. **1**, 38 (1983).
3. K. Y. Song, Y. H. Kim, and B. Y. Kim, Opt. letters **38**, 1805 (2013).
4. Q. Yu, X. Bao, and L. Chen, Opt. letters **29**, 17 (2004).
5. Q. Yu, X. Bao, and L. Chen, Opt. letters **29**, 1605 (2004).
6. W. Zou, Z. He, and K. Hotate, Opt. express **17**, 1248 (2009).
7. Y. Dong, L. Teng, P. Tong, T. Jiang, H. Zhang, T. Zhu, L. Chen, X. Bao, and Z. Lu, Opt. letters **40**, 5003 (2015).
8. Y. Dong, L. Chen, and X. Bao, IEEE Photonics Technol. Lett. **22**, 1364 (2010).
9. C. Baker and M. Rochette, Opt. express **18**, 12391 (2010).
10. H. Wang, S. Gao, C. Baker, Y. Wang, L. Chen, and X. Bao, Opt. Express **28**, 22933 (2020).
11. H. Wang, S. Gao, C. Baker, Y. Wang, L. Chen, and X. Bao, Opt. Lett. **45**, 3301 (2020).
12. S. Gao, C. Baker, L. Chen, and X. Bao, IEEE Photonics Technol. Lett. **30**, 1155 (2018).
13. C. Baker and M. Rochette, Opt. Mater. Express **1**, 1065 (2011).
14. J.-C. Beugnot and V. Laude, Phys. Rev. B **86**, 224304 (2012).
15. B. Saxena, C. Baker, X. Bao, and L. Chen, Opt. express **27**, 13734 (2019).
16. J.-C. Beugnot, R. Ahmad, M. Rochette, V. Laude, H. Maillotte, and T. Sylvestre, Opt. letters **39**, 482 (2014).

## Intermode and intramode SBS

Due to several optical modes of the elliptical-core fiber, Brillouin gain spectra with multiple peaks based on different pairs of pump-probe modes in the elliptical-core fiber have been demonstrated [157]. Intramode SBS between LP01 mode and LP01 mode (LP01-LP01) or between LP11 mode and LP11 mode (LP11-LP11) and the intermode SBS between LP01 mode and LP11 mode (LP01-LP11) can be excited in the fiber. The silica-based elliptical-core fiber has limitations in Brillouin sensing because the maximum BFS difference between different pump-probe mode pairs is only 25 MHz leading to the distortion of the Brillouin gain spectrum.

Measured Brillouin gain spectra in two polarization axes of the elliptical-core chalcogenide microfiber with a core diameter of $a$ =1.99 µm and $b$ =1.80 µm are shown in Fig. 6.1 using circles, where red and black colors are the data of the fast and slow axes, respectively. Unlike one Brillouin peak discussed above, two peaks are measured in the microfiber with a diameter of $b$ =1.80 µm. Because the symmetry breaks seriously in the elliptical-core fiber with a small core, many high-order modes are excited, and each has low power. LP11 mode has less power for the microfiber with a small core than a large core. As a result, SBS related to the LP11 mode is not excited, and one-peak Brillouin gain spectrum of the intramode SBS of LP01-LP01 is measured. The dual-peak Brillouin gain spectrum is measured in the microfiber with a large core diameter because both the intramode SBS of LP01-LP01 and the intermode SBS of LP01-LP11 are excited. The BFS difference is ∼156 MHz, which is six times larger than the elliptical-core silica fiber.

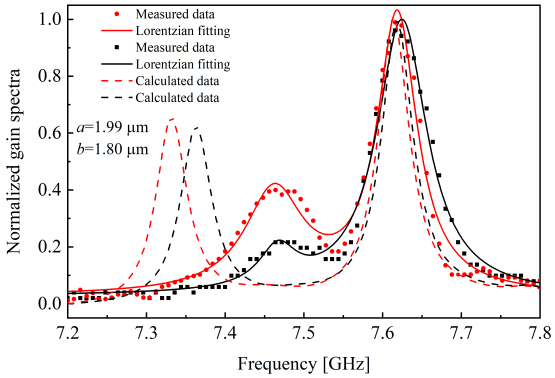


FIGURE 6.1 – Measured and calculated BGS of the fast and slow axes of the tapered e-core fiber with a core diameter of $a$ =1.99 µm and $b$ =1.80 µm

Brillouin gain spectra for mode pairs LP01-LP01 and LP11-LP11 in two polarization axes of the elliptical-core microfiber are calculated as shown in Fig. 6.1 using dashed lines. Effective refractive indices of LP01 and LP11 modes in the microfiber with a diameter of

$b$ =1.8 μm are calculated. Effective refractive indices of LP01 and LP11 in the slow (fast) axis are $n_{01,slow}$=2.6097 ($n_{01,fast}$=2.6082) and $n_{11,slow}$=2.5219 ($n_{11,fast}$=2.5111), respectively. The BFS of the intermode SBS of LP01-LP11 ($v_B$) is given by [157]

$$v_B = \frac{(n_{01} + n_{11})\, V_a}{\lambda} \tag{6.1}$$

where $n_{01}$ and $n_{11}$ represent the effective refractive indices of LP01 and LP11 modes, respectively, the acoustic velocity is $V_a = 2261\,\mathrm{m/s}$ and the laser wavelength is $\lambda = 1550\,\mathrm{nm}$. The calculated BFSs of the intermode SBS are 7.485 GHz and 7.467 GHz in slow and fast axes, which agree with the measured results ( 7.468 GHz and 7.462 GHz in slow and fast axes). The amplitude of the second peak is smaller than that of the main peak because of the lower SBS efficiency of LP01-LP11 than that of LP01-LP01. The intramode SBS of LP11-LP11 is not measured due to the lowest SBS efficiency.

# 7

# Stabilizing Brillouin random fiber laser with photon localization by feedback of distributed random fiber grating array


**Haiyang Wang**, Ping Lu, Chen Chen, Stephen Mihailov, Liang Chen and Xiaoyi Bao
Optics Express. 30(12), 20712-20724 (2022) ;
https ://doi.org/10.1364/OE.460736

## Author contributions

H.W. and X.B. proposed the idea and initiated the project ; P.L. and S.M. fabricated the random fiber grating and random fiber grating array ; H.W. and C.C. designed experimental setup ; H.W. collected experimental data and carried out numerical calculations. H.W and X.B. wrote the paper ; X.B., H.W., C.C., P.L. and L.C. analyzed experimental data ; All authors commented on the paper ; X.B. supervised this project.

We thank Dr. Zichao Zhou for providing the initial code of random fiber grating simulation.

## Summary

Brillouin random fiber lasers (BRFL) based on stimulated Brillouin scattering (SBS) gain and distributed Rayleigh scattering (RS) feedback fibers presented large frequency drift due to randomly amplified modes and fast mode hopping in the random cavity with complex paths [109]. It has been demonstrated that photon localization in random lasers (RL) based on strongly scattering disordered media can increase lasing lifetime [139]. This chapter demonstrates that the BRFL with strong scattering random fiber grating array distributed feedback achieves a small frequency drift and a long-lived lasing mode. Light localization occurs in the strong scattering random fiber grating array (RFGA) due to wave interference and multi-scattering between random fiber grating (RFG) pairs. Light follows the same path in the BRFL due to photon localization, which acts as a seed for Brillouin lasing modes being amplified before dropping to the noise level leading to the long lifetime. Due to light multi-scattering and coherent interference, the RFGA shows high-Q peaks, which can suppress the multi-mode behavior of the random laser. We compare the strong scattering RFGA distributed feedback to the weak scattering RS fiber distributed feedback in a Brillouin random system. The BRFL based on RFGA shows a small frequency drift of sub-MHz and a long-lived mode of 12 s, while the BRFL based on the RS distributed feedback without photon localization exhibits a large frequency drift of a few MHz and fast mode hopping over tens of milliseconds. The spectral evolution is measured by optical heterodyne between the BRFL and the phase-locked laser. The long-lived mode and stabilized frequency in the BRFL induced by photon localization means that it is equivalent to good locking conditions in the phase-locked pump laser. The highly coherent BRFL enabled by light localization offers a new way to reduce optical frequency drift in an all-optical domain without using the additional electrical scheme for active phase locking.

Research Article | Vol. 30, No. 12 / 6 Jun 2022 / Optics Express 20712

Optics EXPRESS

# Stabilizing Brillouin random laser with photon localization by feedback of distributed random fiber grating array

HAIYANG WANG,[1] PING LU,[2] CHEN CHEN,[1] STEPHEN MIHAILOV,[2] LIANG CHEN,[1] AND XIAOYI BAO[1]

[1]Department of Physics, University of Ottawa, Ottawa, Ontario K1N 6N5, Canada
[2]National Research Council Canada, Ottawa, Ontario K1A 0R6, Canada

**Abstract:** Strong scattering random media can localize light and extend photon lifetime through multiple scattering, which offers opportunities for stabilizing random lasers. Here, we demonstrate a frequency stabilized Brillouin random laser with high coherence enabled by photon localization in random fiber grating array (RFGA). Photon trapping is realized due to wave interference in multi-scattering Fabry–Pérot (FP) cavities between random fiber gratings enabling light localization to prolong photon lifetime. The formation of the high finesse peaks of RFGA suppresses multi-longitudinal modes, which offers single-mode operation at high pump power. The RFGA distributed feedback-based Brillouin random fiber laser (BRFL) maintains a small frequency drift with the pump laser (a phase-locked laser with a linewidth of 100 Hz) at 51 kHz/s for a total change of 620 kHz over 12 s. Note there is no locking between the two lasers, and the beat frequency is measured by the optical heterodyne method. The correlation coefficient change of the measured optical beat frequency is maintained at 4.5%. This indicates that the BRFL is capable of maintaining a small optical frequency difference with the phase-locked pump laser over 12 s thanks to the RFGA capable of trapping photons in the same path, which is a remarkable feature for a random fiber laser. Furthermore, we confirm the single-mode lasing with a long lifetime in the stabilizing BRFL by the replica symmetry behavior and ultralow intensity noise at high pump power. Our findings explore a new approach to stabilize the frequency of Brillouin random lasers passively without commonly used active phase locking laser themes, which makes a simple and cost-effective system.



## 1. Introduction

Random lasers (RLs) with disordered scattering feedback media have attracted a great attention due to random lasing nature. Anderson localization, a phenomenon of light confinement in strong scattering random media, has been predicted and demonstrated in RLs [1–3]. Light can be confined in the regime of Anderson localization owing to wave interference in multiple-scattering random media. RLs with high quality factor and long lifetime based on the localization effect have been revealed [4,5]. Random lasing emission in high-dimensional RLs leads to multi-directionality [6]. Recent experiments have shown the reduced threshold and improved lasing efficiency in one dimensional RLs with strong scattering media [7,8]. However, a major challenge for these RLs is multi-mode lasing emission. Multiple lasing modes coexisting in the random system induce broad bandwidth on the order of nanometers and large frequency drift, even though the suppressed mode interaction in the localized regime of the multi-mode RLs is introduced by the reduced spatial overlap of modes [9].

Random fiber lasers (RFL) with transverse confinement imposed by fiber geometry have been demonstrated showing more stable lasing frequency and narrower linewidth [10,11] in comparison to RLs. Different from one-dimensional hollow-core fiber random lasers with filled

#460736 https://doi.org/10.1364/OE.460736
Journal © 2022 Received 8 Apr 2022; revised 14 May 2022; accepted 14 May 2022; published 24 May 2022

Optics EXPRESS

dyes in air holes of the fiber as gain medium [12,13], the gain of RFLs with all-fiber configuration is based on stimulated Brillouin scattering (SBS) [14,15], stimulated Raman scattering (SRS) [16,17], and Erbium-doped fiber (EDF) [18,19]. The light localization in a random grating array in a single-mode fiber has been experimentally demonstrated by measuring the exponential decay of transmissivity along the disordered fiber gratings [20]. Later, EDF gain random lasers based on Bragg gratings via Anderson localization were demonstrated [21–24]. Due to multi-mode lasing emission and broad lasing linewidth of picometers (hundreds of MHz) in the EDF-based RFLs, however, they exhibit large frequency drift and short lifetime of nanoseconds, which impose limits for fiber sensor technologies and optical communications. Brillouin random fiber lasers (BRFL) with a linewidth of kHz have been demonstrated [25,26]. The narrower bandwidth of Brillouin gain (tens of MHz) than EDF gain enables fewer modes with smaller drift in the Brillouin random laser system. Light follows different paths without localization effect in Brillouin random laser systems with weak Rayleigh scattering (RS) random feedback media, leading to a short lifetime of milliseconds and large frequency drift of 10 MHz [27,28]. Random fiber grating (RFG) with large refractive index contrast as distributed feedback medium in BRFL have been investigated [29,30]. The weak multi-scattering of the RFG with random spatial periods of micrometers over several centimeters is not adequate to localize photons for a long time of seconds. Little is known about the characterizations of Brillouin random lasing emission in strong scattering random media. To understand limits in noise features of a Brillouin random laser system with the light localization effect, a strongly scattering disordered random fiber grating array (RFGA) as a distributed feedback of a BRFL is investigated in the current paper. The focus of this work is to characterize the BRFL with the strong scattering RFGA by detecting the lasing modes evolution, frequency drift, and intensity fluctuation.

In this paper, we demonstrate a stabilizing Brillouin random laser with photon localization enabled by strong scattering RFGA. Light is localized in the RFGA due to wave interference in multi-scattering Fabry–Pérot (FP) cavities between random fiber grating pairs. Once a single longitudinal mode lasing is established in the BRFL via the high finesse filter formed between FP cavities at high pump power, a long-lived lasing mode of 12 s is achieved because the light is trapped in the multiple FP cavities. Note, there is no active phase-locking mechanism in the random laser. The established random mode maintains the lasing because the small frequency difference between multiple random modes from RFGA ensures lasing continuously under resonance condition, even though the thermal and acoustic effects induce slight laser frequency drift. The long-lived mode with a small correlation coefficient change of 4.5% and frequency change rate of 51 kHz/s over 12 s leads to the stabilized random lasing with a small frequency drift of 620 kHz. The correlation coefficient change remains constant with time in the RFGA-based BRFL, while it is varied significantly in other weak scattering feedback-based BRFLs, which confirms the frequency stabilized random laser with RFGA enabled by photon localization. The stabilizing BRFL shows replica symmetry behavior at high pump power and ultralow relative intensity noise, which is another indicator of single-mode lasing with a long lifetime.

## 2. Experimental section

### 2.1. Principle and simulation

RFGA provides distributed feedback for the Brillouin random fiber laser. RFGA is fabricated along a polarization-maintaining (PM) fiber by the plane-by-plane inscription method. The refractive index of the PM fiber is modulated spot by spot with random periods by the exposure of a femtosecond (fs)-IR pulse laser through the method [31]. A few dB loss is introduced in the RFGA during the inscription process. The parameters of RFGA, including the length of each grating and distance between two gratings, are characterized by optical frequency domain reflectometry (OFDR). There are 38 random gratings in the RFGA with a distance between two gratings of 15 cm ± a couple of millimeters and the length of each RFG is 5 mm. The

Optics EXPRESS

intrinsic refractive index modulation spots in each 5 mm-long grating of the RFGA are around 9400. The refractive index modulation periods are randomly varied between 0.5180 µm and 0.5464 µm, corresponding to a broad backscattering wavelength range from 1500 nm to 1580 nm. Wave interference between multi-scattering grating pairs in the RFGA plays a key role in improving spatial trapping and lasing stability. The schematic of light propagation in the RFGA with increased pump power is plotted in Fig. 1(a). When light with low pump power transports in the RFGA, it can not pass through all the sub-gratings before it drops below the noise level due to scattering loss suggesting no wave interference between grating pairs. By increasing pump power, light propagates in one FP cavity formed between two gratings, where photons travel back and forward leading to the coherent interference of waves. The spectrum of the RFGA exhibits narrow linewidth with a high finesse $\mathcal{F}$. Light propagates in more FP cavities under higher pump power indicating a higher finesse $\mathcal{F}^N$ contributed to the product of the finesse of N individual resonators with the same resonant frequency. Longitudinal lasing modes in the Brillouin gain region can be remarkably suppressed and a single longitudinal mode emission can be realized in the random laser system at high pump power due to the high finesse of the RFGA. The reflection spectra of the RFGAs with different numbers of random fiber gratings are simulated based on the transfer matrix method. The narrower spectral peaks owing to multiple scattering between gratings confirm the high finesse and quality factor of the RFGA (see Section 1 Figure S1 in the Supporting Information). Reflection and transmission spectra of the RFGA are measured by an optical spectrum analyzer (OSA) with a resolution of 5 MHz as shown in Fig. 1(b). The average transmission at the wavelength of 1550 nm is -20 dB corresponding to the transmittance of 0.01. The reflection spectrum presents a large number of peaks with narrow linewidth as expected. In a strongly scattering disordered medium, wave interference in multi-scattering paths leads to photon localization. The localization length $\xi$ is given by [8]

$$\xi \sim -L/2 \ln\langle T(L)\rangle \tag{1}$$

where $L$ is the RFGA length and $\langle T(L)\rangle$ is the average transmission of the RFGA. The localization length is $\xi = 0.1L$, well within the length limit of the RFGA. Wave interference in many FP cavities gives shorter localization length than the fiber length. Photons are confined in the RFGA when transported in the random laser, which leads to long-lived lasing modes. In addition, there are multiple random modes with small frequency differences due to the scattering paths with small difference, especially under high pump power, where more random modes are survived over the cavity loss. The random modes can be selected to compensate for the small frequency drift due to temperature and acoustic variations, leading to a long-lived modes without mode-hopping.

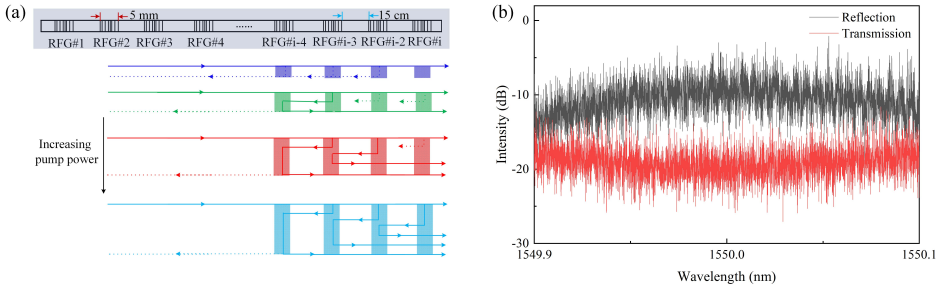


**Fig. 1.** (a) Schematic of light propagation in the RFGA with increased pump power. Photons are localized in the RFGA due to wave interference between many FP cavities at high pump power. (b) Reflection and transmission spectra of RFGA. Multiple narrow peaks with high finesse confirm wave interference between FP cavities in the RFGA.

Optics EXPRESS

### 2.2. Experimental setup

The schematic of the BRFL setup is described in Fig. 2(a). A NKT laser with a linewidth of 100 Hz is used as the pump light, which power is controlled by an erbium-doped fiber amplifier (EDFA). The state of polarization of the pump light is aligned to the slow axis of a polarization beam splitter (PBS) by adjusting a polarization controller (PC). The pump light is injected into the Brillouin gain medium through polarization-maintaining (PM) circulator 1. A 2 km-long Panda-type PM fiber is used as the Brillouin gain medium. The pump light in the Brillouin gain medium stimulates backward Stokes light, which travels anticlockwise in the cavity after Rayleigh scattering provided by a PM random fiber grating array. The lasing output is sent to an OSA for spectrum analysis, an oscilloscope for temporal intensity dynamics analysis and an optical heterodyne system by combining the lasing output of the BRFL and the pump laser after a PM coupler for beat spectral evolution analysis. The beat spectra are detected by a high-speed photodetector with 20 GHz bandwidth and recorded by an electrical spectrum analyzer (ESA). The preserved state of polarization of light in the all PM random fiber laser system leads to a high degree of stability in linear polarization against external perturbations during its propagation, which is beneficial for the Brillouin random lasing with low intensity fluctuation and frequency drift. Furthermore, the PM gain fiber has a smaller effective mode field diameter of 6.48 μm than that of SMF (10.4 μm), which provides a higher Brillouin gain coefficient for the BRFL. More gain from the PM fiber ensures that multiple random modes can sustain the multiple cavity trips to increase the total effective length. This is important to maintain resonant laser condition under the temperature drift and acoustic disturbance from the environment by multiple random modes with small mode frequency differences. Figure 2(b) shows the output power of the BRFL based on RFGA as a function of pump power. At pump power above 7.2 mW, Rayleigh scattering from the RFGA provides the necessary back-scattered Stokes light to enable the gain in the random laser system higher than the loss in a round trip, which leads to laser oscillations. After the lasing threshold, output power linearly increases with pump power. A sharp peak with a red-shift of ~10.34 GHz from the pump laser, corresponding to the Brillouin frequency shift in the slow axis of the PM fiber [32], appears on the output spectrum at the pump power above the threshold as shown in the inset of Fig. 2(b). The side peaks with small amplitudes are attributed by the side modes of the optical local oscillator inside the high-resolution OSA.

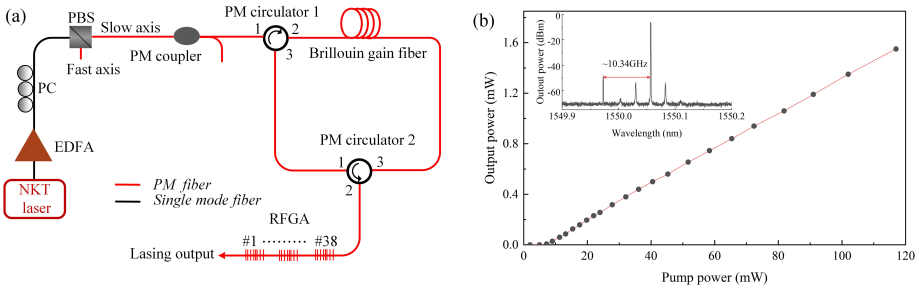


**Fig. 2.** (a) Schematic of the experimental setup for the BRFL based on RFGA. EDFA: erbium-doped fiber amplifier; PC: polarization controller; PBS: polarization beam splitter; RFGA: random fiber grating array; PM: polarization-maintaining. (b) The output power of BRFL as a function of pump power. Inset: optical spectrum with a sharp peak at the Brillouin resonant frequency of ~10.34 GHz away from the pump laser.

Optics EXPRESS

## 3. Results

### 3.1. Lasing mode characterization and spectral evolution

The output lasing spectrum of the BRFL is measured using the heterodyne-based method. We count the number of modes according to the mode amplitude within 20 dB of the maximum value at each pump power. The number of modes as a function of pump power is plotted in Fig. 3(a). The sharply increased lasing modes with increased pump power below 9 mW indicate that more longitudinal modes above the noise floor are excited in the Brillouin gain bandwidth. However, the low finesse of the RFGA is not enough to suppress the lasing modes at the low pump power. Higher pump power enables wave interference in more FP cavities leading to increased finesse of the reflection spectrum of the RFGA. As a result, one mode is selected and other longitudinal modes are suppressed at the pump power above 20 mW. The variation in the number of lasing modes confirms the power-dependent light transportation in the RFGA as expected. Figure 3(b) shows several beat spectra at different pump powers. The bottom four spectra show multi-mode lasing emission with envelopes of quasi-Lorentzian shape, which suggests the lasing modes located at the high gain region of Brillouin bandwidth (20 MHz for the PM gain fiber). The longitudinal mode spacing of 0.1 MHz corresponds to the cavity length of around 2 km. The top spectrum shows a single longitudinal mode lasing with a high signal-to-noise ratio of 60 dB, which suggests the reduced frequency and intensity fluctuations of the random laser.

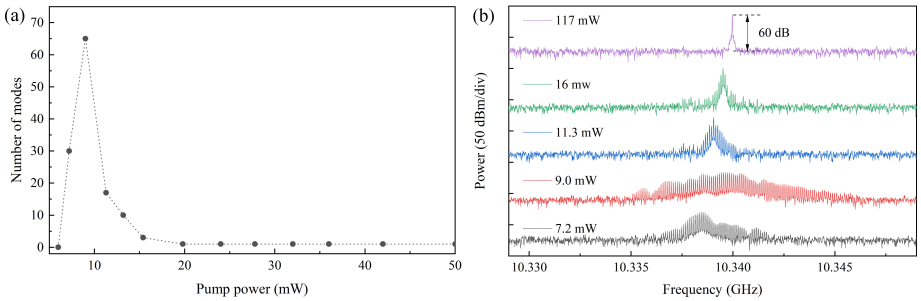


**Fig. 3.** (a) Number of modes of the BRFL as a function of pump power. Single longitudinal mode operation in the random system above 20 mW. (b) Beat spectra of the RFGA-based BRFL with different pump powers. Mode frequency of around 10.34 GHz corresponds to the Brillouin frequency shift in the slow axis of the PM gain fiber.

To illustrate photon trapping via time dependent frequency drift of the random laser with RFGA, we exploit the spectral evolution of the beat signal between the pump laser and the BRFL in a continuous time, which adds a new dimension to show the trapping time and frequency stability of lasing modes for a random laser. The beat spectra at different pump powers are monitored continuously over 15 s in a time interval of 15 ms, as shown in Figs. 4(a-c), in which the color bar represents the power of beat spectra. The frequency resolution of the beat spectrum is 10 kHz. The frequency of beat spectra is normalized to $f - \langle f \rangle$. The frequencies of the lasing modes over their lifetime at different pump powers are plotted in Fig. 4(d). The lifetime of the lasing mode is found to be prolonged to 12 s with increased pump power to 117 mW. When the light with higher pump power transports in the Brillouin random laser system, photons survive for a longer time due to localizing light in more multi-scattering FP cavities of the RFGA, which leads to a longer-lived lasing mode. It is found that the lasing mode at each pump power has a positive chirp over its lifetime as plotted in Fig. 4(d). The mode chirp can be understood through the mode-pulling effect in the stimulated Brillouin scattering process. Mode-pulling is induced by nonlinear phase shift as a result of strong dispersion in the narrow Brillouin gain. As a result, the Stokes lasing mode is pulled away from the Brillouin resonant frequency of the

Optics EXPRESS

cold cavity by an amount during lasing operation [33–35]. The frequency change range of lasing modes depends on the Brillouin gain spectrum and the relative position between the gain peak and the lasing frequency. The same gain spectrum and small change of frequency separation between the Stokes signal and the pump light at different pump powers indicate that the lasing mode moves in a similar range. To prove the stabilization of the BRFL enabled by the RFGA distributed feedback, no external temperature insulation chamber is added to the system. The lasing mode with small difference in chirp rate over 12 s owing to the temperature variation. The sensitivity of Brillouin frequency shift is ~1 MHz/°C. The slight temperature change induces the small Brillouin peak shift. As a result, the different chirp rates over time under the same pump power are achieved as shown in Fig. 4(c). The same lasing mode is kept at around 5 s even with small disturbance because the random fiber laser has a stabilization mechanism enabled by random modes, which shows the self-stabilization ability of the random fiber laser with feedback of RFGA to ignore the small disturbance from environmental change. The frequency drift is 620 kHz over the lifetime of 12 s at the pump power of 117 mW. Compared with demonstrated BRFL based on the Erbium-doped fiber loop, which exhibits a mode-hopping free operation over 0.8 s with the frequency drift of 1.2 MHz owing to the photonic memory in EDF [36], the frequency drift of the long lifetime mode hopping free BRFL enabled by photon localization in RFGA (~40 kHz in 0.8 s) represents a factor of 30 improvement. Figure 4(e) shows that the frequency change rate of lasing modes decreases from 194 kHz/s to 51 kHz/s with increased pump powers from 20 mW to 117 mW. The decreased frequency drift rate is attributed by photon confinement in the specific random mode, which overcomes the loss from the RFGA in one trip as a seed to get the gain from the 2 km Brillouin gain fiber. Such a process is repeated with more cycles because the mode survives for a longer time in the RFGA at higher pump power. As a result, the correlation coefficient has a smaller change (4.5%) at higher pump power as shown in Fig. 4(e). The role of slightly changed scattering length from RFGA over the fixed 2 km gain length is to maintain the resonance condition of random laser under slight temperature variation. Similar to phase-locked cavity change to be adaptable to the laser cavity length change from temperature, here we have many slight different random modes from the RFGA to be selected to match the temperature change simultaneously, rather than sequentially changed round trips with $2\pi$ phase shift in phase-locked feedback cases, which takes a longer time to reach $2\pi$ of constructive mode addition. At the beginning and end of each lasing mode (transient regimes), we observe mode-hopping with a frequency jump of hundreds of kHz. A short-time spectral evolution in the transient regime at the pump power of 117 mW is shown in Fig. 4(f). The mode hopping is because the lasing mode moves to the frequency at which Brillouin gain is not enough to support the lasing mode imposed by the mode-pulling effect. As a result, the random lasing process is rebuilt up and the lasing mode randomly hops to a favorable mode in the high gain position, where the random system can continue to single-mode lasing operation. We observe the multiple longitudinal modes at transient regimes as plotted in the inset of Fig. 4(f). Because of the reconstruction of lasing action at transient regimes, each longitudinal mode has an opportunity to be excited and multiple longitudinal modes suddenly appear in the gain bandwidth leading to an unstable laser system. The multi-mode emission indicates that the random laser approaches and recovers from transient regimes. The stabilization of the RFGA-based BRFL is not affected by the nonlinearities, such as four-wave mixing and cross phase modulation, owing to single longitudinal mode operation in the linearly polarized random system and the 40 dB lower reflected pump wave compared with the Stokes wave.

To confirm the stabilized frequency in BRFL enabled by RFGA, two different distributed feedback fibers such as RS fiber and single RFG are investigated by replacing the RFGA in the BRFL. Spectral evolution of the BRFL based on 500 m-long RS fiber (PM fiber) at the pump power of 90 mW is measured as plotted in Fig. 5(a). We observe a lasing mode rapidly hops to another random mode on the order of milliseconds, even though a few modes survive for a longer

Optics EXPRESS

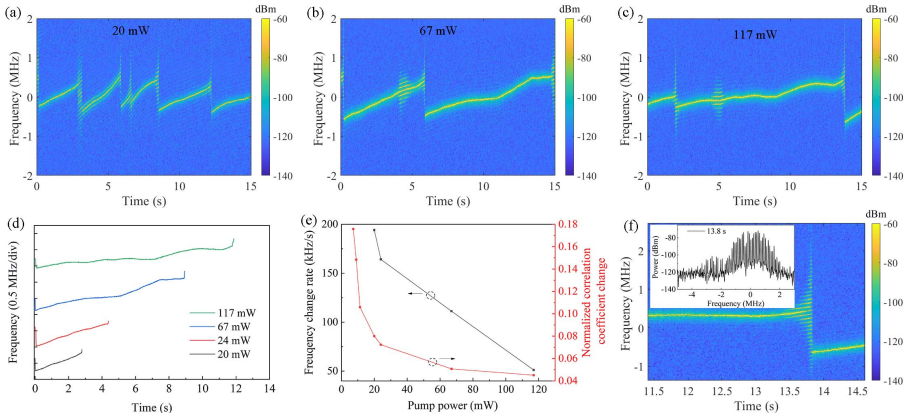


**Fig. 4.** Real-time spatio-temporal evolution of the BRFL based on RFGA at the pump power of (a) 20 mW; (b) 67 mW; (c) 117 mW. (d) Frequency of lasing modes over their lifetimes at different pump powers. The frequency axis is the relative value at 0.5 MHz per division. (e) Frequency change rate and normalized correlation coefficient change as a function of pump powers. The frequency change rates are evaluated by fitting the mode chirps shown in Fig. 4(d) with a linear function. Correlation coefficient is calculated between two neighboring traces over 15 s. (f) Close-up of Fig. 4(c) during the mode-hopping event. Inset: the multi-mode spectrum in the transient regime at 13.8 s.

time of 0.3 s as shown in Fig. 5(b). This is contributed by weak scattering in the 500 m-long RS fiber owing to the nonuniform density induced small refractive index fluctuation. Photons can not be trapped in the weak scattering distributed feedback fiber and escape promptly from the random laser system. As a result, the lifetime of lasing mode in the RS fiber-based BRFL is over 40 times shorter than that of the RFGA-based BRFL. Instead of the small frequency drift in RFGA-based random laser owing to the narrow filter effect and photon localization, lasing modes are randomly selected by the weak RS fiber and amplified in the high gain region of the Brillouin bandwidth in each round trip. The lasing mode drift over 10 s shows a Gaussian distribution in a frequency range of 6 MHz as plotted in Fig. 5(c). The Gaussian distribution of the frequency drift shows that the lasing RS-based system is a random process without mode trapping. Spectral evolution of 5 cm-long polarization-maintaining RFG-based BRFL is presented in Fig. 5(d) showing an unstable random lasing condition with several lasing modes. The lasing lifetime of the RFG-based BRFL is longer than that of RS-based BRFL due to higher refractive index modulation formed frozen scattering centers, which enables photons to be trapped for more time in the RFG compared with RS fiber. However, the weak multi-scattering of light between the sub-gratings of the RFG leads to low quality factor (see Section 1 Figure S2 in the Supporting Information). The lasing modes follow different scattering paths after certain time due to the broad linewidth peaks of the single RFG with weak localization, which leads to the fast mode hopping in a large frequency range of 4 MHz. The longest lifetime of a lasing mode is 1.2 s, as shown in Fig. 5(e). Compared with the single RFG as distributed feedback, the RFGA with 38 RFGs demonstrates 10 times longer lasing lifetime with a smaller frequency drift of 15.5%. The long lifetime in the BRFL based on RFGA is contributed by the light confinement in FP cavities, which acts as a seed for Brillouin lasing modes being amplified before dropping to the noise level. In addition, the high finesse of the RFGA leads to the single-longitudinal mode operation within a small frequency range, while the random laser shows the multi-mode operation in the single RFG-based BRFL owing to the broadband filter effect. As a result, the BRFL based on RFGA with 38 RFGs is free of mode-hopping with single-mode operation over a long time.

Optics EXPRESS

The small correlation coefficient change of 4.5% for the optical beat frequency between the BRFL and the phase-locked laser and the frequency change of 51 kHz/s indicate the potential of self-stabilization capability for the random fiber laser. The upper limit of the grating array number is the balance of the Brillouin gain and RFGA induced loss, which makes the seeded random modes above the lasing threshold level to ensure sustained random modes for low noise random laser operation. The multiple longitudinal modes with an amplitude of around -95 dBm in the RFG-based BRFL as shown in the inset of Fig. 5(e) is over 20 dB higher in comparison to the lasing emission in RFGA-based BRFL at high pump power. This confirms the broadband filter effect of the single RFG. The normalized correlation coefficient change in a step of 1 s over 10 s for RFGA, single RFG and RS fiber-based BRFLs is plotted in Fig. 5(f). The maintained correlation coefficient change over 10 s and small value in each time for the RFGA-based BRFL suggest the stabilized lasing frequency drift due to photon localization. The RS fiber-based BRFL without photon localization and single RFG-based BRFL with weak localization show the large correlation coefficient change with strong fluctuation over time as expected.

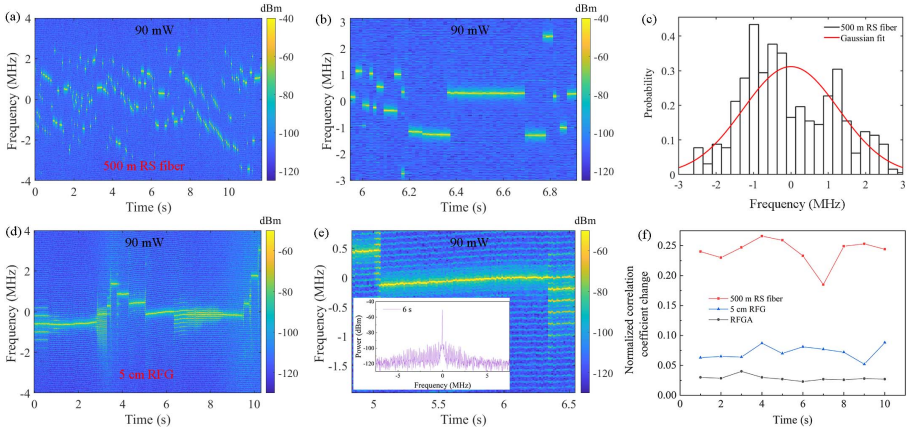


**Fig. 5.** (a) Real-time spatio-temporal evolution of the BRFL based on 500 m RS fiber at pump power of 90 mW. (b) Close-up of Fig. 5(a). (c) Histogram of frequency drift in the RS fiber. (d) Spectral evolution of the BRFL based on 5 cm RFG at pump power of 90 mW. (e) Close-up of Fig. 5(d). Inset: the lasing spectrum at 5.5 s. (f) Normalized correlation coefficient change for three distributed feedback fibers-based BRFLs in a step of 1s over 10 s. The correlation coefficients of the random laser with RFGA are calculated from the beginning of the long-lived lasing mode. The coefficient change in each time is calculated during 1 s.

### 3.2. *Intensity fluctuation*

The intensity dynamics and statistical features are investigated in the BRFL with RFGA. The intensity probability is identified with $\alpha$-stable Lévy distribution (see more details in the Supporting Information Section 2). The Lévy index $\alpha$ as a function of pump power is plotted in Fig. 6(a). There is a transition between statistical behaviors, from Gaussian distribution at the power below the threshold ($\alpha$ = 2 at 6 mW) to a Lévy distribution at the power around the threshold ($0<\alpha<2$ at 16 mW), and the intensity fluctuation is returned to Gaussian distribution at the power well above the threshold ($\alpha$ = 2 at 24 mW). Due to the thermal noise in the prelasing regime, Gaussian distribution at the power below the threshold is expected. The transition from the prelasing Gaussian distribution to the Lévy distribution is a signature of random lasing. The low finesse of the RFGA at the pump power near the threshold indicates multi-mode lasing operation as we discussed in Fig. 3. The strong coupling of longitudinal modes

Optics EXPRESS

in the Brillouin gain bandwidth induces large energy exchange between Stokes photons and phonons, which increases the probability of extreme events. Thus the intensity fluctuation follows Lévy distribution. Unlike the prelasing Gaussian behavior for the power below the threshold, Gaussian behavior at the power well above the threshold indicates a random lasing process with coherent emission. Intensity change range of the BRFL as a function of pump power is shown in Fig. 6(b). By increasing the power above 24 mW, we observe the sharp decrease of intensity fluctuation, which is consistent with the statistical transition from Lévy regime to Gaussian regime, confirming a coherent single-mode lasing operation in the random system. Relative intensity noise (RIN) of the random laser system is characterized at different pump powers as shown in Fig. 6(c). At the pump power of 16 mW, the large RIN with high resonant noise peaks in the frequency range from 0.1 MHz to 1 MHz corresponding to inverse of round trip time of light in the laser shows the coupling of multiple longitudinal modes. High pump power enables one longitudinal lasing mode with high gain to overcome the loss via the RFGA formed high finesse filter. As a result, the number of longitudinal modes and spontaneous scattering from the gain medium are suppressed. The strong intensity fluctuation induced by modes competing for the available gain is alleviated. Thus, we observe the RIN of the random lasing emission operating at the pump power of 117 mW is around 100 dB lower than that at the pump power of 16 mW in the frequency range from 1 Hz to 1 MHz. The RIN of the commercial NKT laser is measured for comparison, which is around 10 dB lower than that of the Brillouin random laser with a pump power of 117 mW. The optimized RIN in the RFGA based BRFL is over 30 dB lower than that of BRFLs with 500 m RS fiber and 5 cm RFG as distributed feedback media (see the Supporting Information Section 3 for detailed discussion and direct comparison).

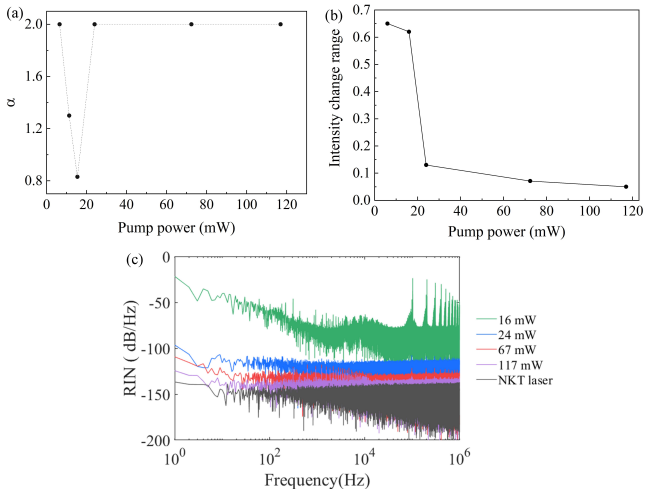


**Fig. 6.** (a) $\alpha$ value as a function of pump power. An initial Gaussian regime ($\alpha = 2$) is followed by Lévy regime ($0<\alpha<2$), and Gaussian regime ($\alpha = 2$) is recovered at high pump power due to power-dependent modes in the random laser. (b) Intensity change range versus pump power. (c) RIN comparison at different pump powers.

We consider the replica symmetry or replica symmetry breaking determined by the distribution of Parisi overlap parameter to demonstrate the characterization of intensity fluctuation in the BRFL with RFGA. Parisi overlap parameter $q$ is given by [37–39]

$$q_{ab} = \frac{\sum_{k=1}^{N} \Delta_a(k)\Delta_b(k)}{\sqrt{\sum_{k=1}^{N} \Delta_a^2(k)}\sqrt{\sum_{k=1}^{N} \Delta_b^2(k)}} \tag{2}$$

Optics EXPRESS

where $N$ is the number of spectral points, $a$ and $b$ are two traces with being $a, b$=1,2,. . . , $N_s$ and $N_s = 100$, $\Delta_a(k) = I_a(k) - \bar{I}(k)$ is the intensity fluctuation, and $\bar{I}(k) = \sum_{a=1}^{N_s} I_a(k)/N_s$ is the average intensity at the frequency indexed by $k$. The intensity fluctuations from trace to trace are uncorrelated if the values of $q_{ab}$ are around zero, which implies the photonic uncorrelated paramagnetic and replica symmetry; otherwise, the intensity fluctuations are correlated between traces, which indicates spin-glass phase and replica symmetry breaking. Fast Fourier transform of the temporal traces is applied to calculate the spectra of the intensity fluctuation and Parisi overlap parameter. The histogram of $q$ is calculated at different pump powers as plotted in Figs. 7(a-d). $q$ value distributions are centered around zero at the pump power below the threshold, which indicates the uncorrelated emission between different traces in the paramagnetic regime (Fig. 7(a)). The spontaneous emission from thermal noise in the gain medium confirms the replica symmetry behavior. By increasing the pump power above the threshold, multiple longitudinal modes are activated in the Brillouin gain bandwidth. Mode competing for the limited gain leads to the correlated intensity fluctuation from trace to trace. The consequence of these strong intensity correlations is a bimodal distribution with the maximum probability at $q = \pm 1$ and replica symmetry breaking (Figs. 7(b-c)). Similar transition from replica symmetry to replica symmetry breaking with increased power has been demonstrated in random lasers [37,40,41] and Erbium-based random fiber laser [42,43]. However, different from these random lasers with maintained replica symmetry breaking at high pump power, the Brillouin random laser based on RFGA shows the transition from replica symmetry breaking back to replica symmetry (Fig. 7(d)). This indicates the suppressed multi-modes and low intensity fluctuation. The replica symmetry behavior at high power is contributed to the reduced number of longitudinal modes and the frequency stabilized lasing mode due to the high finesse filter of the RFGA and long-time mode trapping by the light localization effect in the RFGA. The absolute value of $q$ at the maximum probability ($|q_{\max}|$) as a function of pump power is plotted in Fig. 7(e). The maintained replica symmetry behavior ($|q_{\max}| = 0$) in high power regimes shows the long-lived lasing with low noise of the stabilizing BRFL with RFGA. The $q$ value distribution for the random lasing system without RFGA is measured as shown in Fig. 7(f). The values of $q$ are centered around zero, which means that the intensity fluctuation spectra from trace to trace are independent of the system noise without distributed feedback. The distribution of $q$ values with the smallest range around zero indicates that the random distributed feedback adds uncertainty to the laser system.

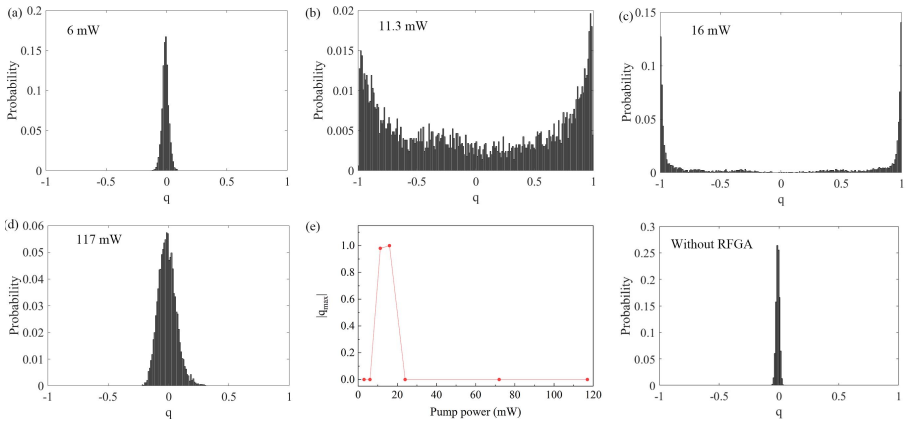


**Fig. 7.** Histograms of $q$ values of the BRFL at the pump power of (a) 6.0 mW; (b) 11.3 mW; (c) 16 mW; (d) 117 mW; (e) $|q_{\max}|$ value as a function of pump power. (f) Histograms of $q$ values without RFGA.

Optics EXPRESS

## 4. Conclusion

In summary, we have demonstrated a stabilizing Brillouin random laser system with a long-lived lasing mode enabled by photon localization in RFGA. More FP cavities in the RFGA at higher pump power lead to higher finesse. As a result, multiple longitudinal modes are suppressed. More strikingly, wave interference in the multi-scattering FP cavities indicates the light localization, which leads to photon trapping in the RFGA based random laser. We have shown that the random laser supports a long-lived lasing mode of 12 s in the BRFL at high pump power. The long lifetime of the localized lasing mode leads to the small frequency shift of 620 kHz over 12 s indicating the stabilized frequency of the RFGA-based random laser with photon localization. We confirm the stabilizing BRFL with the light localizing RFGA feedback by comparing it with the feedback of RS fiber and RFG commonly used in random fiber lasers. Two feedback-based BRFLs exhibit unstable lasing modes with faster mode hopping in larger frequency range and larger correlation coefficient change with stronger fluctuation owing to no light localization in the weak scattering RS fiber and weak light localization in the weak multi-scattering RFG. The photon trapping induced long-lived modes and stabilized frequency in the random laser is equivalent to good locking condition in phase locked laser. The key for the nearly constant lasing frequency is that minor changed cavity length due to the temperature or acoustic wave can always find a "matched length" among many random modes with small spatial separation over long cavity length at given time. Hence the "seeded photons" sustained lasing condition, i.e. long lifetime is achieved. The stabilizing BRFL enabled by RFGA also gives rise to an low intensity noise and replica symmetry behavior at high pump power. Our contribution helps to understand mode propagation and noise properties in localized photons in Brillouin fiber lasers with random distributed feedback and constitutes an important step towards the design of frequency stabilized random fiber lasers with high coherence and low noise without the need for active feedback and locking on the laser cavity.

**Funding.** China Scholarship Council; Natural Sciences and Engineering Research Council of Canada (06071-RGPIN-2015); Canada Research Chairs (75-67138).

**Acknowledgement.** We thank Dr. Zichao Zhou for useful discussion on the simulation of random fiber grating array.

**Disclosures.** The authors declare no conflicts of interest.

**Data availability.** Data underlying the results presented in this paper are not publicly available at this time but may be obtained from the authors upon reasonable request.

**Supplemental document.** See Supplement 1 for supporting content.

### References

1. H. Cao, "Lasing in random media," Waves in random media **13**(3), R1–R39 (2003).
2. F. Riboli, N. Caselli, S. Vignolini, F. Intonti, K. Vynck, P. Barthelemy, A. Gerardino, L. Balet, L. H. Li, A. Fiore, G. Massimo, and W. Diederik, "Engineering of light confinement in strongly scattering disordered media," Nat. Mater. **13**(7), 720–725 (2014).
3. K. Y. Bliokh, Y. P. Bliokh, V. Freilikher, A. Genack, B. Hu, and P. Sebbah, "Localized modes in open one-dimensional dissipative random systems," Phys. Rev. Lett. **97**(24), 243904 (2006).
4. J. Andreasen, A. Asatryan, L. Botten, M. Byrne, H. Cao, L. Ge, L. Labonté, P. Sebbah, A. Stone, H. Türeci, and C. Vanneste, "Modes of random lasers," Adv. Opt. Photonics **3**(1), 88–127 (2011).
5. A. Burin, M. A. Ratner, H. Cao, and S. Chang, "Random laser in one dimension," Phys. Rev. Lett. **88**(9), 093904 (2002).
6. P. Sebbah and C. Vanneste, "Random laser in the localized regime," Phys. Rev. B **66**(14), 144202 (2002).
7. B. Abaie, E. Mobini, S. Karbasi, T. Hawkins, J. Ballato, and A. Mafi, "Random lasing in an anderson localizing optical fiber," Light: Sci. Appl. **6**(8), e17041 (2017).
8. V. Milner and A. Z. Genack, "Photon localization laser: low-threshold lasing in a random amplifying layered medium via wave localization," Phys. Rev. Lett. **94**(7), 073901 (2005).
9. P. Stano and P. Jacquod, "Suppression of interactions in multimode random lasers in the anderson localized regime," Nat. Photonics **7**(1), 66–71 (2013).
10. S. Babin, A. El-Taher, P. Harper, E. Podivilov, and S. Turitsyn, "Tunable random fiber laser," Phys. Rev. A **84**(2), 021805 (2011).

Optics EXPRESS


11. T. Zhu, X. Bao, and L. Chen, "A single longitudinal-mode tunable fiber ring laser based on stimulated rayleigh scattering in a nonuniform optical fiber," J. Lightwave Technol. **29**(12), 1802–1807 (2011).
12. C. J. de Matos, L. d. S. Menezes, A. M. Brito-Silva, M. M. Gámez, A. S. Gomes, and C. B. de Araujo, "Random fiber laser," Phys. Rev. Lett. **99**(15), 153903 (2007).
13. Y. Yonenaga, R. Fujimura, M. Shimojo, A. Kubono, and K. Kajikawa, "Random laser of dye-injected holey photonic-crystal fiber," Phys. Rev. A **92**(1), 013824 (2015).
14. L. Zhang, Y. Xu, S. Gao, B. Saxena, L. Chen, and X. Bao, "Linearly polarized low-noise brillouin random fiber laser," Opt. Lett. **42**(4), 739–742 (2017).
15. G. Song, Z. Liang, Y. Xu, L. Ping, and X. Bao, "Tapered fiber based brillouin random fiber laser and its application for linewidth measurement," Opt. Express **24**(25), 28353 (2016).
16. S. K. Turitsyn, S. A. Babin, A. E. El-Taher, P. Harper, D. V. Churkin, S. I. Kablukov, J. D. Ania-Casta nón, V. Karalekas, and E. V. Podivilov, "Random distributed feedback fibre laser," Nat. Photonics **4**(4), 231–235 (2010).
17. L. Zhang, J. Dong, and Y. Feng, "High-power and high-order random raman fiber lasers," IEEE J. Sel. Top. Quantum Electron. **24**(3), 1–6 (2018).
18. G. Yin, B. Saxena, and X. Bao, "Tunable er-doped fiber ring laser with single longitudinal mode operation based on rayleigh backscattering in single mode fiber," Opt. Express **19**(27), 25981–25989 (2011).
19. H. Shawki, H. Kotb, and D. Khalil, "Single-longitudinal-mode broadband tunable random laser," Opt. Lett. **42**(16), 3247–3250 (2017).
20. O. Shapira and B. Fischer, "Localization of light in a random-grating array in a single-mode fiber," J. Opt. Soc. Am. B **22**(12), 2542–2552 (2005).
21. N. Lizárraga, N. Puente, E. Chaikina, T. Leskova, and E. Méndez, "Single-mode er-doped fiber random laser with distributed bragg grating feedback," Opt. Express **17**(2), 395–404 (2009).
22. W. Zhang, R. Ma, C. Tang, Y. Rao, X. Zeng, Z. Yang, Z. Wang, Y. Gong, and Y. Wang, "All optical mode controllable er-doped random fiber laser with distributed bragg gratings," Opt. Lett. **40**(13), 3181–3184 (2015).
23. J. Deng, M. Han, Z. Xu, Y. Du, and X. Shu, "Stable and low-threshold random fiber laser via anderson localization," Opt. Express **27**(9), 12987–12997 (2019).
24. M. Gagné and R. Kashyap, "Demonstration of a 3 mw threshold er-doped random fiber laser based on a unique fiber bragg grating," Opt. Express **17**(21), 19067–19074 (2009).
25. Z. Zhou, L. Chen, and X. Bao, "Mode characteristic manipulation of random feedback interferometers in brillouin random fiber laser," Opt. Lett. **45**(3), 678–681 (2020).
26. M. Pang, X. Bao, and L. Chen, "Observation of narrow linewidth spikes in the coherent brillouin random fiber laser," Opt. Lett. **38**(11), 1866–1868 (2013).
27. M. Pang, X. Bao, L. Chen, Z. Qin, Y. Lu, and P. Lu, "Frequency stabilized coherent brillouin random fiber laser: theory and experiments," Opt. Express **21**(22), 27155–27168 (2013).
28. H. Wang, Z. Zhou, L. Chen, and X. Bao, "Acoustic wave coupling in dual-wavelength orthogonal polarized brillouin random fiber laser using polarization-maintaining fiber," J. Lightwave Technol. **40**(8), 2541–2547 (2022).
29. Y. Xu, S. Gao, P. Lu, S. Mihailov, L. Chen, and X. Bao, "Low-noise brillouin random fiber laser with a random grating-based resonator," Opt. Lett. **41**(14), 3197–3200 (2016).
30. Z. Zhou, P. Lu, L. Zhang, S. Mihailov, L. Chen, and X. Bao, "Thermal and acoustic noise insensitive brillouin random fiber laser based on polarization-maintaining random fiber grating," Opt. Lett. **44**(17), 4195–4198 (2019).
31. P. Lu, S. J. Mihailov, D. Coulas, H. Ding, and X. Bao, "Low-loss random fiber gratings made with an fs-ir laser for distributed fiber sensing," J. Lightwave Technol. **37**(18), 4697–4702 (2019).
32. Z. Zhou, L. Chen, and X. Bao, "Dynamic detection of acoustic wave generated by polarization maintaining brillouin random fiber laser," APL Photonics **5**(9), 096101 (2020).
33. P.-A. Nicati, K. Toyama, and H. J. Shaw, "Frequency stability of a brillouin fiber ring laser," J. Lightwave Technol. **13**(7), 1445–1451 (1995).
34. Z. Wu, L. Zhan, Q. Shen, J. Liu, X. Hu, and P. Xiao, "Ultrafine optical-frequency tunable brillouin fiber laser based on fiber strain," Opt. Lett. **36**(19), 3837–3839 (2011).
35. J. Li, H. Lee, T. Chen, and K. J. Vahala, "Characterization of a high coherence, brillouin microcavity laser on silicon," Opt. Express **20**(18), 20170–20180 (2012).
36. L. Zhang, Z. Qiu, Z. Xiao, J. Zhang, F. Pang, T. Wang, and X. Bao, "Frequency-stabilized brillouin random fiber laser enabled by self-inscribed transient population grating," Opt. Lett. **47**(1), 150–153 (2022).
37. N. Ghofraniha, I. Viola, F. Di Maria, G. Barbarella, G. Gigli, L. Leuzzi, and C. Conti, "Experimental evidence of replica symmetry breaking in random lasers," Nat. Commun. **6**(1), 6058 (2015).
38. A. S. Gomes, E. P. Raposo, A. L. Moura, S. I. Fewo, P. I. Pincheira, V. Jerez, L. J. Maia, and C. B. De Araújo, "Observation of lévy distribution and replica symmetry breaking in random lasers from a single set of measurements," Sci. Rep. **6**(1), 27987–27988 (2016).
39. Z. Zhou, L. Chen, and X. Bao, "High efficiency brillouin random fiber laser with replica symmetry breaking enabled by random fiber grating," Opt. Express **29**(5), 6532–6541 (2021).
40. F. Tommasi, E. Ignesti, S. Lepri, and S. Cavalieri, "Robustness of replica symmetry breaking phenomenology in random laser," Sci. Rep. **6**(1), 37113–37118 (2016).
41. F. Antenucci, A. Crisanti, and L. Leuzzi, "The glassy random laser: replica symmetry breaking in the intensity fluctuations of emission spectra," Sci. Rep. **5**(1), 16792 (2015).

Optics EXPRESS

42. B. C. Lima, A. S. Gomes, P. I. Pincheira, A. L. Moura, M. Gagné, E. P. Raposo, C. B. de Araújo, and R. Kashyap, "Observation of lévy statistics in one-dimensional erbium-based random fiber laser," J. Opt. Soc. Am. B **34**(2), 293–299 (2017).
43. A. S. Gomes, B. C. Lima, P. I. Pincheira, A. L. Moura, M. Gagné, E. P. Raposo, C. B. de Araújo, and R. Kashyap, "Glassy behavior in a one-dimensional continuous-wave erbium-doped random fiber laser," Phys. Rev. A **94**(1), 011801 (2016).

Supplemental Document

Optics EXPRESS

# Stabilizing Brillouin random laser with photon localization by feedback of distributed random fiber grating array: supplement

HAIYANG WANG,[1] PING LU,[2] CHEN CHEN,[1] STEPHEN MIHAILOV,[2] LIANG CHEN,[1] AND XIAOYI BAO[1]

[1]*Department of Physics, University of Ottawa, Ottawa, Ontario K1N 6N5, Canada*
[2]*National Research Council Canada, Ottawa, Ontario K1A 0R6, Canada*



Supplement DOI: https://doi.org/10.6084/m9.figshare.19786681

Parent Article DOI: https://doi.org/10.1364/OE.460736

# Stabilizing Brillouin random laser with photon localization by feedback of distributed random fiber grating array: Supporting Information

## 1. SIMULATION OF RFGA AND RFG BY TRANSFER MATRIX METHOD

### A. Simulation of RFGA

The reflection spectrum of the random fiber grating array (RFGA) is calculated by the transfer matrix method [1–3]. The amplitude of the reflected and transmitted waves before and after the $n_{th}$ uniform region of the random fiber grating (RFG) is represented in a matrix $M_n$, which is given by

$$\begin{bmatrix} a_n^+ \\ a_n^- \end{bmatrix} = M_n \begin{bmatrix} a_{n-1}^+ \\ a_{n-1}^- \end{bmatrix} \tag{S1}$$

where $a_n^+$ and $a_{n-1}^-$ are the amplitude of transmitted and reflected waves of the $n_{\text{th}}$ uniform region of the RFG, respectively. Based on the coupled-wave equation of the counter-propagating waves, the transfer matrix $M_n$ of an uniform region of the grating can be written as:

$$M_n = \begin{pmatrix} A - i\frac{\Delta\beta}{S}B & -i\frac{\kappa}{S}B \\ i\frac{\kappa}{S}B & A + i\frac{\Delta\beta}{S}B \end{pmatrix} \tag{S2}$$

where $A = \cosh(SL_0)$ and $B = \sinh(SL_0)$ with $L_0$ being the length of each uniform region, $\kappa$ is the coupling coefficient between the counter-propagating beams in the grating, which is determined by the refractive index modulation ($\Delta n$), $\Delta\beta = \beta_1 - \beta_2 - \pi/\Lambda_n$ is the wave-number deviation from the Bragg wavelength with $\Lambda_n$ being sub-grating period, $\beta_1 = 2\pi n/\lambda_1$ and $\beta_2 = 2\pi n/\lambda_2$ being propagation constants of forward and backward waves, respectively, and $S^2 = \left(|\kappa|^2 - \Delta\beta^2\right)$. The transfer matrix of the RFG can be written as the product of the transfer matrix of each uniform region, which is expressed as $G_l = M_1 M_2 ... M_{n-1} M_n$. The transfer matrix for a space of length $d_i$ between two gratings is given by

$$N_m = \begin{bmatrix} \exp(iKd_i) & 0 \\ 0 & \exp(-iKd_i) \end{bmatrix} \tag{S3}$$

where $K = 2\pi n/\Lambda$. The transfer matrix of the RFGA is given by

$$F = G_1 N_1 G_2 N_2 \ldots G_{i-1} N_{i-1} G_i N_i = \begin{pmatrix} F_{11} & F_{12} \\ F_{21} & F_{22} \end{pmatrix} \tag{S4}$$

Reflection coefficient of the RFGA are expressed as

$$R_{RFGA} = \left|\frac{F_{21}}{F_{22}}\right|^2 \tag{S5}$$

Reflection spectra are calculated using the above equations. In simulations, the core refractive index is $n = 1.456$, the laser-induced index change is $\Delta n = 1 \times 10^{-5}$ and the period of sub-gratings $\Lambda_n$ follows uniform distribution from 0.5180 µm to 0.5464 µm. The uniform length of each RFG is $L_0 = 25.9$ µm. The distribution of gratings in the RFGA and reflectivity of each grating are characterized by optical frequency domain reflectometry (OFDR) with a resolution of 8 µm. The distance between neighbor gratings is obtained as shown in Figure S1(a), which

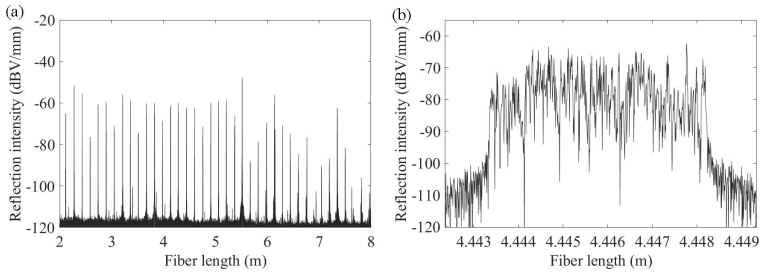


**Fig. S1.** Fig. S1. (a) Measured reflectivity versus distance of RFGA. (b) Measured reflectivity versus distance of one RFG.

changes in the range of 15 cm ± a couple of millimeters. Each grating has a length of 5 mm as plotted in Figure S1(b). The reflection intensity fluctuation indicates the random period change of sub-gratings of the RFG. We calculate the reflection spectrum of the RFGA according to the parameters of the RFGA we fabricated and measured. The reflection spectra of the RFGA with different grating numbers are calculated with a spectral resolution of 5 MHz, as shown in Figures S2(a-e). Due to the periodic variation of the sub-gratings being 28.4 pm, the spectrum shows a wide reflection range for the single RFG as plotted in Figure S2(a). Unlike the spectrum for one grating, the spectra for RFGAs present much narrower peaks induced by the wave interference between grating pairs as shown in Figures S2(c-d). We observe the higher finesse for the RFGA with more gratings due to the product of the finesse of more FP cavities with the same length between grating pairs. The spectrum of RFGA with 38 gratings (Figure S2(e)) is consistent with the measured data (Figure S2(f)), confirming the narrow filter effect of the RFGA from its high finesse and quality factor. The free spectral range (FSR) of the RFGA corresponds to the distance between grating pairs.

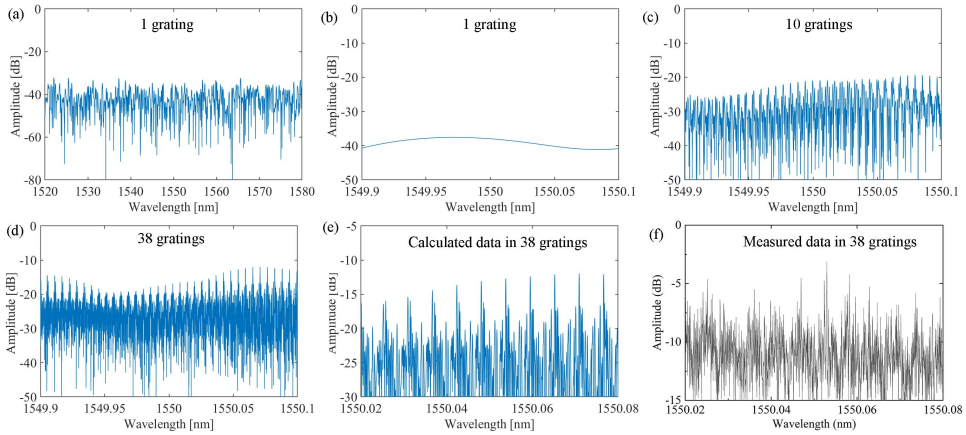


**Fig. S2.** Simulated reflection spectra for the RFGA with (a) single RFG in a large wavelength range. (b) Close-up of Figure S2(a). Simulated reflection spectra for the RFGA with (c) 10 RFGs; (d) 38 RFGs. (e) Close-up of Figure S2(d). (f) Measured reflection spectrum of the RFGA with 38 gratings.

### B. Simulation of 5 cm-long RFG

The reflection spectrum of a 5 cm-long RFG is calculated as shown in Figure S3. The ten times increase of the refractive index modulation points enables higher reflection and narrower spectral peaks of the reflection spectra as presented in Figs. S3(a-b) than that of the 5 mm-long RFG (RFGA with one RFG) as plotted in Figures S2(a-b). The spectrum of the 5 cm-long RFG shows broader linewidth peaks with lower quality factor than that of the RFGA with 38 gratings, suggesting weaker multi-scattering between sub-gratings in the RFG.

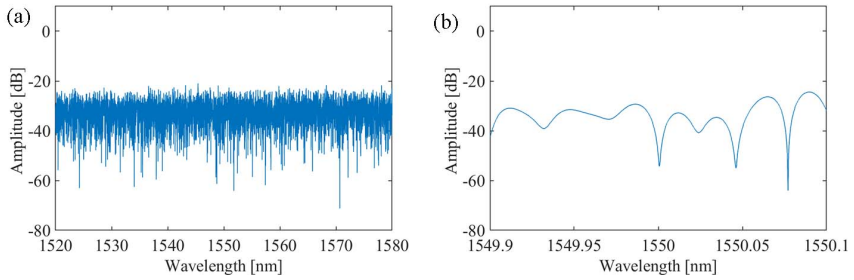


**Fig. S3.** (a) Simulated reflection spectrum for a 5 cm-long RFG. (b) Close-up of Figure S3(a).

## 2. INTENSITY FLUCTUATION AND $\alpha$-STABLE DISTRIBUTION FITTING

The temporal intensity fluctuation is measured in a time scale of 1 s. Time series (left), intensity probability (center) and phase portrait (right) of the random lasing emission at different pump powers are calculated as plotted in Figure S4. The intensity is normalized to the maximum value. The phase portrait is calculated by plotting $I_N$ versus $I_{N+k}$ with a delay of $k = 1$, which exhibits motion on an outward spiraling and folding trajectory. The $N$ in phase portraits is $1\times10^7$ in the temporal trace of 1 s corresponding to the resolution of 100 ns, indicating the minimum response time of 100 ns of the random laser, which is much shorter than the cavity trapping time of tens of μs showing in Figure 6(c) in the main document for the low power of 16 mW. At high pump power, the laser is limited by white noise in MHz frequency range, which means it will ignore ns disturbance. Because spontaneous scattered light generated by random thermal noise dominates the Brillouin scattering process at low pump power below the threshold (6 mW), the intensity presents stochastic behavior with large fluctuation and phase portrait shows chaotic trajectory as plotted in Figure S4(a). We find an asymmetric behavior with a long-tailed statistic in probability distribution and a more centered phase portrait at the pump power above the threshold (16 mW) as shown in Figure S4(b). We conclude that some longitudinal lasing modes dominate the intensity change of the random system. When the BRFL is pumped at 24 mW, however, the large intensity fluctuation is significantly reduced, as shown in Figure S4(c). This is because the number of longitudinal modes is reduced by the high finesse of the RFGA at high pump power. The weak fluctuation of intensity with symmetry distribution indicates single-mode lasing in the random system. The phase portrait with a well-confined cycle signature is expected as the successive temporal points are coherently related in phase relation in single-mode lasing operation. By further increasing the pump power, less intensity and phase changes are achieved (Figure S4(d)), which means the reduced background noise for the lasing emission owing to the narrower filter effect of the RFGA with a higher quality factor.

By analyzing the data in Figure S4, the intensity probabilities are identified with $\alpha$-stable Lévy distribution, which is given by [4]

$$P(k) = \exp\{-|\gamma k|^{\alpha}[1 - i\beta\,\mathrm{sgn}(k)\Phi] + ik\delta\} \tag{S6}$$

where Lévy index $\alpha \in (0, 2]$ governs the intensity fluctuation. The probability distribution follows Lévy behavior in the range of $0 < \alpha < 2$ and Gaussian behavior at the boundary value $\alpha = 2$. $\beta \in [-1, 1]$, $\delta \in (-\infty, \infty)$, and $\gamma \in (0, \infty)$ are the skewness, location and scale parameter, respectively. $\Phi = \tan(\pi\alpha/2)$ if $\alpha \neq 1$, whereas $\Phi = -(2/k)\ln|k|$ if $\alpha = 1$. The fitting curves of the intensity probability are shown in red dashed lines in the center of Figure S4. The fitting values of the parameters are listed in Table S1.

## 3. INTENSITY FLUCTUATIONS IN DIFFERENT DISORDERED FEEDBACK MEDIA

Relative intensity noise (RIN) is characterized by calculating the power spectral density of intensity trace of 1 s. Figure S5(a) and Figure S5(b) show RIN for the BRFLs based on 5 cm-long RFG and 500 m-long Rayleigh scattering fiber at different pump powers, respectively. We observe reduced RIN with increased pump power in the RFG-based BRFL indicating less mode competition. The high-noise peaks at high frequencies from 0.1 MHz to 1 MHz for all powers confirm the mode competition in the RFG-based BRFL in a time scale of 1 s. Different from RFG and RFGA-based random lasers, which have low RIN at high pump power, the Rayleigh scattering fiber-based BRFL has low RIN at low pump power as plotted in Figure S5(b). When the

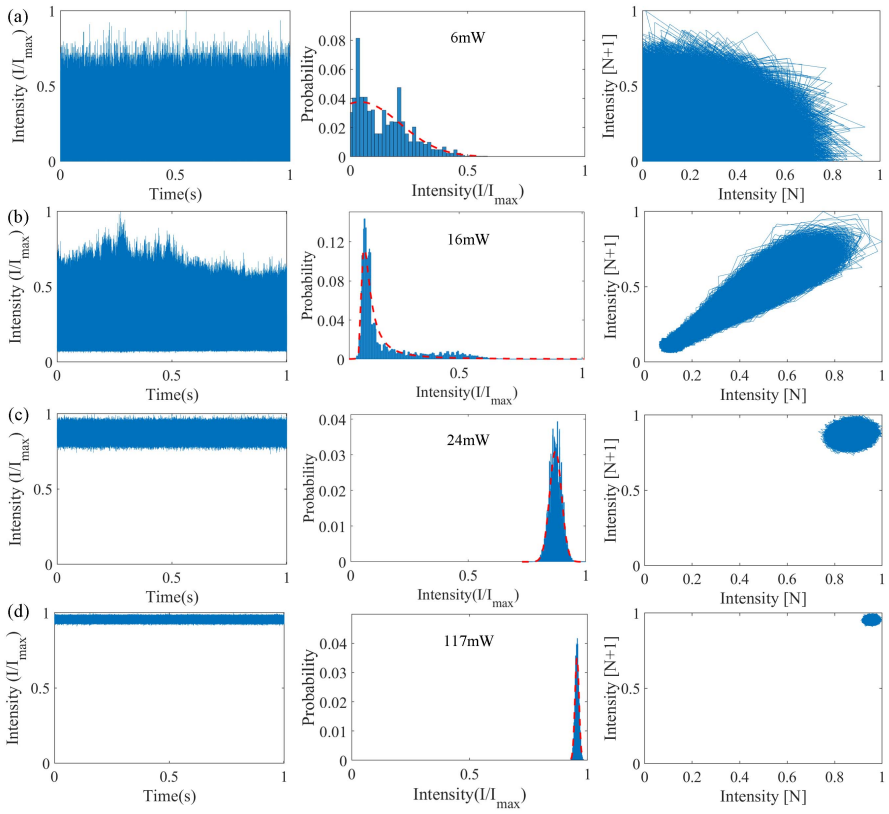


**Fig. S4.** Time varied intensity of BRFL at pump power of (a) 6 mW; (b) 16 mW; (c) 24 mW; (d) 117mW; temporal trace (left), intensity probability (center) and phase portrait (right). Red dash curves are $\alpha$-stable fits to intensity probability distributions.

pump power increases to 33 mW, we observe a sharp increase at low-frequency range from 1 Hz to 10 kHz and several noise peaks at high-frequency above 10 kHz. Similar RIN has been reported in the BRFL with a 10 km-long Brillouin gain fiber/RS fiber [5, 6] and in the multi-wavelength BRFL [7]. The normalized temporal trace of intensity fluctuation at the pump power of 67 mW is plotted in the inset of Figure S5(b). We find several intensity peaks with large fluctuation. Unlike the high finesse RFGA at high pump power, which supports one longitudinal mode owing to narrow filter effect, the multiple modes are coexisted in the random laser based on RS feedback fiber at high pump power. In addition, the nonlinear effects are excited in the long RS fiber at high power of the Stokes wave in the gain fiber under high pump power. The back-scattered Stokes wave is affected not only by the linear Rayleigh scattering but also by nonlinear effects in the RS feedback fiber leading to more modes in the gain bandwidth. The gain competition of modes at high pump power leads to large intensity fluctuation and high intensity noise. The RINs of the RFG and RS-based BRFLs are over 30 dB higher than RFGA-based BRFL due to the

**Table S1. Summary of the fitting parameters for the intensity probability in the BRFL at different pump powers**

| Pump power | $\alpha$ | $\beta$ | $\gamma$ | $\delta$ |
|---|---|---|---|---|
| P = 6 mW ($P/P_{th}$=0.83) | 2 | 0.017 | 0.12 | 0.042 |
| P = 16 mW ($P/P_{th}$=2.22) | 0.83 | 0.98 | 0.02 | 0.12 |
| P = 24 mW ($P/P_{th}$=3.33) | 2 | 0.08 | 0.018 | 0.87 |
| P = 117 mW ($P/P_{th}$=16.25) | 2 | 0.985 | 0.006 | 0.96 |

mode competition contributed by their low-finesse and nonlinear effects.

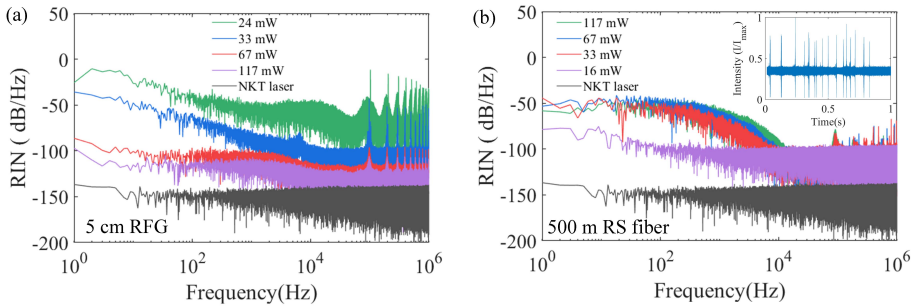


**Fig. S5.** RIN comparison at different pump powers for the BRFL based on (a) 5 cm RFG; (b) 500 m RS fiber. Inset: the temporal trace in 1 s when the pump power is 67 mW.

## REFERENCES


1. R. Kashyap, *Fiber bragg gratings* (Academic press, 2009).
2. O. Shapira and B. Fischer, "Localization of light in a random-grating array in a single-mode fiber," JOSA B **22**, 2542–2552 (2005).
3. Z. Zhou, C. Chen, P. Lu, S. Mihailov, L. Chen, and X. Bao, "Random fiber grating characterization based on ofdr and transfer matrix method," Sensors **20**, 6071 (2020).
4. B. C. Lima, P. I. Pincheira, E. P. Raposo, L. d. S. Menezes, C. B. de Araújo, A. S. Gomes, and R. Kashyap, "Extreme-value statistics of intensities in a cw-pumped random fiber laser," Phys. Rev. A **96**, 013834 (2017).
5. B. Saxena, Z. Ou, X. Bao, and L. Chen, "Low frequency-noise random fiber laser with bidirectional sbs and rayleigh feedback," IEEE Photonics Technol. Lett. **27**, 490–493 (2014).
6. L. Zhang, Y. Xu, S. Gao, B. Saxena, L. Chen, and X. Bao, "Multiwavelength coherent brillouin random fiber laser with ultrahigh optical signal-to-noise ratio," IEEE J. Sel. Top. Quantum Electron. **24**, 1–8 (2017).
7. L. Zhang, Y. Wang, Y. Xu, D. Zhou, L. Chen, and X. Bao, "Linearly polarized multi-wavelength fiber laser comb via brillouin random lasing oscillation," IEEE Photonics Technol. Lett. **30**, 1005–1008 (2018).

# 8 Reducing frequency fluctuation in Brillouin random fiber laser by random fiber grating ring resonator

Reproduce from :
**Haiyang Wang**, Chen Chen, Ping Lu, Stephen Mihailov, Liang Chen and Xiaoyi Bao
Optics Letter. 47(15), 3900-3903. (2022) ;
https ://doi.org/10.1364/OL.464434

## Author contributions

All authors made important contributions to this work ; X.B., H.W. and C.C. conceived and designed experiments ; P.L. and S.M. fabricated the random fiber grating ; C.C. fabricated the random fiber grating ring ; H.W. conducted experiments with assistance of C.C ; H.W. carried out numerical calculations and collected experimental data ; H.W., X.B., and L.C. analyzed experimental data ; All authors contributed to the writing of this paper.

## Summary

The previous chapter demonstrated the stabilization of the Brillouin random fiber laser (BRFL) based on the strong scattering RFGA enabled by light localization. This chapter presents another frequency drift reduction technique achieved by a random fiber grating ring as distributed feedback of the BRFL. The random fiber grating ring (RFGR) consists of a 5 cm long polarization-maintaining random fiber grating (PM-RFG) and a PM fiber coupler with a high split ratio of 95/5. Narrow linewidth peaks are generated due to light confinement in the low-loss RFGR. Due to scattering paths with small differences from the RFGR, many random modes with small frequency differences are excited in the BRFL. Random modes can be chosen to compensate for the small frequency drift caused by temperature and acoustic variations, which provide the resonant condition without mode hopping. Optical injection locking is achieved between the high-Q RFGR and Brillouin random lasing. The frequency stabilized BRFL is demonstrated by taking advantage of the self-injection locking and self-adjusting random modes in the high-Q RFGR. We compare the BRFL with injection locking through high-Q RFGR to the BRFL without injection locking in the RFG distributed feedback. The BRFL with injection locking shows the long-lived single lasing mode operation with a small frequency drift, while the BRFL with the ultra-low-Q RFG shows multiple lasing modes with a small side-mode suppression ratio, leading to fast mode hopping within a large frequency range. The following manuscript provides evidence for the frequency stabilized BRFL via the RFGR in the all-optical locking mechanism. The main drawback of this mechanism is that the RFGR is sensitive to surrounding variations, leading to high intensity noise at low frequencies.

# Reducing frequency fluctuation in Brillouin random fiber laser by random fiber grating ring resonator

HAIYANG WANG[1], CHEN CHEN[1], PING LU[2], STEPHEN MIHAILOV[2], LIANG CHEN[1], AND XIAOYI BAO[1]

[1]Department of Physics, University of Ottawa, Ottawa, Ontario K1N 6N5, Canada
[2]National Research Council Canada, Ottawa, Ontario K1A 0R6, Canada

Compiled September 9, 2022

**Frequency fluctuation is a major problem in high precision metrology as real-time optical frequency measurement is not available with commercial photodetectors, alternatively, frequency stabilized lasers as a reference are also not accessible in most Labs. In this study, we proposed and demonstrated a polarization-maintaining random fiber grating ring (PM-RFGR) resonator in a PM Brillouin random fiber laser (BRFL) to achieve sub-MHz frequency drift, which is measured by the optical beat of the random laser and the pump laser. Experimental results show that longitudinal modes are suppressed in the BRFL owing to the feedback of the RFGR resonating with one longitudinal mode of the random laser. The BRFL shows mode hopping free operation over 14.9 s due to the self-adjustment of random modes with small frequency difference to thermal and acoustic variations and self-injection locking through RFGR. As a result, a small frequency drift of ∼340 kHz with single-longitudinal mode is achieved in the BRFL enabled by the RFGR, which offers an all optical locking mechanism for optical frequency stabilization.** 

https://doi.org/10.1364/OL.464434

## 1. INTRODUCTION

Random fiber lasers (RFLs) with distributed feedback media have attracted attention in the last few decades [1–3]. Randomly scattered light from distributed feedback media traveling in gain media gives rise to more complicated paths compared with light propagation in conventional lasers, which makes unique features for applications in sensing [4] and secure communication [5]. RFLs are accompanied by large frequency drift owing to the variable cavity length. Erbium-doped fiber (EDF)-based RFL with frequency stabilization based on the light localization in distributed grating array has been demonstrated [6]. However, the frequency stabilization is on the order of pm corresponding to hundreds of MHz owing to the large EDF gain bandwidth of tens of nm. Stimulated Brillouin scattering with tens of MHz bandwidth as the gain of RFL, so-called Brillouin random fiber laser (BRFL), has been demonstrated to reduce frequency drift. Few modes from the feedback fiber are amplified above the noise level in the BRFL resulting in several lasing spikes with a frequency drift of 4 MHz [7]. The self-inscribed transient population grating through an EDF loop in BRFL was demonstrated showing a frequency drift of 1.2 MHz over 0.8 s owing to the milliseconds of photonic memory in EDF [8]. Instead of the complex setup by incorporating additional devices to the random cavity, the frequency stabilized BRFL can be achieved in existing components, such as distributed feedback media. Random fiber grating array as distributed feedback with a small frequency drift of 620 kHz over 12 s under high pump power was proposed and demonstrated owing to the light localization and high finesse peaks in the strongly scattering disordered distributed feedback medium [9]. Considering the high density of random mode numbers and insensitivity of external variations of the random fiber grating (RFG) [10] and the narrow bandwidth of the fiber ring [11], the random fiber grating ring (RFGR), formed by inserting a RFG into a fiber ring, can be utilized as distributed feedback to achieve a frequency stabilized BRFL based on the self-injection locking mechanism. Because of multiple reflection planes ($\sim 10^5$) in the RFG of 5 cm, the effective length of the single ring resonator is enhanced, which is equivalent to increased round trip rings. Instead of a single trip in a ring, this is critical for many longitudinal modes rejection and single lasing mode selection. The role of the RFG compared with the fiber Bragg grating (FBG) is to allow multiple random modes lasing with small frequency separation. Whenever temperature or acoustic wave is changed, the resonant lasing condition will be maintained among existing random modes. Hence optical wave will be maintained over many round trips without the need of re-establishment as that in cavity laser or fixed frequency peak in FBGs, which makes all reflections at the same peak of the mode.

In this study, we demonstrate a frequency stabilized polarization-maintaining (PM) BRFL enabled by a PM-RFGR resonator. Longitudinal modes are suppressed by the narrow filter effect of the RFGR leading to a single longitudinal mode operation. The random modes with a small frequency difference from the variable cavity length suggest a smooth frequency drift. In addition, the self-injection locking through the RFGR maintains the lasing frequency. Taking the advantages of the RFGR, the BRFL shows a low frequency drift of ∼340 kHz without mode hopping during 14.9 s for the BRFL in the ring resonant

peak, which is reduced by a factor of 28 than the frequency drift of BRFL out of the ring resonant peak (the reflected signal only from the RFG). The RFGR-based BRFL exhibits 15 dB lower relative intensity noise (RIN) at high frequencies over 1 kHz and 10 dB lower frequency noise compared with those of only RFG as distributed feedback thanks to suppressed mode coupling.

The RFGR consists of a 2×2 PM coupler and a PM-RFG as plotted in Fig. 1(a). For the coupler, light propagates from port 3 to ports 4/2 and from port 4 to ports 3/1, where port 1 and port 2 are tap ports. Figure 1(b) shows the working principle of the RFGR-based BRFL. Due to the recirculating propagation of light in the RFGR, the reflection spectrum shows narrow peaks with a fixed free spectral range (FSR). The BRFL with strong scattering distributed feedback exhibits many longitudinal modes in the Brillouin gain bandwidth. Self-injection locking of the BRFL is achieved through the narrow reflection peaks of the RFGR when the frequency of the RFGR reflected back to the random laser is in resonance with the gain bandwidth. The longitudinal modes are suppressed when the BRFL is self-injection locked to the peaks of the RFGR as shown in Fig. 1(b). The self-injection locking enabled by the RFGR forces lasing frequency to the ring resonant peak enabling stable lasing operation. More strikingly, many cavities with a small difference in length (so-called random modes) in the BRFL can keep lasing resonance around a small frequency range of one longitudinal mode under small thermal and acoustic variations. The established random modes and the self-injection locking reduce lasing frequency drift.

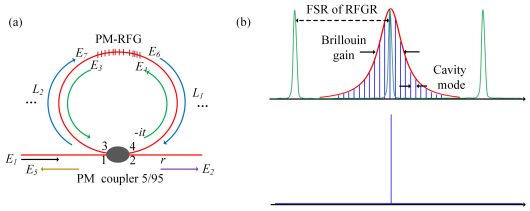


**Fig. 1.** (a) Schematic of a RFGR. (b) The operation scheme of RFGR in a BRFL.

The reflection spectrum of the RFGR is calculated by the transfer matrix and scattering matrix methods [12, 13]. The RFG consists of $n$ grating elements with random periods, and each of them has a uniform length $L_0$. The amplitude of reflected and transmitted waves before and after the $n_{th}$ uniform region is represented in a matrix ($M_n$)

$$M_n = \begin{pmatrix} A - i\frac{\Delta\beta}{S}B & -i\frac{K}{S}B \\ i\frac{K}{S}B & A + i\frac{\Delta\beta}{S}B \end{pmatrix} \quad (1)$$

where $A = \cosh(SL_0)$ and $B = \sinh(SL_0)$, $K$ is the coupling coefficient, which is determined by the refractive index modulation ($\Delta n$), $\Delta\beta = 2\beta - \pi/\Lambda_n$ is the wave-number deviation from the Bragg wavelength with $\Lambda_n$ being grating period of $n_{th}$ uniform region and $\beta = 2\pi n/\lambda$ being propagation constant, and $S^2 = (|K|^2 - \Delta\beta^2)$. The transfer matrix of the RFG ($M_{RFG}$) is the product of the transfer matrix of each uniform region

$$M_{RFG} = M_1 M_2 ... M_{n-1} M_n = \begin{pmatrix} M_{11} & M_{12} \\ M_{21} & M_{22} \end{pmatrix} \quad (2)$$

The relations between the fields $E_3$, $E_4$, $E_6$, and $E_7$ of the circulating waves in the ring can be calculated via scattering matrix

$$\begin{bmatrix} E_3 \\ E_7 \end{bmatrix} = \begin{bmatrix} M_{11} & M_{12} \\ M_{21} & M_{22} \end{bmatrix} \begin{bmatrix} E_4 \\ E_6 \end{bmatrix} \quad (3)$$

where the relations between the optical waves inside the ring and the reflected wave $E_5$ are given by

$$\begin{aligned} E_4 &= -itE_1 e^{i\beta L_1} + rE_3 e^{i\beta L}, \\ E_7 &= rE_6 e^{i\beta L}, \\ E_5 &= -itE_6 e^{i\beta L_1}, \end{aligned} \quad (4)$$

where $L = L_1 + L_2$ is the ring length, and $t$ and $r$ are transmission coefficients of the coupler in port 4 and port 2, with $t^2 : r^2 = \kappa : 1 - \kappa$ being the split ratio and $t^2 + r^2 = \gamma < 1$ by considering the loss of the RFGR. $\gamma = 0.91$ for the RFGR with a loss of 0.4 dB. The imaginary $-i$ in front of $t$ means the $\pi/2$ phase shift between the two ports. By solving the Eqs. (1-4), the reflected field is expressed as

$$\frac{E_5}{E_1} = \frac{t^2 M_{21} e^{2i\beta L_1}}{M_{22} + M_{11} r^2 e^{2i\beta L} - 2re^{i\beta L}} \quad (5)$$

The reflection coefficient of the RFGR is given by $R = |E_5/E_1|^2$. In the simulation, the core refractive index is $n = 1.456$, the laser-induced index change is $\Delta n = 1 \times 10^{-5}$. The 5 cm long RFG consists of around 2000 uniform gratings with the random period $\Lambda_n$ which follows uniform distribution from 0.5180 µm to 0.5464 µm, and each uniform grating is $L_0 = 25.9$ µm.

The reflection spectrum for the coupler with the split ratio of $\kappa = 0.05$ corresponding to 5/95 is calculated and plotted in Fig. 2(a). The reflection coefficient reaches the maximum when the phase of light traveling in the ring satisfies $\beta L = 2\pi m$. The reflection spectrum shows a narrow linewidth of 2.2 MHz and a FSR of 118.8 MHz. The non-uniform amplitude of peaks is contributed by the interference pattern of the reflection spectrum of the RFG as shown in the inset of Fig. 2(a). Figure 2(b) shows the linewidth and finesse as a function of the split ratio. The linewidth (finesse) increases (decreases) with an increased split ratio. This is becasue the less portion of light propagates in the ring for each round trip and light propagates with fewer round trips for the coupler with a larger split ratio before dropping to the noise level. The coupler with a small split ratio is preferred for the BRFL as the narrow linewidth and large finesse suppress longitudinal modes and alleviate mode competition.

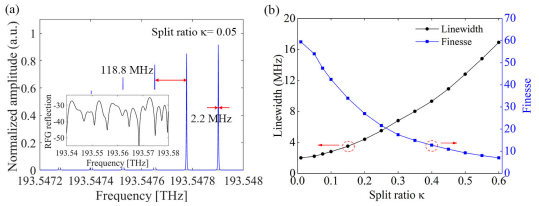


**Fig. 2.** (a) Calculated reflection spectrum of the RFGR with a split ratio $\kappa = 0.05$. Inset: calculated reflection spectrum of RFG. (b) Calculated linewidth and finesse as a function of $\kappa$.

The PM coupler with the split ratio of $\kappa = 0.05$ is selected in the experiment instead of the smaller split ratio of $\kappa = 0.01$ because the resonant peaks are not experimentally observed for

the RFGR with $\kappa = 0.01$ at the same pump power. The power is inadequate to support photons over many round trips in the ring with $\kappa = 0.01$ owing to the loss of the RFGR. The RFGR with $\kappa = 0.05$ is characterized using a frequency scanned laser with a sweeping rate of 100 MHz/ms. The laser is injected into the RFGR by an optical circulator and the back-scattered light is sent to a photodetector (PD) and recorded on an oscilloscope. The reflected signal is shown in Fig. 3(a). The time interval between two resonant peaks is 1.17 ms corresponding to the measured FSR of 117 MHz, which is consistent with the calculated result. Figure 3(b) shows that the measured linewidth is 2.1 MHz, which agrees with the calculated result.

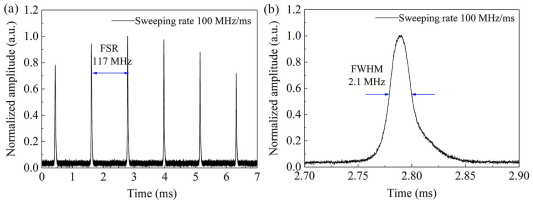


**Fig. 3.** (a) Measured reflection spectrum for the RFGR with a split ratio of $\kappa = 0.05$. (b) Measured linewidth.

The schematic of the BRFL setup is shown in Fig. 4. The pump light from a NKT laser is split into two paths by a coupler. The light in one path is utilized to beat with the BRFL. In the other path, the frequency of pump light is modulated using an EOM driven by a RF source. The up-shifted frequency is selected by a narrow filter, which is adjusted around 4 GHz to align the Brillouin lasing frequency with one of resonant peaks of the RFGR. The amplified pump light after an erbium-doped fiber amplifier (EDFA) is aligned with the slow axis of a polarization beam splitter (PBS) and injected into the 2 km PM Brillouin gain fiber. Backward Stokes light from the gain fiber is launched into the RFGR, which is placed in a sealed box to reduce temperature and acoustic fluctuations, and the reflected Stokes light is sent to the other end of the gain fiber. The heterodyne-based method is utilized to measure the spectral evolution of the narrow linewidth lasing emission. The spectra are detected by a high-speed PD with 20 GHz bandwidth and recorded by an electrical spectrum analyzer (ESA). As the preserved state of polarization of light in the all PM devices -based BRFL, the birefringence effect induced frequency difference of modes is eliminated, which is beneficial for the BRFL with lower frequency drift.

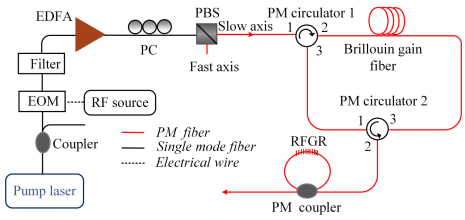


**Fig. 4.** Schematic of the RFGR-based BRFL.

To evaluate the frequency stability of the BRFL, the real-time spatio-temporal evolution of the beat signal between the pump laser and the BRFL is measured in a time step of 22 ms. The BRFL in and out of the ring peaks are characterized to verify that the reducing frequency fluctuation in the BRFL is attributed by RFGR as distributed feedback instead of RFG. The BRFL in the ring peak means the resonant peak frequency of the RFGR ($\nu_R$) is equal to the Brillouin lasing frequency ($\nu_L$) that is $\nu_R = \nu_L$ corresponding to the RFGR as distributed feedback, while BRFL out of the ring peak means $\nu_R \neq \nu_L$, corresponding to only the RFG as distributed feedback. The two cases are measured by changing the Brillouin lasing frequency, which is controlled by changing the pump frequency via driving frequency of EOM. Figure 5(a) and Figure 5(b) show the spectral evolution for the BRFL out of and in the ring peaks, respectively, in which the color bar represents the power and red lines show the frequency drift at peak values. The frequency of beat spectra is normalized to $f - \langle f \rangle$. The BRFL shows a large frequency drift of ~9.6 MHz with rapid mode hopping (the longest mode hopping free time is 2.2 s). This is because the broadband peak of the RFG allows the co-existing of many longitudinal modes within the gain bandwidth. The scattering in the RFG is not enough to realize photon localization and the modes randomly hop over a short time. The beat spectrum without normalization at 12 s is plotted in Fig. 5(c) showing multiple longitudinal modes operation with a side-mode suppression ratio (SMSR) of 35 dB. The multi-mode structure confirms the broadband peak of the reflection spectrum of the RFG. For the BRFL in the ring resonant peak, the evolution spectrum shows a single-longitudinal mode with mode hopping free lasing operation over 14.9 s as plotted in Fig. 5(b). The BRFL exhibits a small frequency drift of ~340 kHz during 14.9 s enabled by self-injection locking through the RFGR and self-adjustment of random modes to slight thermal and acoustic variations. The frequency drift is reduced by a factor of 28 compared with the RFG as distributed feedback. The standard deviation (STD) of frequency drift is reduced from 3.19 MHz to 0.10 MHz due to the smooth change of the lasing mode. The beat spectrum without normalization at 5 s of Fig. 5(b) is plotted in Fig. 5(d). The narrow peak of the RFGR indicates that longitudinal modes are suppressed and one lasing mode with a SMSR of 55 dB is obtained, which is 20 dB higher than RFG as distributed feedback.

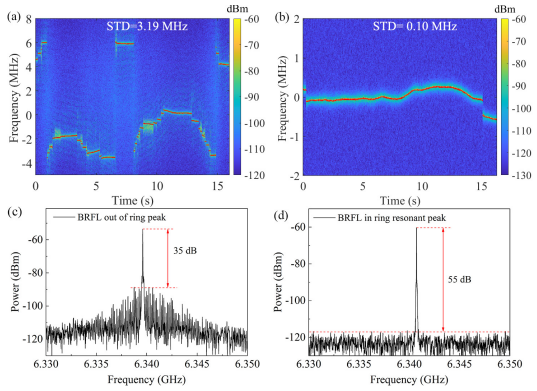


**Fig. 5.** (a) Real-time spatio-temporal evolution of the RFGR-based BRFL for (a) BRFL out of the ring resonant peak; (b) BRFL in the ring resonant peak. (c) The beat spectrum at 12 s of Fig. 5(a). (d) The beat spectrum at 5 s of Fig. 5(b).

Frequency noise is characterized using an imbalanced symmetric 3×3 coupler fiber interferometer [14], in which a 1 km single mode fiber as the delay line is inserted into one arm. The frequency noise spectra of the BRFLs at the same output

power are shown in Fig. 6. The BRFL in the ring peak exhibits 10 dB lower frequency noise than that of BRFL out of the ring peak. The stable frequency drift with single-mode operation enabled by RFGR suggests the reduced mode coupling in the gain bandwidth leading to low frequency noise. The frequency noise spectrum of the BRFL with RFGR is comparable at frequencies below 10 kHz and lower at high frequencies over 10 kHz compared with the phase-locked pump laser. The same level of the frequency noise at low frequencies is attributed by the multiple random modes with small frequency difference from the RFGR, which can keep lasing resonance around a small frequency range without mode hopping under small thermal and acoustic variations. The random modes add a phase averaging effect that mitigated the temperature and acoustic impacts in low frequency range. The lower frequency noise at high frequencies is attributed by the Lorentzian envelop of the random phase noise in the BRFL with distributed Rayleigh scattering [15].

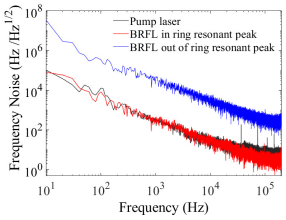


**Fig. 6.** Frequency noise spectra for the BRFL out of ring resonant peak, the BRFL in ring resonant peak and the pump laser.

The RIN of the BRFL is analyzed by applying the Fourier transform of intensity traces as shown in Fig. 7(a). The RIN of the pump laser is measured for comparison. The RIN of BRFL in the ring peak is up to 15 dB lower than that of BRFL out of ring peak over 1 kHz. The noise peaks in the high frequency range from 100 kHz to 1 MHz correspond to the inverse of the round trip time of light in the random system being reduced. The multiple longitudinal modes are suppressed by the narrow peaks of the RFGR and the gain competition is alleviated leading to the low RIN with weak noise peaks in the high frequencies. However, the RIN at frequencies below kHz is higher for the BRFL in of ring peak than that of BRFL out of ring peak. The small frequency drift under the external noises induces large intensity fluctuation because of the narrow linewidth of the RFGR, which is hundreds of times smaller than that of RFG. The small frequency drift due to thermal and acoustic variations (slow process) induces the lasing mode deviation from the narrow resonant peak of the RFGR with steep slope for frequency change conversion to intensity change, which leads to the large

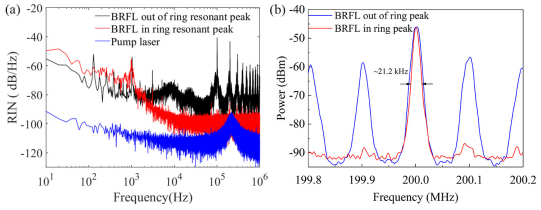


**Fig. 7.** (a) RIN for the BRFL out of ring resonant peak, the BRFL in ring resonant peak and pump laser. (b) Linewidth for the BRFL out of ring resonant peak and in ring resonant peak.

intensity noise at low frequencies (slow event). The high RIN below 1 kHz can be reduced by inserting a EDF into the RFGR because the millisecond photonic memory of EDF [8], which will be investigated in the following experiment. Figure 7(b) shows the averaged linewidth, which is measured using the delayed self-heterodyne method [16] with a 200 km delay fiber and a 200 MHz acousto-optical modulator in two paths. The one dominant peak confirms the single-longitudinal mode propagation in the RFGR-based BRFL. The 20 dB bandwidth of the RFGR-based BRFL is 21.2 kHz corresponding to a 3 dB linewidth of 1.06 kHz.

In conclusion, a frequency stabilized BRFL enabled by RFGR in an all polarization-maintaining system has been proposed and demonstrated. Using the RFGR with narrow reflection peaks, a large number of random modes, and self-injection locking as distributed feedback, the BRFL shows a mode hopping free single-mode operation with a low frequency drift of ∼340 kHz over 14.9 s, which is 28 times smaller than those of the multi-modes BRFL with RFG as distributed feedback. Moreover, the BRFL shows lower RIN at high frequencies over 1 kHz and lower frequency noise enabled by RFGR compared with those of RFG thanks to the suppressed modes coupling. The proposed BRFL with the significant reduction of frequency fluctuation paves the way for applications in optical metrology.

**Funding.** This research was supported in part by Canada Research Chairs (75-67138), by Natural Sciences and Engineering Research Council of Canada (NSERC) (06071-RGPIN-2015), and by China Scholarship Council (CSC).

**Disclosures.** The authors declare no conflicts of interest.

**Data Availability.** Data underlying the results presented in this paper are not publicly available at this time but may be obtained from the authors upon reasonable request.

## REFERENCES

1. C. J. de Matos, L. d. S. Menezes, A. M. Brito-Silva, M. M. Gámez, A. S. Gomes, and C. B. de Araújo, Phys. review letters **99**, 153903 (2007).
2. S. Babin, A. El-Taher, P. Harper, E. Podivilov, and S. Turitsyn, Phys. Rev. A **84**, 021805 (2011).
3. H. Wang, Z. Zhou, L. Chen, and X. Bao, J. Light. Technol. (2022).
4. L. Zhang, P. Lu, Z. Zhou, Y. Wang, S. Mihailov, L. Chen, and X. Bao, IEEE Sensors J. **20**, 5885 (2020).
5. S. Gao, L. Zhang, Y. Xu, L. Chen, and X. Bao, IEEE Photonics Technol. Lett. **29**, 1352 (2017).
6. J. Deng, M. Han, Z. Xu, Y. Du, and X. Shu, Opt. express **27**, 12987 (2019).
7. M. Pang, X. Bao, and L. Chen, Opt. letters **38**, 1866 (2013).
8. L. Zhang, Z. Qiu, Z. Xiao, J. Zhang, F. Pang, T. Wang, and X. Bao, Opt. letters **47**, 150 (2022).
9. H. Wang, P. Lu, C. Chen, S. Mihailov, L. Chen, and X. Bao, Opt. Express **30**, 20712 (2022).
10. Z. Zhou, P. Lu, L. Zhang, S. Mihailov, L. Chen, and X. Bao, Opt. letters **44**, 4195 (2019).
11. J. E. Heebner, V. Wong, A. Schweinsberg, R. W. Boyd, and D. J. Jackson, IEEE journal quantum electronics **40**, 726 (2004).
12. Z. Zhou, C. Chen, P. Lu, S. Mihailov, L. Chen, and X. Bao, Sensors **20**, 6071 (2020).
13. Z. Fang, K. Chin, R. Qu, and H. Cai, *Fundamentals of optical fiber sensors*, vol. 226 (John Wiley & Sons, 2012).
14. D. Xu, F. Yang, D. Chen, F. Wei, H. Cai, Z. Fang, and R. Qu, Opt. express **23**, 22386 (2015).
15. B. Saxena, Z. Ou, X. Bao, and L. Chen, IEEE Photonics Technol. Lett. **27**, 490 (2014).
16. T. Okoshi, K. Kikuchi, and A. Nakayama, Electron. letters **16**, 630 (1980).

# 9 Acoustic wave coupling in dual-wavelength orthogonal polarized Brillouin random fiber laser


**Haiyang Wang**, Zichao Zhou, Liang Chen and Xiaoyi Bao,
Journal of Lightwave Technology. 40(8), 2541-2547 (2022) ;
https ://ieeexplore.ieee.org/document/9672724

## Author contributions

All authors contributed to the preparation of the paper. H.W. and Z.Z. contributed equally to performing lasing measurements. Z.Z and H.W designed experimental setup ; H.W., Z.Z. and X.B wrote the paper ; H.W., Z.Z. and L.C. analyzed measured data ; X.B. supervised measurements and data analysis.

## Summary

The two previous chapters demonstrated frequency-stabilized BRFLs based on RFG distributed feedback by controlling the mode behavior and light propagation. We are considering to manipulate lasing behavior in weak Rayleigh scattering fibers. In polarization-maintaining (PM) fibers, two-dimensional stresses from Boron-doped-silica rods introduce birefringence. Therefore, linear polarized light in the PM fiber gives rise to the preserved polarization state. Compared to BRFLs based on single-mode fibers (SMF), all-PM fiber-based Brillouin random fiber lasers (BRFL) shows lower intensity and frequency noises due to the immunity to external disturbances [112, 113]. We can achieve a orthogonal polarized dual-wavelength BRFL due to the birefringence of the PM fiber. Acoustic wave coupling can be achieved in the BRFL when the pump light is aligned at 45 degrees from the slow/fast axis of the PM fiber. This is because the frequency difference of 5 MHz between two acoustic waves in both polarization axes (corresponding to birefringence of $10^{-4}$) is smaller than the Brillouin gain bandwidth of 20 MHz, leading to the overlapping of Brillouin gain spectra. This chapter presents the effect of acoustic wave coupling on the lasing dynamics of the dual-wavelength BRFL. Acoustic wave coupling leads to higher gain in the overlapped Brillouin spectral region than in other positions. Since the lasing mode is selected in high gain positions of the BRFL, the lasing frequency moves towards the side of the overlapped gain region, and there is little possibility for lasing mode on the other side of the lower gain associated frequencies. Compared to single-wavelength BRFL without acoustic wave coupling at the pump light of 0 degrees or 90 degrees from the slow axis of the PM fiber, the dual-wavelength BRFL with acoustic wave coupling exhibits reduced frequency drift. However, strong mode competition occurs due to acoustic wave coupling, which leads to replica symmetry breaking and high intensity fluctuations.

# Acoustic wave coupling in dual-wavelength orthogonal polarized Brillouin random fiber laser using polarization-maintaining fiber

Haiyang Wang, Zichao Zhou, Liang Chen, and Xiaoyi Bao

***Abstract*—Acoustic wave coupling in dual-wavelength orthogonal polarized Brillouin random fiber laser (BRFL) based on polarization-maintaining (PM) fiber is characterized experimentally for the first time. Dual-wavelength BRFL is generated when the pump light is injected to the Brillouin gain PM fiber at 45 degrees from the slow axis. The dynamics of intensity and frequency of dual-wavelength and single-wavelength BRFLs are investigated. The spectrum of Pearson's correlation coefficient between different frequencies of the dual-wavelength BRFL shows several correlation peaks due to gain competition of two spatially overlapped coupled modes induced by acoustic wave coupling. The dual-wavelength BRFL presents a lower laser frequency drift with a standard deviation of 2.55 MHz and a larger relative intensity fluctuation with a standard deviation of 0.54 compared with that of single-wavelength BRFL (3.68 MHz and 0.32), which is attributed by increased photon-phonon coupling over the Brillouin gain fiber resulting from the coupling of acoustic waves in fast and slow axis due to 45 degrees pumping. In addition, replica symmetry breaking (RSB) is observed in dual-wavelength BRFL due to the increased gain competition of more random modes from acoustic wave coupling, which leads to correlated intensity fluctuations from trace to trace. The exploration of the internal spectral correlation, intensity fluctuation, RSB and frequency drift exposes the acoustic wave coupling in the dual-wavelength Brillouin random lasing process.**

***Index Terms*—Random fiber laser, Brillouin scattering, acoustic wave coupling.**

## I. Introduction

In random fiber laser, the fixed cavity length in normal lasers is replaced by random distributed feedback of Rayleigh scattering (RS) over long fibers. Multiple scattering of photons in random medium increases mean free path length leading to long effective length and narrow-spectrum spikes, especially for high Brillouin gain random laser [1], as high Brillouin gain enables many random modes lasing. Many spikes in random laser represent many random modes co-existing due to the random distributed feedback from RS fiber[2], [3] or random fiber grating [4], [5], [6]. The characteristics of the random fiber lasers show the Lévy distribution [7], [8], [9], replica symmetry breaking (RSB) [10], [11], turbulence hierarchy [12] and optical rogue wave [13]. Several gain mechanics, such as stimulated Raman scattering [14], [15], [16], Erbium-doped fiber [17] and stimulated Brillouin scattering (SBS) [18], [19] based random lasers have been investigated. SBS with a typical gain bandwidth of tens of MHz [20] acts as an optical filter as well as Brillouin gain, which enables the narrow linewidth peaks with a high Q value; however, the Brillouin random fiber laser (BRFL) enables many random modes for lasing, which results in a high relative intensity noise (RIN) due to the gain competition. A BRFL with a configuration of cooperative stimulated Brillouin and Rayleigh back-scattering was proposed in a SMF with a high loss [21]. The BRFL using only one fiber as Brillouin gain and random feedback has a higher threshold, larger linewidth and higher intensity noise compared with the BRFL with separated gain and feedback fibers [22]. The BRFL based on separated gain and feedback fibers using a ring cavity was demonstrated with a linewidth of ~3 kHz under single-frequency lasing operation [23]. A dramatic decrease of the lasing linewidth (~10 Hz) was then achieved [1] via coherent random oscillation, in which the random multi-scattering centers were separated from the Brillouin gain medium leading to multiple frequency components. In SMF-based BRFL, the gain competition of different polarization modes introduces a high RIN. BRFL based on all polarization-maintaining (PM) fiber was introduced [24] with reduced RIN.

To study the role of the acoustic wave in the noise contribution of BRFL, four-wave mixing is introduced in PM fiber to measure the phase-matching condition change with time due to the establishment of the BRFL [25]. The reflection spectrum of the BRFL formed dynamic grating is a few kHz for stimulated acoustic wave (phonon) compared with a few MHz of thermal phonon field without BRFL operation. The process of the excited phonon to reduce random laser linewidth is due to the coherent addition of excited phonon from pump wave and Stokes photon. To increase the SBS gain in PM fiber, we propose to use 45 degrees pumping to excite phonons in fast and slow axes so that more Stokes waves will get energy from the pump wave via excited phonons in both fast and slow axes. Such a process will impact the frequency and intensity noises of BRFL in PM fiber. The 45 degrees pumping leads to the generation of two acoustic waves within the gain bandwidth, which induces the coupling of acoustic waves in

Manuscript received July 8, 2021; revised November 17, 2021 and December 16, 2021; accepted January 4, 2022. Date of publication January 6, 2022. This work was supported in part by the Natural Sciences and Engineering Research Council of Canada (NSERC) (DG2020-06302), in part by the Canada Research Chair Program 75-67138, and in part by the China Scholarship Council. *(Haiyang Wang and Zichao Zhou contributed equally in this work.) (Corresponding author: Xiaoyi Bao)*

The authors are with Department of Physics, University of Ottawa, Ottawa, ON K1N 6N5, Canada

two polarizations varying intensity fluctuation and frequency drift over time. The acoustic wave coupling can be verified by measuring statistical intensity distribution, fluctuation spectra correlation using Parisi overlap parameter and frequencies correlation using Pearson's correlation coefficient.

In this paper, acoustic wave coupling enabled by dual-wavelength polarization-maintaining BRFL is demonstrated. Acoustic waves are coupled because the overlapping of acoustic modes in two polarizations results from the smaller frequency spacing of a few MHz than Brillouin gain bandwidth of tens of MHz. For dual-wavelength BRFL, the spectra of Pearson's correlation coefficient exhibits correlation peaks and the spectra of Parisi overlap parameter show replica symmetry breaking indicting the acoustic wave coupling in two polarizations of the PM gain medium. In addition, the dual-wavelength BRFL exhibits a higher intensity fluctuation with a standard deviation (STD) of 0.54 and a smaller frequency drift with a STD of 2.55 MHz than that of single-wavelength BRFL (0.32 and 3.68 MHz) due to increased photon-phonon coupling that results from acoustic wave coupling. It is not surprising to see replica symmetry breaking in dual-wavelength BRFL, which is attributed by the correlated intensity by the coupling process in Brillouin gain bandwidth from acoustic waves in both axes, while single-polarization BRFL maintains replica symmetry due to no coupling between acoustic waves in two axes.

## II. Experimental Setup and Principal

The experimental setup of the dual-wavelength orthogonal polarized BRFL is shown in Fig. 1. The pump light from a 3.5 kHz linewidth NP fiber laser is amplified by an erbium-doped fiber amplifier (EDFA). After the EDFA, the polarization of the pump light is adjusted by a polarization controller (PC). Then, the pump light is split into two paths by PM coupler 1. One path is utilized to monitor the polarization of the pump light after the PC using a free space polarizer and to generate a beat signal with the BRFL, and the other path is injected into the Brillouin gain medium of the BRFL through circulator 1. The linear orthogonal light with equally distributed power in x and y polarizations is obtained when the output of the polarizer has the maximum power at 45 degrees by adjusting the polarization of the pump to 45 degrees from the slow axis of the PM fiber. The polarization of the lasing output is confirmed. As the polarization preserved light in the all PM random laser, the lasing output also shows the equal power at x and y polarizations, which is monitored by changing the polarizer to 0 degree and 90 degrees. A 2 km-long Panda-type PM fiber with a birefringence of $\Delta n \sim 6.94 \times 10^{-4}$ [25] and a mode field diameter of 6.48 $\mu$m at the wavelength of 1550 nm is utilized as Brillouin gain. The pump light in the Brillouin gain medium stimulates backward Stokes light which travels anticlockwise between PM circulator 1 and PM circulator 2. The Stokes light experiences Rayleigh scattering (RS) provided by a 500 m-long PM fiber with the same type as the Brillouin gain fiber. The RS fiber acts as a narrow bandwidth filter to select longitudinal modes. The Rayleigh scattered Stokes light is then injected back to the Brillouin gain medium, providing feedback for the BRFL.

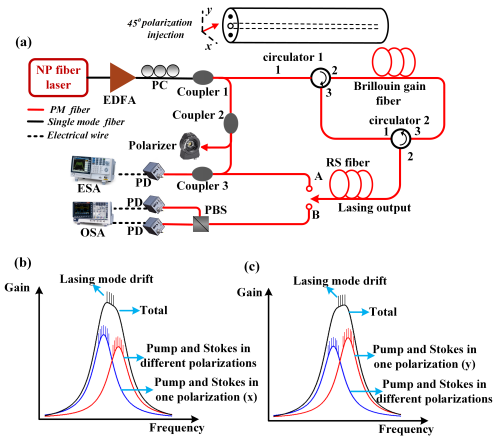


Fig. 1. (a) Experimental setup of the dual-wavelength BRFL. The schematic of Brillouin gain spectra distributions in (b) x polarization and (c) y polarization in dual-wavelength BRFL.

The BRFL is emitted from the RS fiber. The heterodyne-based method is utilized to measure spectral properties of the BRFL, in which the output of the BRFL at port A is combined with the pump light by another PM coupler. The spectra are detected by a photodetector (PD) with a 20 GHz bandwidth and collected by an electrical spectrum analyzer (ESA). The intensity characterization of x and y polarizations in the dual-wavelength BRFL are obtained using a polarization beam splitter (PBS) after the lasing output at port B. The utilization of PM fibers and components offers a unique way to generate dual-wavelength BRFL with orthogonal polarization. As the PM gain fiber has a smaller effective mode field diameter of 6.48 $\mu$m than that of SMF (10.4 $\mu$m), it provides a higher Brillouin gain coefficient for the BRFL. In addition, two-dimensional stresses from Baron-doped-silica rods in the PM fiber introduce different Brillouin frequency shifts in the slow and fast axes, providing dual-wavelength Brillouin random lasing with orthogonal polarization. When pumping a lasing light to the PM fiber at 45 degrees from the slow axis, the state of polarization (SOP) of pump and Stokes waves in Brillouin gain and RS feedback PM fibers changes as the birefringence difference at different positions of the PM fiber [25]. The changed SOP in pump and Stokes lights makes the interaction of pump and Stokes waves in different polarizations. The acoustic modes in two polarizations overlap with each other as the Brillouin frequency shift difference of ~5 MHz between two axes is smaller than the Brillouin gain bandwidth of tens of MHz, which enables acoustic wave coupling in the Brillouin gain fiber. Figure 1(b) and Figure 1(c) present the schematic of lasing gain spectra in x and y polarizations, respectively, showing asymmetric shapes with higher gain between two Brillouin peaks under lasing conditions due to the overlapping of the gain spectra with different gain amplitudes. The acoustic wave coupling increases the relative intensity noise due to gain competition of more random modes and reduces the lasing frequency drift due to the gain overlapping at two frequencies induced higher gain peak.

## III. Experimental Results

### A. Spectral Evolution

The spectral evolution of the beat spectra between the pump laser and the dual-wavelength BRFL is continuously measured, as shown in Fig. 2(a), which is the top view of three-dimensional beat spectra measured within 2 s in a time interval of 2.18 ms. The beat spectra are recorded in a frequency resolution of 10 kHz. Several instances of the spectra are shown in Fig. 2(b). It is seen that the BRFL spectra comprise two narrow-bandwidth lasing wavelengths, differing in the frequency of each polarization and frequency difference between two polarizations. The Brillouin frequency shift difference between two axes is a few MHz, corresponding to position-dependent birefringence in PM fiber on the order of $10^{-4}$, which agrees with the birefringence of the PM fiber. Figure 2(a) shows that the two frequencies change in the same manner and the frequency difference remains relatively stable with time. There are mainly three reasons that lead to the spectral fluctuation of the dual-wavelength BRFL. Firstly, the temperature variation of the SBS gain fiber caused by environmental perturbation provides fluctuating gain spectrum in the Brillouin gain medium, which is the main reason for the frequency fluctuation of the BRFL. As the same temperature perturbation in both x polarization and y polarization, the Brillouin gain spectra in both polarizations fluctuate in the same manner. Secondly, the Rayleigh scattering fiber provides feedback for BRFL, which acts as a narrow linewidth filter. Any perturbation, such as thermal and acoustic variations, on the Rayleigh scattering fiber leads to the change of the filter property, which causes the random lasing frequency fluctuation. Thirdly, the Brillouin gain spectrum of each polarization is different at different locations of the PM Brillouin gain medium as the distributed non-uniform refractive index; hence, the gain competition from different Brillouin frequencies at different locations induce unstable lasing frequency. The changed refractive index makes position-dependent birefringence between two polarizations in the PM fiber leading to the fluctuated frequency difference between two wavelengths. As the NP Photonics laser has a frequency drift of ±20 kHz [26], the pump light from the laser has little influence on the frequency fluctuation of the beat spectra between the pump laser and the BRFL.

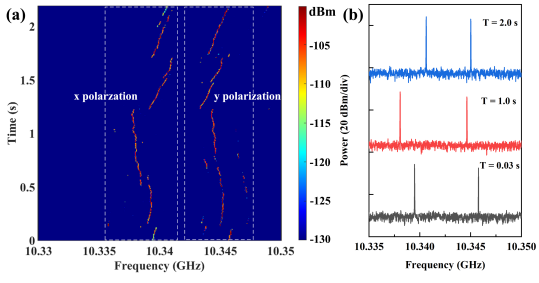


Fig. 2. (a) Dynamic beat spectra evolution of the dual-wavelength orthogonal polarization BRFL. (b) Several instances of the single-record spectrum of the BRFL.

### B. Spectral Correlation

The ensemble-averaged beat spectra are further studied to show the average statistical temporal-spectra as plotted in Fig. 3(a). To discriminate the beat spectra from different polarizations, the power of pump light in the slow axis (y polarization) is decreased to be slightly lower than that in the fast axis (x polarization). Therefore, the intensity of beat spectra from y polarization is lower than that from x polarization. In the BRFL, the narrow-band peaks appear and survive even though the total average time of the beat spectra is on the order of seconds, which is much longer than the time of flight in the 2 km Brillouin gain fiber. In contrast, the ensemble-averaged spectrum of coherent random laser is a smoothed curve [27], which is similar to the spectrum of the random laser with non-resonant feedback. Comparing with the spontaneous Brillouin gain spectrum, the ensemble-averaged spectrum carries the intrinsic signature of the Brillouin gain profile. To characterize spectral correlations between modes of $\lambda_j$ and $\lambda_k$ in BRFLs, Pearson's correlation coefficient is calculated, which is given by

$$C\left(\lambda_j,\lambda_k\right)=\frac{\sum_{i=1}^{N}\Delta_i(\lambda_j)\Delta_i(\lambda_k)}{\sqrt{\sum_{i=1}^{N}\Delta_i^2(\lambda_j)}\sqrt{\sum_{i=1}^{N}\Delta_i^2(\lambda_k)}} \tag{1}$$

where $\Delta_i(\lambda_j)=I_i\left(\lambda_j\right)-\bar{I}\left(\lambda_j\right)$ with being $\bar{I}\left(\lambda_j\right)$ indicates the average over the ensemble given by $N$ analyzed spectra. A zero of coefficient $C$ represents uncorrelated behave between modes. The negative or positive value means the statistical fluctuations in the intensity of two modes are correlated, indicating the gain competition of the spatially overlapped coupled modes over time. Pearson's correlation coefficient has been used to describe underlying spectral correlations between sidebands in modulation stability [28], spectral correlations in supercontinuum generation [29] and in Raman random fiber lasers [30], which are combined with real-time spectral measurement based on dispersive Fourier transformation or Fabry-Perot interferometer (FPI) based configuration. As the spectral resolution of FPI-based configuration is not adequate to measure linewidth of sub kHz and the dispersive

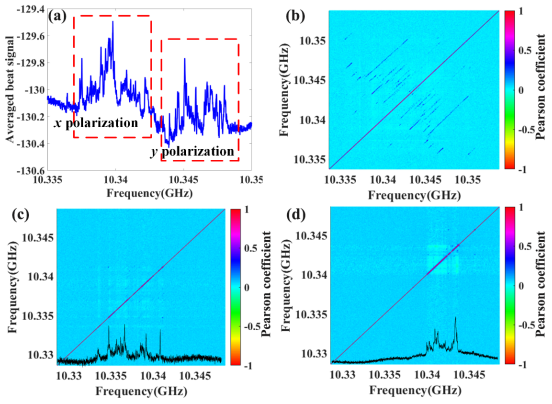


Fig. 3. (a) Averaged beat spectra of the BRFL. Pearson's correlation coefficient of the spectra of (b) dual-polarized BRFL; (c) fast axis of single-polarized BRFL; (d) slow axis of single-polarized BRFL.

Fourier transformation method can only be used in pulse regime, the heterodyne method is adopted for the measurement in ultra-narrow linewidth continuous-wave BRFLs. Fig. 3(b) shows the correlation matrix plot of the beat signal between dual-wavelength BRFL and pump light. The diagonal line represents the autocorrelation peak. The positive Pearson's coefficient up to 0.5 is obtained from the correlation spectra. The coefficient beyond the diagonal line has discrete positions regarding the frequency difference of the dual-wavelength BRFL. These discrete positions are due to the narrow linewidth spectral generation and strong spectral correlations between two lasing wavelengths induced by the acoustic wave coupling, in which the orthogonal polarized modes share the same gain over time. When the frequency of BRFL jumps from one position to another, the frequency difference changes and creates multiple peaks in Pearson's correlation coefficient matrix. The estimation of Pearson's correlation coefficient aided by heterodyne spectral measurement method offers a simple and straightforward method to check spectral correlations in BRFLs. The Pearson's correlation coefficient of the spectra in fast and slow axes of single-wavelength BRFL is also measured and plotted as shown in Fig. 3(c) and Fig. 3(d) by adjusting the polarization of the pump light to the corresponding principal axis of the PM fiber. We note the anti-correlation as the negative Pearson coefficient with a value of -0.07 in the single-wavelength BRFL cases. In the single-wavelength BRFL, many random modes compete with the Brillouin gain and only one dominant lasing mode with random frequency in the gain is selected and propagated along the PM fiber BRFL. The small anti-correlation is induced by the gain competition of random modes in the Brillouin gain region. Similar small anti-correlated dynamics have also been observed in the random fiber laser [30], in which the spectral components compete for gain arising from a single vibrational mode. There is no correlation between the lasing modes of two polarizations with a Brillouin frequency difference of a few MHz in the single-wavelength BRFLs as one acoustic wave is generated that results from the preserved state of polarization, and hence no acoustic wave coupling [22].

### C. Frequency Drift

The frequency drifts of dual-wavelength and single-wavelength BRFL ares measured and recorded over a time scale of 1200 s in a step of 0.2 s, and the results are analyzed statistically by calculating the relative frequency variation. The relative frequency variation denotes $f_x - \langle f_x \rangle$ in x polarization and $f_y - \langle f_y \rangle$ in y polarization, respectively. Figure 4(a) and Figure 4(c) show the fluctuation of the beat frequency in two polarizations of the dual-wavelength BRFL and two axes of single-wavelength BRFL, respectively. The frequency fluctuation of the BRFL arises from acoustic and thermal variations, which shift the Brillouin gain spectra at different positions of the gain medium. The 500 m-long PM feedback fiber acting as a filter also selects different lasing frequencies at external perturbations. In addition, the RS feedback fiber leads to large mode frequency spacing change due to its 500 m length, which results in a frequency fluctuation. The

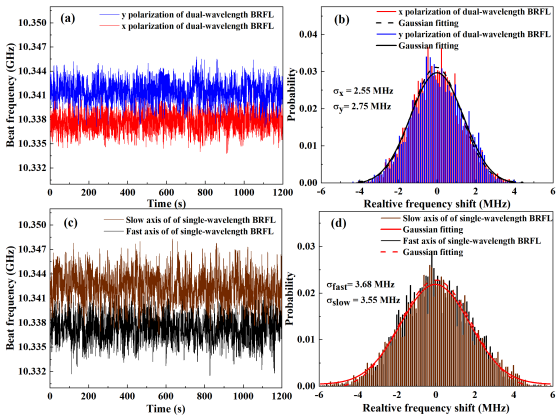


Fig. 4. (a) Frequency drifts of two polarizations of dual-wavelength BRFL. (b) Histogram of frequency drifts. (c) Frequency drifts of two axes of single-wavelength BRFL. (d) Histogram of frequency drifts.

TABLE I
**Frequency drift of dual-wavelength and single-wavelength BRFLs**

| | Dual-wavelength BRFL | | Single-wavelength BRFL | |
|---|---|---|---|---|
| | x polarization | y polarization | slow axis | fast axis |
| STD | 2.55 MHz | 2.75 MHz | 3.55 MHz | 3.68 MHz |

probability distributions of the relative frequency variation of dual-wavelength and single-wavelength BRFLs are plotted in Fig. 4(b) and Fig. 4(d), respectively. The relative frequencies of dual-wavelength BRFL are random fluctuated within ±4 MHz and the probability distributions present Gaussian distributions with a STD of 2.55 MHz and 2.75 MHz at x and y polarizations, respectively. The Gaussian distributions result from the amplified random frequency light after the 500 m-long RS distributed feedback fiber. Comparing with dual-wavelength BRFL, single-wavelength BRFL exhibits a larger frequency drift (±6 MHz) and the Gaussian distributions follow larger standard deviations at fast and slow axes (3.68 MHz and 3.55 MHz). The frequency shift of dual-wavelength BRFL and single-wavelength BRFL is shown in Table I. Acoustic wave coupling under 45 degrees pumping enables the electric field of pump projected to two polarizations interacts with electric field of Stokes waves of two polarizations. Because the phonons in both of fast and slow axes are excited simultaneously, which gives higher Stokes power attributed by excited phonons in fast and slow axes. The large Brillouin gain from the increased photon-phonon coupling introduces a higher Q value for the random laser, which gives higher gain around peak values, and hence those modes are less frequency shift. In addition, the random lasing gain is different from the Brillouin spectrum of x or y polarization, and the highest random mode in each polarization is imbedded it as shown in Fig. 2(b). Such a mode drifts with temperature and acoustic wave is shown in Fig. 2(a). The lasing gain is not a Lorentzian shape, rather it is an asymmetric spectrum with a higher gain between two Brillouin peaks under lasing conditions as shown in Fig. 1(b) and Fig. 1(c). The lasing mode moves to higher gain of the overlapped Brillouin profile, which is responsible

for random lasing process of either x or y polarization as evidenced by Fig. 2(b) of two separated sharp peaks. Hence the lasing frequency is more centered with smaller frequency drift in dual-wavelength BRFL showing in Fig. 4(a) than the lasing frequency drift in single-wavelength BRFL showing in Fig. 4(c). For single-wavelength BRFL, the pump only interacts with the Stokes wave with the same polarization [22], [31], leading to a large frequency shift as the low gain in single-frequency random laser without acoustic wave coupling.

### D. Intensity Fluctuation and Statistics

To comprehensively characterize the temporal dynamics of the BRFLs under the effect of acoustic wave coupling, relative intensity fluctuation and statistical features of dual-wavelength BRFL and single-wavelength BRFL are measured and recorded by an oscilloscope as plotted in Fig. 5. Figure 5(a) shows the intensity fluctuation of dual-wavelength BRFL at two polarizations and single-wavelength BRFL at two axes within 0.1 s. The relative intensity fluctuations of two lower time-domain series show straight lines indicting the single-mode operation of the BRFL, while two upper time-domain series exhibit large intensity fluctuations with several asymmetric intensity spikes due to the co-existing of many lasing modes. The statistical intensity probabilities of the four cases are plotted as shown in Figs. 5(b-e). The output intensities for two axes of single-wavelength BRFL follow a Gaussian distribution, while the cases for two polarizations of dual-wavelength BRFL exhibit a quasi-Gaussian distribution due to the intensity fluctuation with several intensity spikes. The Gaussian distribution happens for an initial partially random signal passing many random lengths [32]. When modes created by the random lengths of frozen scattering centers are matched to a lasing mode of the BRFL, the lasing mode reaches the highest gain with maximum output intensity. The deviation of the lasing mode from the localized mode created by the random scattering medium reduces the output intensity of the lasing peak. The Gaussian distribution of the relative intensity fluctuation of BRFLs manifests that the frequency variation of the lasing peak is a random process induced by environmental perturbation and random mode competition for limited SBS gain. The standard deviation $\sigma$ of the Gaussian fitting in dual-wavelength BRFL is $\sigma$=0.55 and $\sigma$=0.54 for y and x polarizations of dual-wavelength BRFL, respectively, which is larger than the values for slow axis and fast axis of single-wavelength BRFL ($\sigma$=0.33 and $\sigma$=0.32). The relative intensity change of dual-wavelength BRFL and single-wavelength BRFL are summarized in Table II. Two modes with different Brillouin frequencies in fast and slow axes compete for the overlapped total Brillouin gain in dual-wavelength BRFL. More phonons are excited in the fast and slow axes from 45 degrees pump wave, which gives energy to Stokes waves in fast and slow axes simultaneously for a certain time period. More energy exchange between phonons and Stokes photons in dual-wavelength BRFL enables a larger standard deviation of intensity fluctuation than single-frequency BRFL. By doing Fourier transform to the intensity series of the BRFLs, the RIN of dual-wavelength BRFL and single-wavelength BRFL are calculated, as plotted in Fig. 5(f). Compared with the RIN of the fast axis and slow axis of single-wavelength BRFL, the RIN of each polarization of dual-wavelength BRFL is significantly increased by ~10 dB. The large intensity fluctuations of dual-wavelength BRFL induced by the mode coupling and increased energy exchange between phonons and photons in the overlapped Brillouin gain increase RIN.

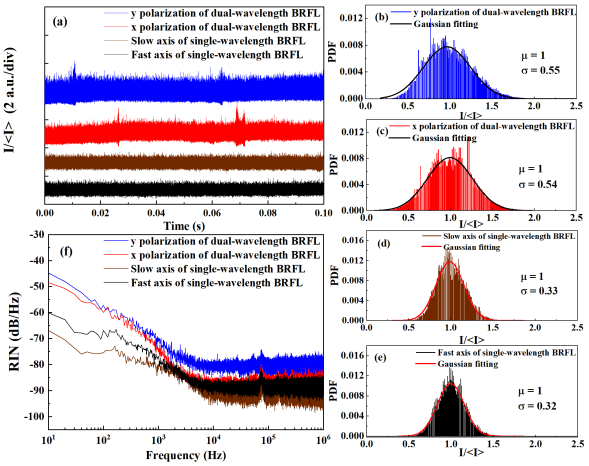


Fig. 5. (a) Relative intensity change of single-wavelength and dual-wavelength BRFLs. Probability density function of the relative intensity of dual-wavelength BRFL in (b) y polarization; (c) x polarization. Probability density function of the relative intensity of single-wavelength BRFL in (d) slow axis; (e) fast axis polarization. (f) Relative intensity noise of the BRFLs.

TABLE II
**Intensity change of dual-wavelength and single-wavelength BRFLs**

| | Dual-wavelength BRFL | | Single-wavelength BRFL | |
|---|---|---|---|---|
| | x polarization | y polarization | slow axis | fast axis |
| STD | 0.54 | 0.55 | 0.33 | 0.32 |

### E. Intensity Correlation

The intensity correlations in the dual-wavelength BRFL and single-wavelength BRFL are calculated for demonstrating the impact of acoustic wave coupling on time-domain traces. The correlation of intensity fluctuation between trace to trace is known as Parisi overlap parameter, which has been applied for characterizing the RSB in random lasers [10], [33], [34]. Parisi overlap parameter $q$ is defined as

$$q_{ab} = \frac{\sum_{k=1}^{N} \Delta_a(k)\Delta_b(k)}{\sqrt{\sum_{k=1}^{N} \Delta_a^2(k)}\sqrt{\sum_{k=1}^{N} \Delta_b^2(k)}} \quad (2)$$

where $N$ is the number of spectral points, $a$ and $b$ are two traces with being $a, b$=1,2,..., $N_s$ and $N_s$ = 100, $\Delta_a(k) = I_a(k) - \bar{I}(k)$ is the intensity fluctuation, and $\bar{I}(k) = \sum_{a=1}^{N_s} I_a(k)/N_s$ is the average intensity at the frequency indexed by $k$. The values of $q_{ab}$ around zero imply that the intensity fluctuations from trace to trace are uncorrelated (no RSB) and the values of $q_{ab}$ around ±1 indicate the correlation of intensity fluctuation between traces (RSB).

Fast Fourier transform of the temporal traces is applied to calculate the spectra of the intensity fluctuation and the RSB. Figure 6(a) and Figure 6(b) show the probability distribution of the $q$ values for y polarization and x polarization of the dual-wavelength BRFL, respectively. Parisi overlap parameter values in both polarizations of dual-wavelength BRFL show bimodal probability in which the distribution of $q$ have all possible values in the range of [-1 1] and two peaks around $\pm 1$, which means strong correlation of intensity fluctuation spectra from trace to trace. The bimodal probability manifests the existence of RSB in the case of dual-wavelength BRFL. The intensity correlation between traces is due to the coupling of acoustic waves in two polarizations of dual-wavelength BRFL. More modes are introduced by acoustic wave coupling enhancing gain competition, which makes correlated intensity fluctuations of modes over time and gives replica symmetry breaking. The probability distribution of $q$ values for the fast-axis single-wavelength BRFL is also calculated as plotted in Fig. 6(c). The probability distribution of $q$ values is around zero, which indicates independent intensity fluctuation between any two traces in the replica-symmetric paramagnetic regime. The distribution of $q$ values for the slow-axis single-wavelength BRFL is similar to that for the fast axis as reported in [35]. The uncorrelated intensity fluctuation from trace to trace in single-wavelength BRFL is because the RS fiber acts as a narrow filter to randomly select a lasing mode generated by the acoustic wave in the axis. The acoustic wave in the other axis can not be excited leading to no acoustic wave coupling. The difference of the $q$ distribution between dual-wavelength and single-wavelength BRFLs verifies the impact of acoustic wave coupling on the correlation of intensity fluctuation between traces over time.

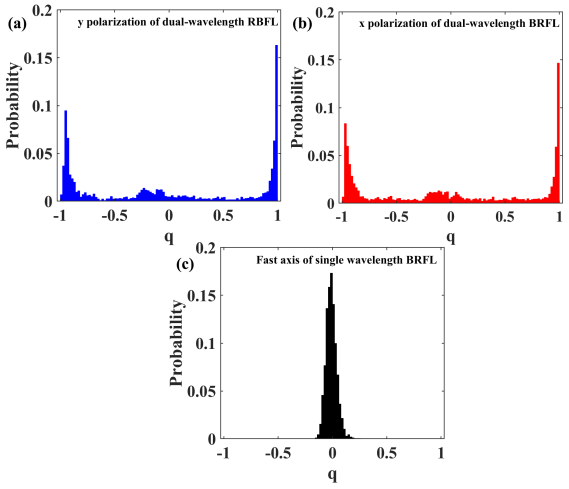


Fig. 6. Histograms of probability distribution of $q$ values for (a) y polarization of dual-wavelength BRFL; (b) x polarization of dual-wavelength BRFL; (c) fast axis of single-wavelength BRFL.

## IV. Conclusion

In conclusion, the acoustic wave coupling in a dual-wavelength BRFL with orthogonal polarization based on polarization-maintaining fiber is demonstrated. The spectral correlation of the dual-wavelength BRFL reflects the acoustic wave coupling and potentially gives spatially dependent spectral dynamics. In addition, the dual-wavelength BRFL exhibits more stable lasing frequencies and high relative intensity fluctuation. As higher gain leads to more mode coupling by acoustic wave coupling, more intensity noise is expected. On the other hand, higher gain with constant loss of the fiber for random lasing process leads to higher Q value, which makes smaller frequency fluctuation for random laser. There is a trade-off between lasing frequency drift and intensity fluctuation, that is, the reduced frequency drift, while the increased intensity fluctuation. The detection of replica symmetry breaking further illustrates the acoustic wave coupling and gain competition in the dual-wavelength BRFL, which leads to the correlation of intensity fluctuation spectra. The exploration of the nature of spectra correlation, intensity fluctuation and its correlation, and frequency drift can have profound implications in the future design of random fiber lasers towards practical applications in the fields of coherent light sources and optical sensing.

## References

[1] M. Pang, X. Bao, and L. Chen, "Observation of narrow linewidth spikes in the coherent brillouin random fiber laser," *Optics letters*, vol. 38, no. 11, pp. 1866–1868, 2013.

[2] S. K. Turitsyn, S. A. Babin, A. E. El-Taher, P. Harper, D. V. Churkin, S. I. Kablukov, J. D. Ania-Castañón, V. Karalekas, and E. V. Podivilov, "Random distributed feedback fibre laser," *Nature photonics*, vol. 4, no. 4, pp. 231–235, 2010.

[3] L. Zhang, H. Jiang, X. Yang, W. Pan, and Y. Feng, "Ultra-wide wavelength tuning of a cascaded raman random fiber laser," *Optics letters*, vol. 41, no. 2, pp. 215–218, 2016.

[4] Y. Xu, M. Zhang, P. Lu, S. Mihailov, and X. Bao, "Multi-parameter sensor based on random fiber lasers," *Aip Advances*, vol. 6, no. 9, p. 095009, 2016.

[5] Y. Li, P. Lu, F. Baset, Z. Ou, J. Song, A. Alshehri, V. R. Bhardwaj, and X. Bao, "Narrow linewidth low frequency noise er-doped fiber ring laser based on femtosecond laser induced random feedback," *Applied Physics Letters*, vol. 105, no. 10, p. 101105, 2014.

[6] Y. Xu, L. Zhang, L. Chen, and X. Bao, "Single-mode soa-based 1khz-linewidth dual-wavelength random fiber laser," *Optics express*, vol. 25, no. 14, pp. 15 828–15 837, 2017.

[7] S. Lepri, S. Cavalieri, G.-L. Oppo, and D. S. Wiersma, "Statistical regimes of random laser fluctuations," *Physical Review A*, vol. 75, no. 6, p. 063820, 2007.

[8] B. C. Lima, A. S. Gomes, P. I. Pincheira, A. L. Moura, M. Gagné, E. P. Raposo, C. B. de Araújo, and R. Kashyap, "Observation of lévy statistics in one-dimensional erbium-based random fiber laser," *JOSA B*, vol. 34, no. 2, pp. 293–299, 2017.

[9] J. Li, H. Wu, Z. Wang, S. Lin, C. Lu, E. P. Raposo, A. S. Gomes, and Y. Rao, "Lévy spectral intensity statistics in a raman random fiber laser," *Optics Letters*, vol. 44, no. 11, pp. 2799–2802, 2019.

[10] N. Ghofraniha, I. Viola, F. Di Maria, G. Barbarella, G. Gigli, L. Leuzzi, and C. Conti, "Experimental evidence of replica symmetry breaking in random lasers," *Nature communications*, vol. 6, no. 1, pp. 1–8, 2015.

[11] F. Tommasi, E. Ignesti, S. Lepri, and S. Cavalieri, "Robustness of replica symmetry breaking phenomenology in random laser," *Scientific reports*, vol. 6, no. 1, pp. 1–8, 2016.

[12] I. R. R. Gonzalez, B. C. Lima, P. I. Pincheira, A. A. Brum, A. M. Macedo, G. L. Vasconcelos, L. d. S. Menezes, E. P. Raposo, A. S. Gomes, and R. Kashyap, "Turbulence hierarchy in a random fibre laser," *Nature communications*, vol. 8, no. 1, pp. 1–8, 2017.

[13] J. Xu, J. Wu, J. Ye, J. Song, B. Yao, H. Zhang, J. Leng, W. Zhang, P. Zhou, and Y. Rao, "Optical rogue wave in random fiber laser," *Photonics Research*, vol. 8, no. 1, pp. 1–7, 2020.

[14] S. Babin, A. El-Taher, P. Harper, E. Podivilov, and S. Turitsyn, "Tunable random fiber laser," *Physical Review A*, vol. 84, no. 2, p. 021805, 2011.

[15] M. Gagné and R. Kashyap, "Random fiber bragg grating raman fiber laser," *Optics letters*, vol. 39, no. 9, pp. 2755–2758, 2014.
[16] J. Xu, L. Huang, M. Jiang, J. Ye, P. Ma, J. Leng, J. Wu, H. Zhang, and P. Zhou, "Near-diffraction-limited linearly polarized narrow-linewidth random fiber laser with record kilowatt output," *Photonics Research*, vol. 5, no. 4, pp. 350–354, 2017.
[17] B. Saxena, X. Bao, and L. Chen, "Suppression of thermal frequency noise in erbium-doped fiber random lasers," *Optics letters*, vol. 39, no. 4, pp. 1038–1041, 2014.
[18] Y. Xu, D. Xiang, Z. Ou, P. Lu, and X. Bao, "Random fabry–perot resonator-based sub-khz brillouin fiber laser to improve spectral resolution in linewidth measurement," *Optics letters*, vol. 40, no. 9, pp. 1920–1923, 2015.
[19] L. Zhang, Y. Xu, S. Gao, B. Saxena, L. Chen, and X. Bao, "Multiwavelength coherent brillouin random fiber laser with ultrahigh optical signal-to-noise ratio," *IEEE Journal of Selected Topics in Quantum Electronics*, vol. 24, no. 3, pp. 1–8, 2017.
[20] G. P. Agrawal, "Nonlinear fiber optics," in *Nonlinear Science at the Dawn of the 21st Century*. Springer, 2000, pp. 195–211.
[21] A. A. Fotiadi and R. V. Kiyan, "Cooperative stimulated brillouin and rayleigh backscattering process in optical fiber," *Optics letters*, vol. 23, no. 23, pp. 1805–1807, 1998.
[22] L. Zhang, C. Wang, Z. Li, Y. Xu, B. Saxena, S. Gao, L. Chen, and X. Bao, "High-efficiency brillouin random fiber laser using all-polarization maintaining ring cavity," *Optics express*, vol. 25, no. 10, pp. 11 306–11 314, 2017.
[23] M. Pang, S. Xie, X. Bao, D.-P. Zhou, Y. Lu, and L. Chen, "Rayleigh scattering-assisted narrow linewidth brillouin lasing in cascaded fiber," *Optics letters*, vol. 37, no. 15, pp. 3129–3131, 2012.
[24] L. Zhang, Y. Xu, S. Gao, B. Saxena, L. Chen, and X. Bao, "Linearly polarized low-noise brillouin random fiber laser," *Optics letters*, vol. 42, no. 4, pp. 739–742, 2017.
[25] Z. Zhou, L. Chen, and X. Bao, "Dynamic detection of acoustic wave generated by polarization maintaining brillouin random fiber laser," *APL Photonics*, vol. 5, no. 9, p. 096101, 2020.
[26] Y. Li, P. Lu, X. Bao, and Z. Ou, "Random spaced index modulation for a narrow linewidth tunable fiber laser with low intensity noise," *Optics letters*, vol. 39, no. 8, pp. 2294–2297, 2014.
[27] R. Uppu and S. Mujumdar, "Statistical fluctuations of coherent and incoherent intensity in random lasers with nonresonant feedback," *Optics letters*, vol. 35, no. 17, pp. 2831–2833, 2010.
[28] D. R. Solli, G. Herink, B. Jalali, and C. Ropers, "Fluctuations and correlations in modulation instability," *Nature Photonics*, vol. 6, no. 7, pp. 463–468, 2012.
[29] T. Godin, B. Wetzel, T. Sylvestre, L. Larger, A. Kudlinski, A. Mussot, A. B. Salem, M. Zghal, G. Genty, F. Dias *et al.*, "Real time noise and wavelength correlations in octave-spanning supercontinuum generation," *Optics express*, vol. 21, no. 15, pp. 18 452–18 460, 2013.
[30] S. Sugavanam, M. Sorokina, and D. V. Churkin, "Spectral correlations in a random distributed feedback fibre laser," *Nature communications*, vol. 8, no. 1, pp. 1–8, 2017.
[31] Z. Zhou, L. Chen, and X. Bao, "Mode characteristic manipulation of random feedback interferometers in brillouin random fiber laser," *Optics letters*, vol. 45, no. 3, pp. 678–681, 2020.
[32] L. Ogorodnikov and S. Vergeles, "Intensity statistics in a long random fiber raman laser," *Optics letters*, vol. 43, no. 4, pp. 651–654, 2018.
[33] L. M. Massaro, S. Gentilini, A. Portone, A. Camposeo, D. Pisignano, C. Conti, and N. Ghofraniha, "Heterogeneous random laser with switching activity visualized by replica symmetry breaking maps," *ACS Photonics*, vol. 8, no. 1, pp. 376–383, 2021.
[34] A. S. Gomes, B. C. Lima, P. I. Pincheira, A. L. Moura, M. Gagné, E. P. Raposo, C. B. de Araújo, and R. Kashyap, "Glassy behavior in a one-dimensional continuous-wave erbium-doped random fiber laser," *Physical Review A*, vol. 94, no. 1, p. 011801, 2016.
[35] Z. Zhou, L. Chen, and X. Bao, "High efficiency brillouin random fiber laser with replica symmetry breaking enabled by random fiber grating," *Optics Express*, vol. 29, no. 5, pp. 6532–6541, 2021.

**Haiyang Wang** is currently working toward the Ph.D. degree in physics from the Department of Physics, University of Ottawa, Ottawa, ON, Canada. His research interests include Brillouin random fiber laser, Brillouin fiber sensing, design and fabrication of tapered chalcogenide-PMMA fiber and its applications.

**Zichao Zhou** received his Ph.D. degrees from University of Ottawa, Ottawa, ON, Canada, in 2021. His research interests include Brillouin random fiber laser and its applications.

**Liang Chen** joined the University of Ottawa in 2000, and since 2012, he has been a Full Professor in the Department of Physics, University of Ottawa. He is the author of more than 200 refereed journal publications. His current research interests include nonlinear fiber optics and fiber optic sensing technologies.

**Xiaoyi Bao** is the Canada Research Chair professor (Tier I) in fiber optics and photonics in Center for Research in Photonics, Department of Physics, the University of Ottawa, ON, Canada. Her research interests include nonlinear effects in fibers to make fiber device, lasers, and sensors.

# 10 Conclusion and Further work

## 10.1 Conclusion

This thesis presents a study of stimulated Brillouin scattering (SBS) in chalcogenide microfibers from fundamental theories to practical applications, as well as SBS in frequency-stabilized random fiber lasers. Unlike silica microfibers, chalcogenide microfibers coated with PMMA have extremely high nonlinearity, low Young's modulus, high mechanical strength, and high design flexibility. Chalcogenide Brillouin sensors open the way for many practical applications in structural health monitoring. SBS gain-based random fiber lasers, also known as Brillouin random fiber lasers (BRFL), enable narrow linewidth random lasing with a low threshold due to the narrow gain bandwidth and high gain coefficient. BRFLs with weak scattering feedback have significant frequency drift and high intensity noise due to complex paths and high density of random modes. It is necessary to manipulate the random modes and their propagation in the BRFL to reduce frequency drift and intensity noise. Random fiber gratings (RFG) with random periods and high refractive index modulations have been developed. We controlled the mode behavior of BRFLs by using the short RFG distributed feedback. Light interference in the multi-scattering RFG distributed feedback is used to determine the dynamics of lasing modes.

We conducted the theoretical SBS calculation and fabrication of chalcogenide microfibers. PMMA-coated chalcogenide microfibers provide high mechanical strength for normal handling. Having the ultrahigh Brillouin gain and low Young's modulus of chalcogenide-PMMA microfibers, the focus then shifted to bringing the microfiber to high-performance sensing applications. We designed a wide-range Brillouin strain sensor in the single-core chalcogenide-PMMA microfiber using Brillouin optical time-domain analysis (BOTDA). The chalcogenide-PMMA fiber enables a strain measurement as high as 15000 $\mu\varepsilon$. Com-

pared to previous polymer optical fiber sensors, no strain memory effect is observed in the chalcogenide microfiber sensor because Young's modulus of the chalcogenide (17.8 Gpa) is larger than that of the polymer (3.5 Gpa). The Brillouin frequency shift (BFS) increases linearly with strain with a sensitivity of 26.4 kHz/με, which is in consistent with theoretical calculations. The nonlinear change of Brillouin linewidth appears in the high-strain region (larger than 1500 με) due to the deformation of the microfiber at certain positions. The wide-stain sensor based on the chalcogenide-PMMA microfiber can potentially be used in monitoring civil infrastructures.

We also investigated SBS in highly birefringent chalcogenide microfibers. In the first part of our work, we measured simultaneous strain and temperature Brillouin sensing in dual-core chalcogenide-PMMA microfibers. Because of the ultrahigh nonlinearity of the chalcogenide, SBS in the 50 cm-long dual-core chalcogenide-PMMA microfibers is excited at a low pump power of 9 dBm. Temperature sensitivities are -3.83 MHz/°C and -3.33 MHz/°C, and the strain sensitivities are -61.14 kHz/με and -34.63 kHz/με in two polarization axes of the chalcogenide microfiber. Different Brillouin frequency responses in two polarization axes enable two-parameter sensing. In the second part of our work, we investigated SBS in high-birefringence elliptical-core microfibers. We measured and calculated the birefringence and Brillouin gain spectra in two axes of the elliptical-core microfibers with different core diameters. The tailorable birefringence causes the tunable Brillouin frequency differences between two polarization axes. The elliptical-core microfiber shows a large frequency difference of 30 MHz at high birefringence of $10^{-2}$. Overall, exploring chalcogenide microfibers with strong SBS is an important step for Brillouin-enabled compact sensors.

We studied BRFLs with strong scattering (multiple scattering) and weak scattering (single scattering) distributed feedback. For the strong scattering distributed feedback, we chose the 10 m-long random fiber grating array (RFGA). By changing the pump power, we controlled the lasing dynamics in the RFGA-based BRFL. The BRFL exhibits a long lifetime of 12 s at high pump power. We clarified the physical mechanism of the BRFL using light localization, which is generated by wave interference in multi-scattering Fabry–Pérot (FP) cavities of the RFGA. Light localization enables photons to follow the same path when propagating in the random cavity. As a result, we obtained a small correlation coefficient change of 4.5% and small frequency drift of 620 kHz over 12 s. The replica symmetry behavior at high pump power confirms the long lifetime of the single-mode BRFL. For weak scattering distributed feedback, we chose the 500 m-long polarization-maintaining (PM) fiber. Due to weak Rayleigh scattering (RS) in the PM fiber, light follows different paths for each round trip. Furthermore, the long cavity of the RS-based BRFL significantly reduces the frequency separation of lasing modes. The reduction of frequency separation

increases the number of lasing modes in the Brillouin gain bandwidth. Due to random modes following complex paths in the random cavity, the BRFL exhibits fast mode hopping (less than 0.3 s) and significant frequency drift (6 MHz).

We investigated BRFLs with high-Q RFGR distributed feedback and low-Q RFG distributed feedback. We measured single-mode lasing emission when the frequency of the high-Q RFGR is in resonance with the Brillouin lasing frequency. The single-mode lasing is attributed to the self-injection locking of Brillouin random lasing and the high-Q RFGR resonator. Due to the self-adjustment of random modes with small frequency differences to thermal and acoustic variations and self-injection locking, the BRFL shows small frequency drift of 340 kHz and mode hopping free operation over 14.9 s. The relative intensity noise is reduced at high frequencies over 1 kHz due to suppressed mode coupling. The low-Q RFG-based BRFL without self-injection locking shows multi-mode emission with fast mode hopping. Due to the broad linewidth of RFG feedback, many modes are amplified and hopped in the gain bandwidth. Therefore, the frequency drift and relative intensity noise over 1 kHz are significantly increased. Our findings offer a new approach to stabilizing Brillouin random lasers passively without using a commonly used active phase-locked laser.

Finally, we illustrated the acoustic wave coupling mechanism in the dual-wavelength BRFL based on the PM fiber. The Brillouin frequency shift difference between two polarization axes is a few MHz in the PM fiber with the birefringence of $10^{-4}$. The BRFL shows dual-wavelength lasing when the pump light is injected into the Brillouin gain PM fiber at 45 degrees from the slow axis. Acoustic wave coupling is generated in the BRFL by using the two lasing modes due to the smaller frequency difference between the two modes than the Brillouin gain bandwidth. The acoustic wave coupling is used to control the mode behavior. Two spatially overlapped modes compete for the Brillouin gain. This leads to correlation peaks in Pearson's correlation coefficient spectra and replica symmetry breaking. The acoustic wave coupling causes a higher gain in the overlapping region. Since the random lasing is possibly generated at high gain positions, the frequency drift of the dual-wavelength BRFL mainly shows in the overlapping region. Therefore, the BRFL with acoustic wave coupling shows less frequency drift than the single-wavelength BRFL without acoustic wave coupling. Due to mode coupling in the dual-wavelength BRFL, the relative intensity noise is increased.

## 10.2 Further work

### 10.2.1 Chalcogenide microfiber Brillouin sensing

Chalcogenide microfibers with high nonlinearity are promising platforms for Brillouin sensing applications. Surface acoustic waves generated in sub-wavelength diameter microfibers are beneficial for sensing applications because the acoustic waves propagate along the surface of the microfiber rather than longitudinal acoustic waves propagating in the core of the microfiber. Brillouin scattering in microfibers is dominated by the photo-elastic effect and the moving boundary effect owing to the vibrating boundary in sub-wavelength microfibers. The moving boundary effect is proportional to the refractive index difference between the core and cladding. PMMA can be removed to increase the refractive index difference, allowing surface acoustic waves to be observed. In addition, the microfiber without PMMA is more sensitive to external refractive index variations. Refractive index sensing can be achieved by measuring BFS in chalcogenide microfibers. Multi-parameter Brillouin sensing can be achieved because of different responses of surface and longitudinal acoustic waves to external environmental variations. Brillouin scattering in high-birefringence fibers has been demonstrated. However, the birefringence effect on Brillouin sensing has never been investigated. The birefringence-dependent Brillouin sensing can be investigated in the elliptical-core microfibers with tailorable birefringence

### 10.2.2 Noise reduction in Brillouin random fiber lasers

Brillouin random fiber lasing with a low frequency drift enabled by RFGR resonator has been demonstrated. However, the fiber ring resonator is sensitive to external variations leading to large relative intensity noise at low frequencies. The intensity noise at frequencies below 1 kHz can be reduced by inserting an Erbium-doped fiber (EDF) into the RFGR because the millisecond photonic memory of the EDF can eliminate the intensity fluctuations. The EDF with high doping gives rise to a large loss in the ring and broad peaks. The EDF with low doping can be inserted into the random fiber ring to suppress intensity fluctuations in the low-frequency range. In addition, the BRFL based on the random grating ring with a long-lived single lasing mode operation without mode hopping offers an approach to investigating the mode behavior in two cases, including random mode change with small frequency differences at one longitudinal mode and longitudinal mode change by mode hopping. We can explore the mode behavior during the lasing establishment in both temporary and frequency domains.

Weak fiber Bragg grating arrays of tens of meters to hundreds of meters can be used as the distributed feedback of BRFLs. The randomly changed distance between fiber Bragg grating pairs in the grating fibers provides many high-Q interference peaks. The random fiber Bragg grating array acting as a narrow-bandwidth mode filter can suppress multiple longitudinal modes and alleviate the mode competition in the gain bandwidth. Single-mode Brillouin random lasing can be achieved by adjusting the length of the gain fiber and random fiber Bragg grating arrays. The short gain fiber length can lead to large mode separation and reduce the mode density in the gain bandwidth. Therefore, the BRFL based on the random fiber grating array resonator with the single mode and low noise can be achieved.

# APPENDIX

# A

# Broadband ultrasound sensing based on fused dual-core chalcogenide-PMMA microfibers


**Haiyang Wang**, Chams Baker, Liam Kelly, Pedro Tovar
Liang Chen and Xiaoyi Bao,
Optics Express. 30(6), 8847-8856 (2022) ;
https ://doi-org.proxy.bib.uottawa.ca/10.1364/OE.450734

## Author contributions

H.W. designed and fabricated microfibers with support from C.B ; H.W. performed measurements and numerical calculations ; X.B., H.W., L.C. and C.B. analyzed measured data. L.K. and P.T. contributed to the calibration of piezoelectric transducers ; All authors contributed to the writing of the paper ; X.B. supervised all aspects of this project.

## Summary

Unlike stimulated Brillouin scattering via electrostriction discussed in previous chapters, acoustic waves driven by electric fields in a piezoelectric transducer (PZT) give rise to mechanical stress, which is converted to strain on optical fibers by the elastic tensor. Therefore, acoustic waves can be detected by high-sensitivity fiber sensors. The detection of acoustic waves, especially ultrasound waves with high frequencies of tens of MHz, is limited due to the small stress of high-frequency waves and the low strain sensitivity of acoustic sensors. Compared to silica fibers, chalcogenide fibers have five times lower Young's modulus, offering a high strain sensitivity. The acoustic sensitivity and ultrasound detection range is proportional to the maximum-spectral-slope of the fiber's spectrum. Ultrasound sensing in polymer-based FBGs and multi-mode interferometers was limited to 25 MHz due to the small spectral slope [158, 159]. The interference spectra of the dual-core chalcogenide microfiber are tailorable. The maximum-spectral-slope is significantly increased in the dual-core microfiber with a small core diameter and close core separation due to the large refractive index difference between two modes in one polarization axis. As a result, broadband ultrasound sensing is achieved in chalcogenide microfibers, as will be presented in this chapter.

The ultrasound measurement in a dual-core chalcogenide microfiber is to detect the power change at one of the output cores. Figure A.1 presents the principle of ultrasound detection. The wavelength of a tunable laser source is adjusted to the quadrature point of the transmission spectrum, where the detected signal with the maximum amplitude is achieved due to the maximum-spectral-slope. The acoustic wave from a PZT induces strain on the chalcogenide microfiber, which changes the microfiber length and the refractive index. The phase change of the propagating light leads to the wavelength shift of the transmission spectrum. The fast wavelength shift caused by acoustic waves can be demodulated by measuring the variation of the laser output intensity.

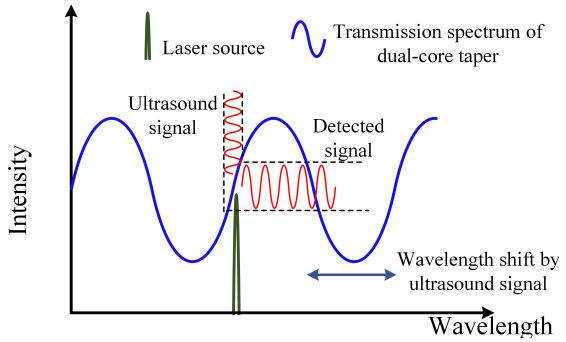


FIGURE A.1 – Principle of ultrasound detection based on a dual-core microfiber.

Research Article | Vol. 30, No. 6 / 14 Mar 2022 / Optics Express 8847
Optics EXPRESS

# Broadband ultrasound sensing based on fused dual-core chalcogenide-PMMA microfibers

HAIYANG WANG, CHAMS BAKER, LIAM KELLY, PEDRO TOVAR, LIANG CHEN, AND XIAOYI BAO

*Department of Physics, University of Ottawa, Ottawa, Ontario K1N 6N5, Canada*

**Abstract:** High-frequency ultrasound sensors are essential for high-resolution medical ultrasonic imaging and industrial ultrasonic non-destructive monitoring. In this paper, we propose highly sensitive broadband ultrasound sensors based on fused dual-core chalcogenide-polymethyl methacrylate ($As_2Se_3$-PMMA) microfibers. We demonstrate that ultrasound response is determined by the differential slope of transmission spectra in the dual-core microfiber, which is verified by detecting the acoustic response in various microfibers of different tapering parameters. A broadband ultrasound frequency range with a high signal-to-noise ratio (SNR) is achieved in the fused dual-core microfiber (DCM) with a sub-micron core diameter and a close core separation due to the large spectral slope at the quadrature points of the transmission spectrum. In addition, we experimentally demonstrate the sensing of ultrasound waves propagating with and without an aluminum plate in the DCM sensor. An ultrasound sensor with a broadband frequency range from 20 kHz to 80 MHz and an average SNR of 31 dB is achieved in a compact fused dual-core $As_2Se_3$-PMMA microfiber when it is directly placed on a piezoelectric transducer (PZT).



## 1. Introduction

Ultrasound sensors with tens of MHz frequency range and a high signal-to-noise ratio (SNR) are sought-after for high-resolution biomedical imaging [1–3] and non-destructive industrial monitoring [4–6]. Conventional piezoelectric ultrasound sensors have a narrow frequency range with a low SNR, and are incapable of detecting high acoustic frequencies. Optical fiber-based ultrasound sensors with high sensitivity are promising alternatives to piezoelectric ultrasound sensors. Ultrasound sensors in polymer optical fiber (POF)-based fiber Bragg gratings (FBG) [7,8] have been proposed and demonstrated, providing ultrasound detection at frequencies of around 25 MHz contributed by the low Young's modulus. However, they have limitations in higher frequency ultrasound detection due to the large grating bandwidth from sub-nanometer to several nanometers. The relatively small slope at the edge of the reflection spectrum and large diameter of the POF-based FBG leads to low ultrasound sensitivity. Strain variations on the order of nano-strain induced by high ultrasound frequencies can not be detected in such grating-based sensors. Detection of weak ultrasound signals requires a fiber device with a steep optical spectral response capable of producing measurable intensity changes from nano-strain acoustic perturbation.

Tapered fiber-based ultrasound sensors have been proposed and demonstrated for the detection of ultrasound frequencies up to 150 kHz [9]. With the core size of sub-micrometers, the nano-strain variation induced intensity change becomes detectable, especially in dual-core microfibers (DCM) with a small core-to-core distance, because the fractional change of core size induced by ultrasound pressure results in a measurable change in the transmitted power. A DCM is analogous to a Mach-Zehnder interferometer (MZI) where each of the even and odd modes represents an arm of the MZI. The phase difference between the even and odd modes is modulated by ultrasound signals leading to intensity variation at the outputs of the DCM, which allows for direct detection

#450734 https://doi.org/10.1364/OE.450734
Journal © 2022 Received 27 Dec 2021; revised 11 Feb 2022; accepted 14 Feb 2022; published 2 Mar 2022

Optics EXPRESS

using a photo-detector and eliminates the need for phase recovery as is the case in single-core taper-based acoustic sensing [10,11]. DCM-based ultrasound sensing with a frequency range of several hundred kHz has been demonstrated by directly measuring the output intensity change [12]. A multi-mode interferometer acoustic sensor based on single-mode fiber (SMF) taper was proposed and demonstrated for the detection of acoustic signals with frequencies up to tens of kHz [13]. The interference spectrum of multi-mode interferometers has low contrast over a large free spectral range (FSR) leading to a relatively small maximum-spectral-slope, which reduces the ultrasound detection sensitivity, and as a result, ultrasound signals with a frequency beyond tens of kHz can not be detected. A frequency response around 25 MHz is detected by introducing elliptical bubbles into the SMF taper to couple power into a larger number of modes and increase the maximum-spectral-slope of the interference spectrum [14]. Ultrasound detection at high frequencies beyond 25 MHz could not be detected as the maximum-spectral-slope is limited by the large FSR of a few nanometers that results from the small refractive-index difference between the modes. In addition, SMF tapers have a large Young's modulus (73 GPa for silica [15]), leading to low sensitivity as ultrasound waves induce a small variation to taper length and refractive index. As SMF taper-based ultrasound sensors have a diameter of a few micrometers, the SMF taper sensors are fragile making them difficult to operate in a harsh environment.

Recently, mechanically robust $As_2Se_3$-PMMA tapers have been designed and demonstrated for ultrasound sensing at frequencies up to 34 MHz [16]. As the lower Young's modulus of the $As_2Se_3$ and PMMA (17.8 GPa for $As_2Se_3$ and 3.5 GPa for PMMA [17]) compared to that of silica, the strain sensitivity of the $As_2Se_3$-PMMA taper is six times higher than that of silica-based tapers [18,19], which allows the highly sensitive broadband ultrasound sensing. The maximum-spectral-slope and FSR of the interference spectrum are tailorable by varying core size and distance between two cores of the dual-core $As_2Se_3$-PMMA microfiber, which enables the design and implementation of ultrasound sensors with a targeted sensing performance. In addition, the design of the DCM of different parameters enables tailorable refractive index difference between even and odd modes, which can be performed to have optical phase comparable to acoustic phase modulation at high frequencies of tens of MHz, leading to detectable high-frequency ultrasound waves.

In this paper, we demonstrate broadband ultrasound sensing based on fused dual-core chalcogenide-PMMA microfibers. DCMs are designed and fabricated with submicron core diameters for increased ultrasound sensitivity. Ultrasound frequency range and SNR of the fabricated DCMs are measured using a piezoelectric transducer (PZT) as an ultrasound source using two arrangements. In the first arrangement, the DCM sensor and the PZT are placed on a 2 mm-thick aluminum plate, and experimental results show a higher SNR and a larger frequency range when the DCM has a smaller core diameter and a closer core separation. In the second arrangement, the aluminum plate is removed and the DCM is placed in direct contact with the PZT to eliminate acoustic attenuation due to propagation through the plate medium allowing for the measurement of higher acoustic frequencies. Ultrasound sensing with an average SNR of 31 dB and a broadband frequency range from 20 kHz to 80 MHz is achieved in a compact dual-core $As_2Se_3$-PMMA with a core diameter of 0.5 μm, core separation of 0.445 μm and waist length of 1 cm. The obtained ultrasound response is compared with the PZT response that is characterized by measuring electrical reflection coefficient $S_{11}$, validating the high sensitivity of the fused dual-core $As_2Se_3$-PMMA microfiber sensor.

## 2. Fabrication, simulation and working principle

The fabrication of dual-core $As_2Se_3$-PMMA fibers has been reported in [20,21]. To make an $As_2Se_3$-PMMA preform with a fused dual-core shape, an assembly with two $As_2Se_3$ fibers and a PMMA tube is placed on a spinning lathe and heated at 220 °C for 48 hours. Figure 1(a) presents the cross-section image of the polished end of a fused dual-core $As_2Se_3$-PMMA fiber. The ratio

Optics EXPRESS

of the core separation ($D_{core}$) and core diameter $d_{core}$ is $D_{core}$=0.89$d_{core}$. The fused dual-core fiber is then tapered using the heat-brush method [22]. A sample profile of a fused DCM with a waist length ($L_w$) of 1 cm and an $As_2Se_3$ core diameter of 2 μm is shown in Fig. 1(b). The section between 2.5 cm and 3.5 cm along the microfiber corresponds to the waist region. One $As_2Se_3$ core of the dual-core $As_2Se_3$-PMMA fiber is butt-coupled with single-mode fibers and the butt-coupling interfaces are fixed using UV-cured epoxy, as illustrated in Fig. 1(c). Four fused dual-core microfibers with the same waist length of 1 cm and different diameters are fabricated and utilized in this investigation. Images and dimensions of the four DCMs are shown in Fig. 1(d). The four microfibers have an $As_2Se_3$ core diameter of 4 μm, 2 μm, 0.75 μm, 0.5 μm and a PMMA cladding diameter of 225.9 μm, 113.5 μm, 42.4 μm and 28.0 μm, respectively.

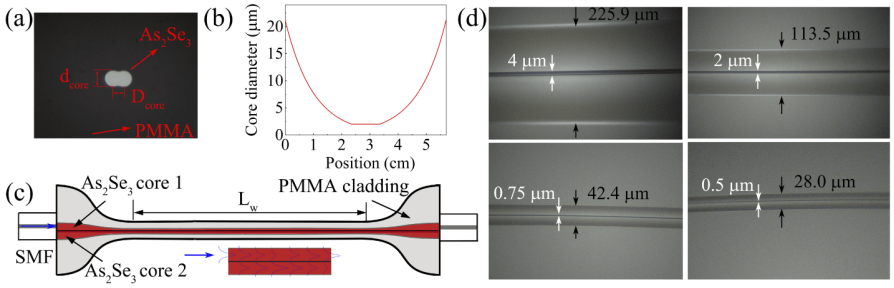


**Fig. 1.** (a) Optical microscope image of a fused dual-core $As_2Se_3$-PMMA fiber. (b) The relationship between a tapered core diameter and the fiber length. (c) Schematic of a coupled DCM. (d) The side views of four DCMs.

Both the even and odd modes are equally excited when a laser is launched into one of the input cores of the DCM. The electric field distributions of even and odd modes of a fused dual-core microfiber are shown in Fig. 2(a) and Fig. 2(b), respectively. The calculated field distributions are obtained using refractive-index values of 2.674 and 1.481 for $As_2Se_3$ cores and PMMA cladding, respectively. Light propagation along a DCM is simulated using the beam propagation method (BPM), as shown in Fig. 2(c). The light power transfers back and forth between the two cores with a constant period ($\Lambda$) when propagating along the DCM. The coupling length is defined as the length required for the power to transfer from one core to the other given by $L_c = \Lambda/2 = \pi/(\beta_e - \beta_o)$, where $\beta_e$ and $\beta_o$ are the propagation constant of the even and odd modes, respectively. The coupling lengths are 4.0 $\mu$m, 9.2 $\mu$m, 98.9 $\mu$m and 458.6 $\mu$m for the four samples with an $As_2Se_3$ core diameter of 0.5 $\mu$m, 0.75 $\mu$m, 2 $\mu$m, 4 $\mu$m, respectively. The short spatial period of 4.0 $\mu$m gives rise to high-frequency ultrasound sensing. The difference between the phases of even and odd modes ($\phi_d$) in the DCM is given by $\phi_d = 2\pi z\Delta n/\lambda$, where $\lambda$ is the wavelength of light, $z$ is the fiber length and $\Delta n$, given by $\Delta n = n_e - n_o$, is the refractive-index difference with $n_e$ and $n_o$ being the effective refractive-indices of the even and odd modes. The output power of the DCM is given by $P = P_0 \cos^2[\pi z\Delta n/\lambda]$ in $As_2Se_3$ core 1 when the input light is injected in the same core, where $P_0$ is the input power. Due to the larger phase difference change over wavelength in the slow axis of the dual-core taper in comparison to the fast axis, the spectral slope at the quadrature point of the transmission spectrum is larger in the slow axis, which leads to a higher sensitivity. The value of $\Delta n$ in the slow axis of the DCM as a function of $\lambda$ is calculated for different core diameters from 0.5 μm to 21.25 μm when the $D_{core}/d_{core}$=0.89 using the finite element method (FEM). The phase difference between even and odd modes at each core diameter of the microfiber, including the core diameters in the waist region and transition region, is calculated in a step of 0.1 μm according to the tapered fiber profiles. The $\phi_d$ is estimated by adding the calculated phase difference at each core diameter of the DCM. Figure 2(d) shows the calculated transmission spectra of the four fused DCMs with the same

Optics EXPRESS

waist length of 1 cm over core diameters of 4 μm, 2 μm, 0.75 μm and 0.5 μm. The FSR of transmission spectra shows a sharp decrease with reduced core diameter, as plotted in the red curve in Fig. 2(e). The FSR of the transmission spectrum for the DCM with a core diameter of 0.5 μm is around 70 times smaller than that of the DCM with 4 μm. The spectral slope is calculated from the first derivative of the function $P(\lambda)/P_0$. The maximum-spectral-slope ($S_m$) at the quadrature point of the normalized transmission spectrum is presented by the black curve in Fig. 2(e). The value of $S_m$ for the DCM with a core diameter of 0.5 μm ($S_m$=14.1) is around 74 times larger than that of the DCM with a core diameter of 4 μm ($S_m$=0.19). The large value of $S_m$ for the fused DCM with a small core diameter is contributed by the small FSR of the transmission spectrum.

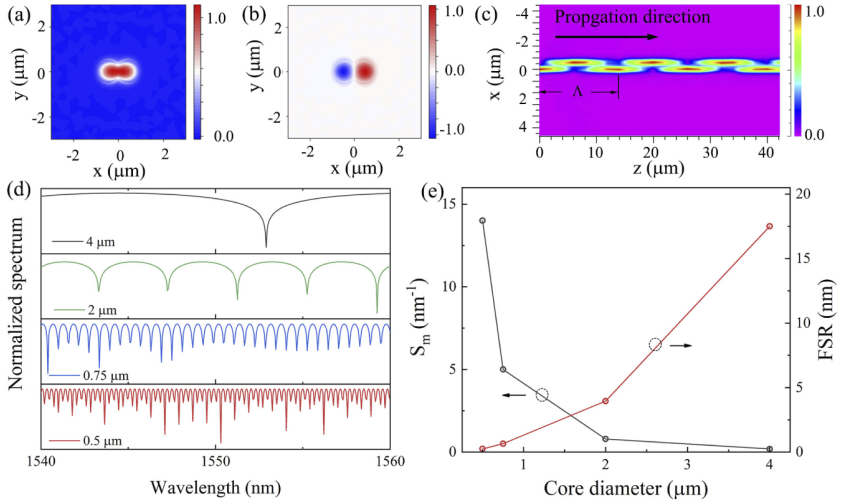


**Fig. 2.** Numerical simulations of fused dual-core $As_2Se_3$-PMMA microfibers. (a) Even mode profile. (b) Odd mode profile. (c) Field distribution of transmitting light. (d) Normalized transmission spectra for four DCMs. (e) Calculated $S_m$ and FSR of the transmission spectra as a function of core diameter.

Real-time ultrasound measurement in a dual-core $As_2Se_3$-PMMA microfiber is based on the detection of power change instead of the spectral shift of the transmission spectrum at one of the output cores. Using a photo-detector to measure the ultrasound induced power variation at the output of the DCM, the measured AC voltage ($V_S$) is given by [23]

$$V_S = R\Delta\lambda_S S P_0 G \tag{1}$$

where $R$ is the responsivity of the photo-detector, $\Delta\lambda_S$ is the spectral shift by strain perturbation, $S$ is the spectral slope at the lasing wavelength and $G$ is the electronic amplifier gain of the photo-detector signal. The detected AC output is determined by $S$ and $\Delta\lambda_S$ in the case of a constant $P_0$, $R$ and $G$. For a strain of 1 $\mu\varepsilon$, the value of $\Delta\lambda_S$ is around 1.5 times smaller for the dual-core microfiber with a core diameter of 0.55 μm ($\Delta\lambda_S$=-4.21 pm) compared with that of a DCM with a core diameter of 2.5 μm ($\Delta\lambda_S$=-6.23 pm) [18,20]. Unlike the relatively small change in $\Delta\lambda_S$, the spectral slope at the quadrature point increases by a factor of 35 as the core diameter of the DCM is reduced from 2.5 μm to 0.55 μm. Therefore, the dual-core microfiber with submicron core diameter is designed and fabricated to achieve a higher ultrasound sensitivity.

Optics EXPRESS

## 3. Experimental results and discussion

Figure 3 presents a schematic setup for ultrasound sensing using a dual-core $As_2Se_3$-PMMA microfiber. Light from an Erbium-doped fiber amplifier (EDFA) is linearly polarized using a linear polarizer (LP) and is launched into one of the input cores of the DCM. The polarized light is aligned to the slow axis of the DCM using a polarization controller (PC). The transmission spectrum of the DCM is recorded by an optical spectrum analyzer (OSA). The transmission spectrum represents the interference between the fields propagating in the even and odd modes of the DCM and varies periodically with wavelength due to the different wavelength-dependence of $\Delta n$. Wavelength dips of the transmission spectrum in the DCM are obtained when the phase difference of two modes satisfies the condition $\phi_d(\lambda) = (2m + 1)\pi$. The normalized transmission spectra of the four fused DCMs are plotted in Fig. 4(a). The value of FSR decreases with reducing core diameter due to the large phase difference of even and odd modes. The FSR of the transmission spectra for different core diameters is plotted by the red curve in Fig. 4(b). The maximum-spectral-slope $S_m$ of the normalized transmission spectra at the quadrature points for the four DCMs is measured as a function of core diameter, as shown in the black curve in Fig. 4(b). The value of $S_m$ for the DCM with a core diameter of 0.5 μm ($S_m$=20.3 $nm^{-1}$) is 72.5 times larger than one with a core diameter of 4 μm ($S_m$=0.28 $nm^{-1}$), in close agreement with the numerical simulations in Fig. 2(e). The $S_m$ for the submicron core microfiber is tens of times larger than that of gratings [23,24] and multi-mode tapers [25].

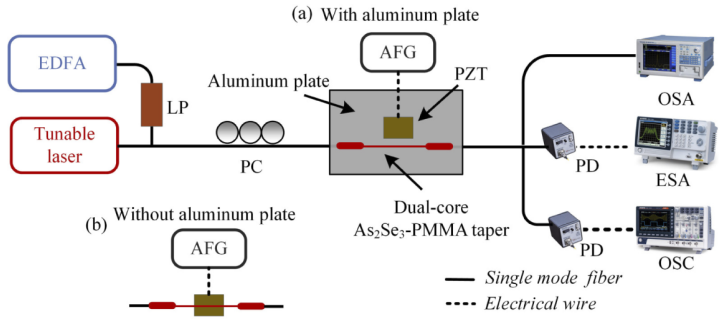


**Fig. 3.** The schematic experimental setup of ultrasound sensing. EDFA: Erbium-doped fiber amplifier; LP: linear polarizer; PC: polarization controller; AFG: arbitrary function generator; PZT: piezoelectric transducer; PD: photo-detector; OSA: optical spectrum analyzer; ESA: electrical spectrum analyzer; OSC: oscilloscope.

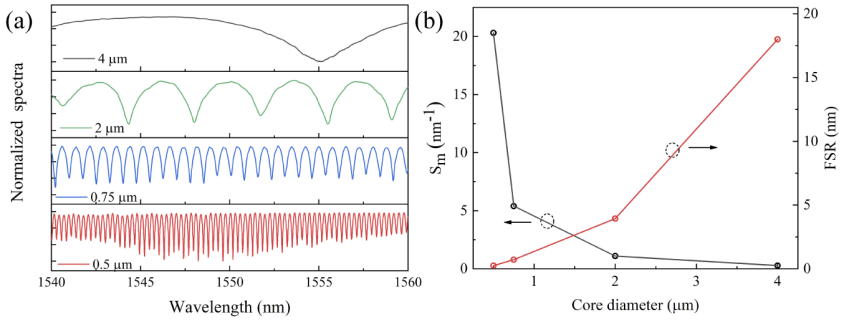


**Fig. 4.** (a) Measured transmission spectra of four DCMs. (b) Maximum slopes ($S_m$) and FSR of the transmission spectra as a function of core diameter.

Optics EXPRESS

For ultrasound detection, the EDFA is replaced by a continuous wave (CW) light from a tunable laser, and the polarization of the laser is adjusted by the PC to align with the slow axis of the dual-core microfiber. The pump power of incident light is 2 dBm. To get the highest SNR and largest ultrasound frequency range, the wavelength of the CW light is tuned to the wavelength of maximum-spectral-slope at a quadrature point of the transmission spectrum. A PZT with a central frequency of ~3.8 MHz is glued onto a 2 mm-thick aluminum plate, and is driven by a sinusoidal electrical signal with a peak-to-peak voltage (Vpp) of 10 V from an arbitrary function generator (AFG). The fused dual-core is placed on the surface of the aluminum plate, 5 mm away from the PZT. The acoustic wave propagation from the PZT results in a variation of the refractive indices of the even and odd modes and the waist length, inducing a wavelength shift in the transmission spectrum. The power of the CW light is changed by the acoustic wave-induced spectral shift, which is detected by a photo-detector (PD) and recorded by an electrical spectrum analyzer (ESA) and an oscilloscope (OSC). To reduced the acoustic attenuation when the acoustic wave propagates through the aluminum plate and increase ultrasound detection range, the fused dual-core $As_2Se_3$-PMMA microfiber is directly placed on the PZT without the aluminum plate.

Figure 5(a) presents the measured signals from the photo-detector as a function of time for the four fused dual-core $As_2Se_3$-PMMA microfibers when the PZT is driven by the function generator with a frequency of 100 kHz and a voltage of Vpp=10 V. The output signals show a sinusoidal waveform with a frequency of 100 kHz as the ultrasound wave induces a periodic perturbation on the dual-core fiber when it propagates along the surface of the aluminum plate. The peak-to-peak voltage of the measured sinusoidal signals is plotted in Fig. 5(b), showing a sharp increase with decreasing core diameter. The peak-to-peak voltage for a fused DCM with a core diameter of 0.5 μm is 65 times greater than that of 4 μm, which is close to the 72.5 fold increase in the maximum slopes $S_m$. The small difference between the increase of Vpp and the increase of $S_m$ is due to the reduced $\Delta\lambda_S$ for a dual-core fiber with a large core diameter [18,20]. The large output voltage for the small-core microfiber ensures high-sensitivity ultrasound sensing.

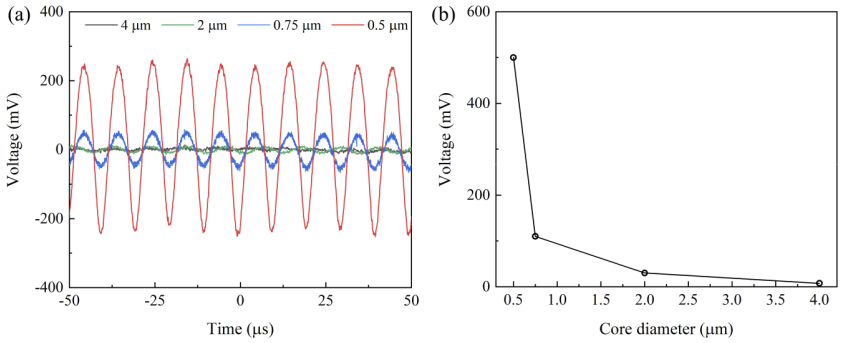


**Fig. 5.** (a) The ultrasound response of four DCMs with different core diameters in the time-domain at the ultrasound frequency of 100 kHz. (b) Output voltage as a function of core diameter.

To characterize the ultrasound sensing frequency response of the dual-core $As_2Se_3$-PMMA microfibers, the frequency is varied from 20 kHz to 50 MHz in step of 100 kHz. SNR is measured at each ultrasound frequency using ESA. The PD and ESA are placed in another room of 20 meters away to avoid the detection of radiated electromagnetic waves from an acoustic source setup, in which the PZT is connected to the function generator by a SubMiniature version A (SMA) connector. The SNR of the detected signal for each of the dual-core $As_2Se_3$-PMMA microfibers is plotted in Fig. 6(a). The SNR shows several peaks at around 4.0 MHz, 12.5 MHz, 21.1 MHz, 29.2 MHz and 37.8 MHz, corresponding to the central frequency and high odd order

Optics EXPRESS

harmonics of the PZT. The SNR increases as the core diameter of the DCM decreases, especially at the low-frequency range below 5 MHz. The SNR of the DCM with a core diameter of 0.5 μm at hundreds of kHz is 3 orders of magnitude higher than the SNR of a DCM with a core diameter of 4 μm. A maximum SNR of >80 dB for the DCM with a core diameter of 0.5 μm and a cladding diameter of 28.0 μm is detected at 200 kHz as plotted in Fig. 6(b). The maximum detected frequency as a function of core diameter is plotted in Fig. 6(c) showing an increase of maximum detected frequency by 15 MHz as the core diameter decreases from 4 μm to 0.5 μm. This is because high spectral slope at the quadrature point of the transmission spectrum for the dual-core taper with small core diameter. The frequency range for the dual-core $As_2Se_3$-PMMA microfiber ultrasound sensor is 30 MHz larger and SNR is up to 30 dB higher than those of silica-based fiber microfiber sensor using the same PZT as an ultrasound source [26]. The larger detection frequency range and higher SNR for the dual-core $As_2Se_3$-PMMA microfiber sensor are due to the smaller Young's modulus, the larger spectral slope at the quadrature point of the transmission spectrum than that of the silica microfiber. Moreover, compared with the silica microfiber-based ultrasound sensing, the dual-core microfiber with a core diameter of 0.5 μm is coated by PMMA cladding with a diameter of 28 μm, which provides more mechanical robustness and reduces the chances of breaking during operation.

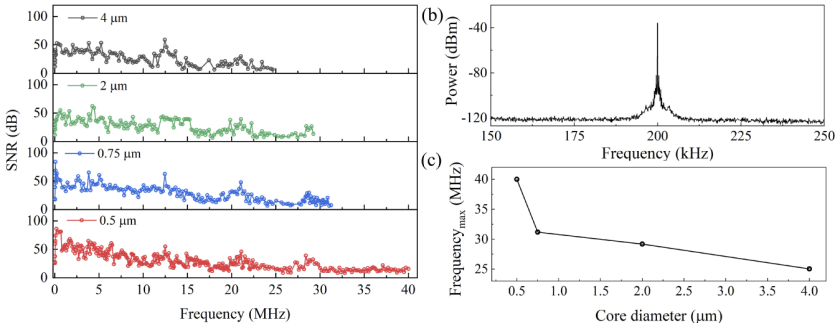


**Fig. 6.** (a) SNR as a function of frequency for four DCMs with different core diameters. (b) Maximum SNR for the DCM with a core diameter of 0.5 μm at 200 kHz sine function. (c) Maximum frequency response as a function of core diameter.

Ultrasound sensing SNR as a function of acoustic frequency is measured for 1 cm-long dual-core $As_2Se_3$-PMMA microfibers with the same core diameter of $d_{core}$=0.75 μm and different core separations of $D_{core}$=0.99$d_{core}$ and $D_{core}$=0.89$d_{core}$, and the results are plotted in Fig. 7. The maximum detection frequency for the dual-core $As_2Se_3$-PMMA microfiber with a core separation of $D_{core}$=0.89$d_{core}$ increase 7.8 MHz, compared with that of the DCM with a core separation of $D_{core}$=0.99$d_{core}$. The transmission spectrum of the DCM with $D_{core}$=0.89$d_{core}$ has a smaller FSR and a sharper spectral slope at the quadrature point than those of the DCM with $D_{core}$=0.99$d_{core}$, as plotted in the inset of Fig. 7, due to the larger rate-of-change of $\phi_d$ with $\lambda$ for the DCM with a smaller $D_{core}$. The value of maximum-spectral-slope for the DCM with $D_{core}$=0.89$d_{core}$ ($S_m$ = 5.2 nm$^{-1}$) is more than twice larger than that of the DCM with $D_{core}$=0.99$d_{core}$ ($S_m$ = 2.5 nm$^{-1}$), which leads to a larger sensitivity resulting in a larger ultrasound frequency range for the ultrasound measurement. To increase the ultrasound sensing maximum detection frequency, a dual-core $As_2Se_3$-PMMA microfiber with a submicron core diameter and a close core separation is favorable.

Ultrasound acoustic waves from the PZT are attenuated when traveling through the aluminum plate, and the attenuation increases as the ultrasound frequency increases resulting in a lower SNR at higher frequencies, leading to the understated measurement of the actual frequency detection range of the fiber ultrasound sensor. To eliminate the effect of acoustic attenuation on

Optics EXPRESS

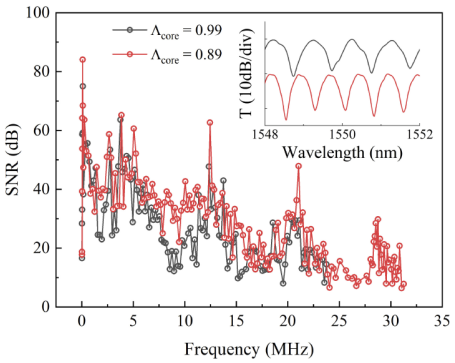


**Fig. 7.** SNR of two DCMs with different core separation $D_{core}$ as a function of frequency. Inset: Transmission spectra for the two microfibers.

the maximum ultrasound frequency detection of the sensor, the compact dual-core chalcogenide-PMMA microfiber with waist length of 1 cm, core diameter of 0.5 μm and core separation of 0.445 μm is directly fixed on the PZT without the aluminum plate avoiding the propagation attenuation of acoustic waves. The SNR as a function of ultrasound frequency in the DCM is measured, as presented by the red curve in Fig. 8(a), showing a broadband ultrasound range from 20 kHz to 80 MHz with an average SNR of 31 dB. The frequency range for the SNR above 10 dB is 68 MHz, and SNR is 5-10 dB for the frequency range of 68-80 MHz. Compared with the ultrasound sensing with the 2 mm thick aluminum plate as plotted by the red curve in Fig. 6(a), the maximum detection frequency increases by 40 MHz for ultrasound sensing without the aluminum plate due to the elimination of the attenuation of acoustic waves. The ultrasound detection with the maximum frequency of 80 MHz offers great potential for high-resolution biomedical imaging.

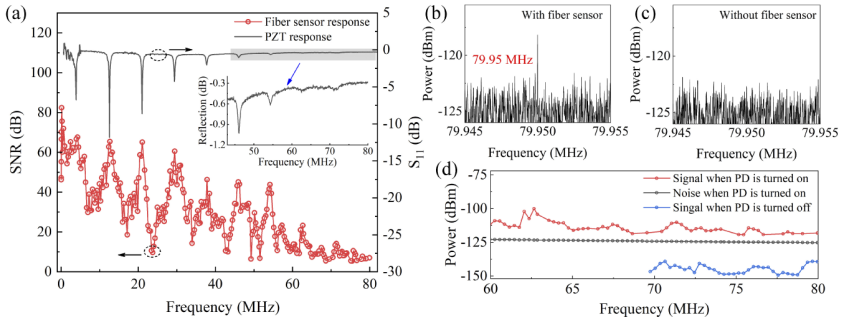


**Fig. 8.** (a) SNR of the fused DCM with a core diameter of 0.5 μm without the aluminum plate, and $S_{11}$ of the PZT for frequencies from 300 kHz to 80 MHz. Inset: Close-up of high frequency range. Frequency response at 79.95 MHz (b) with connecting fiber sensor; (c) without connecting fiber sensor. (d) Detected radiated electromagnetic waves and microfiber sensor ultrasound response.

Furthermore, the amplitude of the generated ultrasound wave from the PZT reduces as the frequency increases for the same driving voltage amplitude. Therefore, the frequency detection range of the sensor must take into account the reduced amplitude of the generated ultrasound signal from the PZT at higher frequencies. Acoustic waves with different frequencies from the PZT are characterized by measuring electrical reflection coefficient $S_{11}$ in a S-parameter

Optics EXPRESS

network analyzer [27]. $S_{11}$ is equal to the ratio of the power of a reflected electromagnetic wave and the power of an incident electromagnetic wave on the PZT. $S_{11}$=0 dB implies that all the power of the incident electromagnetic wave is reflected from the PZT and nothing is radiated. The $S_{11}$ value for a frequency range from 300 kHz to 80 MHz is measured, as presented in the black curve in Fig. 8(a). We observe the first dip at 4 MHz and several dips with a period of ~8 MHz corresponding to the central frequency and high odd order harmonics of the PZT. At higher frequencies, PZT has little absorption to driving power as measured in $S_{11}$ parameter, as presented in the inset of Fig. 8(a), and acoustic periods decrease, resulting in a reduction in the amplitude of the generated acoustic waves and the fiber sensor displacement. Indeed, the SNR decreases at high frequencies due to the reduced phase change of the dual-core taper. Figure 8(a) shows that the peaks of SNR coincide with the dips in the $S_{11}$ frequency response of the PZT confirming that the amplitude of generated acoustic waves from the PZT correlates with the amplitude of the electromagnetic reflection from the PZT. Due to the non-zero radiated acoustic wave of the PZT response at the non-resonant frequencies and the large acoustic wave induced-strain at low ultrasound frequencies, the ultrasound signals with high SNR are obtained. The weak amplitude of ultrasound waves from the PZT at higher frequencies indicates that a wider ultrasound detection frequency range for the $As_2Se_3$-PMMA microfiber sensor can be measured in the presence of an ultrasound source that can produce waves at such high frequencies.

Finally, it is essential to ensure that the measured signal at the ESA does not include the radiated signal from the acoustic source setup. The ultrasound responses at 79.95 MHz in the cases with and without connecting the DCM sensor are measured as shown in Fig. 8(b) and Fig. 8(c), respectively. The ultrasound response at 79.95 MHz is selected rather than 80 MHz to eliminate the artifact harmonics that appear at integer multiples of the reference frequency of 10 MHz of the function generator. The measured response in Fig. 8(c) shows that radiated signal from the acoustic source setup is not captured by the ESA. The measurement is repeated for ultrasound frequencies from 20 kHz to 80 MHz without connecting the DCM sensor, and no signal is detected above the noise floor, which indicates that the radiated electromagnetic wave from the acoustic source setup does not affect the ultrasound measurement. To further ensure that the radiated electromagnetic waves from the acoustic source setup do not affect the ultrasound measurement, the power of the radiated electromagnetic waves as a function of frequency is measured by the ESA when PD is turned off, as presented by the blue curve in Fig. 8(d). The power of the radiated electromagnetic waves from the acoustic source setup is at least 15 dB below the noise floor measured when the PD is turned on, confirming that the radiated electromagnetic waves do not affect the high-frequency ultrasound measurement using the dual-core $As_2Se_3$-PMMA microfiber sensor.

## 4. Conclusion

In conclusion, we have demonstrated broadband ultrasound sensing based on fused dual-core $As_2Se_3$-PMMA microfibers. The ultrasound detection frequency range and SNR have been measured in dual-core microfibers with different core diameters and core separations. The dual-core taper sensor with a large spectral slope at the quadrature point of the transmission spectrum contributes to high-frequency ultrasound sensing. Ultrasound sensing with a broadband acoustic frequency range from 20 kHz to 80 MHz and an average SNR of 31 dB is achieved in a compact, mechanically robust, dual-core microfiber with a waist length of 1 cm, an $As_2Se_3$ core diameter of 0.5 μm and a core separation of 0.445 μm. The fused dual-core $As_2Se_3$-PMMA microfiber sensors with high-performance ultrasound detection can potentially be used for a variety of practical applications including biomedical and industrial high-resolution imaging.

**Funding.** China Scholarship Council; Natural Sciences and Engineering Research Council of Canada (DG-2020-06302); Canada Research Chairs (75-67138).

**Disclosures.** The authors declare no conflicts of interest.

Optics EXPRESS

**Data Availability.** Data underlying the results presented in this paper are not publicly available at this time but may be obtained from the authors upon reasonable request.

## References


1. V. M. Murukeshan and L. H. Ta, "Hybrid-modality high-resolution imaging: for diagnostic biomedical imaging and sensing for disease diagnosis," Proc. SPIE **9268**, 92680U (2014).
2. R. Ansari, E. Z. Zhang, A. E. Desjardins, and P. C. Beard, "All-optical forward-viewing photoacoustic probe for high-resolution 3d endoscopy," Light: Sci. Appl. **7**(1), 75 (2018).
3. R. Acharya, R. Wasserman, J. Stevens, and C. Hinojosa, "Biomedical imaging modalities: a tutorial," Computerized Medical Imaging and Graphics **19**(1), 3–25 (1995).
4. X. Zhen, Y. Yong, X. C. Guang, X. D. Guo, L. F. Fang, and L. X. Liang, "Profile tracking with ultrasonic alignment for automatic non-destructive testing of complex structures," Robotics and Computer-Integrated Manufacturing **49**, 134–142 (2018).
5. B. Fischer, "Optical microphone hears ultrasound," Nat. Photonics **10**(6), 356–358 (2016).
6. S. Gholizadeh, "A review of non-destructive testing methods of composite materials," Procedia Structural Integrity **1**, 50–57 (2016).
7. C. Broadway, G. Woyessa, O. Bang, P. Mégret, and C. Caucheteur, "An l-band ultrasonic probe using polymer optical fibre," Proc. SPIE **10878**, 22 (2019).
8. C. Broadway, R. Min, A. G. Leal-Junior, C. Marques, and C. Caucheteur, "Toward commercial polymer fiber bragg grating sensors: Review and applications," J. Lightwave Technol. **37**(11), 2605–2615 (2019).
9. W. Kuang, S. Y. Dong, M. Zhang, and Y. B. Liao, "Acoustic emission sensor based on a tapered single-mode fiber," Proc. SPIE **5577**, 678–682 (2004).
10. Y. Li, X. Wang, and X. Bao, "Sensitive acoustic vibration sensor using single-mode fiber tapers," Appl. Opt. **50**(13), 1873–1878 (2011).
11. D. Gallego and H. Lamela, "High-sensitivity ultrasound interferometric single-mode polymer optical fiber sensors for biomedical applications," Opt. Lett. **34**(12), 1807–1809 (2009).
12. R. Chen, G. Fernando, T. Butler, and R. Badcock, "A novel ultrasound fibre optic sensor based on a fused-tapered optical fibre coupler," Meas. Sci. Technol. **15**(8), 1490–1495 (2004).
13. B. Xu, Y. Li, M. Sun, Z.-W. Zhang, X.-Y. Dong, Z.-X. Zhang, and S.-Z. Jin, "Acoustic vibration sensor based on nonadiabatic tapered fibers," Opt. Lett. **37**(22), 4768–4770 (2012).
14. W. Ma, H. Fan, L. Chen, and X. Bao, "Tapered assisted dual micro-bubble-device for ultrasound sensor," IEEE Photonics Technol. Lett. **32**(18), 1219–1222 (2020).
15. S. Liu, K. Yang, Y. Wang, J. Qu, C. Liao, J. He, Z. Li, G. Yin, B. Sun, and J. Zhou, "High-sensitivity strain sensor based on in-fiber rectangular air bubble," Sci. Rep. **5**, 7624 (2015).
16. S. Gao, C. Baker, W. Cai, L. Chen, and X. Bao, "10 khz-34 mhz ultrasound detection based on a dual-core hybrid taper," APL Photonics **4**(11), 110805 (2019).
17. H. Wang, S. Gao, C. Baker, Y. Wang, L. Chen, and X. Bao, "Wide-range strain sensor based on brillouin frequency and linewidth in an as 2 se 3-pmma hybrid microfiber," Opt. Express **28**(15), 22933–22945 (2020).
18. S. Gao, C. Baker, L. Chen, and X. Bao, "Simultaneous measurement of temperature and strain in a dual-core as 2 se 3-pmma taper," IEEE Photonics Technol. Lett. **30**(1), 79–82 (2018).
19. N. Zhang, W. Xu, S. You, C. Yu, C. Yu, B. Dong, and K. Li, "Simultaneous measurement of refractive index, strain and temperature using a tapered structure based on smf," Opt. Commun. **410**, 70–74 (2018).
20. S. Gao, C. Baker, L. Chen, and X. Bao, "High-sensitivity temperature and strain measurement in dual-core hybrid tapers," IEEE Photonics Technol. Lett. **30**(12), 1155–1158 (2018).
21. H. Wang, S. Gao, C. Baker, Y. Wang, L. Chen, and X. Bao, "Stimulated brillouin scattering in a tapered dual-core as 2 se 3-pmma fiber for simultaneous temperature and strain sensing," Opt. Lett. **45**(12), 3301–3304 (2020).
22. C. Baker and M. Rochette, "A generalized heat-brush approach for precise control of the waist profile in fiber tapers," Opt. Mater. Express **1**(6), 1065–1076 (2011).
23. Q. Wu and Y. Okabe, "High-sensitivity ultrasonic phase-shifted fiber bragg grating balanced sensing system," Opt. Express **20**(27), 28353–28362 (2012).
24. L. Zhang, P. Lu, Z. Zhou, Y. Wang, S. Mihailov, L. Chen, and X. Bao, "High-efficiency random fiber laser based on strong random fiber grating for mhz ultrasonic sensing," IEEE Sens. J. **20**(11), 5885–5892 (2020).
25. H. Fan, W. Ma, L. Chen, and X. Bao, "Ultracompact twisted silica taper for 20 khz to 94 mhz ultrasound sensing," Opt. Lett **45**(14), 3889–3892 (2020).
26. H. Fan, L. Chen, and X. Bao, "Chalcogenide microfiber-assisted silica microfiber for ultrasound detection," Opt. Lett. **45**(5), 1128–1131 (2020).
27. A. Shimko, K. Stroganov, and V. Kalinin, "Saw resonator defects identification technique," in *2014 European Frequency and Time Forum (EFTF)*, (IEEE, 2014), pp. 150–152

# Publications during four years Ph.D (Sept 2018-Sept 2022)

## Journal paper

1. **Wang, H.**, Chen, C., Lu, P., Mihailov, S., Chen, L., & Bao, X. (2022). Reducing frequency fluctuation in Brillouin random fiber laser by random fiber grating ring resonator. *Optics Letter*, 47(15), 3900-3903.

2. **Wang, H.**, Lu, P., Chen, C., Mihailov, S., Chen, L., & Bao, X. (2022). Stabilizing Brillouin random laser with photon localization by feedback of distributed random fiber grating array. *Optics Express*, 30(12), 20712-20724.

3. **Wang, H.**, Baker, C., Kelly, L., Tovar, P., Chen, L., & Bao, X. (2022). Broadband ultrasound sensing based on fused dual-core chalcogenide-PMMA microfibers. *Optics Express*, 30(6), 8847-8856.

4. **Wang, H.**, Zhou, Z., Chen, L., & Bao, X. (2022). Acoustic wave coupling in dual-wavelength orthogonal polarized Brillouin random fiber laser using polarization-maintaining fiber. *Journal of Lightwave Technology*, 40(8), 2541-2547.

5. **Wang, H.**, Baker, C., Chen, L., & Bao, X. (2021). Stimulated Brillouin scattering in high-birefringence elliptical-core $As_2Se_3$-PMMA microfibers. *Optics Letters*, 46(5), 945-948.

6. **Wang, H.**, Gao, S., Baker, C., Wang, Y., Chen, L., & Bao, X. (2020). Wide-range strain sensor based on Brillouin frequency and linewidth in an $As_2Se_3$-PMMA hybrid microfiber. *Optics Express*, 28(15), 22933-22945.

7. **Wang, H.**, Gao, S., Baker, C., Wang, Y., Chen, L., & Bao, X. (2020). Stimulated

brillouin scattering in a tapered dual-core $As_2Se_3$-PMMA fiber for simultaneous temperature and strain sensing. *Optics Letters*, 45(12), 3301-3304.

8. **Wang, H.**, Chen, L., & Bao, X. (2021). Salinity Concentration Sensing Based on a Tapered Dual-Core $As_2Se_3$-PMMA Hybrid Fiber. *IEEE Photonics Technology Letters*, 33(4), 181-184.

9. Zhou, Z., **Wang, H.**, Wang, Y., Chen, L., & Bao, X. (2021). Distributed static and dynamic detection of an acoustic wave in a Brillouin random fiber laser. *Photonics Research*, 9(5), 772-780.

10. Gao, S., **Wang, H.**, Wang, Baker, C., Chen, L., Wen, Z., Cai, Y. & Bao, X. (2022). Monitoring local temperature and longitudinal strain along a nonuniform $As_2Se_3$-PMMA tapered fiber by Brillouin gain-profile tracing, *Optics Express*, 30(16), 29655-29755.

11. Gao, S., Wen, Z., **Wang, H.**, Wang, Baker, C., Chen, L., Cai, Y. & Bao, X. (2022). Longitudinal strain performance of BOTDA-based nonuniform $As_2Se_3$-PMMA tapered fibers. *Journal of Lightwave Technology.*

# Conference paper

1. Zhou, Z., **Wang, H.**, Wang, Y., Chen, L., & Bao, X. (6-11, June 2021). Distributed acoustic wave sensing in a Brillouin random fiber laser. OFC 2021. Washington, DC, United States.

# References


[1] Léon Brillouin. Diffusion de la lumière et des rayons x par un corps transparent homogène. In *Annales de physique*, volume 9, pages 88–122, 1922.

[2] RY Chiao, CH Townes, and BP Stoicheff. Stimulated brillouin scattering and coherent generation of intense hypersonic waves. *Physical Review Letters*, 12(21) :592, 1964.

[3] K Charles Kao and George A Hockham. Dielectric-fibre surface waveguides for optical frequencies. In *Proceedings of the Institution of Electrical Engineers*, volume 113, pages 1151–1158. IET, 1966.

[4] EP Ippen and RH Stolen. Stimulated brillouin scattering in optical fibers. *Applied Physics Letters*, 21(11) :539–541, 1972.

[5] Govind P Agrawal. Nonlinear fiber optics. In *Nonlinear Science at the Dawn of the 21st Century*, pages 195–211. Springer, 2000.

[6] Lufan Zou, Xiaoyi Bao, Fabien Ravet, and Liang Chen. Distributed brillouin fiber sensor for detecting pipeline buckling in an energy pipe under internal pressure. *Applied optics*, 45(14) :3372–3377, 2006.

[7] Aldo Minardo, Romeo Bernini, Lucio Amato, and Luigi Zeni. Bridge monitoring using brillouin fiber-optic sensors. *IEEE Sensors Journal*, 12(1) :145–150, 2011.

[8] NS Kapany and RJ Simms. Recent developments in infrared fiber optics. *Infrared Physics*, 5(2) :69–80, 1965.

[9] Guangming Tao, Heike Ebendorff-Heidepriem, Alexander M Stolyarov, Sylvain Danto, John V Badding, Yoel Fink, John Ballato, and Ayman F Abouraddy. Infrared fibers. *Advances in Optics and Photonics*, 7(2) :379–458, 2015.

[10] KO Hill, DC Johnson, and BS Kawasaki. cw generation of multiple stokes and anti-stokes brillouin-shifted frequencies. *Applied Physics Letters*, 29(3) :185–187, 1976.

[11] SP Smith, F Zarinetchi, and S Ezekiel. Narrow-linewidth stimulated brillouin fiber laser and applications. *Optics letters*, 16(6) :393–395, 1991.

[12] Joseph B Murray, Alex Cerjan, and Brandon Redding. Distributed brillouin fiber laser sensor. *Optica*, 9(1) :80–87, 2022.

[13] RV Ambartsumyan, NG Basov, PG Kryukov, and VS Letokhov. A laser with a nonresonant feedback. *IEEE J. Quantum Electron*, 2(9) :442–446, 1966.

[14] Suchara Sriratanavaree. *The characterisation of acoustic waves in optical waveguides*. PhD thesis, City University London, 2014.

[15] Gordon S Kino. *Acoustic waves : devices, imaging, and analog signal processing*, volume 107. Prentice-hall Englewood Cliffs, NJ, 1987.

[16] Bertram Alexander Auld. *Acoustic fields and waves in solids*. Ripol Classic, 1973.

[17] Peter T Rakich, Paul Davids, and Zheng Wang. Tailoring optical forces in waveguides through radiation pressure and electrostrictive forces. *Optics express*, 18(14) :14439–14453, 2010.

[18] Xiaoyi Bao. Optical fiber sensors based on brillouin scattering. *Optics and Photonics News*, 20(9) :40–45, 2009.

[19] Dengwang Zhou, Yongkang Dong, Benzhang Wang, Chao Pang, Dexin Ba, Hongying Zhang, Zhiwei Lu, Hui Li, and Xiaoyi Bao. Single-shot botda based on an optical chirp chain probe wave for distributed ultrafast measurement. *Light : Science & Applications*, 7(1) :1–11, 2018.

[20] Tsuneo Horiguchi, Kaoru Shimizu, Toshio Kurashima, Mitsuhiro Tateda, and Yahei Koyamada. Development of a distributed sensing technique using brillouin scattering. *Journal of lightwave technology*, 13(7) :1296–1302, 1995.

[21] Thomas Kessler, Christian Hagemann, C Grebing, T Legero, Uwe Sterr, Fritz Riehle, MJ Martin, L Chen, and J Ye. A sub-40-mhz-linewidth laser based on a silicon single-crystal optical cavity. *Nature Photonics*, 6(10) :687–692, 2012.

[22] Jihong Geng, Sean Staines, Zuolan Wang, Jie Zong, Mike Blake, and Shibin Jiang. Highly stable low-noise brillouin fiber laser with ultranarrow spectral linewidth. *IEEE Photonics Technology Letters*, 18(17) :1813–1815, 2006.

[23] Haiyang Wang, Ping Lu, Chen Chen, Stephen Mihailov, Liang Chen, and Xiaoyi Bao. Stabilizing brillouin random laser with photon localization by feedback of distributed random fiber grating array. *Optics Express*, 30(12) :20712–20724, 2022.

[24] Kwang Yong Song and Kazuo Hotate. 25 ghz bandwidth brillouin slow light in optical fibers. *Optics letters*, 32(3) :217–219, 2007.

[25] Miguel Gonzalez-Herraez, Kwang-Yong Song, and Luc Thévenaz. Optically controlled slow and fast light in optical fibers using stimulated brillouin scattering. *Applied Physics Letters*, 87(8) :081113, 2005.

[26] David Marpaung, Blair Morrison, Mattia Pagani, Ravi Pant, Duk-Yong Choi, Barry Luther-Davies, Steve J Madden, and Benjamin J Eggleton. Low-power, chip-based stimulated brillouin scattering microwave photonic filter with ultrahigh selectivity. *Optica*, 2(2) :76–83, 2015.

[27] Weiwei Zhang and Robert A Minasian. Widely tunable single-passband microwave photonic filter based on stimulated brillouin scattering. *IEEE Photonics Technology Letters*, 23(23) :1775–1777, 2011.

[28] Jiang Li, Myoung-Gyun Suh, and Kerry Vahala. Microresonator brillouin gyroscope. *Optica*, 4(3) :346–348, 2017.

[29] Tobias J Kippenberg, Ronald Holzwarth, and Scott A Diddams. Microresonator-based optical frequency combs. *science*, 332(6029) :555–559, 2011.

[30] DS Ballantine Jr, Robert M White, Stephen J Martin, Antonio J Ricco, ET Zellers, GC Frye, and H Wohltjen. *Acoustic wave sensors : theory, design and physico-chemical applications*. Elsevier, 1996.

[31] R Chen, GF Fernando, T Butler, and RA Badcock. A novel ultrasound fibre optic sensor based on a fused-tapered optical fibre coupler. *Measurement Science and Technology*, 15(8) :1490, 2004.

[32] Allan F Bower. *Applied mechanics of solids*. CRC press, 2009.

[33] GB Hocker. Fiber-optic sensing of pressure and temperature. *Applied optics*, 18(9) :1445–1448, 1979.

[34] Aldo Minardo, Andrea Cusano, Romeo Bernini, Luigi Zeni, and Michele Giordano. Response of fiber bragg gratings to longitudinal ultrasonic waves. *IEEE transactions on ultrasonics, ferroelectrics, and frequency control*, 52(2) :304–312, 2005.

[35] Dnyandeo Pawar, Ch N Rao, Ravi Kant Choubey, and SN Kale. Mach-zehnder interferometric photonic crystal fiber for low acoustic frequency detections. *Applied Physics Letters*, 108(4) :041912, 2016.

[36] Huibo Fan, Liang Zhang, Song Gao, Liang Chen, and Xiaoyi Bao. Ultrasound sensing based on an in-fiber dual-cavity fabry–perot interferometer. *Optics letters*, 44(15) :3606–3609, 2019.

[37] Qi Wu and Yoji Okabe. High-sensitivity ultrasonic phase-shifted fiber bragg grating balanced sensing system. *Optics express*, 20(27) :28353–28362, 2012.

[38] Xiaoyi Bao and Liang Chen. Recent progress in distributed fiber optic sensors. *sensors*, 12(7) :8601–8639, 2012.

[39] Toshio Kurashima, Tsuneo Horiguchi, and Mitsuhiro Tateda. Distributed-temperature sensing using stimulated brillouin scattering in optical silica fibers. *Optics letters*, 15(18) :1038–1040, 1990.

[40] Xiaoyi Bao, David J Webb, and David A Jackson. 32-km distributed temperature sensor based on brillouin loss in an optical fiber. *Optics letters*, 18(18) :1561–1563, 1993.

[41] Xiaoyi Bao and Liang Chen. Recent progress in brillouin scattering based fiber sensors. *Sensors*, 11(4) :4152–4187, 2011.

[42] Wenhai Li, Xiaoyi Bao, Yun Li, and Liang Chen. Differential pulse-width pair botda for high spatial resolution sensing. *Optics express*, 16(26) :21616–21625, 2008.

[43] Kinzo Kishida, Che-Hien Li, and Ken'ichi Nishiguchi. Pulse pre-pump method for cm-order spatial resolution of botda. In *17th International Conference on Optical Fibre Sensors*, volume 5855, pages 559–562. International Society for Optics and Photonics, 2005.

[44] Kazuo Hotate and Takemi Hasegawa. Measurement of brillouin gain spectrum distribution along an optical fiber using a correlation-based technique–proposal, experiment and simulation–. *IEICE transactions on electronics*, 83(3) :405–412, 2000.

[45] Kwang Yong Song, Zuyuan He, and Kazuo Hotate. Distributed strain measurement with millimeter-order spatial resolution based on brillouin optical correlation domain analysis. *Optics letters*, 31(17) :2526–2528, 2006.

[46] Atiyeh Zarifi, Birgit Stiller, Moritz Merklein, Yang Liu, Blair Morrison, Alvaro Casas-Bedoya, Guanghui Ren, Thach G Nguyen, Khu Vu, Duk-Yong Choi, et al. On-chip correlation-based brillouin sensing : design, experiment, and simulation. *JOSA B*, 36(1) :146–152, 2019.

[47] Kwang Yong Song, Weiwen Zou, Zuyuan He, and Kazuo Hotate. All-optical dynamic grating generation based on brillouin scattering in polarization-maintaining fiber. *Optics letters*, 33(9) :926–928, 2008.

[48] Taofei Jiang, Dengwang Zhou, Meng Xia, Lei Teng, Dexin Ba, and Yongkang Dong. Distributed birefringence measurement of a polarization-maintaining fiber with an extended range based on an enhanced brillouin dynamic grating. *IEEE Photonics Journal*, 12(4) :1–7, 2020.

[49] Kwang Yong Song, Sanghoon Chin, Nikolay Primerov, and Luc Thévenaz. Time-domain distributed fiber sensor with 1 cm spatial resolution based on brillouin dynamic grating. *Journal of Lightwave Technology*, 28(14) :2062–2067, 2010.

[50] Hongying Zhang, Lei Teng, and Yongkang Dong. Distributed salinity sensor with a polyimide-coated photonic crystal fiber based on brillouin dynamic grating. *Journal of Lightwave Technology*, 2020.

[51] Yongkang Dong, Lei Teng, Peilin Tong, Taofei Jiang, Hongying Zhang, Tao Zhu, Liang Chen, Xiaoyi Bao, and Zhiwei Lu. High-sensitivity distributed transverse load

sensor with an elliptical-core fiber based on brillouin dynamic gratings. *Optics letters*, 40(21) :5003–5006, 2015.

[52] RM Shelby, MD Levenson, and PW Bayer. Guided acoustic-wave brillouin scattering. *Physical Review B*, 31(8) :5244, 1985.

[53] Yair Antman, Alex Clain, Yosef London, and Avi Zadok. Optomechanical sensing of liquids outside standard fibers using forward stimulated brillouin scattering. *Optica*, 3(5) :510–516, 2016.

[54] Jean-Charles Beugnot, Sylvie Lebrun, Gilles Pauliat, Hervé Maillotte, Vincent Laude, and Thibaut Sylvestre. Brillouin light scattering from surface acoustic waves in a subwavelength-diameter optical fibre. *Nature communications*, 5(1) :1–6, 2014.

[55] Omar Florez, Paulo F Jarschel, Yovanny AV Espinel, CMB Cordeiro, TP Mayer Alegre, Gustavo S Wiederhecker, and Paulo Dainese. Brillouin scattering self-cancellation. *Nature communications*, 7(1) :1–8, 2016.

[56] Peter T Rakich, Charles Reinke, Ryan Camacho, Paul Davids, and Zheng Wang. Giant enhancement of stimulated brillouin scattering in the subwavelength limit. *Physical Review X*, 2(1) :011008, 2012.

[57] Gustavo S Wiederhecker, Paulo Dainese, and Thiago P Mayer Alegre. Brillouin optomechanics in nanophotonic structures. *APL Photonics*, 4(7) :071101, 2019.

[58] Chenhui Huang, Huojiao Sun, Hao Liang, Linghao Cheng, Liang Chen, Xiaoyi Bao, and Bai-Ou Guan. Refractive index sensing based on brillouin scattering in a micro fiber. *Applied Physics Express*, 12(8) :082013, 2019.

[59] Jinding Huang, Xiaoxuan Zhong, Hao Liang, Linghao Cheng, Jie Li, and Bai-Ou Guan. Brillouin scattering from hybrid acoustic wave in a microscaled fiber for gas pressure sensing. *IEEE Photonics Journal*, 9(2) :1–6, 2017.

[60] Yi Liu, Yuanqi Gu, Yu Ning, Pengfei Chen, Yao Yao, Yajun You, Wenjun He, and Xiujian Chou. Temperature and strain sensitivities of surface and hybrid acoustic wave brillouin scattering in optical microfibers. *Chinese Physics B*, 2022.

[61] Mbaye Diouf, Abderrahmen Trichlli, and Mourad Zghal. Stimulated brillouin scattering-based slow light using singlemode as2s3 chalcogenide photonic crystal fiber for temperature sensing. In *Laser Science*, pages JTu3A–63. Optical Society of America, 2019.

[62] Guanshi Qin, Atsushi Mori, and Yasutake Ohishi. Brillouin lasing in a single-mode tellurite fiber. *Optics letters*, 32(15) :2179–2181, 2007.

[63] Kazi S Abedin. Observation of strong stimulated brillouin scattering in single-mode as 2 se 3 chalcogenide fiber. *Optics Express*, 13(25) :10266–10271, 2005.

[64] Kazi S Abedin. Brillouin amplification and lasing in a single-mode as 2 se 3 chalcogenide fiber. *Optics letters*, 31(11) :1615–1617, 2006.

[65] Eric C Mägi, LB Fu, Hong C Nguyen, MRE Lamont, DI Yeom, and BJ Eggleton. Enhanced kerr nonlinearity in sub-wavelength diameter as2se3 chalcogenide fiber tapers. *Optics Express*, 15(16) :10324–10329, 2007.

[66] Chams Baker and Martin Rochette. Highly nonlinear hybrid asse-pmma microtapers. *Optics express*, 18(12) :12391–12398, 2010.

[67] Jean-Charles Beugnot, Raja Ahmad, Martin Rochette, Vincent Laude, Hervé Maillotte, and Thibaut Sylvestre. Reduction and control of stimulated brillouin scattering in polymer-coated chalcogenide optical microwires. *Optics letters*, 39(3) :482–485, 2014.

[68] Bhavaye Saxena, Chams Baker, Xiaoyi Bao, and Liang Chen. High birefringent brillouin frequency shifts in a single-mode as 2 se 3-pmma microtaper induced by a transverse load. *Optics Letters*, 44(19) :4789–4792, 2019.

[69] Song Gao, Chams Baker, Liang Chen, and Xiaoyi Bao. Simultaneous measurement of temperature and strain in a dual-core as 2 se 3-pmma taper. *IEEE Photonics Technology Letters*, 30(1) :79–82, 2017.

[70] Haiyang Wang, Liang Chen, and Xiaoyi Bao. Salinity concentration sensing based on a tapered dual-core as 2 se 3-pmma hybrid fiber. *IEEE Photonics Technology Letters*, 33(4) :181–184, 2021.

[71] Brandon Redding, Michael A Choma, and Hui Cao. Speckle-free laser imaging using random laser illumination. *Nature photonics*, 6(6) :355–359, 2012.

[72] Michele Gaio, Soraya Caixeiro, Benedetto Marelli, Fiorenzo G Omenetto, and Riccardo Sapienza. Gain-based mechanism for p h sensing based on random lasing. *Physical Review Applied*, 7(3) :034005, 2017.

[73] Jiancheng Deng, DV Churkin, Zuowei Xu, and Xuewen Shu. Random fiber laser based on a partial-reflection random fiber grating for high temperature sensing. *Optics Letters*, 46(5) :957–960, 2021.

[74] Kyungduk Kim, Stefan Bittner, Yongquan Zeng, Stefano Guazzotti, Ortwin Hess, Qi Jie Wang, and Hui Cao. Massively parallel ultrafast random bit generation with a chip-scale laser. *Science*, 371(6532) :948–952, 2021.

[75] Johannes Fallert, Roman JB Dietz, Janos Sartor, Daniel Schneider, Claus Klingshirn, and Heinz Kalt. Co-existence of strongly and weakly localized random laser modes. *Nature Photonics*, 3(5) :279–282, 2009.

[76] Valery Milner and Azriel Z Genack. Photon localization laser : low-threshold lasing in a random amplifying layered medium via wave localization. *Physical review letters*, 94(7) :073901, 2005.

[77] Behnam Abaie, Esmaeil Mobini, Salman Karbasi, Thomas Hawkins, John Ballato, and Arash Mafi. Random lasing in an anderson localizing optical fiber. *Light : Science & Applications*, 6(8) :e17041–e17041, 2017.

[78] Hui Cao. Lasing in random media. *Waves in random media*, 13(3) :R1, 2003.

[79] Christiano JS de Matos, Leonardo de S Menezes, Antonio M Brito-Silva, MA Martinez Gámez, Anderson SL Gomes, and Cid B de Araujo. Random fiber laser. *Physical review letters*, 99(15) :153903, 2007.

[80] Sergei K Turitsyn, Sergey A Babin, Atalla E El-Taher, Paul Harper, Dmitriy V Churkin, Sergey I Kablukov, Juan Diego Ania-Castañón, Vassilis Karalekas, and Evgenii V Podivilov. Random distributed feedback fibre laser. *Nature photonics*, 4(4) :231–235, 2010.

[81] SA Babin, AE El-Taher, P Harper, EV Podivilov, and SK Turitsyn. Tunable random fiber laser. *Physical Review A*, 84(2) :021805, 2011.

[82] Guolu Yin, Bhavaye Saxena, and Xiaoyi Bao. Tunable er-doped fiber ring laser with single longitudinal mode operation based on rayleigh backscattering in single mode fiber. *Optics express*, 19(27) :25981–25989, 2011.

[83] Türeci Hakan, Ge Li, Rotter Stefan, and Stone A. Douglas. Strong interactions in multimode random lasers. https://www.eng.yale.edu/stonegroup/science.html.

[84] Han Wu, Zinan Wang, Wei Sun, Qiheng He, Zedong Wei, and Yun-Jiang Rao. 1.5 $\mu$m low threshold, high efficiency random fiber laser with hybrid erbium–raman gain. *Journal of Lightwave Technology*, 36(4) :844–849, 2018.

[85] Meng Pang, Shangran Xie, Xiaoyi Bao, Da-Peng Zhou, Yuangang Lu, and Liang Chen. Rayleigh scattering-assisted narrow linewidth brillouin lasing in cascaded fiber. *Optics letters*, 37(15) :3129–3131, 2012.

[86] Sergei K Turitsyn, Sergey A Babin, Dmitry V Churkin, Ilya D Vatnik, Maxim Nikulin, and Evgenii V Podivilov. Random distributed feedback fibre lasers. *Physics reports*, 542(2) :133–193, 2014.

[87] N Lizárraga, NP Puente, EI Chaikina, TA Leskova, and ER Méndez. Single-mode er-doped fiber random laser with distributed bragg grating feedback. *Optics express*, 17(2) :395–404, 2009.

[88] Mathieu Gagné and Raman Kashyap. Demonstration of a 3 mw threshold er-doped random fiber laser based on a unique fiber bragg grating. *Optics express*, 17(21) :19067–19074, 2009.

[89] Ping Lu, Stephen J Mihailov, David Coulas, Huimin Ding, and Xiaoyi Bao. Low-loss random fiber gratings made with an fs-ir laser for distributed fiber sensing. *Journal of Lightwave Technology*, 37(18) :4697–4702, 2019.

[90] Yuan Wang, Ping Lu, Stephen Mihailov, Liang Chen, and Xiaoyi Bao. Distributed time delay sensing in a random fiber grating array based on chirped pulse $\varphi$-otdr. *Optics Letters*, 45(13) :3423–3426, 2020.

[91] Zichao Zhou, Ping Lu, Liang Zhang, Stephen Mihailov, Liang Chen, and Xiaoyi Bao. Thermal and acoustic noise insensitive brillouin random fiber laser based on polarization-maintaining random fiber grating. *Optics letters*, 44(17) :4195–4198, 2019.

[92] Yanping Xu, Song Gao, Ping Lu, Stephen Mihailov, Liang Chen, and Xiaoyi Bao. Low-noise brillouin random fiber laser with a random grating-based resonator. *Optics letters*, 41(14) :3197–3200, 2016.

[93] Bahaa EA Saleh and Malvin Carl Teich. *Fundamentals of photonics*. john Wiley & sons, 2019.

[94] EI Chaikina, N Lizárraga, and ER Mendez. Random cavity formation in an er-doped fiber laser. In *The European Conference on Lasers and Electro-Optics*, page CK10_6. Optica Publishing Group, 2007.

[95] Liang Zhang, Ping Lu, Zichao Zhou, Yuan Wang, Stephen Mihailov, Liang Chen, and Xiaoyi Bao. High-efficiency random fiber laser based on strong random fiber grating for mhz ultrasonic sensing. *IEEE Sensors Journal*, 20(11) :5885–5892, 2020.

[96] Lulu Wang, Xinyong Dong, Perry Ping Shum, Changqing Huang, and Haibin Su. Erbium-doped fiber laser with distributed rayleigh output mirror. *Laser Physics*, 24(11) :115101, 2014.

[97] Bhavaye Saxena, Xiaoyi Bao, and Liang Chen. Suppression of thermal frequency noise in erbium-doped fiber random lasers. *Optics letters*, 39(4) :1038–1041, 2014.

[98] Yang Li, Ping Lu, Xiaoyi Bao, and Zhonghua Ou. Random spaced index modulation for a narrow linewidth tunable fiber laser with low intensity noise. *Optics letters*, 39(8) :2294–2297, 2014.

[99] Lulu Wang, Xinyong Dong, Perry Ping Shum, and Haibin Su. Tunable erbium-doped fiber laser based on random distributed feedback. *IEEE Photonics Journal*, 6(5) :1–5, 2014.

[100] Suhairie Saleh, Noran Azizan Cholan, Abdul Hadi Sulaiman, and Mohd Adzir Mahdi. Stable multiwavelength erbium-doped random fiber laser. *IEEE Journal of Selected Topics in Quantum Electronics*, 24(3) :1–6, 2017.

[101] Bhavaye Saxena. *Noise characteristics for random fiber lasers with Rayleigh distributed feedback*. PhD thesis, Université d'Ottawa/University of Ottawa, 2014.

[102] Sergei K Turitsyn, Juan D Ania-Castañón, SA Babin, Vasileios Karalekas, Paul Harper, D Churkin, SI Kablukov, AE El-Taher, EV Podivilov, and VK Mezentsev. 270-km ultralong raman fiber laser. *Physical review letters*, 103(13) :133901, 2009.

[103] Atalla E El-Taher, Paul Harper, SA Babin, DV Churkin, EV Podivilov, Juan Diego Ania-Castanon, and SK Turitsyn. Effect of rayleigh-scattering distributed feedback on multiwavelength raman fiber laser generation. *Optics letters*, 36(2) :130–132, 2011.

[104] Zinan Wang, Han Wu, Mengqiu Fan, Li Zhang, Yunjiang Rao, Weili Zhang, and Xinhong Jia. High power random fiber laser with short cavity length : theoretical and experimental investigations. *IEEE Journal of Selected Topics in Quantum Electronics*, 21(1) :10–15, 2014.

[105] SR Abdullina, MI Skvortsov, AA Vlasov, EV Podivilov, and SA Babin. Coherent raman lasing in a short polarization-maintaining fiber with a random fiber bragg grating array. *Laser Physics Letters*, 16(10) :105001, 2019.

[106] Xin-Hong Jia, Yun-Jiang Rao, Fei Peng, Zi-Nan Wang, Wei-Li Zhang, Hui-Juan Wu, and Yun Jiang. Random-lasing-based distributed fiber-optic amplification. *Optics express*, 21(5) :6572–6577, 2013.

[107] ZN Wang, YJ Rao, Han Wu, PY Li, Y Jiang, XH Jia, and WL Zhang. Long-distance fiber-optic point-sensing systems based on random fiber lasers. *Optics express*, 20(16) :17695–17700, 2012.

[108] Andrei A Fotiadi and Roman V Kiyan. Cooperative stimulated brillouin and rayleigh backscattering process in optical fiber. *Optics letters*, 23(23) :1805–1807, 1998.

[109] Meng Pang, Xiaoyi Bao, and Liang Chen. Observation of narrow linewidth spikes in the coherent brillouin random fiber laser. *Optics letters*, 38(11) :1866–1868, 2013.

[110] Meng Pang, Xiaoyi Bao, Liang Chen, Zengguang Qin, Yang Lu, and Ping Lu. Frequency stabilized coherent brillouin random fiber laser : theory and experiments. *Optics express*, 21(22) :27155–27168, 2013.

[111] Yuxi Pang, Yanping Xu, Xian Zhao, Zengguang Qin, and Zhaojun Liu. Stabilized narrow-linewidth brillouin random fiber laser with a double-coupler fiber ring resonator. *Journal of Lightwave Technology*, 2022.

[112] Liang Zhang, Chen Wang, Zhengying Li, Yanping Xu, Bhavaye Saxena, Song Gao, Liang Chen, and Xiaoyi Bao. High-efficiency brillouin random fiber laser using all-polarization maintaining ring cavity. *Optics express*, 25(10) :11306–11314, 2017.

[113] Liang Zhang, Yanping Xu, Song Gao, Bhavaye Saxena, Liang Chen, and Xiaoyi Bao. Linearly polarized low-noise brillouin random fiber laser. *Optics letters*, 42(4) :739–742, 2017.

[114] Zichao Zhou, Liang Chen, and Xiaoyi Bao. Dynamic detection of acoustic wave generated by polarization maintaining brillouin random fiber laser. *APL Photonics*, 5(9) :096101, 2020.

[115] Zichao Zhou, Haiyang Wang, Yuan Wang, Liang Chen, and Xiaoyi Bao. Distributed static and dynamic detection of an acoustic wave in a brillouin random fiber laser. *Photonics Research*, 9(5) :772–780, 2021.

[116] Srikanth Sugavanam, Mariia Sorokina, and Dmitry V Churkin. Spectral correlations in a random distributed feedback fibre laser. *Nature communications*, 8(1) :1–8, 2017.

[117] Y Bliokh, EI Chaikina, ID Vatnik, and DV Churkin. Temporal variation of the spectrum of a continuously pumped random fiber laser : phenomenological model. *JOSA B*, 36(2) :408–414, 2019.

[118] Pedro Tovar and Jean Pierre von der Weid. Dynamic evolution of narrow spectral modes in stochastic brillouin random fiber lasers. *IEEE Photonics Technology Letters*, 33(24) :1471–1474, 2021.

[119] Paul Lévy and Paul Lévy. *Calcul des probabilités*. Gauthier-Villars, 1925.

[120] Stefano Lepri, Stefano Cavalieri, Gian-Luca Oppo, and Diederik S Wiersma. Statistical regimes of random laser fluctuations. *Physical Review A*, 75(6) :063820, 2007.

[121] Emilio Ignesti, Federico Tommasi, Lorenzo Fini, Stefano Lepri, Vivekananthan Radhalakshmi, Diederik Wiersma, and Stefano Cavalieri. Experimental and theoretical investigation of statistical regimes in random laser emission. *Physical Review A*, 88(3) :033820, 2013.

[122] Anderson SL Gomes, Ernesto P Raposo, André L Moura, Serge I Fewo, Pablo IR Pincheira, Vladimir Jerez, Lauro JQ Maia, and Cid B De Araújo. Observation of lévy distribution and replica symmetry breaking in random lasers from a single set of measurements. *Scientific reports*, 6(1) :1–8, 2016.

[123] Bismarck C Lima, Anderson SL Gomes, Pablo IR Pincheira, André L Moura, Mathieu Gagné, Ernesto P Raposo, Cid B de Araújo, and Raman Kashyap. Observation of lévy statistics in one-dimensional erbium-based random fiber laser. *JOSA B*, 34(2) :293–299, 2017.

[124] Jiaqi Li, Han Wu, Zinan Wang, Shengtao Lin, Chongyu Lu, Ernesto P Raposo, Anderson SL Gomes, and Yunjiang Rao. Lévy spectral intensity statistics in a raman random fiber laser. *Optics Letters*, 44(11) :2799–2802, 2019.

[125] N Ghofraniha, I Viola, F Di Maria, G Barbarella, G Gigli, L Leuzzi, and C Conti. Experimental evidence of replica symmetry breaking in random lasers. *Nature communications*, 6(1) :1–8, 2015.

[126] Anderson SL Gomes, Bismarck C Lima, Pablo IR Pincheira, André L Moura, Mathieu Gagné, Ernesto P Raposo, Cid B de Araújo, and Raman Kashyap. Glassy behavior in a one-dimensional continuous-wave erbium-doped random fiber laser. *Physical Review A*, 94(1) :011801, 2016.

[127] Zichao Zhou, Liang Chen, and Xiaoyi Bao. High efficiency brillouin random fiber laser with replica symmetry breaking enabled by random fiber grating. *Optics express*, 29(5) :6532–6541, 2021.

[128] Immanuil L Fabelinskii. *Molecular scattering of light*. Springer Science & Business Media, 2012.

[129] Robert W Boyd. *Nonlinear optics*. Academic press, 2020.

[130] Philip W Anderson. Absence of diffusion in certain random lattices. *Physical review*, 109(5) :1492, 1958.

[131] Sajeev John. Localization of light. *Phys. Today*, 44(5) :32–40, 1991.

[132] Arash Mafi. Transverse anderson localization of light : a tutorial. *Advances in Optics and Photonics*, 7(3) :459–515, 2015.

[133] Jonathan Andreasen, AA Asatryan, LC Botten, MA Byrne, Hui Cao, Li Ge, Laurent Labonté, Patrick Sebbah, AD Stone, HE Türeci, et al. Modes of random lasers. *Advances in Optics and Photonics*, 3(1) :88–127, 2011.

[134] Bhupesh Kumar, Ran Homri, Santosh K Maurya, Melanie Lebental, Patrick Sebbah, et al. Localized modes revealed in random lasers. *Optica*, 8(8) :1033–1039, 2021.

[135] Aart Lagendijk, Bart Van Tiggelen, and Diederik S Wiersma. Fifty years of anderson localization. *Phys. today*, 62(8) :24–29, 2009.

[136] John David Jackson. Classical electrodynamics, 1999.

[137] MV Berry and S Klein. Transparent mirrors : rays, waves and localization. *European Journal of Physics*, 18(3) :222, 1997.

[138] Ofer Shapira and Baruch Fischer. Localization of light in a random-grating array in a single-mode fiber. *JOSA B*, 22(12) :2542–2552, 2005.

[139] AL Burin, Mark A Ratner, H Cao, and SH Chang. Random laser in one dimension. *Physical review letters*, 88(9) :093904, 2002.

[140] Max Schiemangk, Stefan Spießberger, Andreas Wicht, Götz Erbert, Günther Tränkle, and Achim Peters. Accurate frequency noise measurement of free-running lasers. *Applied optics*, 53(30) :7138–7143, 2014.

[141] Dan Xu, Fei Yang, Dijun Chen, Fang Wei, Haiwen Cai, Zujie Fang, and Ronghui Qu. Laser phase and frequency noise measurement by michelson interferometer composed of a 3× 3 optical fiber coupler. *Optics express*, 23(17) :22386–22393, 2015.

[142] Y Takushima, HY Choi, and Yun Chur Chung. Measurement of differential phasor diagram of multilevel dpsk signals by using an adjustment-free delay interferometer composed of a 3*times*3 optical coupler. *Journal of lightwave technology*, 27(6) :718–730, 2009.

[143] Peter Welch. The use of fast fourier transform for the estimation of power spectra : a method based on time averaging over short, modified periodograms. *IEEE Transactions on audio and electroacoustics*, 15(2) :70–73, 1967.

[144] Takanori Okoshi, Kazuro Kikuchi, and Akira Nakayama. Novel method for high resolution measurement of laser output spectrum. *Electronics letters*, 16(16) :630–631, 1980.

[145] Linden B Mercer. 1/f frequency noise effects on self-heterodyne linewidth measurements. *Journal of Lightwave Technology*, 9(4) :485–493, 1991.

[146] P Gallion and Guy Debarge. Quantum phase noise and field correlation in single frequency semiconductor laser systems. *IEEE Journal of Quantum Electronics*, 20(4) :343–349, 1984.

[147] Dao Xiang, Ping Lu, Yanping Xu, Song Gao, Liang Chen, and Xiaoyi Bao. Truly random bit generation based on a novel random brillouin fiber laser. *Optics letters*, 40(22) :5415–5418, 2015.

[148] Song Gao, Liang Zhang, Yanping Xu, Liang Chen, and Xiaoyi Bao. High-speed random bit generation via brillouin random fiber laser with non-uniform fibers. *IEEE Photonics Technology Letters*, 29(16) :1352–1355, 2017.

[149] Song Gao, Liang Zhang, Yanping Xu, Ping Lu, Liang Chen, and Xiaoyi Bao. Tapered fiber based brillouin random fiber laser and its application for linewidth measurement. *Optics express*, 24(25) :28353–28360, 2016.

[150] Jean-Charles Beugnot and Vincent Laude. Electrostriction and guidance of acoustic phonons in optical fibers. *Physical Review B*, 86(22) :224304, 2012.

[151] Chams Baker. Hybrid as2se3-pmma microtapers and applications. 2013.

[152] Jeff Smith, Anthony Brown, Michael DeMerchant, and Xiaoyi Bao. Simultaneous distributed strain and temperature measurement. *Applied optics*, 38(25) :5372–5377, 1999.

[153] Neisei Hayashi, Yosuke Mizuno, and Kentaro Nakamura. Brillouin gain spectrum dependence on large strain in perfluorinated graded-index polymer optical fiber. *Optics express*, 20(19) :21101–21106, 2012.

[154] Yosuke Mizuno, Masato Kishi, Kazuo Hotate, Takaaki Ishigure, and Kentaro Nakamura. Observation of stimulated brillouin scattering in polymer optical fiber with pump–probe technique. *Optics letters*, 36(12) :2378–2380, 2011.

[155] Kentaro Nakamura, Irwan R Husdi, and Sadayuki Ueha. A distributed strain sensor with the memory effect based on the pof otdr. In *17th International Conference on Optical Fibre Sensors*, volume 5855, pages 807–810. International Society for Optics and Photonics, 2005.

[156] Song Gao, Chams Baker, Liang Chen, and Xiaoyi Bao. Approach for temperature-insensitive strain measurement using a dual-core as 2 se 3-pmma taper. *Optics letters*, 43(7) :1523–1526, 2018.

[157] Kwang Yong Song, Yong Hyun Kim, and Byoung Yoon Kim. Intermodal stimulated brillouin scattering in two-mode fibers. *Optics letters*, 38(11) :1805–1807, 2013.

[158] Christian Broadway, Rui Min, Arnaldo Gomes Leal-Junior, Carlos Marques, and Christophe Caucheteur. Toward commercial polymer fiber bragg grating sensors : Review and applications. *Journal of Lightwave Technology*, 37(11) :2605–2615, 2019.

[159] Wenwen Ma, Huibo Fan, Liang Chen, and Xiaoyi Bao. Tapered assisted dual micro-bubble-device for ultrasound sensor. *IEEE Photonics Technology Letters*, 32(18) :1219–1222, 2020.